THE UNIVERSITY OF MICHIGAN
ANN ARBOR, MICHIGAN

LOW-FREQUENCY BEAM-PLASMA INTERACTIONS IN A FINITE-SIZED PLASMA

Technical Report No. 121

Electron Physics Laboratory
Department of Electrical Engineering

By (Ved Prakash)
V. P. Bhatnagar

Project 034510

RESEARCH GRANT NO. GK-15689
DIVISION OF ENGINEERING
NATIONAL SCIENCE FOUNDATION
WASHINGTON, D. C. 20550

August, 1971

ensm

UMR8544

ABSTRACT

This study is concerned with the experimental and theoretical investigation of ion heating via the generation of a large, low-frequency RF electric field in a plasma by a modulated electron beam.

The beam-generated plasma is approximately 60 cm in length and 6 mm in diameter. An electron beam with 400 to 1000 V energy and 2 to 3 mA of current is used. Either hydrogen, deuterium, neon or argon gas is used with pressures in the range of 10^{-4} to 10^{-3} Torr. The plasma has a density in the range of 5×10^{8} to $5 \times 10^{9}/cm^{3}$ and a typical electron temperature of 6 eV. The ratio of plasma density to beam density is approximately 25, and an axial magnetic field of 300 to 400 G is used.

The RF field in the plasma is observed with an RF Langmuir probe, and energetic ions are detected by a retarding potential energy analyzer. Two or three resonances which lie just above the ion-plasma frequency (i.e., in the range of 2 to 25 MHz) are typically observed in the probe responses. The two lowest resonances are found to be half- and full-wavelength resonances of axisymmetric modes. The retarding potential energy analyzer curves indicate that the largest ion energy spread occurs when the beam is modulated at a resonant frequency.

The beam-plasma system is analyzed as a finite-length, boundary value problem with a specified driving current. The cold-plasma, quasi-static dispersion equation for the axial propagation constant k_z includes the effect of finite beam and plasma radii, electron-beam space charge, uniform axial magnetic field and plasma electron-neutral collisions. The dispersion equation is solved for the lowest-order radial, axisymmetric mode.

The quasi-static potential, beam-modulation current and beam-modulation velocity are expressed as superpositions of four normal modes of the beam-plasma waveguide. The appropriate boundary conditions are applied at the two ends of the system. The phases and amplitudes of the total electric field, beam current and beam velocity at an arbitrary position are calculated as functions of frequency.

The results of the normal-mode analysis are in good agreement with the experiment and can be used to predict the values of the resonant frequencies and their variations with plasma density, beam voltage, ion mass and magnetic field.

The ion heating process suggested by the analysis and experiment is that the electron beam excites resonant modes of the plasma-cavity resonator, and that at these resonances a large radial electric field is created in the plasma which excites ion oscillations. The generation of this large RF field at low frequencies results in the observed ion heating. The importance of this result is that the electron beam can transfer energy directly to the plasma ions at frequencies other than those at which there is a strong beam-plasma instability.

ACKNOWLEDGMENT

The author wishes to express his sincere gratitude to his doctoral committee. In particular, the constant help, guidance and encouragement of his doctoral committee chairman, Professor Ward D. Getty, throughout the course of this work are deeply appreciated. Special thanks are due to Mr. M. Gene Robinson and his technical staff for their help in constructing the experimental device. Finally, the author is grateful to Miss Betty Cummings, editor; Mrs. Wanita Rasey, typist; and Mr. Leslie Shive, draftsmar. for their excellent work in the preparation of the manuscript.

The work was supported by the National Science Foundation under Research Grant No. GK-15689.

TABLE OF CONTENTS

LIST OF ILLUSTRATIONS

LIST OF TABLES

CHAPTER I. INTRODUCTION

One of the important problems of thermonuclear research is to heat an initially cold plasma to very high temperatures necessary for controlled thermonuclear reactions to occur. This investigation is concerned with the generation of a large low-frequency radial RF electric field in a plasma for the purpose of ion heating. The main task is to understand the basic mechanism of excitation of the RF electric field and its propagation characteristics. Only small-signal behavior is studied and no efforts are directed toward achieving a very energetic plasma.

In the present investigation, experimental and theoretical evidence is presented which shows that a modulated electron beam excites resonances in a beam-generated plasma, and that at the resonant frequencies a relatively large radial RF electric field is excited in the plasma which produces the observed ion heating. The excitation frequency is near the electron-ion lower-hybrid frequency and is of particular interest because at this frequency the ions oscillate with an average kinetic energy equal to or greater than that of the electrons in the presence of an RF electric field.

1.1 General Theoretical Background

In this section some basic plasma physics is discussed which is of general interest in the present study. Section 1.1.1 gives a general definition of a plasma and introduces a few characteristic quantities such as plasma frequency, cyclotron frequency, Debye length, etc.

Section 1.1.2 contains a list of a few of the important engineering applications of plasmas and briefly describes the controlled fusion program which promises a potentially great future source of energy. Section 1.1.3 presents briefly a classification of different waves that exist in an infinite plasma. It is noted in this section that many types of plasma waves can propagate in a plasma depending on the model. Dispersion characteristics for waves in longitudinally magnetized plasma waveguides have been given for different cases as these are of utmost importance in the present investigation. Section 1.1.4 describes the electron beam-plasma systems and their use in generation and amplification of microwaves and plasma heating.

1.1.1 General Description of Plasmas. The term plasma is in general used to describe a large class of essentially neutral mixtures containing some charged particles. However, the definition of a plasma in its strict sense must include additional characteristics that are described here. The most notable feature which distinguishes plasmas from ordinary solids, liquids or gases is that the charged particles in a plasma interact with each other in accordance with Coulomb's law. The coulomb force falls off very slowly with distance as compared with most of the other interparticle forces. Hence in a plasma every charged particle interacts simultaneously with many of its neighbors, giving the plasma a cohesiveness which is often compared to that of a mold or jelly.

The charged particles in a plasma tend to rearrange themselves in such a way as to effectively shield any electrostatic fields that are due either to a charge within the plasma or to a surface (for example, a probe) at some nonzero potential. The distance in which this

rearrangement of charged particles cancels out any electrostatic fields is known as the Debye length and is given by

$$\lambda_D^2 = \frac{kT\epsilon_o}{nq^2} \quad , \tag{1.1}$$

where k is the Boltzmann constant, T is the temperature in °K characterising the motion of the particles, ϵ_o is the permittivity of free space, n is the particle density in particles/m^3 and q is the charge of the particles. The obvious requirement for shielding to occur in a plasma is that the physical dimension of the system be much larger than a Debye length. In addition, there must be enough charged particles within a distance λ_D to produce this shielding. Thus the number of charged particles N_D in a Debye sphere of radius λ_D must be much greater than unity. Therefore

$$N_D = \frac{4\pi}{3} \lambda_D^3 n \gg 1 \quad . \tag{1.2}$$

Equation 1.2 implies that the average distance between the charged particles $d \cong n^{-1/3}$ must be small in comparison with the Debye length.

The average potential energy of the charged particles is given by

$$\langle PE \rangle \simeq \frac{q^2}{4\pi\epsilon_o d} = \frac{q^2 n^{1/3}}{4\pi\epsilon_o} \tag{1.3}$$

and the average kinetic energy of the particles is kT. Therefore

$$\frac{\langle KE\rangle}{\langle PE\rangle} = \frac{kT}{q^2 n^{1/3}/4\pi\epsilon_o} = 4\pi \cdot \frac{kT\epsilon_o}{nq^2} \cdot n^{2/3} \quad . \tag{1.4}$$

Using Eq. 1.1 gives

$$\frac{\langle KE\rangle}{\langle PE\rangle} = 4\pi\lambda_D^2 n^{2/3}$$

and from Eq. 1.2,

$$\frac{\langle KE\rangle}{\langle PE\rangle} = (36\pi)^{1/3} N_D^{2/3} \gg 1 \quad . \tag{1.5}$$

Thus for a gas to remain ionized the average kinetic energy of the particles should be greater than the average potential energy of the particles.

In conclusion, plasmas may include all media which have some charged particles provided they satisfy the shielding criteria, $N_D > 1$ and λ_D less than the smallest linear dimension of the plasma.

In most plasmas a charged particle is in constant interaction with the surrounding space charge via the coulomb forces. However, in a quiescent plasma the microscopic space-charge fields cancel each other and no net space charge exists over macroscopic distances. Plasmas thus do not support large potential variations and have a tendency to maintain macroscopic space-charge neutrality. This tendency leads to a characteristic oscillation of the plasma which was first observed by Tonks and Langmuir[1] in a plasma of electrons and positive ions. The

characteristic oscillation frequency of electrons about their mean position in a cold plasma in the presence of a neutralizing stationary ion background was derived by Tonks and Langmuir in 1929. The method employed for this purpose was analogous to that used for deriving the frequency of oscillation of an ordinary pendulum under the action of a restoring force. The characteristic frequency generally known as the "electron-plasma frequency" or simply "plasma frequency" is given by

$$\omega_{pe}^2 = \frac{ne^2}{m\epsilon_o} , \tag{1.6}$$

where ω_{pe} is the electron-plasma frequency and e and m are the charge and mass of the electron, respectively. These space-charge oscillations remain localized and do not propagate away from the point of disturbance. If the ion motion were included in deriving Eq. 1.6, the oscillation frequency would be somewhat higher because the electron mass m would have to be replaced by the reduced mass

$$\mu = \left(\frac{1}{m} + \frac{1}{M} \right)^{-1} , \tag{1.7}$$

where M is the ion mass. The plasma frequency with the reduced mass is written without a subscript as

$$\omega_p^2 = \frac{ne^2}{\epsilon_o} \left(\frac{1}{m} + \frac{1}{M} \right) = \omega_{pe}^2 + \omega_{pi}^2 \tag{1.8}$$

and ω_{pi} is known as the "ion-plasma frequency."

Another characteristic frequency for particles situated in a steady magnetic field is now introduced. It is the cyclotron frequency of gyration of particles about the magnetic field lines and is given by

$$\omega_{ck} = \frac{q_k B_o}{m_k} , \qquad k = e,i , \tag{1.9}$$

where q_k and m_k are the charge and mass of the particle and B_o is the steady magnetic field.

1.1.2 Application of Plasma Physics and Controlled Fusion. The history of plasma research and the development of plasma devices can be divided into two periods separated by World War II. In the first period researchers produced such devices as mercury-arc rectifiers, gas-filled diodes and triodes and ordinary fluorescent tubes for illumination and signs. In the second period rather sophisticated research areas were uncovered which dealt with magnetohydrodynamic generators, thermionic converters, microwave plasma amplifiers, gas lasers, arc jets, plasma propulsion systems and, perhaps potentially most important of all, the idea of a new source of energy through controlled thermonuclear fusion.

The objective of the controlled thermonuclear fusion research is to provide a new source of energy. The requirements for achieving useful power from controlled thermonuclear reactions are: (1) to heat a plasma of fusion fuel (for example, isotopes of hydrogen) to temperatures of hundreds of millions of degrees, (2) to contain it without contact with material walls and without contamination by impurities long enough for a significant fraction of fuel to react and (3) to extract the fusion energy released and convert it to a useful form.

Nuclear fusion reactions occur when two light nuclei such as deuterium (D), tritium (T) or helium (He^3) collide and react to rearrange themselves so as to form two other nuclei of smaller mass with a consequent release of energy. The reactions of primary interest in controlled fusion research are given in Table 1.1.[2] The energy of the fusion reaction is carried away by the reaction products. In some cases energy is carried away by the released neutrons and in others, by charged particles. When the energy is carried by charged particles, a unique direct conversion of their energy to electricity is possible. This has a potential for very high efficiency and hence low thermal pollution.

Table 1.1

Some Nuclear Reactions for Controlled Fusion

Energy Required	Fusion Reaction	Energy Released
~ 10 keV	$D + T \rightarrow He^4 + n$	17.6 MeV
~ 50 keV	$D + D \rightarrow He^3 + n$	3.3 MeV
	$D + D \rightarrow T + p$	4.0 MeV
~ 100 keV	$D + He^3 \rightarrow He^4 + p$	18.3 MeV
~ 200 keV	$p + Li^6 \rightarrow He^3 + He^4$	4.0 MeV

Confining the plasma long enough so that a significant number of reactions can take place and sustain the process has presented serious problems. Several confinement schemes are available but almost all of them are unstable in one way or another. This problem of instability is of a fundamental nature and is likely to arise in any confinement scheme. However, under certain conditions the rate of growth of the instabilities can be reduced to a point such that the confinement time is long enough

for a practical fusion device to operate. According to the Lawson criterion[3] for a self-sustained D-T reactor device, a requirement on the density-containment time product is

$$n\tau > 10^{20} \text{ s/m}^3 \text{ for an ion temperature } T_i \sim 10 \text{ keV} .$$

Several configurations for plasma confinement such as magnetic mirror and toroidal geometry are being pursued. At the present time, Tokamak devices utilizing toroidal geometry are believed to be close to achieving sustained fusion.

1.1.3 Wave Propagation Through Plasmas. A number of plasma waves have been described in the literature. These waves or modes are often identified by the name of their discoverer or by a descriptive title, but more often they are identified by their dispersion relations. The dispersion relations are complicated for the general case and are thus derived for special cases to obtain various modes. The relationship between different modes is usually not very clear. However, the Clemmow-Mullaly-Allis (CMA) diagram[4] leads to one of the ways to identify and relate various plasma modes.

If a dimensionless vector $\bar{n}$ is introduced which has the direction of the propagation vector $\bar{k}$ and has the magnitude of the refractive index, then

$$\bar{n} = \frac{\bar{k}c}{\omega} . \qquad (1.10)$$

The wave-normal surface is the locus of the tip of the vector $\overline{n^{-1}} \equiv \bar{n}/n^2$ and $|1/\bar{n}| = v_p/c$, where v_p is the phase velocity of the wave

and c is the velocity of light. For certain values of plasma parameters, n^2 goes to zero or to infinity. The former is termed a "cutoff" and the latter a "resonance."

In the CMA diagram the quantities $\omega_{ce}\omega_{ci}/\omega^2$ and $(\omega_p/\omega)^2$ are chosen as the ordinate and abscissa, respectively. For a two-component temperate collisionless plasma the two-dimensional coordinate space, which is called the "parameter space," is sufficient to describe the modes. The parameter space is divided into thirteen regions by boundary lines that represent the cutoff and resonances. The general shape of the wave-normal surface remains the same in a given region and changes its shape only on crossing the boundary lines in the parameter space. Thus a particular mode is identified by its wave-normal surface in a given region in parameter space.

A general description of the wave-normal surfaces and their relation to a number of specific modes of a cold uniform plasma is given by Allis et al.[4] and Stix.[5] Ranking them by ascending frequency, they are the Alfvén-Åström hydromagnetic waves, the ion-cyclotron waves, the lower-hybrid mode, the electromagnetic plasma wave, the Langmuir-Tonks plasma oscillations, the whistler mode, the electron-cyclotron waves and the upper-hybrid mode. For the first two modes, the frequency is relatively low and the electrons may be considered as a uniform massless fluid. The lower-hybrid mode occurs at an intermediate frequency and both electron and ion motion must be considered. For the remaining modes the frequency is relatively high and the ions are considered as a uniform fluid of infinite mass. There are two waves which occur only in hot

plasmas and do not have their counterparts in cold plasmas. These waves are the ion-acoustic wave and the electrostatic ion-cyclotron wave.

It was pointed out in Section 1.1.1 that the space-charge fluctuations in a cold, stationary, infinite, isotropic plasma are nonpropagating. This is evident from their dispersion equation which was derived by Langmuir and Tonks:[1]

$$1 - \frac{\omega_p^2}{\omega^2} = 0 \quad . \tag{1.11}$$

Oscillations can occur only at ω_p and a disturbance does not propagate away from its original location. However, these fluctuations can propagate and transfer wave energy away from the source under the following conditions: (1) the electron temperature is finite, (2) the plasma electrons have a drift velocity and (3) the plasma is finite.

When the electron temperature is taken into account the dispersion relation for the longitudinal plasma oscillations is given by[6,7]

$$1 - \frac{\omega_p^2}{\omega^2}\left(1 + \frac{3k^2v_T^2}{\omega^2}\right) = 0 \quad , \tag{1.12}$$

where v_T is the mean square longitudinal thermal velocity and k is the propagation constant. The oscillations now propagate with a definite phase velocity ω/k, whereas in the cold plasma they were essentially stationary. Equation 1.12 is the correction of Bohm and Gross[6,7] to the Langmuir-Tonks formula given in Eq. 1.11.

If the plasma electrons are given a drift velocity v_o, the plasma oscillations will be convected along at the drift velocity. Two space-charge

waves would exist, one having a phase velocity slightly higher and the other slightly lower than the drift velocity. These are called fast and slow space-charge waves.[8] The propagation constants for the two waves for a one-dimensional system are given by

$$k_z = (\omega \pm \omega_{pe})/v_o \quad , \tag{1.13}$$

where z is taken as the direction of propagation.

Trivelpiece and Gould[9,10] showed that a finite electron temperature or an average drift velocity is not essential to the propagation of space-charge disturbances and that finite size also leads to propagation. Assuming that the first-order quantities vary with z and t as $\exp[j(\omega t - k_z z)]$ and neglecting the ion motion, they found the dispersion equation for the E-mode (transverse magnetic) of a plasma-filled, metallic, cylindrical waveguide under the influence of an <u>infinite</u> magnetic field to be

$$k_z^2 = k_o^2 - \frac{T^2}{1 - \omega_p^2/\omega^2} \quad , \tag{1.14}$$

where $k_o = \omega\sqrt{\mu_o \epsilon_o}$ is the free-space wave number, $T = p_{mn}/d$, d is the waveguide radius and p_{mn} is the nth root of mth order Bessel function of the first kind. From Eq. 1.14 it is found that the cutoff frequency is given by

$$\omega_{co}^2 = T^2 c^2 + \omega_p^2 \quad . \tag{1.15}$$

The quantity Tc is the cutoff frequency for an empty waveguide. Thus, the cutoff frequency for a plasma-filled waveguide is higher than that of an empty waveguide. In addition, the presence of plasma allows the propagation constant to take on positive real values for $0 < \omega < \omega_p$, thus giving rise to propagating waves in this frequency range. Figure 1.1 shows the dispersion diagram for such a case.

An interesting feature of the plasma waveguide modes is that the resonant frequency is independent of the waveguide dimensions and depends only on the plasma frequency. Moreover, within the passband ($0 < \omega < \omega_p$) all the higher-order modes ($n > 0$, $m > 1$) will propagate simultaneously if they are excited. This is in contrast with the empty waveguide case in which the number of propagating modes continues to increase with frequency.

The plasma waveguide modes are electromechanical in nature in that the role played by the magnetic field in electromagnetic propagation has been taken over by the mass velocity of the plasma electrons. The presence of the metallic conductor around the plasma is not essential to the propagation of waves. A plasma column in free space would have the same qualitative propagation characteristics as the filled plasma waveguide.

In contrast to the infinite magnetic field case, the plasma-filled waveguide in a finite magnetic field has an additional passband above either the electron-plasma frequency or the electron-cyclotron frequency, depending on which is higher. The phase characteristic of the additional passband is that of a backward wave. For a backward wave, the group velocity and phase velocity have opposite signs. The dispersion diagram for such a case is shown in Fig. 1.2.

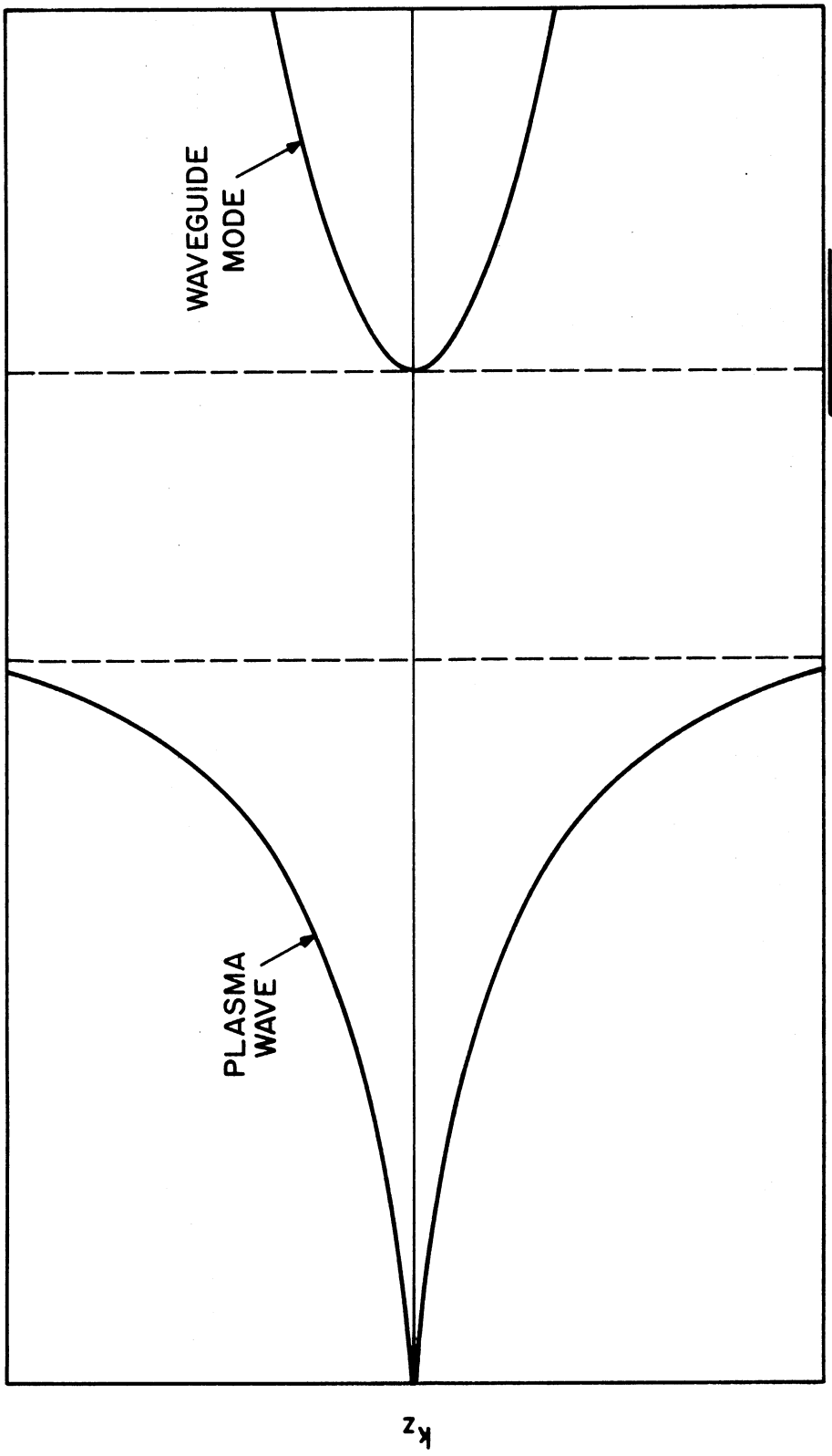

FIG. 1.1 SCHEMATIC OF DISPERSION CHARACTERISTICS OF WAVES IN A PLASMA-FILLED WAVEGUIDE WITH INFINITE AXIAL MAGNETIC FIELD.

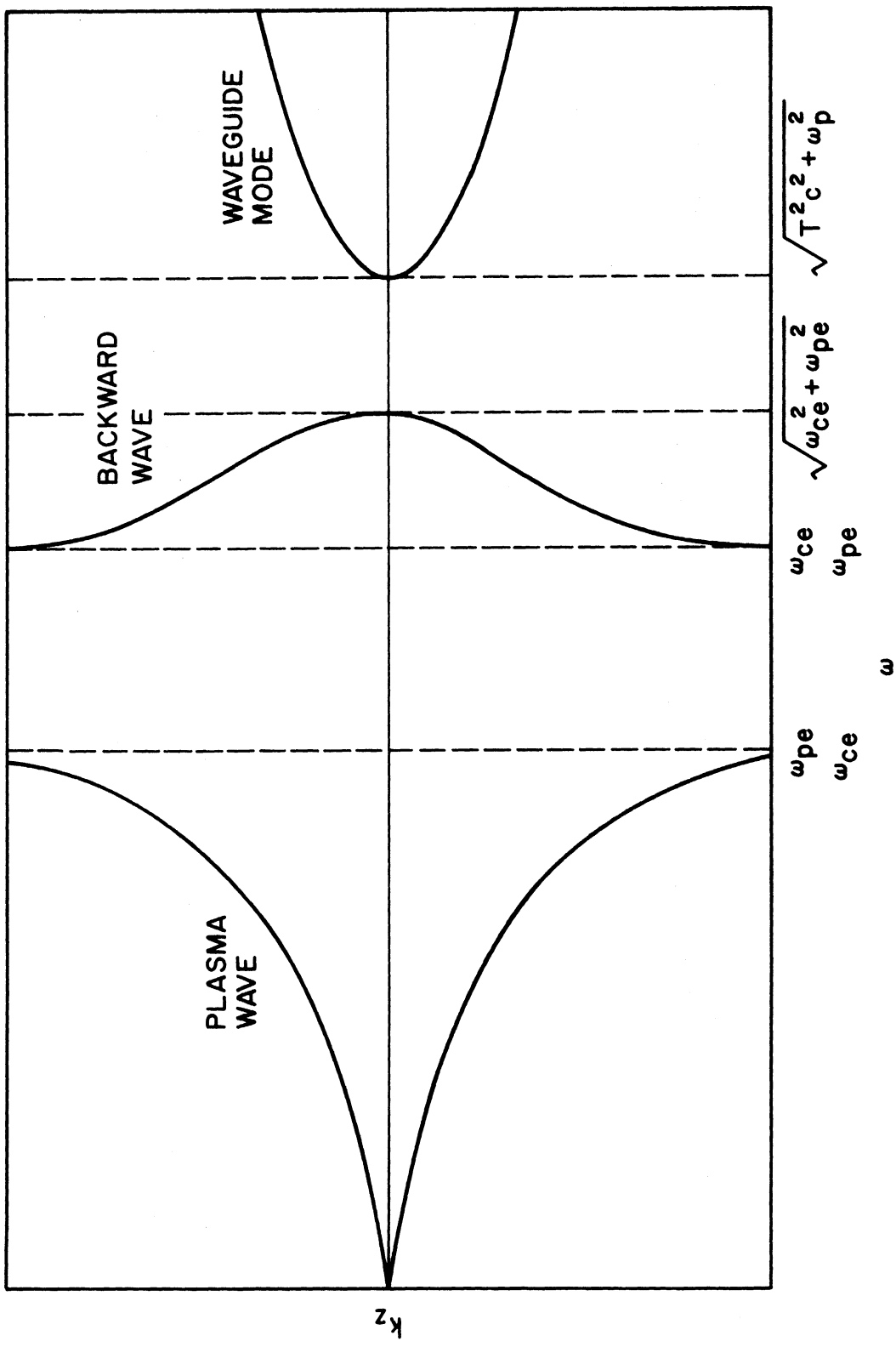

FIG. 1.2 SCHEMATIC OF DISPERSION CHARACTERISTICS OF A PLASMA-FILLED WAVEGUIDE IN A FINITE STEADY MAGNETIC FIELD.

If the magnetic field is reduced to zero, propagation is no longer possible in the plasma-filled waveguide. However, if the plasma only partially fills the waveguide, a surface wave mode of propagation exists. Let $d > a$ where d and a are the waveguide and plasma radii and let ϵ be the dielectric constant of a homogeneous isotropic dielectric in a region between the waveguide and the plasma. For this system ($\omega_{ce}/\omega_{pe} = 0$), a passband from $\omega = 0$ to $\omega = \omega_p/\sqrt{1 + \epsilon/\epsilon_o}$ exists and the wave energy is carried by surface rippling of the plasma. When $\omega_{ce}/\omega_{pe} \gg 1$, most of the wave energy is carried by charge accumulation within the plasma column with little surface rippling. These waves are "body waves" and have a passband for $0 < \omega < \omega_p$ similar to one-dimensional space-charge waves ($\omega_{ce}/\omega_{pe} = \infty$). The backward wave characteristic is not influenced by the geometry and it has a passband characteristic similar to that in the case of the plasma-filled waveguide.

Until now ions in the plasma were assumed to be stationary. If the ion motion is also taken into account, the propagation characteristics change significantly for the finite magnetic field case. First consider the plasma-filled waveguide. In this case a propagating plasma wave appears which has a passband from $\omega = 0$ to $\omega = \omega_{ci}$ and a resonance at $\omega = \omega_{ci}$, where ω_{ci} is the ion-cyclotron frequency. The plasma wave is cut off from ω_{ci} to ω_{LH}, where ω_{LH} is the lower-hybrid frequency which will be defined in detail in Section 2.1.2 and is given by

$$\frac{1}{\omega_{LH}^2} \cong \frac{1}{\omega_{ce}\omega_{ci}} + \frac{1}{\omega_{pi}^2 + \omega_{ci}^2} \quad . \tag{1.16}$$

A plasma wave again propagates from ω_{LH} to ω_{ce} or ω_{pe}, whichever is smaller. The situation above ω_{ce} or ω_{pe} is the same as that for stationary ions. The dispersion curve for this case is shown in Fig. 1.3.

If the plasma only partially fills the waveguide and the region between the plasma and the waveguide is surrounded by an isotropic homogeneous dielectric of dielectric constant ϵ, then body waves as well as surface waves exist. Again two cases are considered: (1) $\omega_{ce} > \omega_{pe}$ and (2) $\omega_{ce} < \omega_{pe}$. For $\omega_{ce} > \omega_{pe}$, a surface wave exists which has a passband from $\omega = 0$ to $\omega = \omega_1$, where ω_1 is given by[11]

$$\omega_1 = \omega_{LH}\left[1 - \frac{m}{M}\cdot\frac{[1 + (\omega_{pe}/\omega_{ce})^4]}{[1 + (\omega_{pe}/\omega_{ce})^2]}\right]^{1/2} \qquad (1.17)$$

and is the resonant frequency of the surface wave. Above ω_{LH}, the dispersion is qualitatively the same as for the plasma-filled waveguide and $\omega_{ce} > \omega_{pe}$.

For $\omega_{ce} < \omega_{pe}$, two surface waves exist. The first one is the same as for the first case from $\omega = 0$ to $\omega = \omega_1$. The second surface wave has a passband from $\omega = \omega_{LH}$ to $\omega = \omega_2$ and ω_2 is given by

$$\omega_2 = \sqrt{(\omega_{ce}^2 + \omega_{pe}^2)/2}\ . \qquad (1.18)$$

The dispersion characteristics above ω_{pe} are qualitatively the same as in the plasma-filled waveguide when $\omega_{pe} > \omega_{ce}$. The dispersion diagrams for the two cases of a partially filled waveguide are shown in Fig. 1.4.

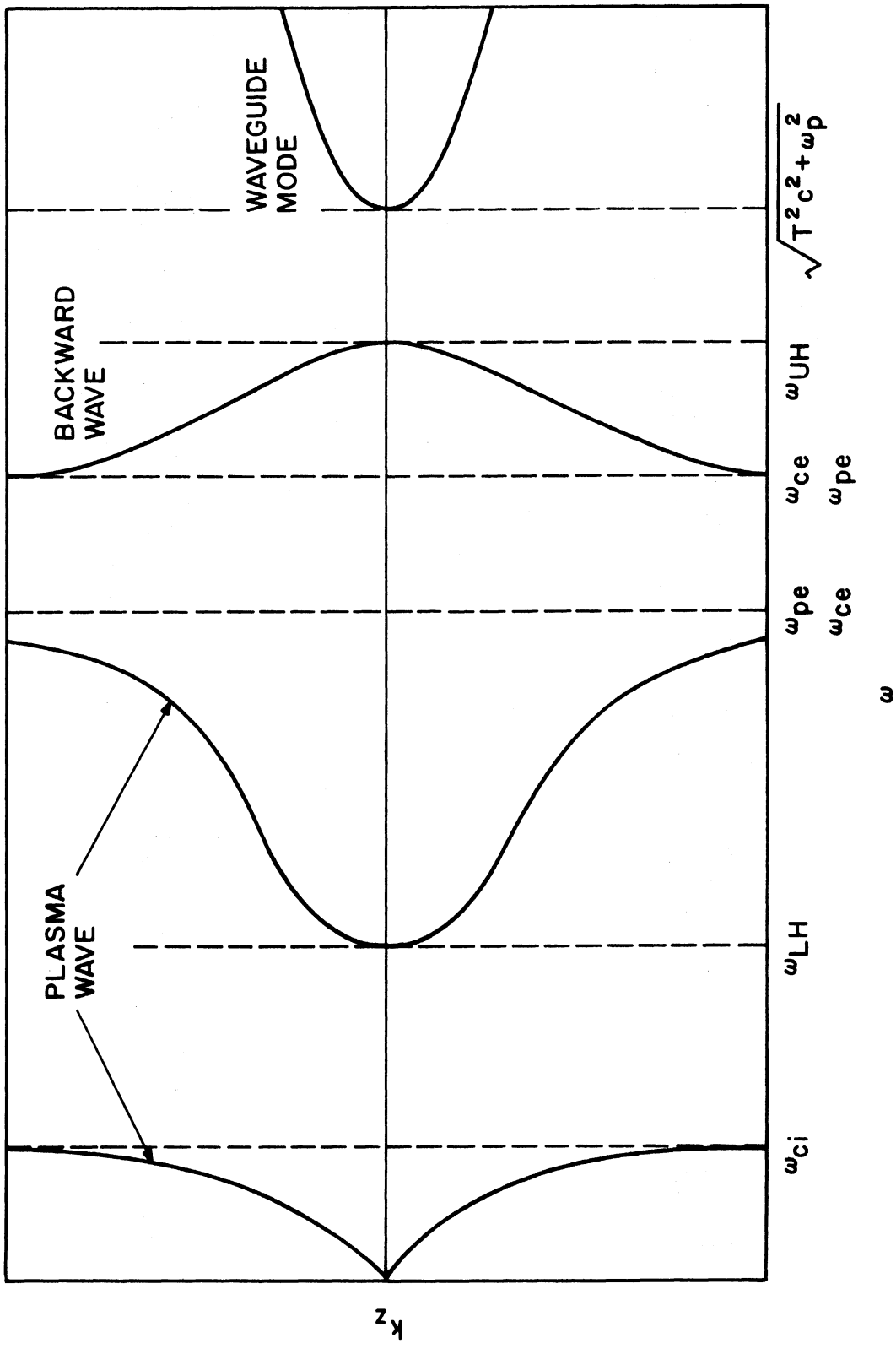

FIG. 1.3 SCHEMATIC OF DISPERSION CHARACTERISTICS OF A PLASMA-FILLED WAVEGUIDE IN A FINITE STEADY MAGNETIC FIELD WITH ION MOTION INCLUDED.

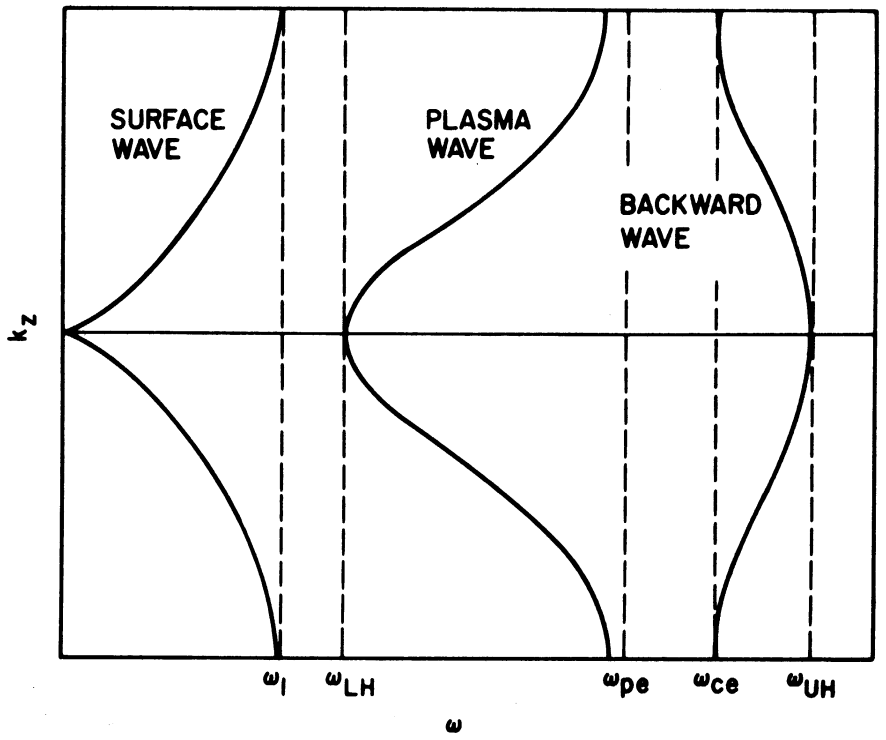

(a) $\omega_{ce} > \omega_{pe}$

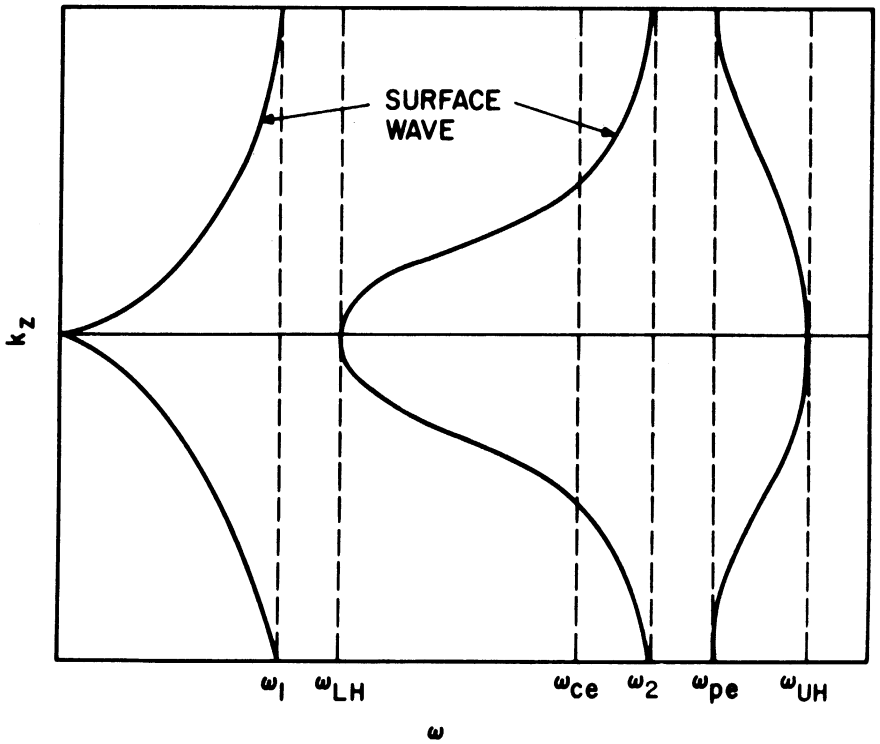

(b) $\omega_{ce} < \omega_{pe}$

FIG. 1.4 SCHEMATIC OF AXISYMMETRIC LOWEST-ORDER DISPERSION CHARACTERISTICS OF A PARTIALLY FILLED WAVEGUIDE IN A STEADY MAGNETIC FIELD WITH ION MOTION INCLUDED. (CHORNEY[11])

Since all the plasma modes in the preceding discussion were slow waves, the quasi-static assumption ($v_p/c \ll 1$) was used here. In other words, the ac magnetic field of the wave in Faraday's law was neglected and curl $\overline{E} \cong 0$ was assumed. However, at certain frequencies (for example, the cutoff frequencies) the phase velocity of the waves becomes very large and thus the quasi-static assumption may not be valid near cutoff. Several workers[4,12-20] have dealt with the guided-wave problem without using the quasi-static assumption but generally have resorted to other simplifications. When the ac magnetic field of the wave is taken into account, the dispersion equation for a bounded plasma in a finite, steady magnetic field becomes very complicated. The modes become hybrid modes (E-H modes) instead of pure E-modes. For certain parameters, the backward wave having a passband between ω_{pe} and $\sqrt{\omega_{pe}^2 + \omega_{ce}^2}$ may become a forward wave. Likuski[20] has compared dispersion curves for quasi-static and nonquasi-static cases. A steady finite magnetic field was included in his model but ion motions were neglected. He found that the quasi-static assumption is good for a waveguide of radius d such that $(d\omega_p/c) < 1$ and for any guide radius if $k_z^2 \gg k_o^2$.

1.1.4 Electron Beam-Plasma Systems. The interaction of an electron beam traversing a plasma column in a waveguide has been of considerable interest not only as a system for amplifying microwave power but also as a method for heating a plasma. There is considerable similarity between the slow space-charge waves propagating along an axially magnetized, plasma-filled waveguide and the electromagnetic waves supported by a metallic slow-wave structure of the type used in traveling-wave amplifiers and backward oscillators.[21] In the beam-plasma

system the upper limit of frequency would not be set by the difficulties of producing small mechanical slow-wave structures but by the magnetic fields and plasma densities attainable. This will allow generation and amplification in the millimeter and submillimeter frequency ranges. The interpenetration of the beam and plasma ensures very strong coupling between them, thus leading to very high gains per unit length compared with those of conventional microwave tubes. However, due to several shortcomings such as difficulties in coupling microwave power at the input and output ports, strong nonthermal noise excitation and reduced gun cathode life due to ion bombardment, no competitive beam-plasma amplifier has been achieved. There has been a reduction of interest in recent years for attaining the potential of such a device.[22]

The study of the beam-plasma mechanism still continues due to its relevance to plasma heating for controlled fusion. A heating scheme of considerable interest was proposed by Smullin and Getty[23] and Kharchenko et al.[24,25] This scheme is based on the utilization of the instabilities which occur when an electron beam interacts with a plasma. The instabilities are able to convert the ordered energy of the beam into large-amplitude plasma oscillations which, given sufficient time, should heat the plasma.

It is clear that thermonuclear plasma must have hot ions. The energy transfer between the plasma electrons and the plasma ions is a relatively inefficient process, thus it is necessary to seek conditions under which ions are heated directly. The work reported here utilizes an interaction frequency range near the lower-hybrid resonant frequency where the ions and electrons are excited to roughly equal energetic levels.

1.2 Review of the Literature

This section contains a review of the work done by other authors in the area of wave propagation and ion heating near the lower-hybrid frequency. Section 1.2.1 briefly identifies the different approaches taken to study waves near the lower-hybrid frequency. Section 1.2.2 describes the work done by several workers by studying the propagation of plane waves in a source-free region. In Section 1.2.3, a second approach taken by several other workers is described. It is the study of driven waves in the far field in an infinite plasma. The bounded, guided-wave approach is described in Section 1.2.4. In this section the transverse reactive-medium instability and the slow-cyclotron beam-wave interaction with plasma near the lower-hybrid frequency are described.

Most of the beam-plasma interaction work near the lower-hybrid frequency has been done under the approximation of a cold plasma or a very hot plasma. The effects of inhomogeneity, collisions and finite temperature have rarely been taken into account in most of the work done so far. Some of the work done at high frequencies (near ω_{pe}) which has included these effects, is described in Section 1.2.4. The results of this work will aid at least empirically in predicting the effects of inhomogeneity, collisions and finite temperature on the low-frequency beam-plasma interaction. Section 1.2.5 describes the study of ion interactions in a beam-plasma discharge. The two special cases of cold electrons and very hot electrons have been separated. Finally, in Section 1.2.6 finite-length system models for electron-beam and beam-plasma systems are described.

This review is not exhaustive because many articles have not been included due to the unavailability of their English translations.

1.2.1 Study of Waves near the Lower-Hybrid Resonant Frequency. The waves near the lower-hybrid resonant frequency are important because appreciable RF oscillations near this frequency involve significant ion oscillations. For a wave propagating perpendicularly to the magnetic field, the lower-hybrid resonant frequency in the high-density limit ($\omega_{pe}^2 \gg \omega_{ce}^2$) becomes the geometric mean frequency ($\omega_{LH} = \sqrt{\omega_{ce}\omega_{ci}}$) and in the low-density limit ($\omega_{pe}^2 \ll \omega_{ce}^2$) it reduces to the ion-plasma frequency ($\omega_{LH} = \omega_{pi}$).* Some authors have worked in the high-density regime and others, in the low-density regime.

After reviewing the literature on the work at the electron-ion hybrid resonance, three distinct approaches to the problem have been found: (1) plane waves in a source-free region, (2) driven waves in the far field in an infinite plasma and (3) bounded guided waves.

Work on the first approach has been done mainly by Oakes and Schluter,[26] Frank-Kamenetskii[27] and Haas et al.[28] Theoretical work has also been done by Korper[29] and Auer et al.[30] The second approach has been considered by Seshadri,[31] Kuehl,[32] Demidov,[33] Mikhailovskii and Pashitskii[34] and Aleksin and Stepanov.[35] Kino and Gerchberg[36] and Vermeer et al.[37] took the third approach.

1.2.2 Experimental and Theoretical Study of Plane Waves in a Source-Free Region. Schluter et al.[38-41] observed experimentally the lower-hybrid (LH) resonance in a steady-state RF discharge. The leading

---

* The lower-hybrid resonant frequency is derived for different limiting cases in Section 2.1.2.

of an RF oscillator vs. magnetic field was plotted. The maxima of the loading was interpreted as a resonance. However, there were small deviations between the theoretical and observed LH resonance frequency. In order to explain the above deviations, Oakes et al.[42] considered partial propagation along the magnetic field using the two-fluid model including collisions. They showed that with the partial propagation along the field B_o, the resonant frequency departs considerably from the geometric mean frequency (also see Reshotko,[43] Frank-Kamenetskii[44] and Yakimenko[45]). Later Oakes and Schluter[26] included temperature effects using the three-fluid model (ions, electrons and neutrals). It was shown that collisions of electrons and ions with neutrals increase the damping near the LH frequency and dominate the temperature effects.

Frank-Kamenetskii[27,46] has been active in the investigation of waves for $\omega \leq \omega_{LH}$ which he has termed "magnetic sound."* As in the case of Oakes and Schluter[26] he considered these waves in a three-component,

---

* Apparently for the following reason: For cold collisionless plasma, the phase velocity of the wave propagating perpendicular to magnetic field for a plasma in the high-density limit, i.e., $\omega_p^2 \gg \omega_{ce}^2$, is

$$v_p = \sqrt{2 \frac{B_o^2}{2\mu_o \rho_m}} \left(1 - \frac{\omega^2}{\omega_{LH}^2}\right)^{1/2} ,$$

where $\rho_m = mn$ is the mass density. For $\omega \ll \omega_{LH}$, $v_p = \sqrt{2B_o^2/2\mu_o \rho_m}$ which is analogous to the velocity of ordinary sound supported by magnetic pressure.

infinite plasma using hydrodynamic equations. Neglecting temperature effects and assuming negligible k_z component, he investigated the effect of neutral particles. He also pointed out that the collision cross section for charge exchange between ions and neutrals is the highest. He showed that the resonant frequency becomes

$$\omega_{LH} = \sqrt{\omega_{ci}\omega_{ce}\left(1 - \frac{N}{N + n_i}\,\frac{\bar{\nu}^2}{\bar{\nu}^2 + \omega^2}\right)}\ , \qquad (1.19)$$

where $\bar{\nu}$ is the charge-exchange collision frequency, N is the neutral density and n_i is the ion density. Clearly, if $\omega \gg \bar{\nu}$, $\omega_{LH} = \sqrt{\omega_{ce}\omega_{ci}}$ but for $\omega \ll \bar{\nu}$, ω_{LH} is reduced by a factor of $\sqrt{n_i/(N + n_i)}$. Moreover, the damping of the wave is proportional to ν^* where

$$\nu^* = \nu_{ei} + \nu_{eN} + \frac{\omega_{ci}\omega_{ce}}{\bar{\nu}^2 + \omega^2}\,\nu_{iN}\ . \qquad (1.20)$$

ν_{ei}, ν_{eN} and ν_{iN} are the electron-ion, electron-neutral and ion-neutral collision frequencies, respectively. It is noted that the resonant frequency does not depend on the coulomb collisions and electron-neutral collision frequency ($\omega \gg \bar{\nu}$) but the damping depends on them. Demidov et al.[47] considered a fully ionized, hot, magnetized plasma with coulomb collisions. Deriving the dispersion equation for perpendicular propagation, they showed that the damping of the wave due to coulomb collisions is small for all temperature ranges.

When the above two groups are summarized, it is noted that Frank-Kamenetskii considered the effects of neutral particles including charge-exchange collisions but neglected temperature effects, and in a

second paper he considered a hot plasma but did not include the effects of neutrals. Schluter and his co-workers considered a hot plasma with coulomb collisions, electron-neutral and ion-neutral collisions all in one treatment but did not consider the charge-exchange process.

Shvets et al.[48] have performed an experiment on the excitation of waves at the lower-hybrid frequency in a plasma located in a corkscrew magnetic field. A high-frequency (130 to 150 MHz) large radial electric field is used both for generation of the plasma and excitation of the waves. The axial component of the ac magnetic field was measured by a magnetic probe. The ac magnetic field has a peak at the lower-hybrid frequency. Hiroe and Ikegami[49] have reported the observation of oscillations at the lower-hybrid frequency which are parametrically excited by microwaves at the upper-hybrid frequency $\omega_{UH} = (\omega_p^2 + \omega_{ce}^2)^{1/2}$.

Haas et al.[28,50] of the third group previously mentioned, have reported an experiment concerning ion heating using a modulated electron beam. Ion energy was measured by a gas stripping cell and analyzing system which detected charge-exchange neutrals from the plasma. They observed that the ion current is maximum at $\omega \cong \omega_{pi}$ in the low-density regime ($\omega_p^2 \ll \omega_{ce}^2$) of a beam-generated plasma in mirror geometry. As was mentioned in Section 1.2.1, $\omega_{LH} = \omega_{pi}$ for perpendicular propagation in the low-density limit. As an extension of their work Haas and Eisner[51] recently reported that in their experiment the resonant frequency is independent of ion mass. They attempted to explain this result by stating that the lower-hybrid frequency is independent of ion mass in the low-density regime for propagation close to 90 degrees. As pointed out by Bhatnagar and Getty,[52] they were led to this incorrect conclusion

due to an error in their approximate equation. The error was corrected and an alternative explanation was given.[52]

Without going into detail, it is mentioned here that large-signal ion heating experiments have been done by Kovan and Spektor,[53] Bartov et al.[54] and Akhmartov et al.[55] at $\omega \leq \omega_{LH}$. Coupling of RF energy is done with a coil around the middle portion of the discharge.

1.2.3 Driven Waves in the Far-Field in an Infinite Plasma. Several authors have considered the wave propagation problem in plasma using the antenna approach under varying approximations.

Seshadri[31] and Kuehl[32] calculated the radiated fields by a thin cylindrical wire fed by specified currents and immersed in a plasma. Kuehl derived the expressions for the fields using Green's function and neglecting the ion motion. Demidov[33] considered the excitation of a uniform, infinite waveguide filled with cold, lossless plasma in a longitudinal magnetic field. The exciting system consists of conductors located in the plasma in which specified currents flow. Mikhailovskii and Pashitski[34,56,57] have analyzed the excitation of different characteristic plasma waves at low frequencies by an inhomogeneous electron beam.

Aleksin and Stepanov[35] have used kinetic theory to analyze the excitation of electromagnetic waves in an unbounded magnetoactive plasma by azimuthal and axial currents. They have derived general expressions for electromagnetic field and energy losses. However, expressions are solved only for special cases such as that of a cold plasma or a collisionless plasma under the hydrodynamic approximation.

Vodyanitiski and Kondratenko[58] have derived the expression for energy loss of a modulated axial current in a bounded magnetoactive plasma.

The method of solving for the driven electric field in a plasma can be used for an appropriate external current as well as a charge source that represents a modulated electron beam. A simplified analysis is presented in Section 2.2 to investigate the excitation of waves in a temperate plasma near the lower-hybrid frequency by a line charge and a current source produced by an appropriately modulated electron beam.

1.2.4 Bounded Guided Waves. Kino and Gerchberg[36] have predicted (for a cold collisionless plasma) that an electron beam transversely modulated through a pair of plates at the entrance to a plasma has a maximum growth rate at the LH frequency. The interaction is nonaxisymmetric and is between the space-charge waves of the beam and the plasma. The plasma has a negative dielectric constant in this frequency range and the instability is known as the transverse reactive-medium instability.

Vermeer et al.[37,59] have reported the observation of an instability near the ion-plasma frequency. The dispersion diagram for a cold, homogeneous beam-plasma system in which the beam and plasma fill a hypothetical metal waveguide was used to investigate the interaction. The measured axial wavelengths were of the order of the cyclotron wavelength v_o/f_{ce}. This shows that the instability is caused by the interaction of a beam slow-cyclotron wave and plasma. As an extension of their work, Vermeer and Kistemaker[60] reported the observation of multiple modes of an interaction peak. These multiple modes at the

same frequency are explained in terms of the interaction with axisymmetric as well as nonaxisymmetric modes in a beam-plasma system.

A tremendous amount of work has been done on the interaction of an electron beam and plasma at high frequencies around the electron-plasma frequency. Several authors have used idealized models for the beam and plasma but others have attempted to include in their models finite temperature and inhomogeneities in the beam and plasma. Here mention is made of only a few results which deal with finite temperature and inhomogeneity.

In the study of the interaction between a cold beam and a warm plasma Crawford[61] pointed out that the boundary condition at the beam and plasma edge would be different from that due to Hahn[62] which is generally applied in the cold case. Hahn's method is to calculate the charge perturbation at the surface of the plasma column caused by the radial motion of the electrons and ions and to make the normal component of the electric field discontinuous by the amount of the surface charge density associated with the perturbation. In the warm plasma, if the Debye length is long compared to the transverse RF excursions of the beam electrons, then the surface charge effects in the plasma may be neglected. If the contrary is true, then Hahn's approximation is appropriate for both the beam and plasma.

Shoucri[63] and Seidl[64] have also studied the effects of finite temperature on the interaction of an electron beam and plasma. The interaction was studied near ω_{pe} and ion motions were neglected. It was found that when the plasma is warm, a stopband below ω_{ce} ($\omega_{ce} > \omega_{pe}$) disappears. Finite temperature of the plasma decreases the growth rates

but does not change the excited frequency much in the axisymmetric case. However, for the nonaxisymmetric interaction, the excited frequency becomes a multivalued function of the plasma density and growth rates at the cylotron frequency are reduced.

The propagation of slow waves in a waveguide containing a plasma with a nonuniform electron density has been investigated by Rogashkova and Tseitlin.[65] They found that if the density decreases along the plasma column, the gain of the beam-plasma interaction increases. On the other hand, an increase in the density along the column leads to a reduction in the gain. The frequency band is increased rather insignificantly in both cases ($\simeq$ 5 percent). It was shown that the phase velocity of the wave decreases in the direction of propagation for a decreasing plasma density. It is known from the nonlinear theory of traveling-wave tubes that a decrease in the phase velocity in the direction of propagation can lead to an increase in the efficiency of the device as a consequence of continued synchronism of the beam and wave.

1.2.5 Ion Interactions in a Beam-Plasma Discharge.

1.2.5a Cold Electrons. When an electron beam is injected into a cold electron-ion plasma, a wide variety of interactions are possible.[66] Several of these interactions are ion interactions and they occur for frequencies below or near the lower-hybrid frequency. One of the interactions is at the ion-cyclotron frequency which is due to the synchronism between the beam slow-cyclotron wave and a propagating plasma wave. However, the maximum growth rate of this synchronous interaction is found to be very small and is of little importance for physically reasonable beam-plasma systems.

For a relatively dense plasma and large plasma diameter such that $\omega_{pe}/T > v_o$, where T is the transverse propagation constant, synchronism between the beam slow-cyclotron wave or the beam space-charge wave does not occur in the low-frequency range but is close to ω_{pe} ($\omega_{ce} > \omega_{pe}$). For a relatively tenuous plasma ($\omega_{pe}/T < v_o$) the space-charge wave synchronism shifts down to a frequency just above the lower-hybrid frequency. In this interaction as well, it turns out that the growth rates are small.

Since the beam flows through a medium which has a dielectric constant quite different from that for free space, the reactive-medium amplification is expected in regions where the plasma dielectric constant is negative. Intuitively, when a bunched electron beam passes through a medium with a negative dielectric constant, the electrons in a bunch attract rather than repel each other and hence the bunching is further enhanced. Reactive-medium amplification occurs in a low-frequency band from ω_{ci} to approximately ω_{LH} and maximum amplification occurs near ω_{LH}.

The interaction of a thin electron beam with a cold plasma that fills a metal waveguide has been studied[66] under the filamentary-beam approximation. This approximation considerably simplifies the dispersion equation. Physically, the approximation requires that the fields be relatively constant over the cross section of the beam. Under this assumption, it has been shown[67] that the effect of small beam radius was to reduce the maximum amplification rates obtained at synchronous frequencies and to increase the reactive-medium amplification rates.

In fact, the reactive-medium amplification rate tends toward infinity near the lower-hybrid frequency. However, the filamentary-beam assumption is not applicable near the lower-hybrid frequency. Near the lower-hybrid frequency, the transverse wavelength in the plasma tends to zero, and a wave will be heavily damped by finite Debye length and Larmor radii effects. Nevertheless, by neglecting the effects of finite Debye length and Larmor radii, calculations of the growth rates made under the filamentary-beam approximation represent the upper bound on the amplification rate.

In conclusion, the synchronous interactions at low frequencies in a cold plasma are not strong ion interactions. The reactive-medium amplification may possibly be strong enough but an exact calculation is required that accounts for the finite diameter of the beam in a self-consistent manner.

1.2.5b Hot Electrons. In this section the interaction of an electron beam with a hot-electron plasma that fills a waveguide is reviewed. A dispersion diagram for a waveguide filled with plasma with very hot electrons is shown in Fig. 1.5. It has resonances at the ion-cyclotron frequency and at the ion-plasma frequency. In addition, it has a cutoff frequency ω_k which for a reasonable temperature of plasma electrons lies between ω_{ci} and ω_{pi}. The plasma supports a forward wave between ω_k and ω_{pi}. For small beam densities it is expected that the interaction between the beam space-charge waves and the propagating plasma wave should give rise to a convective instability. Briggs[66] discovered that a nonconvective instability is also present just below ω_{pi} provided that the plasma frequency of the beam electrons

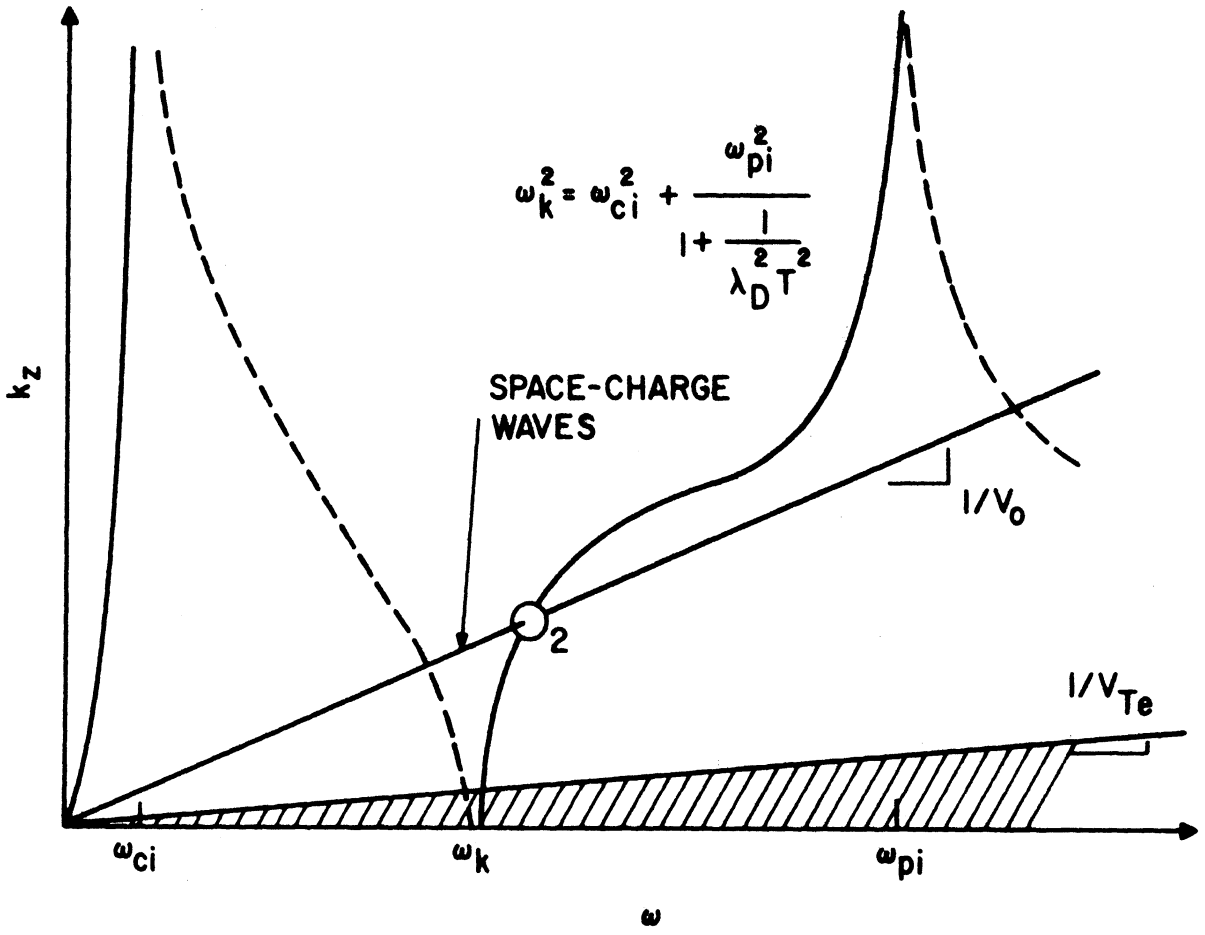

FIG. 1.5 SCHEMATIC DISPERSION DIAGRAM FOR A VERY HOT ELECTRON PLASMA FILLING A WAVEGUIDE. THE DASHED LINES SHOW PURELY IMAGINARY ROOTS. FINITE STEADY MAGNETIC FIELD AND ION MOTION ARE INCLUDED. ROOTS FOR HIGH FREQUENCIES ARE NOT SHOWN. (BRIGGS[66])

exceeds the plasma frequency of the ions and that the electron thermal velocity is much greater than the phase velocity of beam and plasma waves. Puri[68] and Wallace[69] have extended this analysis of the beam-plasma ion interaction to a system of finite transverse dimensions and to lower plasma-electron thermal velocities. Neglecting Landau damping, they found that the absolute instability can be obtained for values of electron thermal velocity approximately equal to the beam velocity. However, the necessary beam density is increased correspondingly. Lieberman[67] extended this analysis by including the effect of Landau damping. In this case, the threshold conditions were observed to be more restrictive than the previous analysis neglecting Landau damping.

Chou[70] has applied a rigid-beam model* to the interaction of an electron beam and a hot-electron plasma near the ion-plasma frequency. The effect of a contaminant of cold electrons was also considered. Landau damping was not included in his treatment. A nonconvective instability was predicted for the synchronous beam-plasma wave interaction under certain conditions similar to the analysis of Briggs,[66] Puri[68] and Wallace.[69]

1.2.6 Finite-Length System Models.

1.2.6a Finite-Length Electron-Beam Models. The simplest case in which an electron beam excites oscillations in a spatially uniform, time-varying electric field in a finite-length system is the

---

* In this model the displacement $\bar{\delta}(z,t)$ of the beam is assumed to be a function of z only and it is independent of the position in a transverse plane. The "rigid-beam" model allows a great simplification of the analysis.

diode oscillator. Benham[71] and Llewellyn and Bowen[72] gave the first small-signal explanation of this device in which a negative-conductance model was used to indicate how the electron beam can give up energy to the RF oscillations. Marcum[73] extended their analysis to the case of arbitrary strength RF electric fields restricted only by the condition that the total velocity of any electron in the diode region never reverses direction. He found that the negative conductance was maximum for certain transit angles. Jepsen[74] included the effect of a spatially varying electric field but for transit times small compared to the period of oscillation. Jepsen's results have been numerically extended by Bartsch[75] to arbitrary transit angles. The general relation between the small-signal beam current and an externally applied standing-wave electric field has been determined by Wesselberg[76] for arbitrary transit angles. It was found that in the one-dimensional analysis, negative conductance was maximum at different transit angles for different axial modes. In particular, for a half-wave axial mode pattern, negative conductance was maximum for a transit angle of approximately π rad. The effect of the beam on the fields was neglected in this treatment.

1.2.6b Self-Consistent, Finite-Length, Two-Stream Model. Frey and Birdsall[77] have examined instabilities in a finite-length, neutralized electron beam in a drift tube. Boundary conditions were applied at the ends and system walls. The beam was unmodulated at the injection plane in their model. A set of homogeneous equations was solved to obtain complex eigenfrequencies. The value of $\mathrm{Im}(\omega)$ thus gives the time rate of growth or decay of oscillations starting at $t = 0$.

Gerwin and Nelson[78] applied a self-consistent solution to the two-stream instability problem in a finite-length system in which the beams were assumed to enter the system unmodulated. The results of the self-consistent solutions indicated that the dispersion relation for the infinitely long system could be directly used to predict the starting length for oscillations. Ketterer[79] used a self-consistent solution to treat electromechanical streaming interactions in a finite-length system.

1.3 Statement of the Problem

From the review of the literature in Section 1.2, it is found that only a few experiments have been done on the heating of ions by an electron beam in a plasma near the lower-hybrid frequency. Some of the experiments performed lack sound theoretical explanations. Moreover, observations usually have been made on the heating of ions only and very little attempt has been devoted to bring out the basic physics involved by measuring the dispersion characteristics of the involved waves.

In this investigation both experimental and theoretical efforts are concentrated on understanding the basic mechanism which causes ion heating in a modulated electron beam-plasma system near the lower-hybrid frequency. For such a task, it is profitable to initially confine the study to the small-signal regime. Therefore, in the present work only linear theory is carried out.

In the experiment, an electron beam is passed through a beam-generated plasma. The length and diameter of the plasma column are finite. The electron-beam current is modulated near the lower-hybrid frequency by a grid in the electron gun. The small-signal response of the system

as a function of frequency and radial and axial distance is measured by RF Langmuir probes. Low-level ion heating is observed by a gridded probe. No efforts are directed to observe very hot ions by driving the electron beam with large signals.

A theoretical model of such a beam-plasma system has to include the finite radial and axial boundaries. First the dispersion characteristics [$D(\omega, k_z) = 0$] of a beam-plasma system of finite transverse dimension but of infinite axial extent is analyzed. This determines the different waves that exist in such a system. The boundary conditions are then applied at the two ends of the system to determine the amplitude of each excited wave. Total fields are then obtained by carrying out a summation of all the amplitudes of the different waves. Thus the theoretical and experimental responses as a function of frequency and axial and radial distance can then be compared.

1.4 Outline of the Present Investigation

The basic purpose of this study is to investigate ion heating by a modulated electron beam in a finite-sized plasma. To achieve this end experimental and theoretical studies of the excitation of large, low-frequency (near the lower-hybrid resonant frequency) radial RF electric fields in a plasma are performed. The resultant production of energetic ions is experimentally observed with the help of a gridded probe velocity analyzer. In order to understand the basic mechanism of the excitation of RF electric fields, only small-signal behavior is studied.

Theoretical analyses of the lower-hybrid resonance and the dispersion characteristics of beam-plasma waveguide systems are given

in Chapter II. The basic features of the lower-hybrid resonance are investigated with the help of a plane-wave analysis in a cold anisotropic plasma. Expressions for the lower-hybrid resonant frequency and particle kinetic energies for arbitrary angle of propagation are obtained. A simplified analysis is given which predicts a peak in the radial RF electric field at the lower-hybrid frequency for 90-degree propagation. The dispersion equations for three beam-plasma configurations (including the experimental configuration) are given. These equations are solved by a computer. The roots of the dispersion equations are required for the normal-mode analysis given in Chapter IV.

Chapter III describes the experimental studies which have been performed in a bounded beam-plasma system. A description of the experimental arrangement is given. Plasma densities deduced from Langmuir probe data and microwave cavity measurements are compared. The gridded probe observations on the presence of energetic ions are given. The frequency response and spatial distribution of the RF electric field which are measured by a Langmuir probe are presented. The variations of the resonant frequencies as a function of beam and plasma parameters are also given.

In Chapter IV a theoretical model based on the experimental arrangement is established and analyzed. Expressions for the electric field in a bounded beam-plasma system in terms of beam-modulation current are obtained by a normal-mode summation. The normal-mode field equations are solved with the help of a computer. The frequency response and spatial distribution of the RF electric field are computed for parameters which were used in the experiment. The variations of the resonant frequencies as functions of the beam and plasma parameters are also

predicted. The normal-mode field calculations are extended to a frequency range near the lower-hybrid frequency. A possible mechanism of energy transfer from the beam to the plasma ions is also described.

The experimental and theoretical results are compared in Chapter V. The resonant frequencies, their relative RF amplitudes and their dependence on beam and plasma parameters are compared. It is found that the agreement between the experiment and theory is good.

A summary of the work and conclusions are given in Chapter VI. Suggestions for further study are also made in Chapter VI.

CHAPTER II. THEORETICAL ANALYSIS OF THE LOWER-HYBRID RESONANCE AND DISPERSION CHARACTERISTICS OF BEAM-PLASMA WAVEGUIDES

2.1 Plane-Wave Analysis of the Lower-Hybrid Resonance

In order to discuss the basic theoretical features of the electron-ion lower-hybrid resonance, the propagation of plane waves in a uniform, cold, anisotropic plasma will be investigated. Auer et al.,[30] Stix,[5] Allis et al.,[4] Buchsbaum,[80] Yakimenko[45] and Reshotko[43] have given good accounts of the lower-hybrid resonance in the cold, collisionless, infinite plasma approximation. In most of the previous work, it has been customary to examine primarily the lower-hybrid resonance of the extraordinary wave propagating perpendicularly to the magnetic field. In a finite-sized laboratory plasma, the propagation vector of an excited wave will have a small but finite longitudinal component. Thus the propagation vector will not be exactly at 90 degrees to the magnetic field direction.

In this section, the dispersion relation for plane-wave propagation in a cold plasma will be derived and a resonance condition will be obtained from the dispersion relation. The expressions for the lower-hybrid resonant frequency in different density regimes will be obtained for the extraordinary wave propagating at 90 degrees.

For a better understanding of the physical nature of the lower-hybrid resonance, an investigation of the particle orbits, velocities and resultant current densities will be made. Moreover, the relation between the direction of the propagation vector and the electric field will be pointed out.

The effect of the direction of propagation on the nature of the lower-hybrid resonance will be studied in some detail. In particular, the sensitivity of the lower-hybrid resonant frequency on the direction of propagation will be examined. It will be shown that the lower-hybrid resonant frequency is of importance in the present study because at this resonant frequency the ratio of the average kinetic energies of ions and electrons is equal to or greater than unity.

A resonance is defined to occur when the index of refraction n (the ratio c/v_p, where c is the velocity of light and v_p is the phase velocity) becomes infinite. In a laboratory plasma, it will not be truly infinite but may be sufficiently large such that $v_p/c \ll 1$. For a wave propagating perpendicular to the steady magnetic field, the lower-hybrid resonant frequency is designated by ω_{LH} and for an arbitrary angle of propagation θ, it is represented by $\omega_{LH\theta}$.

2.1.1 Dispersion Relation for the Propagation of Plane Waves. The dispersion relation for a plasma is generally obtained from the condition for a nontrivial solution of a homogeneous set of field equations. For substitution into Maxwell's equations, it is necessary to express the current density $\bar{J}$ in terms of the electric field $\bar{E}$ using a conductivity tensor $\bar{\bar{\sigma}}$ for a magnetized plasma. Alternatively, it is permissible to think of a plasma as a charge-free dielectric medium with an equivalent frequency-dependent dielectric. The dielectric tensor $\bar{\bar{K}}$ is dimensionless and will be used for the description of a plasma in the present study.

Consider the propagation of plane waves in an infinite, cold, uniform plasma of electrons and ions of one species only. A steady, uniform magnetic field is impressed along the z-axis of a rectangular

coordinate system. Only a small-signal analysis is considered and the first-order quantities are assumed to vary as $\exp[j(\omega t - \bar{k} \cdot \bar{r})]$, where $\bar{k}$ is the propagation vector.

Maxwell's equations are

$$\nabla \cdot \bar{E} = \rho/\epsilon_o \quad , \tag{2.1}$$

$$\nabla \cdot \bar{B} = 0 \quad , \tag{2.2}$$

$$\nabla \times \bar{E} = -\frac{\partial \bar{B}}{\partial t} \tag{2.3}$$

and

$$\nabla \times \bar{B} = \mu_o \bar{J} + \frac{1}{c^2} \frac{\partial \bar{E}}{\partial t} \tag{2.4}$$

in which the plasma appears through the space-charge density ρ and the conduction current density $\bar{J}$. By taking the divergence of Eq. 2.4 together with the time derivative of Eq. 2.1, the following equation of continuity is obtained:

$$\nabla \cdot \bar{J} + \frac{\partial \rho}{\partial t} = 0 \quad . \tag{2.5}$$

The total electric displacement density $\bar{D}$ includes the vacuum displacement density plus the plasma polarization density $\bar{J}/j\omega$ according to the relation

$$\bar{D} = \epsilon_o \bar{\bar{K}} \cdot \bar{E} = \epsilon_o \bar{E} + \bar{J}/j\omega \quad , \tag{2.6}$$

where $\bar{\bar{K}}$ is the dielectric tensor.

The plasma current density $\bar{J}$ is given in terms of macroscopic particle velocities $\bar{v}_k$ by the relation

$$\bar{J} = \sum_k n_k Z_k \epsilon_k e \bar{v}_k \quad , \qquad k = e,i \quad , \tag{2.7}$$

where n_k is the number density of the particles with a charge of magnitude $Z_k e$. The positive or negative sign of the charge is given by $\epsilon_k = \pm 1$.

The velocities $\bar{v}_k$ are obtained from the equation of motion

$$m_k \frac{d\bar{v}_k}{dt} = Z_k \epsilon_k e \, (\bar{E} + \bar{v}_k \times \bar{B}) - m_k \nu_{kN} \bar{v}_k \quad , \tag{2.8}$$

where ν_{kN} is the collision frequency for momentum transfer between the kth charged particle and the neutrals and is assumed to be independent of the particle velocities. The ratio of the magnetic force due to the ac magnetic field of the wave to the electric force is $|\bar{v}_k/c|$. In the nonrelativistic case, therefore, the ac magnetic field of the wave can be neglected. By solving for the components of velocities for a species it is found that for $e^{j\omega t}$ time variation

$$\begin{bmatrix} v_{k,x} \\ v_{k,y} \\ v_{k,z} \end{bmatrix} = \frac{Z_k e \epsilon_k}{m_k} \begin{bmatrix} \dfrac{-j\omega}{\omega'^2 - \omega_{ck}^2} & \dfrac{-\epsilon_k \omega_{ck}}{\omega'^2 - \omega_{ck}^2} & 0 \\ \dfrac{\epsilon_k \omega_{ck}}{\omega'^2 - \omega_{ck}^2} & \dfrac{-j\omega'}{\omega'^2 - \omega_{ck}^2} & 0 \\ 0 & 0 & \dfrac{1}{j\omega'} \end{bmatrix} \begin{bmatrix} E_x \\ E_y \\ E_z \end{bmatrix} \quad , \tag{2.9}$$

where ω_{ck} is defined as $\omega_{ck} = Z_k e B_o / m_k$ and $\omega' = \omega(1 - j\nu_{kN}/\omega)$. Substitution of $\bar{v}_k$ from Eq. 2.9 into Eq. 2.7 gives

$$\bar{J} = \bar{\bar{\sigma}} \cdot \bar{E} \quad , \tag{2.10}$$

where $\bar{\bar{\sigma}}$ is the conductivity tensor and is given by

$$\bar{\bar{\sigma}} = \begin{bmatrix} \sigma_\perp & -\sigma_x & 0 \\ \sigma_x & \sigma_\perp & 0 \\ 0 & 0 & \sigma_\parallel \end{bmatrix} , \tag{2.11}$$

where

$$\sigma_\perp = -j\epsilon_o \left(\frac{\omega_{pe}^2(\omega - j\nu_{eN})}{(\omega - j\nu_{eN})^2 - \omega_{ce}^2} + \frac{\omega_{pi}^2 \omega}{\omega^2 - \omega_{ci}^2} \right) ,$$

$$\sigma_x = -\epsilon_o \left(\frac{\omega_{pe}^2 \omega_{ce}}{(\omega - j\nu_{eN})^2 - \omega_{ce}^2} - \frac{\omega_{pi}^2 \omega_{ci}}{\omega^2 - \omega_{ci}^2} \right) ,$$

$$\sigma_\parallel = -j\epsilon_o \left(\frac{\omega_{pe}^2}{\omega - j\nu_{eN}} + \frac{\omega_{pi}^2}{\omega} \right) \tag{2.12}$$

in which only ν_{eN} is assumed to be nonzero. From Eq. 2.6 the following is obtained:

$$\bar{D} = \epsilon_o \left(\bar{\bar{U}} - j \frac{\bar{\bar{\sigma}}}{\omega\epsilon_o} \right) \cdot \bar{E} = \epsilon_o \bar{\bar{K}} \cdot \bar{E} , \tag{2.13}$$

where $\bar{\bar{U}}$ is the unity tensor,

$$\bar{\bar{K}} = \begin{bmatrix} K_\perp & -K_x & 0 \\ K_x & K_\perp & 0 \\ 0 & 0 & K_\parallel \end{bmatrix} , \tag{2.14}$$

$$K_\perp = 1 - \frac{\omega_{pe}^2(\omega - j\nu_{eN})/\omega}{(\omega - j\nu_{eN})^2 - \omega_{ce}^2} - \frac{\omega_{pi}^2}{\omega^2 - \omega_{ci}^2} ,$$

$$K_x = j\left(\frac{\omega_{pe}^2\omega_{ce}/\omega}{(\omega - j\nu_{eN})^2 - \omega_{ce}^2} - \frac{\omega_{pi}^2\omega_{ci}/\omega}{\omega^2 - \omega_{ci}^2} \right) ,$$

$$K_\parallel = 1 - \frac{\omega_{pe}^2}{\omega^2} - \frac{\omega_{pi}^2}{\omega^2} = 1 - \frac{\omega_p^2}{\omega^2} . \tag{2.15}$$

Maxwell's equations are now solved for plane-wave propagation in terms of the dielectric tensor $\bar{\bar{K}}$. Using Fourier analysis in time and space and combining Eqs. 2.3 and 2.4 gives

$$\bar{k} \times (\bar{k} \times \bar{E}) - \frac{\omega^2}{c^2} \bar{\bar{K}} \cdot \bar{E} = 0 . \tag{2.16}$$

The dimensionless vector $\bar{n}$ is now introduced which has the direction of the propagation vector $\bar{k}$ and the magnitude of the refractive index n such that

$$\bar{n} = \frac{\bar{k}c}{\omega} . \tag{2.17}$$

Thus Eq. 2.16 can be written as

$$\bar{n} \times (\bar{n} \times \bar{E}) - \bar{\bar{K}} \cdot \bar{E} = 0 \quad . \tag{2.18}$$

Without loss of generality, the propagation vector $\bar{k}$ and hence $\bar{n}$ are taken to lie in the x-z plane. Let θ be the angle between the dc magnetic field $\bar{B}_o = \hat{z}B_o$ and $\bar{n}$. In the notation of Allis et al.,[4] Eq. 2.18 can be written as

$$\begin{bmatrix} K_\perp - n^2 \cos^2\theta & -K_x & n^2 \sin\theta \cos\theta \\ K_x & K_\perp - n^2 & 0 \\ n^2 \sin\theta \cos\theta & 0 & K_\parallel - n^2 \sin^2\theta \end{bmatrix} \begin{bmatrix} E_x \\ E_y \\ E_z \end{bmatrix} = 0 \quad . \tag{2.19}$$

The condition for the nontrivial solution is that the determinant of the square matrix be zero. This condition gives the dispersion relation which can be written as

$$An^4 - Bn^2 + C = 0 \quad , \tag{2.20}$$

where

$$\begin{aligned} A &= K_\perp \sin^2\theta + K_\parallel \cos^2\theta \quad , \\ B &= (K_\perp^2 + K_x^2) \sin^2\theta + K_\parallel K_\perp (1 + \cos^2\theta) \quad , \\ C &= (K_\perp^2 + K_x^2) K_\parallel \quad . \end{aligned} \tag{2.21}$$

The dispersion relation can be put into another form as was done by Åström:[81]

$$\tan^2 \theta = - \frac{K_{\|}(n^2 - K_r)(n^2 - K_\ell)}{(n^2 - K_{\|})(K_\perp n^2 - K_r K_\ell)} , \tag{2.22}$$

where

$$K_\ell = 1 - \frac{\omega_{pe}^2/\omega}{\omega - j\nu_{eN} + \omega_{ce}} - \frac{\omega_{pi}^2/\omega}{\omega - \omega_{ci}} ,$$

$$K_r = 1 - \frac{\omega_{pe}^2/\omega}{\omega - j\nu_{eN} - \omega_{ce}} - \frac{\omega_{pi}^2/\omega}{\omega + \omega_{ci}} ,$$

$$K_\perp = \frac{K_\ell + K_r}{2} , \quad K_x = j\left(\frac{K_\ell - K_r}{2}\right) . \tag{2.23}$$

The dispersion equation for $\theta = 90$ degrees is then quickly obtained as

$$n^2 = \frac{K_r K_\ell}{K_\perp}$$

which represents an extraordinary wave and

$$n^2 = K_{\|}$$

which represents an ordinary wave.

2.1.2 Expressions for the Lower-Hybrid Resonant Frequency for Perpendicular Propagation. In this section the expressions for the lower-hybrid resonant frequency for $\theta = 90$ degrees will be obtained and its dependence on the ratio of ω_{ce}/ω_{pe} will be investigated. The dependence of this resonant frequency on the angle of propagation will be studied later in Section 2.1.4.

A resonance occurs when the index of refraction becomes infinite ($n^2 \to \infty$). For a wave propagating at an angle θ, the resonance condition

from Eq. 2.20 is A = 0 or

$$\tan^2 \theta = -K_{\parallel}/K_{\perp} \quad . \tag{2.24}$$

For a wave propagating at θ = 90 degrees, it can be seen from Eq. 2.24 that resonance occurs when

$$K_{\perp} = 1 - \frac{\omega_{pe}^2}{\omega^2 - \omega_{ce}^2} - \frac{\omega_{pi}^2}{\omega^2 - \omega_{ci}^2} = 0 \tag{2.25}$$

and ν_{eN} = 0 has been assumed. Assuming M/m $\gg$ 1, Eq. 2.25 can be factored such that

$$(\omega^2 - \omega_{LH}^2)(\omega^2 - \omega_{UH}^2) = 0 \quad , \tag{2.26}$$

where

$$\omega_{LH}^2 \cong \omega_{ce}\omega_{ci}\left(\frac{\omega_{ce}\omega_{ci} + \omega_{pe}^2}{\omega_{pe}^2 + \omega_{ce}^2}\right) \tag{2.27}$$

and

$$\omega_{UH}^2 \cong \omega_{pe}^2 + \omega_{ce}^2 \quad . \tag{2.28}$$

Equation 2.27 can be put into an alternative approximate form that is well known in the literature:[4,5]

$$\frac{1}{\omega_{LH}^2} \cong \frac{1}{\omega_{ce}\omega_{ci}} + \frac{1}{\omega_{pi}^2 + \omega_{ci}^2} \quad . \tag{2.29}$$

In the high-density limit ($\omega_{pe}^2 \gg \omega_{ce}^2$) Eq. 2.27 reduces to

$$\omega_{LH} \cong \sqrt{\omega_{ce}\omega_{ci}} \tag{2.30}$$

which is the "geometric mean" frequency. In the low-density limit ($\omega_{ce}^2 \gg \omega_{pe}^2 \gg \omega_{ce}\omega_{ci}$) Eq. 2.27 reduces to

$$\omega_{LH} \cong \omega_{pi} \quad . \tag{2.31}$$

In the very low density limit such that $\omega_{pe}^2 \ll \omega_{ce}\omega_{ci}$, the lower-hybrid frequency approaches ω_{ci}.

The lower-hybrid resonant frequency for $\theta = 90$ degrees is plotted in Fig. 2.1 for different values of ω_{ce}/ω_{pe}. It is clearly seen that for very high densities the lower-hybrid frequency becomes the geometric mean frequency and for very low densities it approaches the ion-cyclotron frequency. In the intermediate range it is near the ion-plasma frequency.

2.1.3 Motion of Charged Particles near Resonance for Perpendicular Propagation. In order to describe the physical nature of the lower-hybrid resonance, the motion of electrons and ions near the resonant frequency will be investigated. The investigation will be restricted to a frequency region such that the resonance occurs well above the ion-cyclotron frequency and well below the electron-cyclotron frequency ($\omega_{ci}^2 \ll \omega^2 \ll \omega_{ce}^2$). It is assumed that the wave electric field is in the x-direction and the dc magnetic field is in the z-direction. This assumption is valid at the hybrid resonance for a wave propagating in the x-direction (perpendicular propagation). From Eq. 2.9 the equations of the orbits of ions and electrons can be written as[5]

$$\frac{|X_i|^2}{\omega^2} + \frac{|Y_i|^2}{\omega_{ci}^2} = \frac{2e^2}{M^2\omega^2} \frac{E_x^2}{(\omega^2 - \omega_{ci}^2)^2} \tag{2.32}$$

and

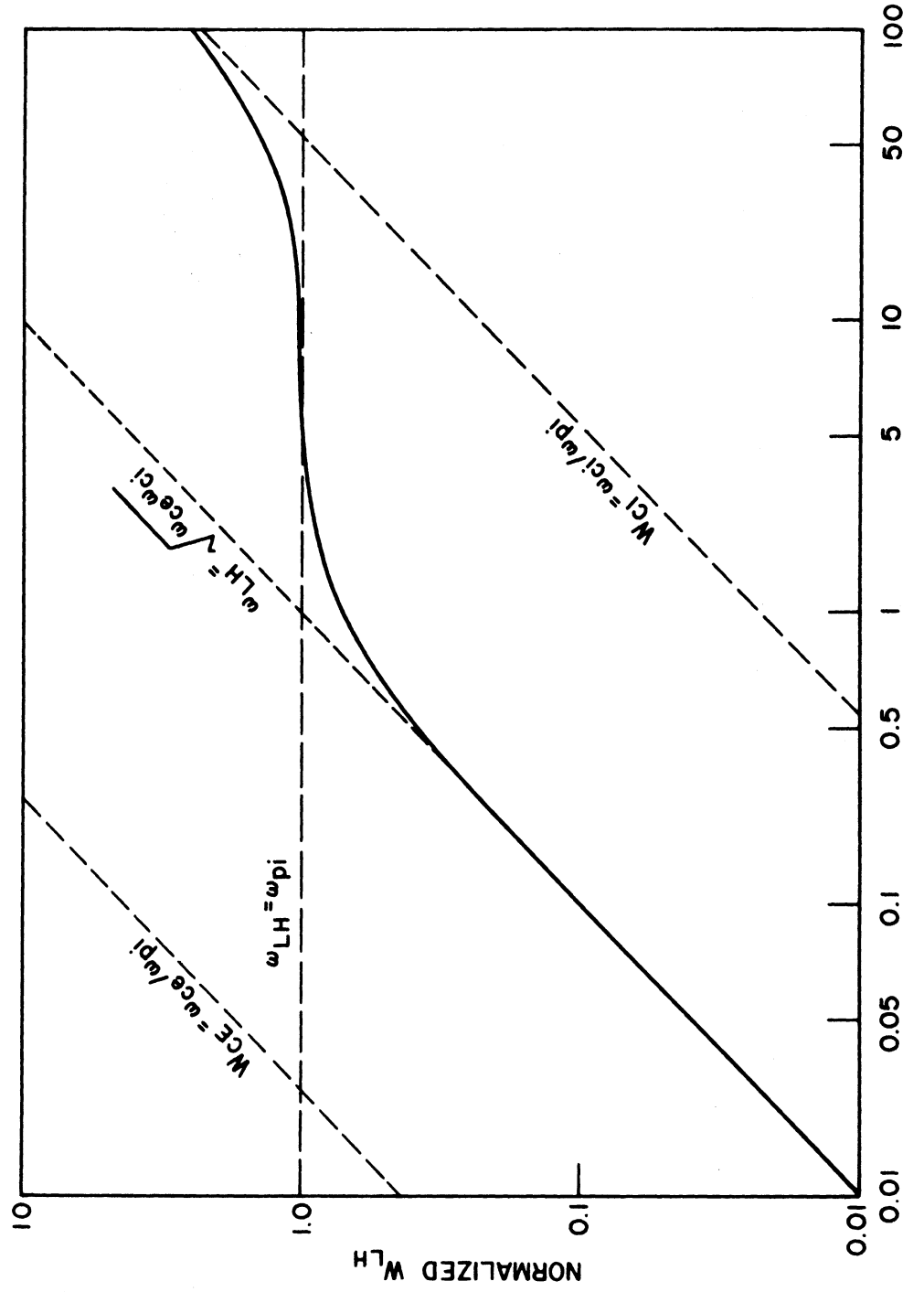

FIG. 2.1 NORMALIZED LOWER-HYBRID RESONANT FREQUENCY AS A FUNCTION OF ω_{ce}/ω_{pe}. ($W_{LH} = \omega_{LH}/\omega_{pi}$)

$$\frac{|X_e|^2}{\omega^2} + \frac{|Y_e|^2}{\omega_{ce}^2} = \frac{2e^2}{m^2\omega^2} \frac{E_x^2}{(\omega^2 - \omega_{ce}^2)^2} , \tag{2.33}$$

where X_k and Y_k (k = e,i) are the x- and y-displacements of the particles. It is clear that the ion motion thus will be principally in the x-direction, oscillating back and forth in almost a straight line unaffected by the magnetic field. The electrons will move predominantly in the y-direction with an $\bar{E} \times \bar{B}_o$ drift.

The major diameter of the ion elliptical trajectory (along the x-axis) is given by

$$2a_i = 2\sqrt{2}\,\frac{e}{M} \cdot \frac{E_x}{\omega^2 - \omega_{ci}^2} \tag{2.34}$$

and the minor diameter of the electron elliptical trajectory (along the x-axis) is given by

$$2b_e = 2\sqrt{2}\,\frac{e}{m} \cdot \frac{E_x}{\omega^2 - \omega_{ce}^2} . \tag{2.35}$$

The major diameter of the ion trajectory and the minor diameter of the electron trajectory are equal when the resonance is at the geometric mean frequency $\omega = \sqrt{\omega_{ce}\omega_{ci}}$. The electron and ion orbits are shown schematically in Fig. 2.2 for resonance at the geometric mean frequency (high-density limit) and at ω_{pi} (low-density limit). From Fig. 2.2a it is noted that the x-displacement of the electrons is in phase with and equal to the x-displacement of the ions at the geometric mean frequency. In the low-density limit the transverse electron displacement is small compared to that of the ions, as shown by Fig. 2.2b.

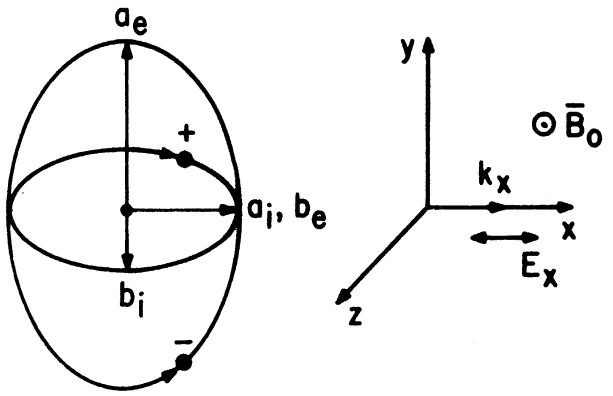

(a) $\omega = \sqrt{\omega_{ce}\omega_{ci}}$, $a_e/b_i = M/m$, $b_e/b_i = \sqrt{M/m}$

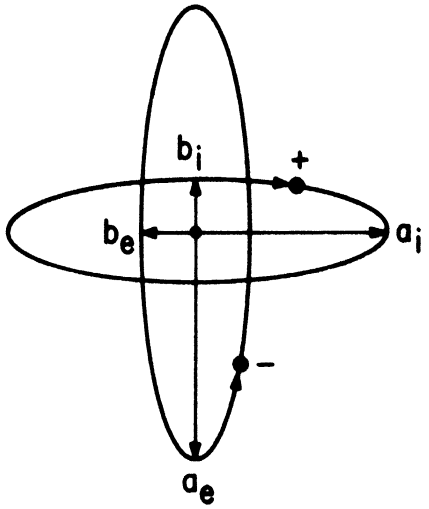

(b) $\omega = \omega_{pi}$, $a_e/b_i = (M/m)\cdot(\omega_{pe}^2/\omega_{ce}^2)$, $a_i/b_i = \sqrt{a_e/b_i}$,

$b_e/b_i = \sqrt{(M/m)}\cdot(\omega_{pe}/\omega_{ce})^3$

FIG. 2.2 SCHEMATIC DRAWING OF THE ELECTRON AND ION ORBITS AT ω_{LH} IN THE HIGH- AND LOW-DENSITY LIMITS. [a_k AND b_k (k = e,i) ARE THE MAJOR AND MINOR RADII OF THE ELLIPSES]

To explain the implication of the preceding result in regard to the lower-hybrid resonance at $\omega = \sqrt{\omega_{ce}\omega_{ci}}$, Eq. 2.5 is written for plane waves as

$$\rho = \frac{1}{\omega} \bar{k} \cdot \bar{J} \quad . \tag{2.36}$$

The bound charge ρ is due to the relative displacement of the ions and electrons. From Eq. 2.10 with $\bar{k} = k_x \hat{x}$ (90-degree propagation) the following is obtained ($\nu_{eN} = 0$)

$$\bar{k} \cdot \bar{J} = -j\epsilon_o \left(\frac{\omega_{pe}^2}{\omega^2 - \omega_{ce}^2} + \frac{\omega_{pi}^2}{\omega^2 - \omega_{ci}^2} \right) k_x E_x \quad . \tag{2.37}$$

Equation 2.37 can be written as

$$\bar{k} \cdot \bar{J} = -j\epsilon_o \left[\frac{\omega_p^2(\omega^2 - \omega_{ce}\omega_{ci})}{(\omega^2 - \omega_{ce}^2)(\omega^2 - \omega_{ci}^2)} \right] k_x E_x \quad . \tag{2.38}$$

In the high-density limit where $\omega_{LH} \simeq \sqrt{\omega_{ce}\omega_{ci}}$, Eq. 2.38 gives $\bar{k} \cdot \bar{J} = 0$ and therefore from Eq. 2.36 $\rho = 0$. Thus at resonance in the high-density limit no space charge is developed. This is a direct consequence of the identical displacement of the electrons and ions in the x-direction as shown in Fig. 2.2a. Since in this limit the electrons are not highly magnetized ($\omega_{pe}^2 \gg \omega_{ce}^2$), the finite x-displacement of the electrons allows the space charge to vanish (space-charge neutralization) at the lower-hybrid resonance. The neutralization of the space charge in the high-density limit is of importance since otherwise the wave field may be shielded by unneutralized space charge. This physical aspect of the

lower-hybrid resonance has been emphasized by Auer et al.[30] and Stix.[5] However, in the low-density limit there is no space-charge neutralization.

For an arbitrary angle of propagation Eqs. 2.1 and 2.13 give

$$\nabla \cdot \bar{D} = 0 \tag{2.39}$$

or

$$\bar{k} \cdot \bar{D} = \bar{k} \cdot \left(\epsilon_o \bar{E} + \frac{\bar{J}}{j\omega} \right) = 0 \quad . \tag{2.40}$$

The net conduction current always cancels the displacement current in the longitudinal direction, i.e.,

$$J_{\bar{k}} = - j\omega\epsilon_o E_{\bar{k}} \quad , \tag{2.41}$$

where $J_{\bar{k}}$ and $E_{\bar{k}}$ represent the conduction current and electric field, respectively, in the direction of propagation. The transverse current at an arbitrary angle of propagation is derived in Appendix A for a frequency range such that $\omega_{ci}^2 \ll \omega^2 \ll \omega_{ce}^2$ and is given by

$$\frac{J_t}{J_{\bar{k}}} = - \frac{j}{\sin \theta} \left[\frac{\omega\omega_{ce}}{\omega^2 - \omega_{ce}\omega_{ci} \left(1 + \frac{M}{m} \cot^2 \theta \right)} \right] \quad . \tag{2.42}$$

It can be shown from Eq. 2.42 that the ratio of the transverse and longitudinal current is very large at the lower-hybrid resonant frequency for an arbitrary angle of propagation (defined in Section 2.1.4).

For 90-degree propagation, the transverse current is given by

$$\frac{J_t}{J_{\bar{k}}} = -j \frac{\omega\omega_{ce}}{\omega^2 - \omega_{ce}\omega_{ci}} \tag{2.43}$$

and Eq. 2.41 gives

$$J_x = -j\omega\epsilon_o E_x \quad . \tag{2.44}$$

In the low-density limit ($\omega_{ce}^2 \gg \omega_{pe}^2 \gg \omega_{ce}\omega_{ci}$) the electrons are highly magnetized and have almost no displacement in the x-direction whereas the ions are nearly unmagnetized and move freely as shown in Fig. 2.2b. The space charge is thus not neutralized and the resonance is at ω_{pi}. The conduction current and the displacement current cancel in the x-direction but the transverse current is still much larger than the longitudinal current.

In the very low density limit, significant space charge does not exist ($\omega_{pe} \to 0$) and the resonance occurs at the ion-cyclotron frequency. The transverse and longitudinal currents have the same magnitude in this limit.

2.1.4 Lower-Hybrid Resonant Frequency for Oblique Propagation. For a wave propagating at an arbitrary angle, the resonance condition is given by Eq. 2.24 which can be written as

$$[(1 + \cot^2\theta)\omega^2 - (\omega_{pe}^2 + \omega_{pi}^2)\cot^2\theta]\,(\omega^2 - \omega_{ci}^2)(\omega^2 - \omega_{ce}^2)$$

$$- \omega^2(\omega_{pe}^2 + \omega_{pi}^2)(\omega^2 - \omega_{ce}\omega_{ci}) = 0 \quad . \tag{2.45}$$

This equation has three possible solutions of ω^2 for a given angle θ. The solution which lies in the frequency range $\omega_{LH} < \omega < \omega_{ce}$ or ω_{pe} is designated as the lower-hybrid resonant frequency for oblique

propagation ($\omega_{LH\theta}$). For a frequency of operation such that the inequality $\omega_{ce}^2 \gg \omega^2 \gg \omega_{ci}^2$ is satisfied, Eq. 2.45 gives the lower-hybrid resonant frequency for oblique propagation

$$\omega_{LH\theta}^2 \cong \frac{\omega_{ce}\omega_{ci} + \omega_{ce}^2 \cot^2 \theta}{\frac{\omega_{ce}^2}{\omega_{pe}^2}\left(1 + \cot^2 \theta\right) + 1} . \tag{2.46}$$

This approximation reduces to the high-density limit $\sqrt{\omega_{ce}\omega_{ci}}$ and the low-density limit ω_{pi} for $\theta = 90$ degrees, but does not give the very low density limit ω_{ci}.

In the high-density limit ($\omega_{pe}^2 \gg \omega_{ce}^2$) and for angles of propagation close to 90 degrees, the expression for the lower-hybrid resonance is given by

$$\omega_{LH\theta}^2 = \omega_{ce}\omega_{ci}\left(1 + \frac{M}{m}\cot^2 \theta\right) \tag{2.47}$$

which reduces to Eq. 2.30 for $\theta = 90$ degrees.

In the low-density limit ($\omega_{ce}\omega_{ci} \ll \omega_{pe}^2 \ll \omega_{ce}^2$), the expression for the lower-hybrid resonance is given by

$$\omega_{LH\theta}^2 = \omega_{pi}^2 \frac{1 + M/m \cot^2 \theta}{1 + \cot^2 \theta} . \tag{2.48}$$

Using this equation, the lower-hybrid resonant frequency is plotted as a function of angle of propagation for $\omega_{ce}/\omega_{pe} = 5$ in Fig. 2.3. It shows that at angles close to 90 degrees the lower-hybrid frequency decreases with increasing ion mass. However, if the angle of propagation moves

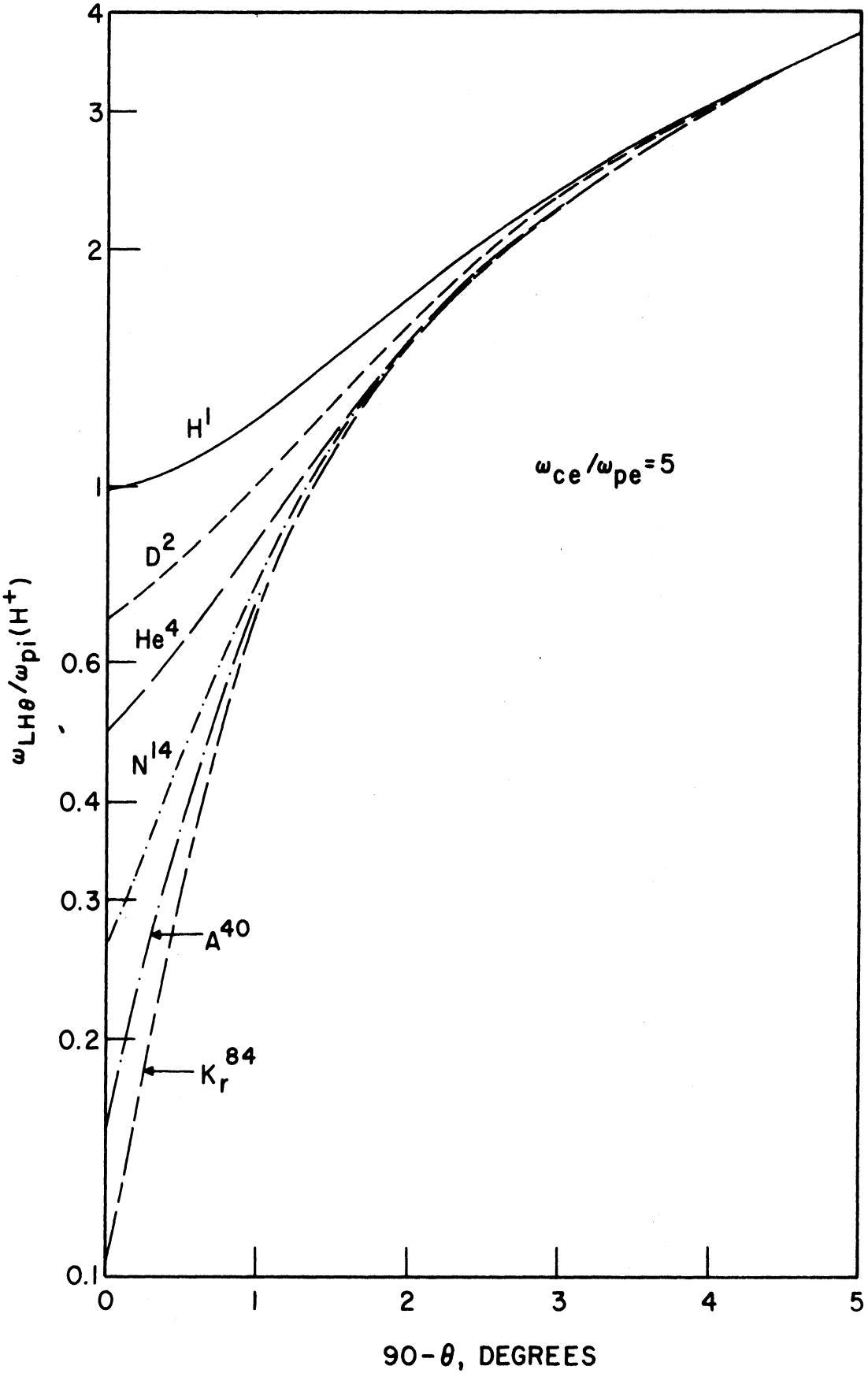

FIG. 2.3 LOWER-HYBRID FREQUENCY $\omega_{LH\theta}$ AS A FUNCTION OF ANGLE OF PROPAGATION. FREQUENCY HAS BEEN NORMALIZED WITH RESPECT TO THE ION-PLASMA FREQUENCY OF H^+.

sufficiently away from 90 degrees, the resonant frequency tends to become independent of ion mass. The condition for independence of ion mass is $\cot \theta \gg (m/M)^{1/2}$.

The effect of finite axial and transverse plasma boundaries is to establish the value of the angle θ and thus the resonant frequency. It will be shown in Section 2.3.2a that the quasi-static dispersion relation for a cylindrical longitudinally magnetized plasma waveguide is given by

$$T^2 = -k_z^2 \frac{K_\parallel}{K_\perp} , \qquad (2.49)$$

where k_z and T are the axial and transverse propagation constants, respectively, and are related by $\tan^2 \theta = T^2/k_z^2$. When Eqs. 2.49 and 2.24 are compared, it can be seen that in the quasi-static approximation ($\nabla \times \bar{E} \approx 0$) the wave propagates at the resonant cone angle at any frequency. The propagation constant k_z is large but finite. The propagation of waves in a finite diameter plasma column can therefore be considered as the superposition of plane waves in an infinite plasma at an angle θ_{res}, where θ_{res} is the resonant cone angle given by Eq. 2.24. The importance of this equivalence is that the angle θ_{res} can be theoretically computed using the quasi-static dispersion equation for a finite-sized laboratory plasma that partially or completely fills a cylindrical waveguide. This angle of propagation can then be used in the theory of plane waves to obtain other quantities of interest such as average particle kinetic energies, resonant frequencies, etc., near the lower-hybrid frequency.

2.1.5 Particle Kinetic Energies. In this section the small-signal electron and ion oscillation energies for oscillations occurring near the lower-hybrid resonance are investigated. The oscillation energies are independent of the particular mechanism which drives the oscillations of a cold electron-ion plasma.

In the absence of a dc magnetic field, oscillations of charged particles in a cold isotropic plasma are mainly electronic for any frequency ω and the ratio of ion to electron kinetic energies is given by

$$\frac{U_i}{U_e} = \frac{m}{M} \quad . \tag{2.50}$$

U_i and U_e are defined as

$$U_i = \frac{1}{2} n_i M \overline{\tilde{v}_i^2} \tag{2.51}$$

and

$$U_e = \frac{1}{2} n_e m \overline{\tilde{v}_e^2} \quad , \tag{2.52}$$

where $\overline{\tilde{v}_i^2}$ and $\overline{\tilde{v}_e^2}$ are the mean square macroscopic ac velocities of ions and electrons, respectively.

The effect of a finite dc magnetic field is to make U_i/U_e frequency dependent. Using the equation of motion and describing the propagation in terms of a plane wave propagating at an arbitrary angle in the x-z plane gives[67]

$$\frac{U_i}{U_e} = \frac{m}{M} \cdot \frac{1 + \omega^2 \tan^2 \theta \dfrac{\omega^2 + \omega_{ci}^2}{(\omega^2 - \omega_{ci}^2)^2}}{1 + \omega^2 \tan^2 \theta \dfrac{\omega^2 + \omega_{ce}^2}{(\omega^2 - \omega_{ce}^2)^2}} \quad . \tag{2.53}$$

For operation in a frequency range such that $\omega_{ce}^2 \gg \omega^2 \gg \omega_{ci}^2$, Eq. 2.52 reduces to

$$\frac{U_i}{U_e} = \frac{m}{M} \frac{1 + \cot^2 \theta}{\frac{\omega^2}{\omega_{ce}^2} + \cot^2 \theta} \tag{2.54}$$

For investigation near a resonant frequency in this range, $\omega \simeq \omega_{LH\theta}$ is substituted from Eq. 2.46 into Eq. 2.54 yielding

$$\frac{U_i}{U_e} = \frac{m}{M} \cdot \frac{1 + \cot^2 \theta}{\cot^2 \theta + \left[\frac{\frac{\omega_{ci}}{\omega_{ce}} + \cot^2 \theta}{1 + \frac{\omega_{ce}^2}{\omega_{pe}^2} (1 + \cot^2 \theta)} \right]} \tag{2.55}$$

For angles of propagation near 90 degrees ($\cot^2 \theta \ll 1$),

$$\frac{U_i}{U_e} = \frac{1 + \frac{\omega_{ce}^2}{\omega_{pe}^2}}{1 + \frac{M}{m} \cot^2 \theta \left(2 + \frac{\omega_{ce}^2}{\omega_{pe}^2} \right)} . \tag{2.56}$$

For propagation perpendicular to the magnetic field (θ = 90 degrees),

$$\frac{U_i}{U_e} = 1 + \frac{\omega_{ce}^2}{\omega_{pe}^2} . \tag{2.57}$$

Thus in the high-density limit ($\omega_{pe}^2 \gg \omega_{ce}^2$) electrons and ions oscillate with equal kinetic energies at the lower-hybrid frequency. In the low-density limit ($\omega_{pe}^2 \ll \omega_{ce}^2$), the ion oscillation energy is greater than that of the electrons at the lower-hybrid frequency.

For propagation at an arbitrary angle in the high-density limit,

$$\frac{U_i}{U_e} = \frac{1}{1 + 2\frac{M}{m}\cot^2\theta} \tag{2.58}$$

and in the low-density limit,

$$\frac{U_i}{U_e} = \frac{\frac{\omega_{ce}^2}{\omega_{pe}^2}}{1 + \frac{M}{m}\cdot\frac{\omega_{ce}^2}{\omega_{pe}^2}\cot^2\theta} \quad . \tag{2.59}$$

Thus it is clear that the particle kinetic energies are quite sensitive to the angle of propagation and the ratio of ion to electron energies decreases as the angle of propagation moves away from 90 degrees. Equations 2.58 and 2.59 show that the ratio of ion energy to electron energy is greater in the low-density limit as compared to the high-density limit.

In Section 2.1 it has been shown that the lower-hybrid resonant frequency (ω_{LH}) for 90-degree propagation reduces to $\sqrt{\omega_{ce}\omega_{ci}}$, ω_{pi} and ω_{ci} in the high-, low- and very low density ranges, respectively. For 90-degree propagation it was found that the space charge is neutralized in the high-density limit. The lower-hybrid frequency for oblique propagation ($\omega_{LH\theta}$) departs considerably (even for small angles away from 90 degrees) from ω_{LH}. Moreover, the angle of propagation can be determined from the quasi-static dispersion relation for a finite-sized plasma column. At ω_{LH} the ratio of ion to electron kinetic energies in the high-density limit is unity and in the low-density limit it is greater

than unity. However, as the angle of propagation departs from 90 degrees, this ratio goes down rapidly.

In a cylindrical configuration at resonance, the wave propagation and the electric field are in the radial direction. The radial current will be negligible but the azimuthal current J_φ may be large. The azimuthal current J_φ can be thought of as a Hall current due to E_r in the presence of a steady magnetic field in the z-direction. Conversely, it appears that if the wave propagation is purely in the radial direction, an azimuthal current may strongly excite the resonance.

In the next section the excitation of the resonance by azimuthal currents is shown from another point of view, i.e., the excitation of the extraordinary wave by external current and charge sources.

2.2 Simplified Theoretical Analysis Using a Sinusoidally Varying Line Charge

To excite significant ion oscillations in a plasma by an external source (e.g., by a modulated electron beam), it is interesting to investigate the driven RF electric field in the low-frequency region (near the lower-hybrid resonance) and to determine the frequencies at which the RF field has a maximum. As mentioned in Section 1.2.3, several authors[31,32,35] have studied the problem of driven RF field by an external current or a charge source in an infinite plasma. In this section a simplified analysis is presented to show that in a plasma the RF electric field excited by an infinitely long sinusoidally varying line charge (used to represent a modulated electron beam) has a maxima at the lower-hybrid resonant frequency.

Consider a cold electron-ion cylindrical plasma column in a dc magnetic field $\bar{B}_o$ along the z-axis. The plasma is described by the temperate plasma dielectric tensor $\bar{\bar{K}}$. A source current density $\bar{J}_s$ and a source charge density ρ_s at the axis of the plasma column is included. A source current density, a charge density or a combination of both may be used to represent the electron beam.

The pertinent equations for $e^{j\omega t}$ time variations are:

$$\nabla \times \bar{E} = -j\omega\mu_o \bar{H} \quad , \tag{2.60}$$

$$\nabla \times \bar{H} = \bar{J}_s + j\omega\epsilon_o \bar{\bar{K}} \cdot \bar{E} \quad , \tag{2.61}$$

$$\nabla \cdot \bar{H} = 0 \tag{2.62}$$

and

$$\nabla \cdot \bar{\bar{K}} \cdot \bar{E} = \rho_s/\epsilon_o \quad . \tag{2.63}$$

From Eqs. 2.61 and 2.63 the charge conservation equation for the source current and charge is obtained as follows:

$$\nabla \cdot \bar{J}_s + j\omega\rho_s = 0 \quad . \tag{2.64}$$

It is known that in a plasma waveguide where the propagation along the axis is assumed to be as $e^{-jk_z z}$, the fields at cutoff ($k_z = 0$) split into transverse electric (TE) and transverse magnetic (TM) modes.[4] The TE mode is characterized by

$$E_z = 0 \quad , \tag{2.65}$$

$$\bar{H}_t = 0 \tag{2.66}$$

and

$$\partial/\partial z = 0 \qquad (k_z = 0) \ , \tag{2.67}$$

where E_z is the axial component of the electric field $\bar{E}$ and $\bar{H}_t$ is the perpendicular component of the magnetic field $\bar{H}$. The TE mode is the extraordinary wave propagating in the radial direction and it will have a resonance at the lower-hybrid frequency. The field solutions for the TM mode are the same as the fields of an ordinary wave.

In the present analysis, the extraordinary wave is of interest and the solutions of the field equations (Eqs. 2.60 through 2.63) are desired subject to the assumptions of Eqs. 2.65 through 2.67. From Eqs. 2.60 and 2.61 the following is obtained:

$$H_z = \frac{j}{\omega\mu_o}\left[\frac{1}{r}\frac{\partial}{\partial r}(rE_\varphi) - \frac{1}{r}\frac{\partial E_r}{\partial \varphi}\right] \ , \tag{2.68}$$

$$E_r = \frac{K_\perp}{j\omega\epsilon_o K_r K_\ell}\left[\frac{1}{r}\frac{\partial H_z}{\partial \varphi} - J_{sr} - \frac{K_x}{K_\perp}\left(\frac{\partial H_z}{\partial r} + J_{s\varphi}\right)\right] \ , \tag{2.69}$$

$$E_\varphi = -\frac{K_\perp}{j\omega\epsilon_o K_r K_\ell}\left[\frac{\partial H_z}{\partial r} + J_{s\varphi} + \frac{K_x}{K_\perp}\left(\frac{1}{r}\frac{\partial H_z}{\partial \varphi} - J_{sr}\right)\right] \tag{2.70}$$

and

$$D_r = \frac{1}{j\omega}\left(\frac{1}{r}\frac{\partial H_z}{\partial \varphi} - J_{sr}\right) \ , \tag{2.71}$$

where $K_r K_\ell = K_\perp^2 + K_x^2$ and $K_\perp$ and K_x are the components of the dielectric tensor $\bar{\bar{K}}$ and have been defined in Eq. 2.15.

From Eq. 2.61 and using $\bar{H}_t = 0$ and $E_z = 0$,

$$J_{sz} = 0 \ . \tag{2.72}$$

This is an important result and it implies that a z-directed source current does not couple to the extraordinary wave for the case when $\partial/\partial z = 0$.

By substituting the values of E_r and E_φ into Eq. 2.68, after some manipulation, the following is obtained

$$\nabla^2 H_z + p_h^2 H_z = -j\omega \frac{K_x}{K_\perp} \rho_s - \hat{a}_z \cdot \nabla \times \bar{J}_s \quad , \tag{2.73}$$

where

$$p_h^2 = k_o^2 \frac{K_r K_\ell}{K_\perp} \tag{2.74}$$

and

$$k_o^2 = \omega^2 \mu_o \epsilon_o \quad . \tag{2.75}$$

The Helmholtz equation (Eq. 2.73) for H_z contains two source terms on the right-hand side. The first term is proportional to the source charge density (the charge density can be eliminated in favor of the source current density using Eq. 2.64) and is the source term of interest for the purpose of electron-beam excitation. The modulated electron beam produces a net ac charge density and therefore excites the extraordinary wave, whereas it appears from Eq. 2.72 that a neutralized axial current flow, as in a wire, will not.

The second term on the right-hand side of Eq. 2.73 is proportional to the z-component of $\nabla \times \bar{J}_s$. If it is assumed that there is no φ-variation of the source current, then this term can arise from an azimuthal current with a radial variation such as would be produced by

a solenoid around the plasma. However, it is easy to find source currents for which this term vanishes, and only the charge source term need be used.

For simplicity, the source is assumed to be singular at the axis of the cylindrical coordinate system and zero elsewhere. The source current distribution is assumed to have a zero curl, i.e., $\nabla \times \bar{J}_s = 0$. Therefore only the ρ_s term of Eq. 2.73 is required. The source will thus be a line charge of density ρ_L C/m. The line charge is the ac perturbation charge of the electron beam.

The fields are found from the homogeneous equation for H_z and then the proper limit at $r = 0$ is required to match the source amplitude. The expressions for H_z, E_φ and E_r for an $m = 0$ mode are

$$H_z = \frac{\omega\rho_L}{4} \frac{K_x}{K_\perp} H_o^{(2)}(p_h r) \quad , \tag{2.76}$$

$$E_\varphi = -j \frac{\rho_L}{4\epsilon_o} \frac{K_x}{K_\perp} \frac{k_o^2}{p_h} H_1^{(2)}(p_h r) \tag{2.77}$$

and

$$E_r = -j \frac{\rho_L}{4\epsilon_o} \frac{K_x^2}{K_\perp^2} \frac{k_o^2}{p_h} H_1^{(2)}(p_h r) \quad . \tag{2.78}$$

Equation 2.78 can be written as

$$E_r = -j \frac{\rho_L k_o}{4\epsilon_o K_\perp^{3/2}} \cdot \left(\frac{K_x^4}{K_\perp^2 + K_x^2} \right)^{1/2} H_1^{(2)}(p_h r) \quad . \tag{2.79}$$

Near $K_\perp = 0$ it becomes

$$E_r = -j \frac{\rho_L k_o K_x}{4\epsilon_o K_\perp^{3/2}} H_1^{(2)} (p_h r) \tag{2.80}$$

and the amplitude of the radial RF electric field tends to infinity as $K_\perp$ tends to zero. As is known from Eq. 2.25, $K_\perp = 0$ has roots at the lower-hybrid and upper-hybrid frequency. Thus the radial electric field excited by a line charge on the axis of a plasma column tends to infinity at the lower-hybrid frequency. However, the presence of electron-neutral collision limits the amplitude of the radial RF field to finite values. The excitation of this large field may result in significant ion oscillation and thus ion heating.

2.3 Beam-Plasma System Models and Solutions of Their Dispersion Relations

To study the excitation of large RF electric fields in a plasma by an electron beam, the electron beam and plasma must be taken into account in a self-consistent manner. The potential and field solutions must be obtained by solving the differential equation for such a system. This involves the study of the dispersion characteristics of waves that exist in such a system. However, merely obtaining the formal solutions of the differential equation does not constitute the complete answer, it is also necessary to determine the amplitude of the various waves by fitting the boundary conditions in a particular physical problem.

The dispersion relations studied in this section are for radially bounded but axially infinite beam-plasma systems. The frequency range studied is near the ion-plasma frequency. The roots of the dispersion

equations obtained in this section will be used in Chapter IV in carrying out the normal mode field calculations for an axially bounded system.

Investigations of beam-plasma system models and their solutions that account for finite dimensions in a direction transverse to the beam velocity usually deal with a cold collisionless plasma. Most of the previous work reported in the literature was done near the electron-plasma frequency and ion motion and electron collisions were neglected. However, in the present investigation the ion motion is of prime importance since the frequency of interest is in the low-frequency region. Moreover, the electron-neutral collision frequency is comparable to the frequency of operation and is thus included in the present work. The effect of the finite axial magnetic field has been included, but the resultant complexity of the problem is reduced with the aid of the quasi-static assumption. If the quasi-static assumption is not used, the dispersion equation becomes quite complex and is very difficult to solve. Section 2.3.1 defines different geometrical configurations of a cylindrical beam-plasma waveguide. In Section 2.3.2, the derivation of the dispersion relations for the different geometrical configurations is presented. The computer solutions of the dispersion relation for different cases are then presented in Section 2.3.3.

2.3.1 Geometrical Configurations. The geometrical configurations of a cylindrical beam-plasma waveguide are defined in this section. One of these configurations is used hereafter when referring to a beam-plasma waveguide. Physically, these configurations are limiting cases of the general case given in Section 2.3.1a but differences exist in the mathematical solutions since the radial boundary condition is different

for each case. The beam-plasma waveguide is immersed in a dc magnetic field parallel to the axis of the waveguide.

2.3.1a Coaxial Beam-Plasma Waveguide. The "coaxial" beam-plasma waveguide is essentially the same as an ordinary coaxial waveguide except that the inner metal conductor is replaced by a longitudinally magnetized plasma of diameter 2a and a beam of diameter 2b ($b \leq a$). The region between the central plasma column and the outer metal conductor of diameter 2d ($d \geq a \geq b$) can contain any dielectric without changing the analysis but vacuum is generally assumed when performing the numerical analysis. The general configuration of a beam-plasma system is shown in Fig. 2.4.

2.3.1b Beam-Plasma Filled Waveguide. The beam-plasma "filled" waveguide consists of the beam and plasma of the same diameter that fill the waveguide ($d = a = b$). This configuration is of interest since it is much simpler to analyze than the coaxial beam-plasma waveguide, yet it contains most of the propagation features of the coaxial system.

2.3.1c Unfilled-Beam, Filled-Plasma Waveguide. The unfilled-beam, filled-plasma waveguide is obtained from the coaxial beam-plasma waveguide when the vacuum region is completely filled by plasma. In this case the diameters of the beam, plasma and waveguide are such that $b < a = d$. Experimentally, this configuration is obtained when a thin electron beam streams through a plasma which is separately generated and fills a waveguide.

2.3.1d Open Beam-Plasma Waveguide. The "open" beam-plasma waveguide configuration consists of a beam and plasma column of equal diameter surrounded by an infinite isotropic dielectric or a vacuum.

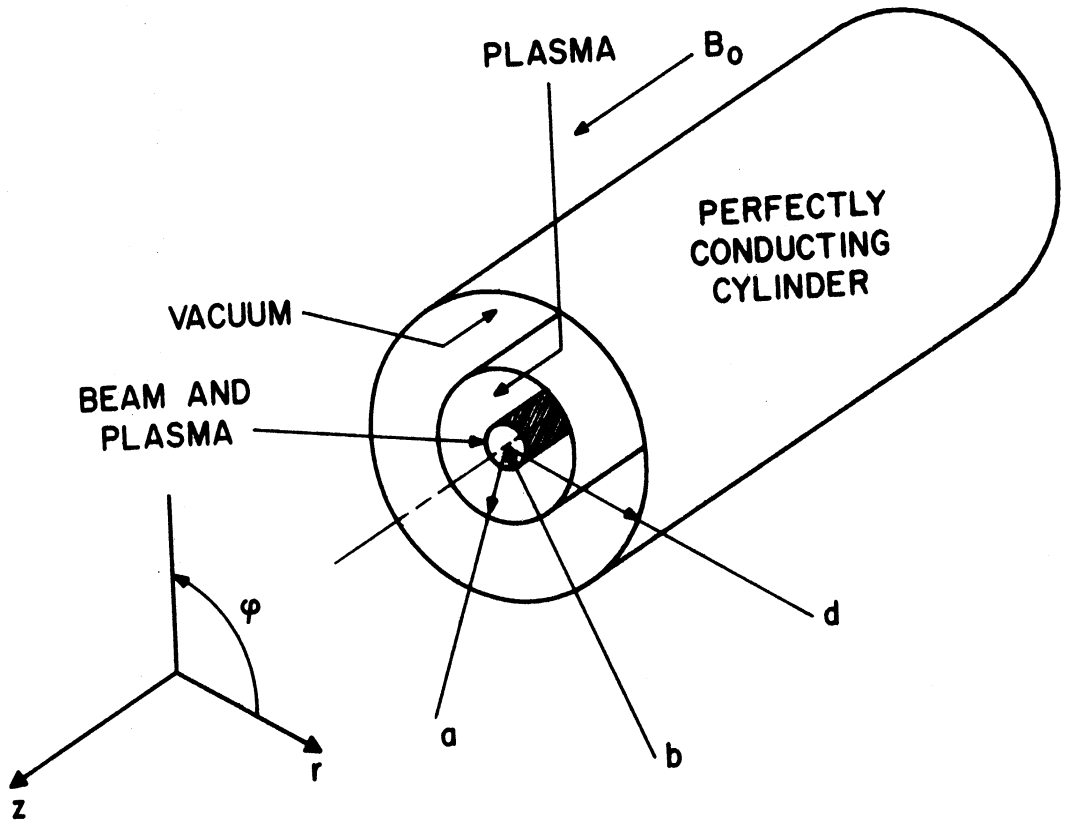

FIG. 2.4 GENERAL CONFIGURATION OF A BEAM-PLASMA SYSTEM.

This geometry is physically identical to the coaxial beam-plasma waveguide except that the radius of the metal waveguide goes to infinity (b = a, $d \rightarrow \infty$). Experimentally, this situation exists when the plasma is generated by the beam itself (in the quiescent mode[82]) in a relatively large-diameter waveguide.

2.3.2 Dispersion Relations for the Beam-Plasma System Models. The various dispersion relations presented in this section for the waves which exist in a beam-plasma system of the type shown in Fig. 2.4 are obtained by matching the various radial boundary conditions. An electron beam traverses the cylindrical plasma column along the z-axis with velocity v_o. The plasma is assumed to be stationary, uniform and cold. Only electron-neutral collisions of plasma electrons are included in the analysis. The wave in such a system can propagate at frequencies below the waveguide cutoff frequencies and at phase velocities which are much less than the velocity of light. A considerable simplification results in this case, since the electric fields can be assumed to be quasi-static and can be derived from a scalar potential. Throughout this discussion, the small-signal approximation is assumed to be valid and first-order perturbations are taken to vary as $\exp[j(\omega t - k_z z)]$ where k_z is the propagation constant along the z-axis.

When electron and ion thermal velocities are neglected, the properties of the plasma can be described by a dielectric tensor $\bar{\bar{K}}$ as given in Eq. 2.14. In a region where both the beam and plasma are present, the elements of dielectric tensor are modified and are given by

$$K_{\parallel}^{o} = K_{\parallel} - \frac{\omega_{pb}^2}{(\omega - k_z v_o)^2} , \tag{2.81}$$

$$K_{\perp}^{o} = K_{\perp} - \frac{\omega_{pb}^2}{(\omega - k_z v_o)^2 - \omega_{ce}^2} \tag{2.82}$$

and

$$K_{x}^{o} = K_{x} + j \frac{\omega_{ce}}{\omega - k_z v_o} \cdot \frac{\omega_{pb}^2}{(\omega - k_z v_o)^2 - \omega_{ce}^2} , \tag{2.83}$$

where $K_{\parallel}$, $K_{\perp}$ and K_{x} are given by Eq. 2.15 for the plasma alone and the superscript "o" in Eqs. 2.81 through 2.83 signifies that both the beam and plasma are present. ω_{pb} is the plasma frequency for the beam electrons and is given by

$$\omega_{pb}^2 = \frac{n_b e^2}{m\epsilon_o} , \tag{2.84}$$

where n_b is the density of the beam electrons.

Under the quasi-static approximation, the electric field vector can be written as the gradient of a scalar potential Φ:

$$\bar{E} = -\nabla\Phi . \tag{2.85}$$

There is no free charge when using the equivalent dielectric tensor; therefore from Maxwell's equation,

$$\nabla \cdot \bar{D} = \nabla \cdot (\epsilon_o \bar{\bar{K}} \cdot \bar{E}) = 0 \tag{2.86}$$

which leads to a modified Laplace's equation for an anisotropic medium:

$$\nabla \cdot \bar{\bar{K}} \cdot \nabla\varphi = 0 \quad . \tag{2.87}$$

In the cylindrical coordinate system, Eq. 2.87 can be written explicitly for a cold beam-plasma system as

$$\frac{1}{r} \frac{\partial}{\partial r}\left(r \frac{\partial \Phi}{\partial r}\right) + \frac{1}{r^2} \frac{\partial^2 \Phi}{\partial \varphi^2} + \frac{K_{\parallel}^{o}}{K_{\perp}^{o}} \frac{\partial^2 \Phi}{\partial z^2} = 0 \quad . \tag{2.88}$$

To solve this partial differential equation, assume solutions for the potential of the form

$$\Phi = R(r) \cdot \exp[-j(m\varphi + k_z z)] \quad , \tag{2.89}$$

where m is an integer. Substituting Eq. 2.89 into Eq. 2.88 yields the linear differential equation in the radial variable:

$$\frac{1}{r} \frac{d}{dr}\left(r \frac{dR}{dr}\right) - \left(\frac{m^2}{r^2} + k_z^2 \frac{K_{\parallel}^{o}}{K_{\perp}^{o}}\right) R = 0 \quad . \tag{2.90}$$

Substituting

$$T_1^2 = -k_z^2 \frac{K_{\parallel}^{o}}{K_{\perp}^{o}} \tag{2.91}$$

into Eq. 2.90 yields Bessel's equation for the radial variable R:

$$\frac{1}{r} \frac{d}{dr}\left(r \frac{dR}{dr}\right) + \left(T_1^2 - \frac{m^2}{r^2}\right) R = 0 \tag{2.92}$$

in a region where both beam and plasma are present.

The solution of Bessel's equation inside the beam and plasma region is given by

$$R(r) = AJ_m(T_1 r) + BN_m(T_1 r) \quad , \tag{2.93}$$

where J_m and N_m are the ordinary Bessel functions of the first and second kind. Since the fields on the axis must be finite, B = 0 because N_m is infinite at r = 0.

The complete time-dependent potential and field components in the beam and plasma region are:

$$\left.\begin{aligned} \Phi(r,\varphi,z,t) &= AJ_m(T_1 r) \\ E_r(r,\varphi,z,t) &= -AT_1 J_m'(T_1 r) \\ E_\varphi(r,\varphi,z,t) &= j\frac{m}{r}\Phi(r,\varphi,z,t) \\ E_z(r,\varphi,z,t) &= jk_z\Phi(r,\varphi,z,t) \end{aligned}\right\} \exp[j(\omega t - m\varphi - k_z z)] \quad , \tag{2.94}$$

where A is an arbitrary constant.

For a region filled with plasma only, the partial differential equation is identical to Eq. 2.88 except that $K_{\|}^o$ and $K_{\perp}^o$ are replaced by $K_{\|}$ and $K_{\perp}$, respectively. Again, substituting

$$T_2^2 = k_z^2 \frac{K_{\|}}{K_{\perp}} \tag{2.95}$$

into Eq. 2.90 permits the solution of the Bessel equation. The solution can be written as a combination of the modified Bessel function of the

first and second kind. However, the combination must be such that the radial boundary conditions are satisfied.

For a vacuum region, $K_{\|}$ and $K_{\perp}$ become unity and T_2^2 is equal to k_z^2 from Eq. 2.95. The solution is again a combination of the modified Bessel functions.

The dispersion relations will now be obtained for three of the four configurations described in Section 2.3.1. For the coaxial beam-plasma waveguide, there are radial boundaries at the beam edge and at the plasma edge where the solutions must be matched. The dispersion relation for such a case includes two transcendental equations which must be solved simultaneously. Although the dispersion relation can be written in a reasonably simple form, its solution is very involved and is beyond the scope of this work. The experimental beam-plasma geometry encountered in this work is adequately described by simpler configurations, and therefore the coaxial configuration will not be considered in detail.

2.3.2a Dispersion Relation for the Beam-Plasma Filled Waveguide. As mentioned in Section 2.3.1b this configuration is the simplest to analyze. In this case the dispersion relation reduces to an algebraic equation. The configuration for this case is shown in Fig. 2.5a and has one region which includes both the beam and plasma. The solutions given by Eq. 2.94 are applicable to this case.

Since the potential must vanish at the metallic cylindrical waveguide boundary (r = b), set

$$J_m(T_1 b) = 0 \qquad (2.96)$$

or

$$T_1 = p_{mn}/b \ , \qquad (2.97)$$

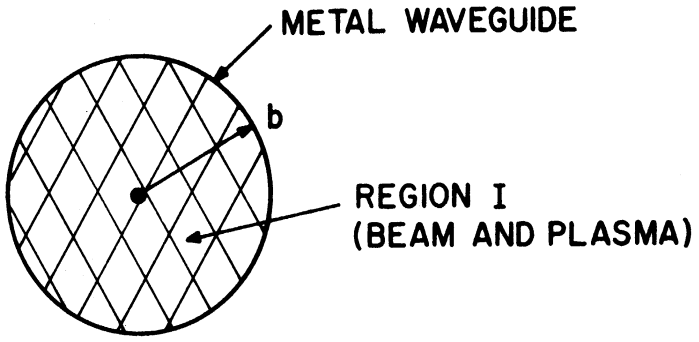

(a) BEAM-PLASMA FILLED WAVEGUIDE

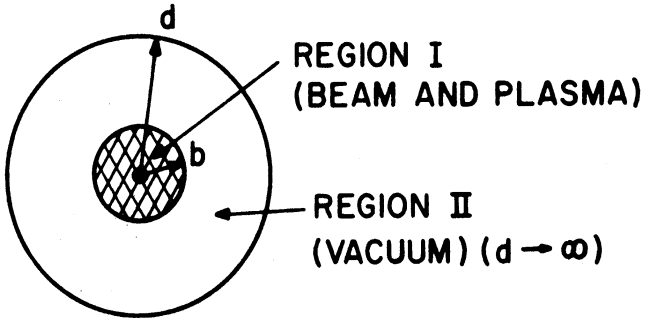

(b) OPEN BEAM-PLASMA WAVEGUIDE

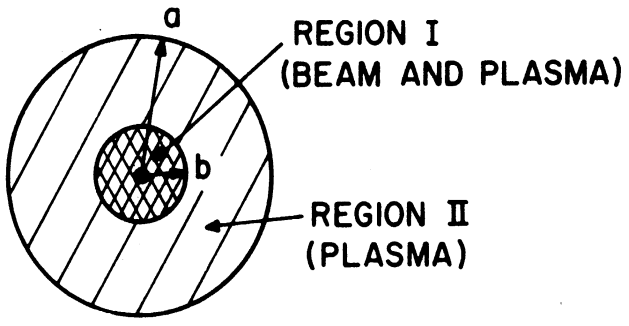

(c) UNFILLED-BEAM, FILLED-PLASMA WAVEGUIDE

FIG. 2.5 CROSS SECTION OF THE BEAM-PLASMA WAVEGUIDES.

where p_{mn} is the nth zero of the mth order Bessel function of the first kind.

The dispersion relation for the beam-plasma filled waveguide is given by

$$\left(\frac{p_{mn}}{b}\right)^2 = -k_z^2 \frac{K_{\parallel}^o}{K_{\perp}^o} \quad . \tag{2.98}$$

For the lowest mode $p_{mn} = 2.405$. Equation 2.98 is a sextic algebraic equation in k_z and is solved numerically in Section 2.3.3. The potential and field components are given by Eq. 2.94.

2.3.2b Dispersion Relation for the Unfilled-Beam, Filled-Plasma Waveguide. A cross section of this configuration is shown in Fig. 2.5c. In Region I, both the beam and plasma are present and Region II consists of the plasma alone. As discussed in Section 2.3.2 the potential function solution for Region I is proportional to the Bessel function of the first kind and the solution for Region II is proportional to a combination of the modified Bessel functions of the first and second kind. The potential function in both regions must satisfy the following radial boundary conditions:

1. At the waveguide boundary (r = a) the potential must vanish ($\Phi^{II} = 0$). Therefore Φ^{II} is written as

$$\Phi^{II} = C\left(I_m(T_2 r)K_m(T_2 a) - I_m(T_2 a)K_m(T_2 r)\right) \quad , \qquad b < r < a \quad , \tag{2.99}$$

where C is an arbitrary constant and I_m and K_m are the mth order modified Bessel functions of the first and second kind.

2. At the beam edge (r = b) the potential must be continuous ($\Phi^I = \Phi^{II}$). Therefore Φ^I and Φ^{II} are written as

$$\Phi^I = A \cdot \frac{J_m(T_1 r)}{J_m(T_1 b)} \tag{2.100}$$

and

$$\Phi^{II} = A \cdot \frac{I_m(T_2 r)K_m(T_2 a) - I_m(T_2 a)K_m(T_2 r)}{I_m(T_2 b)K_m(T_2 a) - I_m(T_2 a)K_m(T_2 b)} , \tag{2.101}$$

where A is an arbitrary constant.

3. At the beam edge (r = b) the normal displacement must be continuous, i.e.,

$$E_r^I K_\perp^o + K_x^o E_\varphi^I = E_r^{II} K_\perp + K_x E_\varphi^{II} \tag{2.102}$$

or

$$K_\perp^o T_1 b \cdot \frac{J_n'(T_1 b)}{J_n(T_1 b)} + \frac{m}{b} \cdot \frac{\omega_{ce}}{\omega - k_z v_o} \cdot \frac{\omega_{pb}^2}{(\omega - k_z v_o)^2 - \omega_{ce}^2}$$

$$= K_\perp T_2 b \left(\frac{I_m'(T_2 b)K_m(T_2 a) - I_m(T_2 a)K_m'(T_2 b)}{I_m(T_2 b)K_m(T_2 a) - I_m(T_2 a)K_m(T_2 b)} \right) , \tag{2.103}$$

where

$$T_1^2 = -k_z^2 \frac{K_\parallel^o}{K_\perp^o} , \tag{2.104}$$

$$T_2^2 = k_z^2 \frac{K_\parallel}{K_\perp} \tag{2.105}$$

and the prime indicates the differentiation with respect to the argument. Equations 2.103 through 2.105 constitute the dispersion relation for the

unfilled-beam, filled-plasma waveguide. It is a transcendental equation which has six roots of k_z at a given frequency for a particular radial and azimuthal mode. The arguments of the Bessel functions may, in general, be complex. This equation is solved numerically with the help of a computer in Section 2.3.3. The complete space and time-dependent potential and field components in this case are as follows.

Region I $(0 \leq r \leq b)$:

$$\Phi^{I}(r,\varphi,z,t) = A \frac{J_m(T_1 r)}{J_m(T_1 b)} \exp[j(\omega t - m\varphi - k_z z)] \quad , \tag{2.106}$$

$$E_r^{I}(r,\varphi,z,t) = -AT_1 \frac{J_m'(T_1 r)}{J_m(T_1 b)} \exp[j(\omega t - m\varphi - k_z z)] \quad , \tag{2.107}$$

$$E_\varphi^{I}(r,\varphi,z,t) = j \frac{m}{r} \Phi^{I}(r,\varphi,z,t) \quad , \tag{2.108}$$

$$E_z^{I}(r,\varphi,z,t) = jk_z \Phi^{I}(r,\varphi,z,t) \quad . \tag{2.109}$$

Region II $(b \leq r \leq a)$:

$$\Phi^{II}(r,\varphi,z,t) = A \frac{I_m(T_2 r)K_m(T_2 a) - I_m(T_2 a)K_m(T_2 r)}{I_m(T_2 b)K_m(T_2 a) - I_m(T_2 a)K_m(T_2 b)} \exp[j(\omega t - m\varphi - k_z z)] \quad , \tag{2.110}$$

$$E_r^{II}(r,\varphi,z,t) = -AT_2 \frac{I_m'(T_2 r)K_m(T_2 a) - I_m(T_2 a)K_m'(T_2 r)}{I_m(T_2 b)K_m(T_2 a) - I_m(T_2 a)K_m(T_2 b)} \exp[j(\omega t - m\varphi - k_z z)] \quad , \tag{2.111}$$

$$E_\varphi^{II}(r,\varphi,z,t) = j \frac{m}{r} \Phi^{II}(r,\varphi,z,t) \quad , \tag{2.112}$$

$$E_z^{II}(r,\varphi,z,t) = jk_z \Phi^{II}(r,\varphi,z,t) \quad . \tag{2.113}$$

2.3.2c Dispersion Relation for the Open Beam-Plasma Waveguide. A cross section for this configuration is shown in Fig. 2.5b. In Region I, both beam and plasma are present and Region II consists of a vacuum of permittivity ϵ_o that extends to infinity. Again the potential function in Regions I and II must satisfy the boundary conditions:

1. As $r \to \infty$ the potential in the region must tend toward zero. To satisfy this condition, the potential in Region II is written as

$$\Phi^{II} = CK_m(T_2 r) \quad , \tag{2.11-}$$

where C is an arbitrary constant.

2. At the beam edge (r = b) the potential must be continuous. Therefore Φ^I and Φ^{II} are written as

$$\Phi^I = A \frac{J_m(T_1 r)}{J_m(T_1 b)} \tag{2.115}$$

and

$$\Phi^{II} = A \frac{K_m(T_2 r)}{K_m(T_2 b)} \quad , \tag{2.11e}$$

where A is an arbitrary constant.

3. At the beam-plasma edge (r = b) the normal component of displacement must be continuous. Therefore

$$K_1^o T_1 b \frac{J'_m(T_1 b)}{J_m(T_1 b)} + \frac{m}{b} \frac{\omega_{ce}}{\omega - k_z v_o} \frac{\omega_{pb}^2}{(\omega - k_z v_o^2) - \omega_{ce}^2} = T_2 b \frac{K'_m(T_2 b)}{K_m(T_2 b)} \quad , \tag{2.11-}$$

where T_1 is given by Eq. 2.104. Again, this transcendental equation has six roots of k_z at a given frequency and for a particular radial and

azimuthal mode. It is also solved numerically in Section 2.3.3. The potential and field components in Region I are the same as those given in Section 2.3.2b, and for Region II they are given by

$$\Phi^{II}(r,\varphi,z,t) = A \frac{K_m(T_2 r)}{K_m(T_2 b)} , \tag{2.118}$$

$$E_r^{II}(r,\varphi,z,t) = -AT_2 \frac{K_m'(T_2 r)}{K_m(T_2 b)} , \tag{2.119}$$

$$E_\varphi^{II}(r,\varphi,z,t) = j \frac{m}{r} \Phi^{II}(r,\varphi,z,t) \tag{2.120}$$

and

$$E_z^{II}(r,\varphi,z,t) = jk_z \varphi^{II}(r,\varphi,z,t) , \tag{2.121}$$

where A is an arbitrary constant.

2.3.3 Numerical Solutions of the Dispersion Relations. The dispersion relations derived in Section 2.3.2 for the three configurations are given by Eqs. 2.98, 2.103 and 2.117. There are six roots for each mode and because of the transcendental nature of the Bessel functions there are an infinite number of radial modes for each of the azimuthal modes which are denoted by m = 0,1,2,.... Therefore, to determine all six roots at a given frequency, each root must be identified with a particular branch for a particular mode.

A Fortran IV computer program[83] was used to trace the roots (which may be complex) of the dispersion relations. The computer program requires an initial guess for a root on a particular branch. Given a starting point, the computer program checks the accuracy of this point and corrects any error to a desired accuracy. The correction procedure

is that of "Newton's method" applied to a function of complex variables. If the starting point is fairly accurate, the desired accuracy is quickly obtained in two or three corrections. If the starting point is inaccurate the convergence may be very slow and, if the dispersion relation is very complicated, the error may not decrease or the root may jump to another branch of the dispersion relation. Therefore, the prediction of each new point should be as accurate as possible. Points on a particular branch are corrected by using the slope of that branch in predicting the new point.

A four-point predictor formula[84] has been used to predict the new point accurately. After correcting the starting point, the slope at that point is used to make a linear extrapolation to the next point. After correcting the second point, the first point and the slope at the second point are used to predict the position of the third point. The fourth point is then found by using the first point and the slopes at the first and third point. Thereafter the four-point predictor formula is used. The accuracy of the four-point formula is such that only one or two applications of the corrector are required. If the accuracy after the first application of the corrector is an order of magnitude more than the required accuracy, the step size is doubled to increase the speed of computation. If the number of steps required to correct the predicted point to a desired accuracy is more than a predetermined number M (usually $M = 3$ or 4), the step size is halved for the next point.

In some cases it may not be possible to trace the entire branch by making a constant increment in ω (for example if $\partial\omega/\partial k$ is very small).

Thus ω or k is chosen as the independent variable depending on which variable is the most rapidly varying one.

The computer program requires a subroutine called FUNCT. This subroutine contains the dispersion function $D(\omega, k) = 0$ and its derivative with respect to ω and k. To solve a new dispersion equation, only the subroutine FUNCT is changed. A listing and the description of the subroutine FUNCT for each dispersion equation solved is given in Appendix B.

An approximate schematic plot of the dispersion diagram for a beam-plasma filled waveguide is shown in Fig. 2.6. For a particular mode, the dispersion equation has six roots for a given frequency. Two roots represent the plasma waves and the other four represent the beam waves. Two of these four roots are beam slow and fast space-charge waves. The remaining two are the beam slow and fast cyclotron waves. In the dispersion diagram (Fig. 2.6), collisions between particles and the coupling of beam and plasma waves are not included. The roots in the cutoff region are purely imaginary and are not shown. The fast waveguide modes have also been excluded.

Experimental data presented in Chapter III reveal that only axisymmetric modes (m = 0) of large axial wavelength are of interest. Therefore in computing the dispersion diagrams, the two branches which represent the beam slow and fast cyclotron waves are not traced. Only the axisymmetric (m = 0) mode is studied. Since the experiments were carried out in the low-density regime ($\omega_{ce}^2 \gg \omega_{pe}^2 \gg \omega_{ce}\omega_{ci}$), the dispersion diagram for this case only is computed. The region of interest for the present investigation has been marked by a circle in Fig. 2.6.

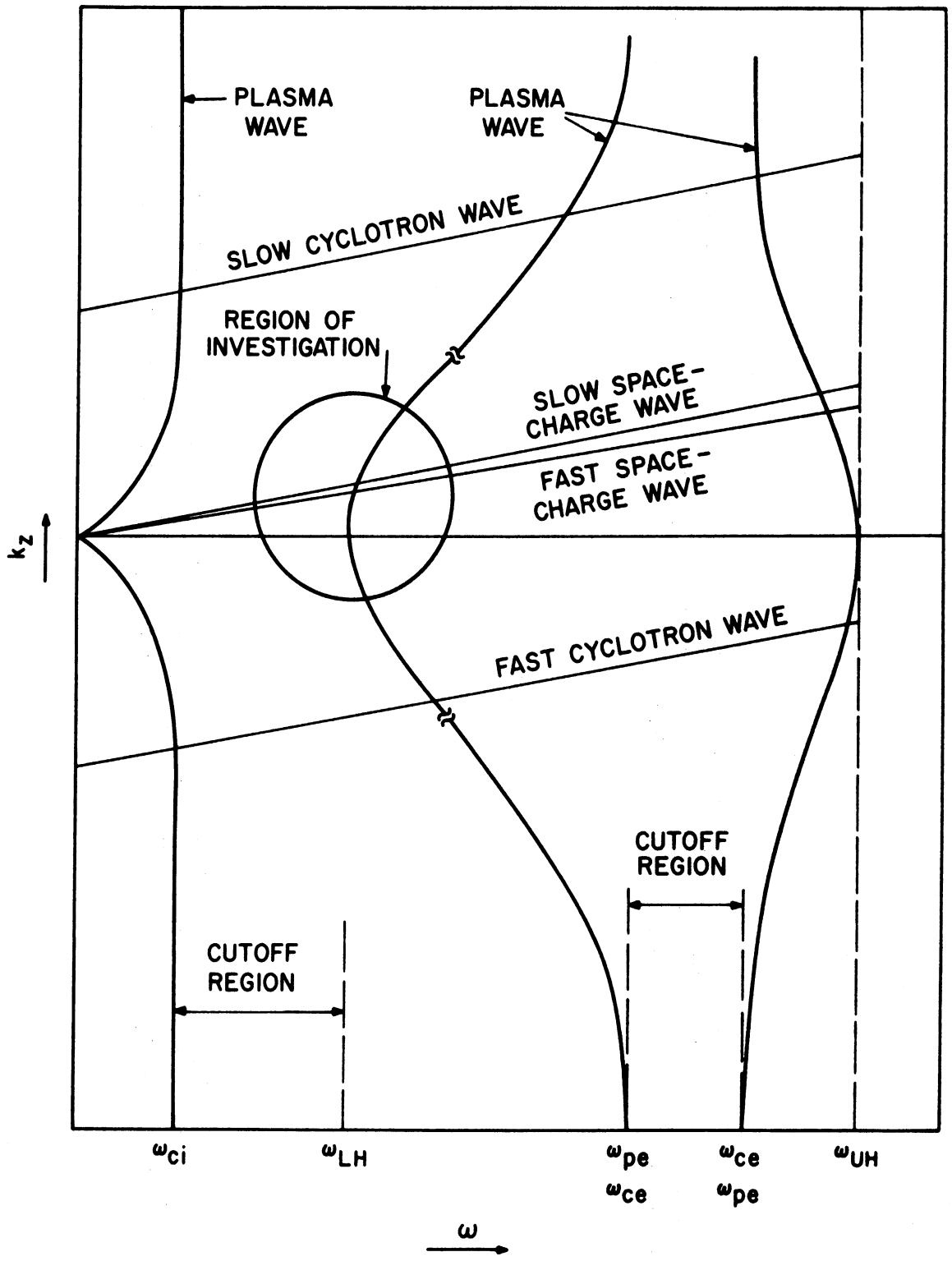

FIG. 2.6 SCHEMATIC DISPERSION DIAGRAM FOR A BEAM-PLASMA FILLED WAVEGUIDE. COUPLING OF THE BEAM AND PLASMA WAVES IS NOT SHOWN.

The detailed dispersion diagram of the beam slow and fast space-charge waves in a finite-diameter beam in an infinite-diameter waveguide (the open waveguide case) is shown in Fig. 2.7. For the m = 0 mode, each beam slow and fast space-charge wave has an infinite number of radial modes packed into a small region. Each pair may interact with the plasma modes, but only the lowest-order (n = 1) mode is included in the computations.

Figure 2.8 shows the various radial modes which are present in a finite-diameter plasma and infinite-diameter waveguide (open waveguide) for an axisymmetric (m = 0) mode. Once again an infinite number of radial modes exists for each azimuthal mode (m = 0,1,2,...). A propagating surface wave appears in the low-frequency region, which is a cutoff region in a filled-plasma waveguide.

Thus it is noted that for the lowest azimuthal mode in a frequency range $\omega_{LH} \leq \omega < \omega_{pe}$, there is an infinite number of beam radial modes and an infinite number of plasma radial modes which would couple. However, usually the lowest-order modes give the principal part of the solution, and therefore in the present study only the lowest-order azimuthal and radial modes will be considered.

2.3.3a Normalization of Parameters for Computer Solution of the Dispersion Equation. In the present investigation the frequency of operation is near the ion-plasma frequency, and therefore all the characteristic frequencies have been normalized with respect to the ion-plasma frequency. Moreover, since the wavelength of interest is of the order of a beam wavelength, the propagation constant has been normalized by ω_{pi}/v_o, where v_o is the beam velocity.

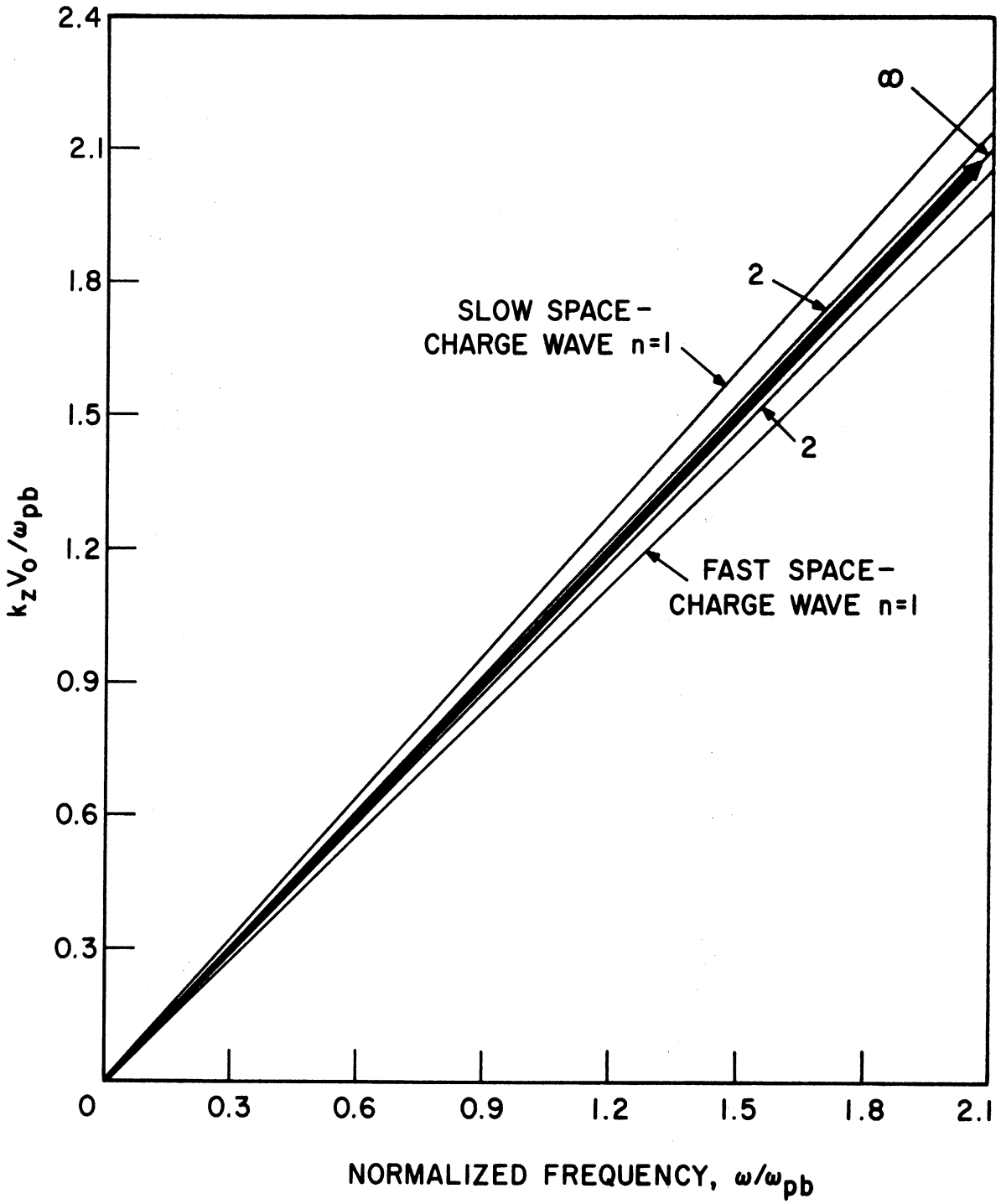

FIG. 2.7 PROPAGATION CONSTANT AS A FUNCTION OF FREQUENCY SHOWING DIFFERENT RADIAL MODES FOR A FINITE-DIAMETER ELECTRON BEAM IN AN INFINITE-DIAMETER WAVEGUIDE. ($m = 0$, $W = \omega/\omega_{pi}$)

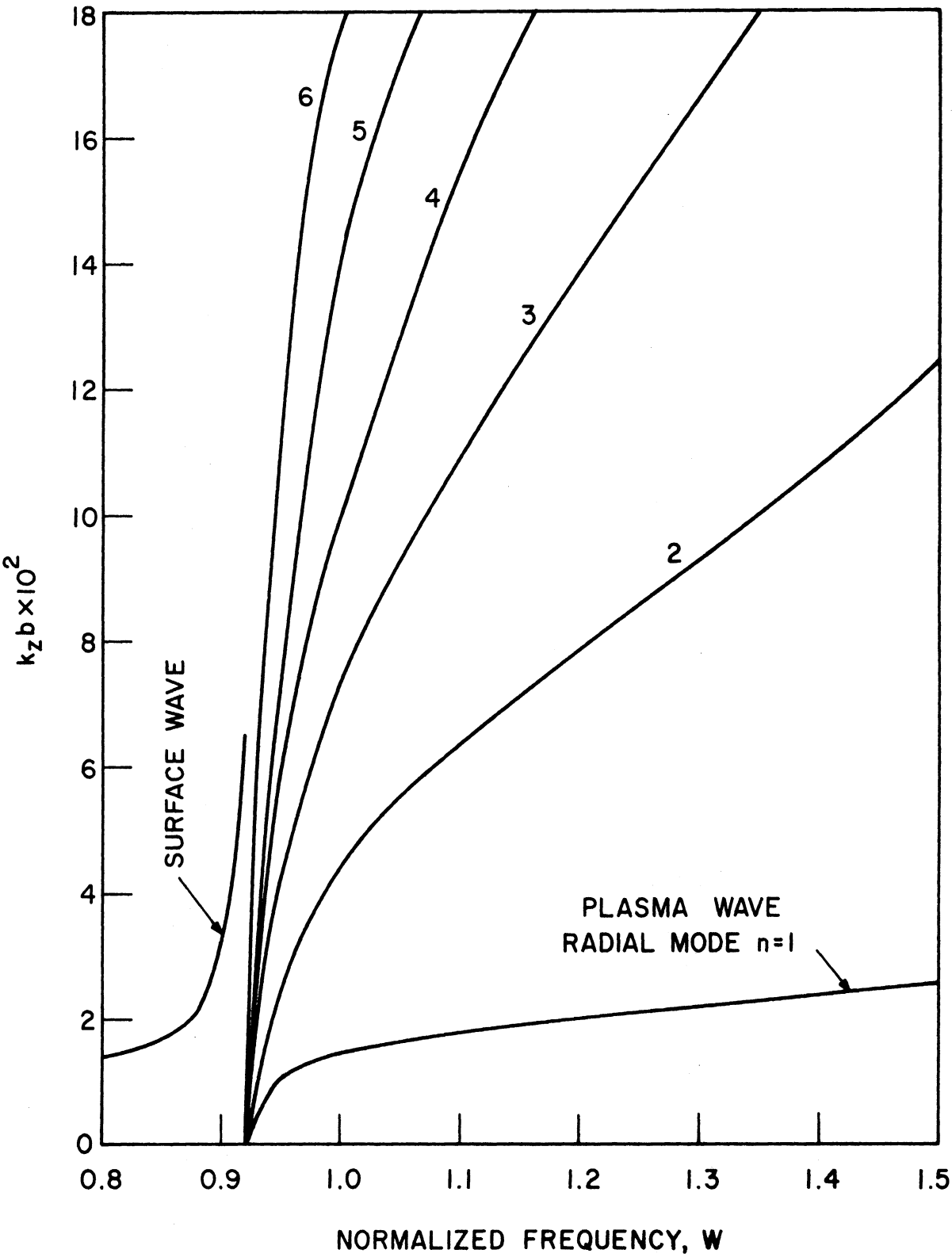

FIG. 2.8 PROPAGATION CONSTANT AS A FUNCTION OF FREQUENCY SHOWING DIFFERENT RADIAL MODES FOR A FINITE-DIAMETER PLASMA IN AN INFINITE-DIAMETER WAVEGUIDE. ($m = 0$, $W = \omega/\omega_{pi}$)

The normalized parameters are:

$$W = \omega/\omega_{pi} \quad , \tag{2.122}$$

$$K = k_z v_o/\omega_{pi} \quad , \tag{2.123}$$

$$WCE = \omega_{ce}/\omega_{pi} \quad , \tag{2.124}$$

$$WCI = \omega_{ci}/\omega_{pi} \quad , \tag{2.125}$$

$$NU = \nu_{eN}/\omega_{pi} \tag{2.126}$$

and

$$R = \omega_{pb}^2/\omega_{pi}^2 \quad . \tag{2.127}$$

The ratio of the beam density to the plasma density is given by

$$\rho_{ob}/\rho_{op} = R/G \quad , \tag{2.128}$$

where G is the ion-to-electron mass ratio (M/m). The normalized electron-beam radius b is represented by the symbol

$$CV = b\omega_{pi}/v_o \quad . \tag{2.129}$$

The electron-beam perveance is defined as

$$S = 10^6 \cdot I/V^{3/2} \quad \text{(micropervs)} \quad , \tag{2.130}$$

where I is the beam current in amperes and V is the beam voltage in volts. The beam radius can be found in terms of S and R since

$$I = \pi b^2 \rho_{ob} v_o \tag{2.131}$$

and

$$v_o = \sqrt{\frac{2e}{m} V} \quad . \tag{2.132}$$

Substituting for I from Eq. 2.130, ρ_{ob} from Eq. 2.128 and v_o from Eq. 2.132 into Eq. 2.131 yields

$$b = 0.173 \frac{v_o}{\omega_{pi}} \sqrt{S/R} \tag{2.133}$$

or

$$CV = 0.173 \sqrt{S/R} \quad . \tag{2.134}$$

As a result of the present normalization, the normalized value of $K = k_z v_o/\omega_{pi}$ can be quickly plotted as a function of the normalized frequency $W = \omega/\omega_{pi}$ to obtain the dispersion diagram. However, to bring out the dependence of certain parameters such as ion mass; beam voltage; etc., for a fixed beam-plasma diameter, the dispersion diagram will be plotted in an alternative way. i.e., $k_z b$ vs. W. The normalized propagation constant $k_z b$ is easily obtained as

$$k_z b = K \cdot CV \quad , \tag{2.135}$$

where K and CV have been previously defined.

2.3.3b Dispersion Diagram for a Beam-Plasma Filled Waveguide.

The dispersion relation for the beam-plasma filled waveguide for the lowest-order mode is obtained from Eq. 2.98 and is given by

$$\left(\frac{2.405}{b}\right)^2 = -k_z^2 \cdot \frac{1 - \frac{\omega_{pe}^2}{\omega^2} - \frac{\omega_{pi}^2}{\omega^2} - \frac{\omega_{pb}^2}{(\omega - k_z v_o)^2}}{1 - \frac{\omega_{pe}^2}{\omega^2 - \omega_{ce}^2} - \frac{\omega_{pi}^2}{\omega^2 - \omega_{ci}^2} - \frac{\omega_{pb}^2}{(\omega - k_z v_o)^2 - \omega_{ce}^2}} \quad . \tag{2.136}$$

Using the normalization procedure given in Section 2.3.3a yields

$$K_\perp^o + (0.416 \cdot K \cdot CV)^2 K_\parallel^o = 0 \quad , \tag{2.137}$$

where

$$K_\perp^o = K_\perp - \frac{R}{(W - K)^2 - WCE^2} \quad , \tag{2.138}$$

$$K_\parallel^o = K_\parallel - \frac{R}{(W - K)^2} \quad , \tag{2.139}$$

$$K_\perp = 1 - \frac{G(W - jNU)}{W[(W - jNU)^2 - WCE^2]} - \frac{1}{W^2 - WCI^2} \tag{2.140}$$

and

$$K_\parallel = 1 - \frac{G + 1}{W^2} \quad . \tag{2.141}$$

The complex K roots of the dispersion equation (Eq. 2.131) are obtained for real W with the computer. The resulting dispersion diagram

for the beam-plasma filled waveguide is shown in Fig. 2.9 in which the normalized propagation constant $k_z b$ is plotted as a function of normalized frequency $W = \omega/\omega_{pi}$. The frequency range covered is near $W = 1$ and particle collisions have been neglected. The dispersion diagram shows the two plasma waves (which appear for $W > W_{LH} \simeq 0.95\ W$), one of which propagates in the positive z-direction and the other in the negative z-direction. There are two beam waves, one is the slow space-charge wave and the other is the fast space-charge wave.

The coupling of the plasma wave and the beam space-charge waves is shown in the figure near and below $W = W_{LH}$. At synchronism (where the phase velocity of the plasma wave is equal to the phase velocity of the beam waves) the coupling of the waves produces complex conjugate roots (without collisions). In the region $W < W_{LH}$, there is no propagating plasma wave and the beam waves result in the reactive-medium type of instability. The roots in this region are complex conjugate and represent reactive-medium amplification. However the growth rates are very small in this frequency range.

When the effect of electron-neutral collisions is taken into account, the resulting dispersion diagram is as shown in Fig. 2.10. The roots of the beam and plasma waves in the region $W > W_{LH}$ become complex and acquire small imaginary parts. The propagating plasma wave roots (real part) penetrate into the cutoff region with increasing imaginary parts. The growth rate corresponding to the positive imaginary part which represents the amplifying wave is slightly reduced. The negative imaginary part, which is an evanescent wave, is slightly increased.

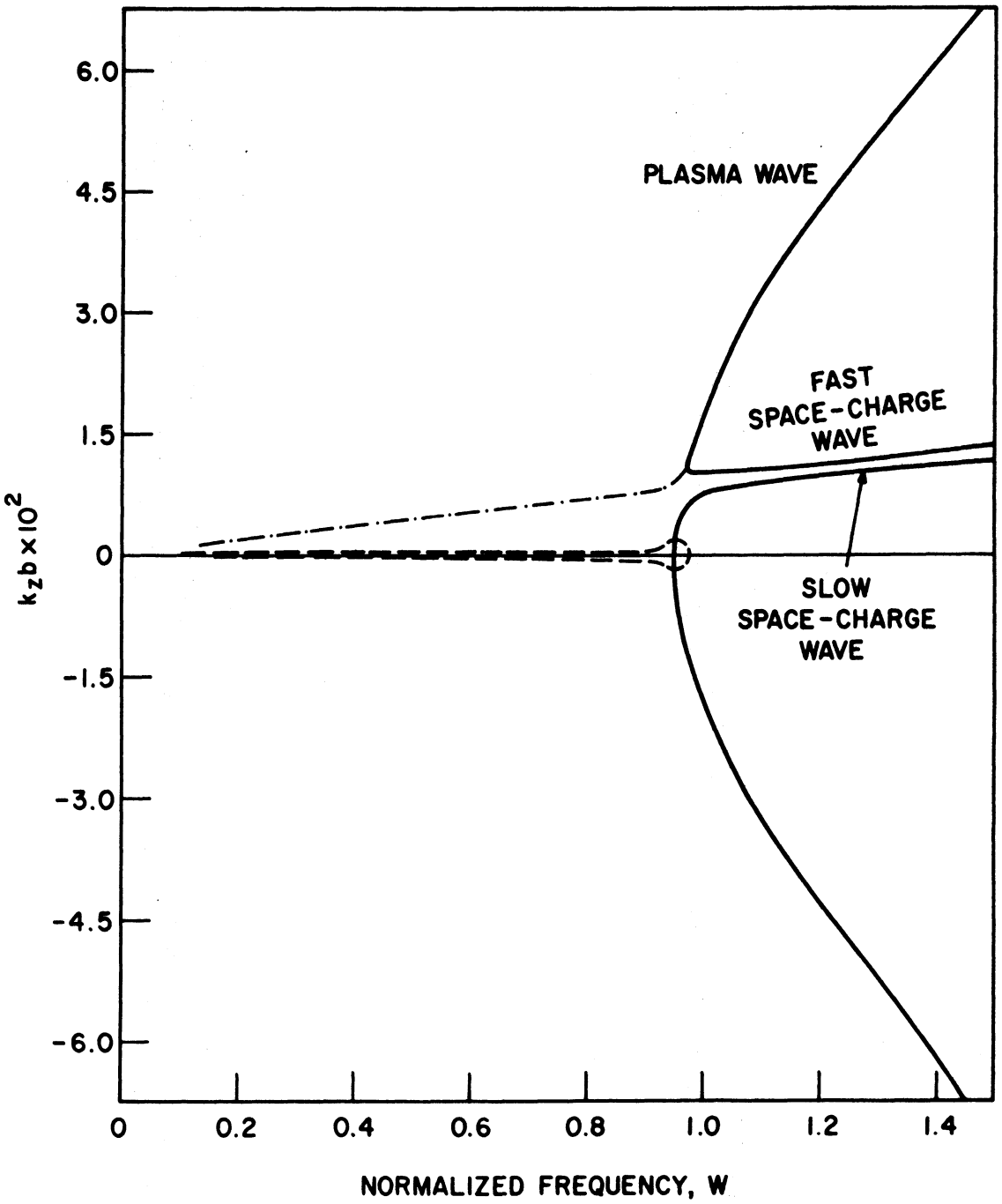

FIG. 2.9 PROPAGATION CONSTANT AS A FUNCTION OF FREQUENCY FOR A BEAM-PLASMA FILLED WAVEGUIDE. (R = 66.5, V_b = 600 V, NU = 0, ω_{ce}/ω_{pe} = 3)

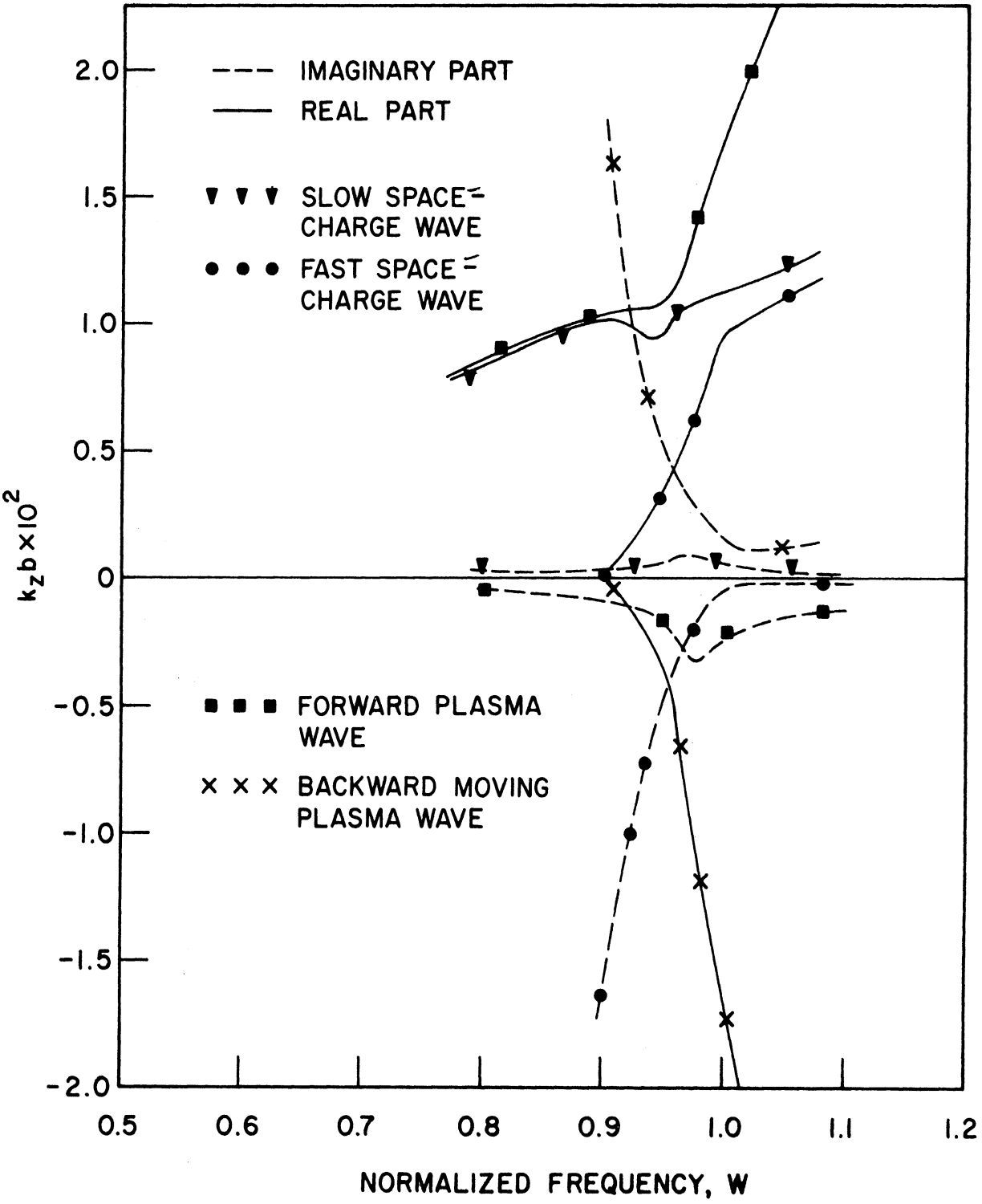

FIG. 2.10 PROPAGATION CONSTANT AS A FUNCTION OF FREQUENCY FOR A BEAM-PLASMA FILLED WAVEGUIDE. (R = 66.5, V_b = 600 V, NU = 0.1, ω_{ce}/ω_{pe} = 3)

In conclusion, the collisions have little effect on the real part of the roots and they reduce the amplification rate near $W \simeq W_{LH}$. The small positive imaginary part that appears for $W > W_{LH}$ represents amplification resulting from the interaction of the beam slow space-charge wave with the resistive plasma medium. This is analogous to the resistive-wall amplification in microwave tube theory.[85]

2.3.3c Dispersion Diagram for the Unfilled-Beam, Filled-Plasma Waveguide. The dispersion relation for the lowest azimuthal mode (m = 0) for the unfilled-beam, filled-plasma waveguide is obtained from Eq. 2.103 as

$$K_{\perp}^{o} T_{1b} \frac{J_1(T_{1b})}{J_o(T_{1b})} = K_{\perp} T_{2b} \left(\frac{I_1(T_{2b})K_o(T_{2a}) + I_o(T_{2a})K_1(T_{2b})}{I_o(T_{2b})K_o(T_{2a}) - I_o(T_{2a})K_o(T_{2b})} \right) . \quad (2.142)$$

Equation 2.136 can be written as

$$\pm j\sqrt{K_{\parallel}^{o} K_{\perp}^{o}} \cdot \frac{J_1(T_{1b})}{J_o(T_{1b})} = \sqrt{K_{\parallel} K_{\perp}} \left(\frac{I_1(T_{2b})K_o(T_{2a}) + I_o(T_{2a})K_1(T_{2b})}{I_o(T_{2b})K_o(T_{2a}) - I_o(T_{2a})K_o(T_{2b})} \right) . \quad (2.143)$$

The negative and positive signs on the left-hand side of the equation give the positive $\mathrm{Re}(k_z)$ and negative $\mathrm{Re}(k_z)$, respectively, for $\omega_{LH} < \omega < \omega_{pe}$. This distinction must be made when tracing the roots in order to obtain all of the branches. The dispersion diagram for the coaxial unfilled-beam, filled-plasma waveguide is similar to the one for the beam-plasma filled waveguide and is shown in Fig. 2.11.

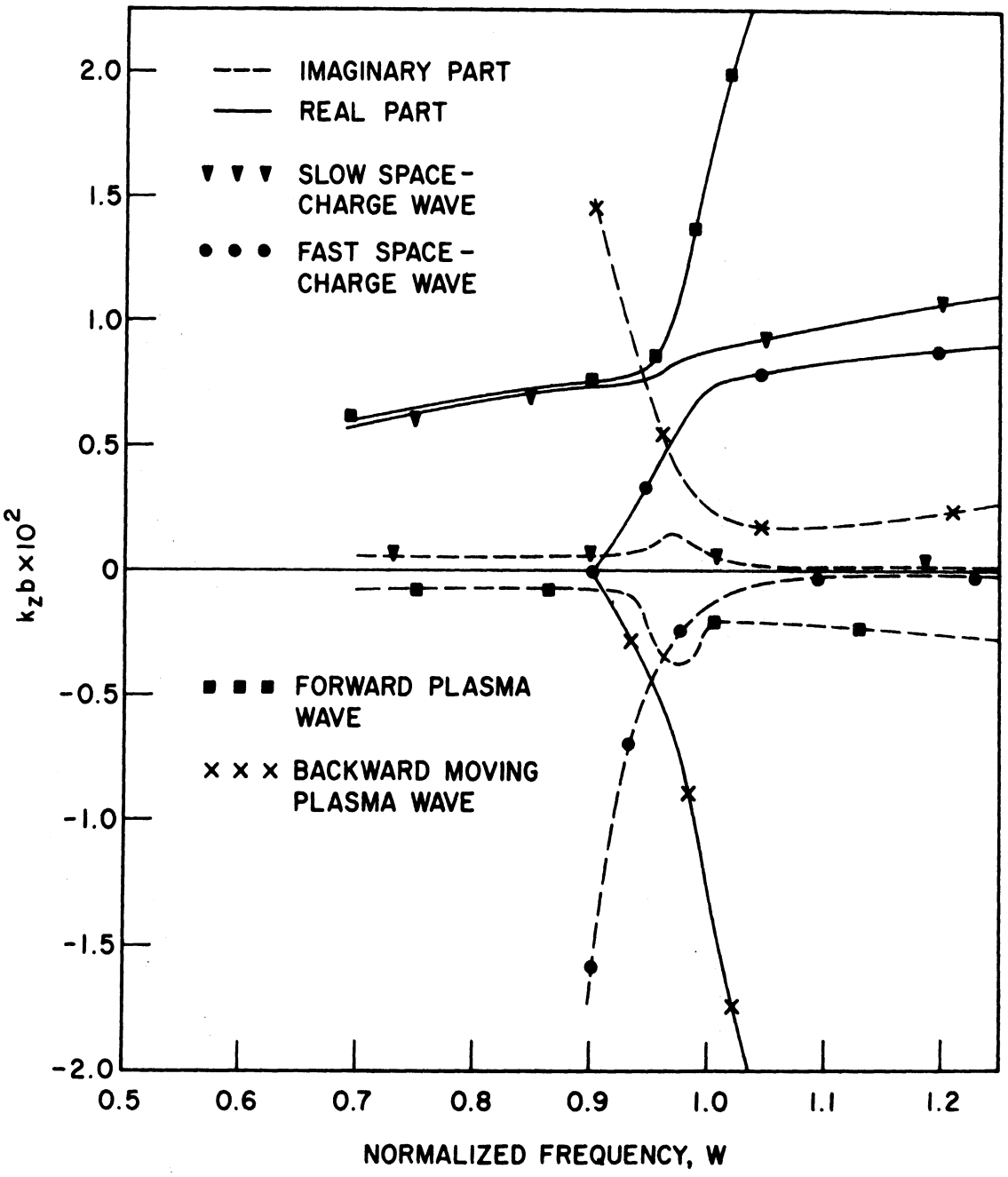

FIG. 2.11 PROPAGATION CONSTANT AS A FUNCTION OF FREQUENCY FOR AN UNFILLED-BEAM, FILLED-PLASMA WAVEGUIDE. (R = 190, V_b = 1000 V, NU = 0.1, ω_{ce}/ω_{pe} = 3)

2.3.3d Dispersion Diagram for an Open Beam-Plasma Waveguide.

The dispersion relation for the lowest-order azimuthal mode (m = 0) for an open beam-plasma waveguide is obtained from Eq. 2.117 and is given by

$$K_1^o T_1 b \frac{J_1(T_1 b)}{J_o(T_1 b)} = T_2 b \frac{K_1(T_2 b)}{K_o(T_2 b)} \quad . \tag{2.144}$$

Equation 2.144 can be written as

$$\pm j \sqrt{K_\parallel^o K_\perp^o} \frac{J_1(T_1 b)}{J_o(T_1 b)} = \frac{K_1(\mp k_z b)}{K_o(\mp k_z b)} \quad . \tag{2.145}$$

Again, the negative and positive signs on the left-hand side give positive $\mathrm{Re}(k_z)$ and negative $\mathrm{Re}(k_z)$, respectively, for $\omega_{LH} < \omega < \omega_{pe}$. Moreover, in this case the positive and negative sign in the arguments of K_1 and K_o are to be taken according as $\mathrm{Re}(k_z) \gtrless 0$ to keep the potential and field finite for large values of r.[86]

The dispersion diagram for an open beam-plasma waveguide is shown in Fig. 2.12. In this case, for the given parameters the beam and plasma are synchronous over a relatively large frequency range and therefore complex roots due to the coupling of the plasma wave and the beam slow space-charge wave are obtained over a wide frequency range. If the electron-neutral collisions are not included, complex conjugate roots are obtained from $W \cong 1$ to $W \cong 5$. However, the collisions reduce the magnitude of the positive imaginary part and increase the magnitude of the negative imaginary part. Moreover, the complex roots are now obtained even for $W > 5$ and represent the resistive-medium interaction. Again, the real parts of the complex roots are not changed significantly except for the

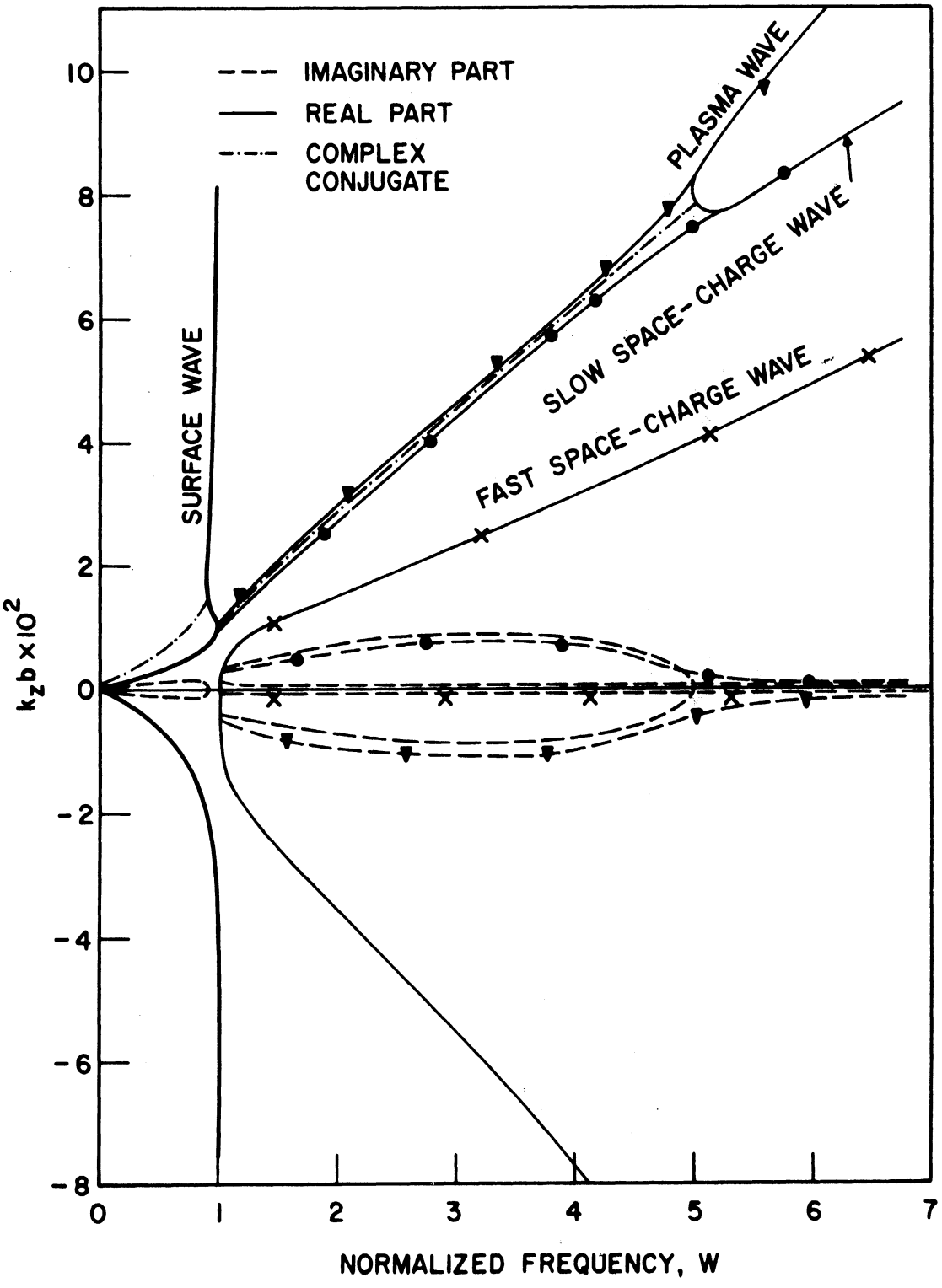

FIG. 2.12 PROPAGATION CONSTANT AS A FUNCTION OF FREQUENCY FOR AN OPEN BEAM-PLASMA WAVEGUIDE. COMPLEX CONJUGATE ROOTS ARE OBTAINED FOR NU = 0. REAL PARTS OF THE COMPLEX ROOTS FOR NU = 0.1 ARE APPROXIMATELY THE SAME AS THE REAL PARTS OF THE ROOTS FOR NU = 0. NU = 0 FOR W < 1. (R = 300, V_b = 500 V, ω_{ce}/ω_{pe} = 10)

real parts of the complex conjugate roots. The real part in this case actually splits into two different real parts which merge into the plasma wave and the slow space-charge wave.

Below $W < W_{LH}$ an interaction between the propagating plasma surface wave and the beam space-charge waves is found. The effect of electron-neutral collisions on this interaction was not studied.

In conclusion, the dispersion diagrams for the three cases are basically of the same form. However, in the open beam-plasma waveguide for $W < W_{LH}$, a surface-wave interaction is obtained. In all three cases the axisymmetric mode ($m = 0$) is considered and only the lowest-order radial mode is shown. The dispersion diagrams have been computed only in the low-density regime and the interaction of the beam-cyclotron waves with the plasma waves is not shown.

The growth rates for reactive-medium amplification, space-charge wave amplification and surface-wave amplification are quite small in the frequency range studied. As is discussed in Chapter IV, the fact that a weak amplifying wave exists in the frequency range under consideration is not of prime importance in the present investigation. However, the complex roots will be used in Chapter IV for the normal-mode field calculations of plasma-cavity resonances.

CHAPTER III. EXPERIMENTAL STUDIES

3.1 Description of the Experimental Setup

A schematic diagram of the experimental setup is shown in Fig. 3.1. The essential components of the apparatus are (1) a vacuum system, (2) a plasma source, (3) an electron gun and associated modulation circuit, (4) an electron-beam collector and associated biasing circuit, (5) an Einzel lens, (6) a solenoid and (7) diagnostic apparatus.

3.1.1 Vacuum System. The vacuum system consists of a central vacuum chamber where the plasma column is located, a pumping system to evacuate it to a desired base pressure and a leak valve to introduce a gas for plasma production.

The vacuum chamber consists of a cylindrical stainless steel tube of 4-inch diameter and approximately one meter in length, as shown in the schematic drawing of Fig. 3.1. Several ports are provided along the length of the tube for inserting the radial diagnostic probes and for observing the plasma through the glass windows. One end of the tube is connected to the pumping system through a metal cross and a bellows. The other end of the tube is blocked by a metal end plate and sealed through an O-ring seal.

An electron gun is connected to one end of the cross and a plexiglass window is placed on the top end for viewing purposes. The third end is joined to the cylindrical tube and the bottom end is connected to the upper end of the bellows which leads to the pumping system. The use of the bellows allowed the tube to be moved slightly under vacuum for the purpose of aligning the axis of the tube with the steady magnetic field.

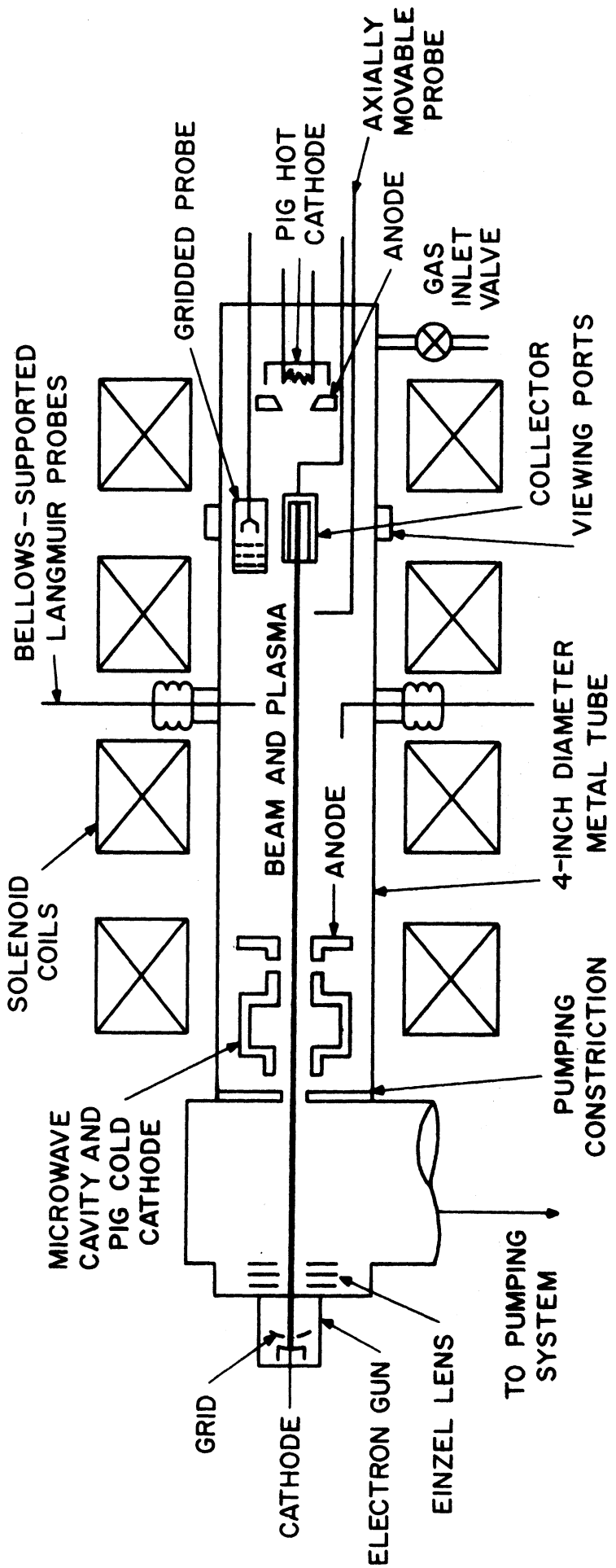

FIG. 3.1 SCHEMATIC DIAGRAM OF THE EXPERIMENTAL APPARATUS.

An oil diffusion pump backed up by a mechanical forepump was used to evacuate the central vacuum chamber. A molecular-sieve trap was provided to prevent the diffusion pump oil from backstreaming into the central vacuum chamber. A gate valve is connected between the bellows and the trap. When exposing the vacuum chamber to atmospheric pressure, the gate valve is closed so that the diffusion pump does not have to be shut down.

Base pressure of the order of 1×10^{-6} Torr is maintained in the central vacuum chamber. For plasma generation, hydrogen, deuterium, neon or argon is continuously admitted through a needle valve provided at the end away from the vacuum pump. The needle valve can be controlled to produce the desired gas pressure. The main plasma region and the electron-gun region are separated by a pumping constriction. The pressure in the gun region was lower by a factor of 2.5 as compared to that in the plasma region. The pressure in the two regions was measured by ionization gauges located in each region. The vacuum chamber was baked to 100°C for several hours each time it had been exposed to atmospheric pressure.

3.1.2 Plasma Source. Two methods of generating a plasma were employed during the course of the present investigation. They were (1) hot-cathode Penning discharge and (2) beam-generated plasma.

3.1.2a Penning Discharge. The hot cathode (a mercury rectifier, oxide-coated, heavy-duty cathode) is located at one end of the tube as shown in Fig. 3.1. Just in front of it is a hollow cylindrical metal anode whose inner diameter of 0.8 inch determines the plasma diameter. At the other end of the tube (gun end) there is a cylindrical hollow anode and a hollow aluminum cold cathode which is a part of the microwave cavity itself. The microwave cavity is used for plasma density measurements and is

described in Section 3.1.7a. A dc axial magnetic field is required for the operation of the Penning discharge.

A typical range of parameters for the operation of the Penning discharge is given in Table 3.1. No instability has been predicted for this type of hot-cathode discharge in the frequency range of interest (2 to 30 MHz).[87] It was anticipated at the beginning of the experimental work that the Penning discharge would be used considerably. It was found, however, that the plasma generated by this means was somewhat noisy. Thus it was harder to take RF measurements with the Penning discharge than with the beam-generated plasma described in the next section. In the present investigation, therefore, beam-generated plasma has been used almost exclusively for the RF plasma-ion heating experiments.

Table 3.1

Typical Range of Parameters of the Penning Discharge

Discharge voltage	100 to 200 V
Discharge current	200 to 1000 mA
Hydrogen gas pressure	1×10^{-3} to 1×10^{-4} Torr
Magnetic field	100 to 600 G
Discharge density	1×10^{9} to $5 \times 10^{10}/cm^3$
Electron temperature	5 to 10 eV
Discharge diameter	0.8 to 1 inch

3.1.2b Beam-Generated Plasma. An electron beam passing through a gas-filled region produces a beam-generated plasma as a result of ionizing collisions of the beam electrons with the gas atoms. These ionizing collisions yield both a positive ion and a slow plasma electron at each

encounter. The rate of production is determined by the beam current, collision cross section and the gas pressure. The ultimate density is established by a balance between the rate of production and the rate of recombination at the walls and in the volume of the gas. In the presence of a dc magnetic field along the beam, radial flow of slow plasma electrons is inhibited and a long, thin plasma column is formed. For a weak beam, a "quiescent" plasma is generated and visual observation in this case indicates that the beam and plasma have approximately the same diameter.[82]

However, if the beam current is increased at a fixed beam voltage an instability is observed. This is characterized by increased RF noise and the expansion of visible plasma diameter to several times that of the beam diameter. This is the "beam-plasma discharge" mode. In the present investigation the quiescent mode is used almost exclusively.

The typical plasma parameters for the beam-generated plasma in the quiescent mode are given in Table 3.2.

Table 3.2

Typical Plasma Parameters for a Beam-Generated Plasma in the Quiescent Mode

Dc beam voltage	400 to 1000 V
Average beam current	2 to 2.5 mA
Hydrogen gas pressure	8×10^{-5} to 8×10^{-4} Torr
Plasma Density	5×10^{8} to $5 \times 10^{9}/cm^{3}$
Electron temperature	5 to 6 eV
Discharge diameter	~ 6 mm
Magnetic Field	300 to 400 G

3.1.3 Electron Gun and Associated Modulation Circuit. The electron gun is a Pierce type of traveling-wave tube gun with a grid located very near the cathode. The perveance of the gun is 1.6×10^{-6} $A/V^{3/2}$ and the effective amplification factor is approximately 60. The gun is capable of giving 240 mA at an anode voltage of 3 kV with a grid voltage of 30 V and a grid current of 10 mA. However in the present experiment the gun was operated at a relatively low voltage and low current with a negative grid bias.

For current modulation any desired signal including CW-RF or AM-RF can be applied at the grid electrode. The upper frequency limit is caused by cathode lead inductance and is approximately 30 MHz. The modulation signal is applied to the grid through a coupling circuit that is shown in Fig. 3.2a. The output of a wideband signal generator is amplified by a wideband transformer to obtain a maximum of approximately 10 V rms. The RF voltage is capacitively coupled to the grid of the electron gun. The other capacitors were used to provide a shorted path for the RF current. The length of the leads of the RF circuit were kept as short as possible.

3.1.4 Electron-Beam Collector. The electron beam produced by the electron gun is collected by a collector. It is made of nonmagnetic stainless steel and is shaped like a cup to trap the secondary electrons within it. The electrical connection to the collector is through a rigid coaxial cable from one of the end plates as shown in the schematic drawing of Fig. 3.1. This collector can be moved axially as well as azimuthally with the help of a double Wilson seal.

In order to monitor the RF current modulation on the beam, the beam current is returned to ground from the collector through a 50-Ω resistor

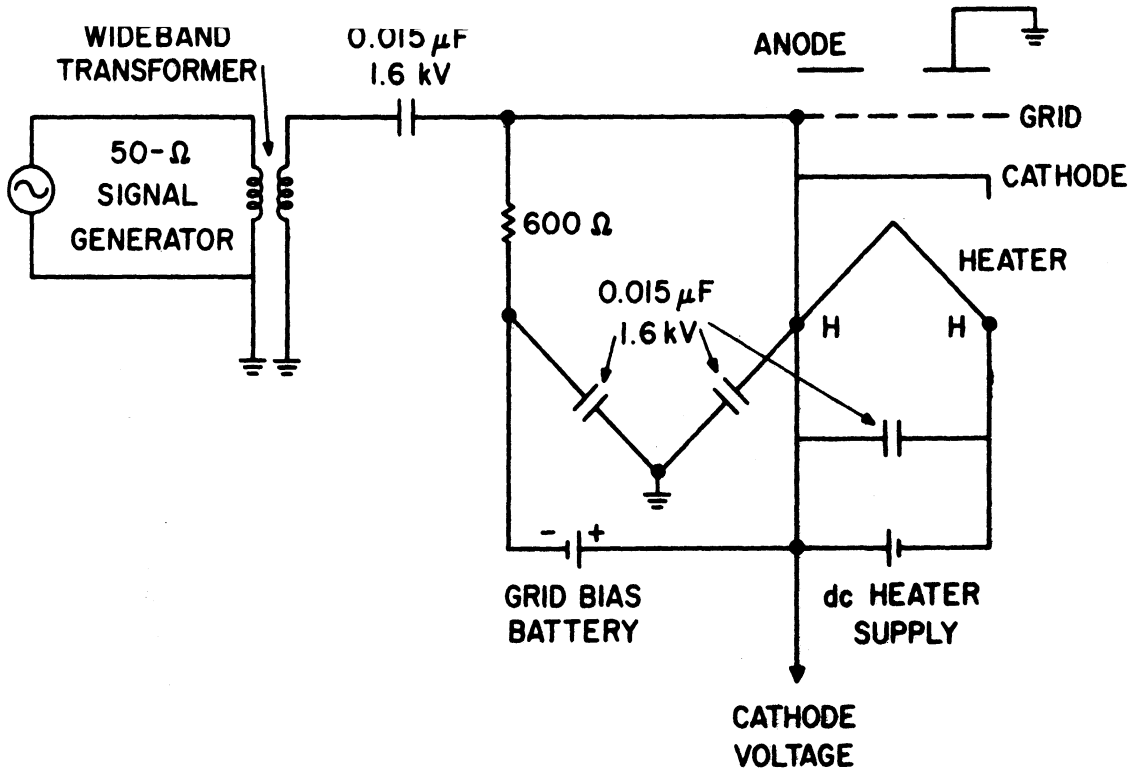

(a) CIRCUIT DIAGRAM FOR ELECTRON-BEAM CURRENT MODULATION

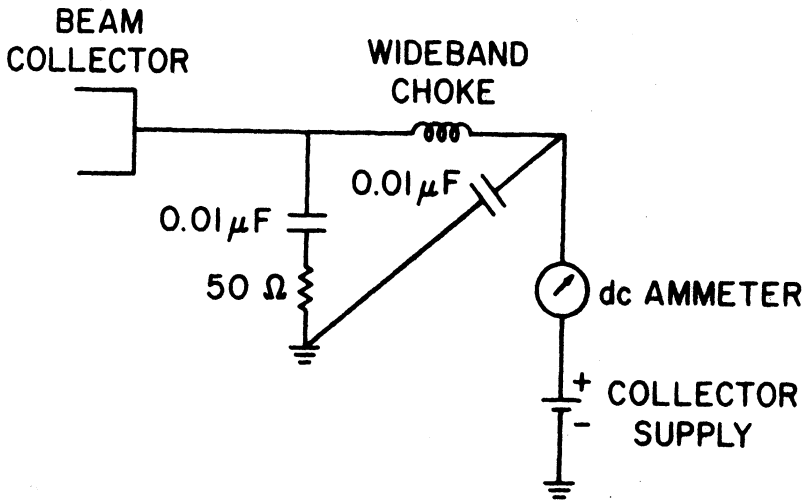

(b) COLLECTOR BIAS CIRCUIT

FIG. 3.2 CIRCUIT DIAGRAMS FOR BEAM MODULATION AND COLLECTOR BIASING.

and monitored on a high-frequency oscilloscope. In the case of the beam-generated plasma, the dc potential on the collector has a significant effect on the plasma parameters. To bias the collector with an appropriate dc potential, a circuit was used as shown in Fig. 3.2b. This circuit was required to prevent the RF current from going through the power supply circuit and to minimize the effect of stray capacitances on the RF circuit. The RF response of this circuit was flat over the frequency range of interest (2 to 30 MHz).

3.1.5 Einzel Lens. In order to reduce the ion bombardment of the cathode of the electron gun by the ions produced in the plasma located in the central vacuum chamber, an "Einzel lens" was used. It acts as a mirror for ions and does not affect the electrons when biased appropriately.

The Einzel lens[88] consists of three equally spaced apertures, the outer two of which are maintained at the ground potential while the middle aperture may be at either a higher or a lower potential. In the present case, for the Einzel lens to act as a mirror for ions, the inner electrode is kept at a positive potential (22 V) with respect to the two outer electrodes. The focal characteristics of an Einzel lens are described in Reference 88.

The effectiveness of the Einzel lens in improving the gun cathode life was not determined. However, it seems that it will only be partially effective since it does not inhibit the ions produced in the region between the cathode and the lens from impinging on the cathode.

3.1.6 Magnetic Field Solenoid. The magnetic field solenoid consists of 8 coils which have an inside diameter of 10 inches. Two dc power supplies

rated at 550 A/80 V and 1050 A/150 A are used to energize the coils. The coils are used to produce either a uniform or magnetic mirror field of 200 to 600 G in the middle position. A mirror ratio of 2:1 is usually used. An extra coil of 7-inch inside diameter is used to adjust the magnetic field in the gun region for maximum beam transmission from the gun to the collector.

3.1.7 Diagnostic Apparatus.

3.1.7a Microwave Cavity. A microwave cavity is used for plasma density measurements by observing the shift of the cavity resonant frequency caused by the introduction of the plasma.

A cylindrical microwave cavity, 3.021 inches in diameter and 2 inches in length, is constructed out of copper. It is designed to operate in the TM_{010} mode with an empty cavity resonant frequency of approximately 5 GHz. Two cylinders of approximately 1 inch in diameter and 1.5 inches in length are provided at the two ends of the cavity and they act as waveguides beyond cutoff for the frequency of operation. The TM_{010} mode is used since its electric field is parallel to the axis and thus the dc magnetic field should have no effect on the resonant frequency. Coaxial coupling into and out of the cavity is accomplished by using a loop for magnetic coupling which has its plane oriented perpendicular to the cavity magnetic field at the loop position. In the present case two coaxial leads were inserted into two holes in a flat end of the cavity with the individual loops protruding into the cavity.

The frequency shift $\Delta\omega/\omega_r$ caused by the presence of a plasma has been calculated by Buchsbaum et al.[89] using a perturbation analysis and neglecting the fringing fields due to the presence of the end holes in the cavity. It is given by

$$\frac{\Delta\omega}{\omega_r} = \frac{1}{2}\left(\frac{\omega_{po}}{\omega_r}\right)^2 \frac{\int_0^R \frac{n(r)}{n_p} J_o^2\left(\frac{2.4\ r}{d}\right) r\ dr}{\int_0^d J_o^2\left(\frac{2.4\ r}{d}\right) r\ dr}\ , \qquad (3.1)$$

where R and d are the plasma and cavity radii, respectively, n(r) is the density profile, n_p is the peak density, ω_{po} is the plasma frequency at the peak and ω_r is the resonant frequency of the empty cavity. The density profile can be obtained by other means such as by measuring the saturation ion current drawn by a Langmuir probe. Usually, the density profile is not a simple function of r and one must numerically evaluate the integral in Eq. 3.1 as was done by Chen et al.[90] Thus a theoretical curve is obtained by plotting the resonant frequency ($\omega_r d/c$) as a function of plasma density (ω_p^2/ω_r^2) for a given value of R/d. The resulting curve is a straight line as obtained by the perturbation analysis, which is valid for values in the range of $\omega_p/\omega_r \leq 1.5$. However, the perturbation and exact analysis depart considerably for larger values of ω_p/ω_r. The cavity measurement is usually limited to $\omega_p/\omega_r < 1$ since otherwise the resonance peak becomes very broad and is hard to distinguish from other spurious resonances.

If the density is assumed to be uniform over the plasma diameter, Eq. 3.1 can be written as[91]

$$\frac{\Delta\omega}{\omega_r} = \left(\frac{S}{2.4}\right)\left(\frac{\omega_p^2}{\omega_r^2}\right)\ , \qquad (3.2)$$

where S is the slope of the theoretical curve and is given by

$$S = 2.4(R/d)^2 \frac{1}{2} \frac{J_o^2(k_o R) + J_1^2(k_o R)}{J_1^2(2.4)} , \qquad (3.3)$$

where $k_o = 2.4/d$. The plasma density is determined by measuring the shift in the resonant frequency of the cavity which is due to the presence of a plasma.

In certain cases the plasma may be nonuniform and the effect of the end holes may be significant.[91,92] Thomassen[91] showed that neglecting the nonuniformity of the plasma and the fringing field due to the end holes results in a smaller slope S and thus gives an underestimate of the plasma density. This was also found by Chen et al.[90] who estimated the effect of fringing fields experimentally.

A schematic of the circuit diagram for the measurement of the shift in resonant frequency of the microwave cavity is shown in Fig. 3.3. An S-band (2 to 4 GHz) signal generator and a microwave leveler are used to obtain a constant RF output at all frequencies when the frequency band is swept electronically. A signal proportional to the swept frequency is fed to the horizontal deflection input terminals of the oscilloscope. The RF signal is amplitude modulated by a 1000 Hz square-wave signal and the modulated RF signal is fed to one of the two ports of the microwave cavity. The output of the microwave cavity is coupled through the second port to a microwave frequency meter after which is is detected by a crystal detector. The output of the crystal detector is fed to the vertical deflection input terminals of the oscilloscope. When the frequency is swept through the resonant frequency of the cavity a resonance-type trace is obtained on the

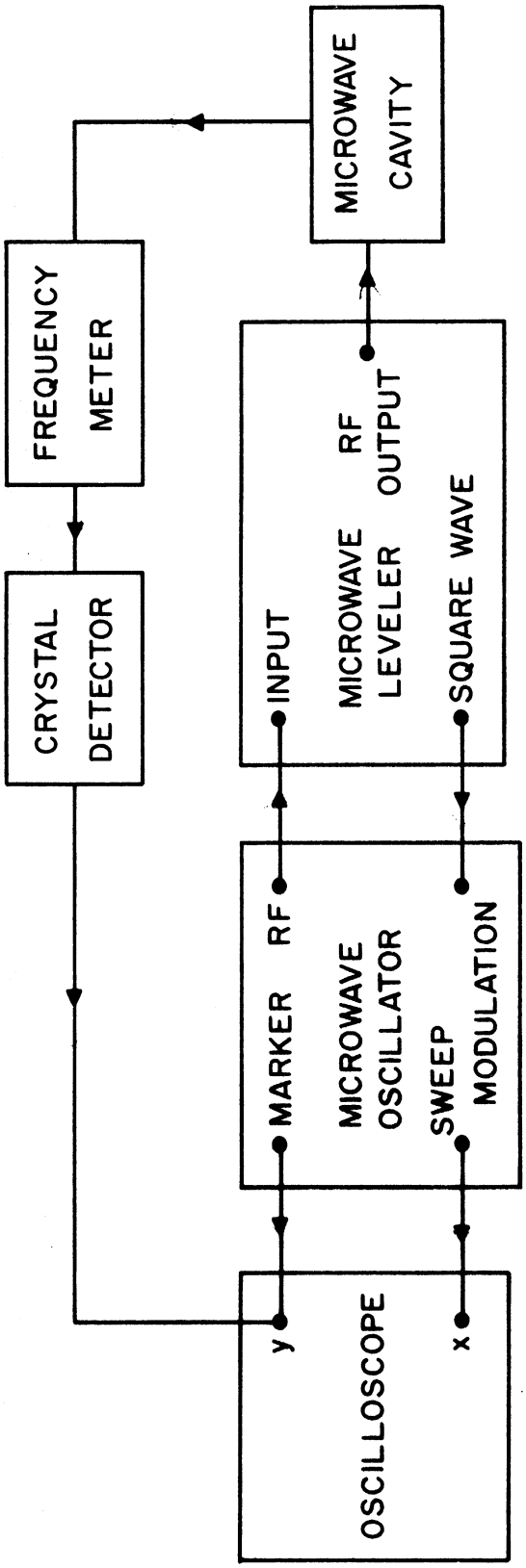

FIG. 3.3 SCHEMATIC OF THE CIRCUIT DIAGRAM FOR MICROWAVE CAVITY MEASUREMENTS.

oscilloscope. The x-axis of the oscilloscope trace can be calibrated with the help of the markers provided in the signal generator. The frequency meter can also be used to spot-check the calibration. The peak frequency is observed in the presence and in the absence of the plasma and a shift in the frequency is noted. This shift in the frequency along with the observation of plasma diameter can be used to determine the average plasma density. The plasma density measured by this means will be presented in Section 3.2.3 and will be compared with that obtained from Langmuir probe curves.

3.1.7b Langmuir Probes for Density Measurements. The Langmuir probe is essentially a small metallic electrode, usually a wire, inserted into a plasma. By observing the current flowing to the probe from the plasma as the probe potential is varied, the plasma-electron temperature and density can be determined. Under a wide range of conditions the disturbances caused by the probe are localized and can usually be tolerated. In the presence of a strong magnetic field, the disturbance is not localized and the plasma density and electron temperature determination is tedious. However, a Langmuir probe can make local measurements while most of the other techniques such as microwave or spectroscopic measurements give information averaged over a plasma volume.

The Langmuir probe used in the present work consists of a tungsten wire of 0.005-inch diameter. The wire is bent at a 90-degree angle so that its axis is parallel to the plasma axis and the length of the wire along the plasma axis is 1.25 cm. The probe can be moved radially by a motor-driven bellows. The probe data is obtained with the biasing circuit shown in Fig. 3.4. This circuit can smoothly drive the probe potential from

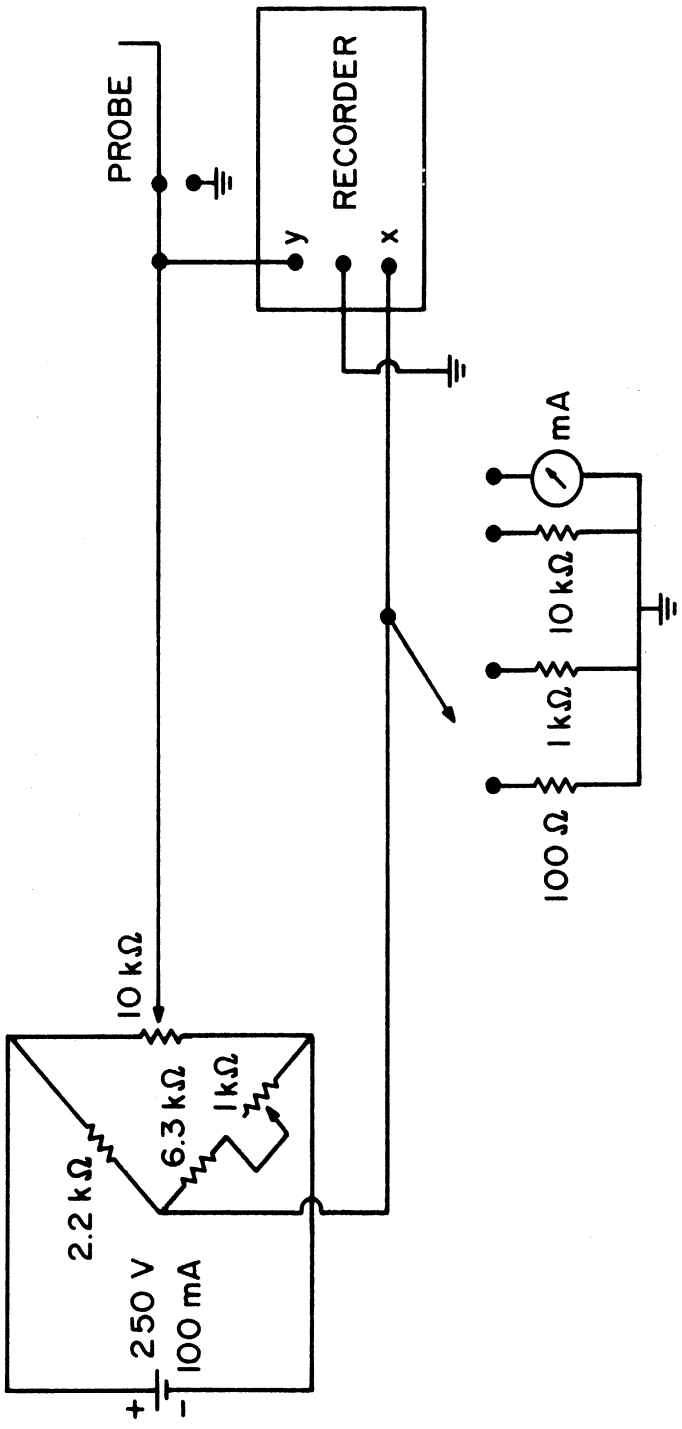

FIG. 3.4 CIRCUIT DIAGRAM FOR BIASING THE LANGMUIR PROBE FOR DENSITY MEASUREMENTS.

30 to -150 V. A voltage proportional to the probe current (across a known resistor) and the probe potential are fed to the y-axis and x-axis, respectively, of an x-y recorder. The probe potential is varied manually to obtain the x-y plot of the Langmuir probe.

A probe acts as a boundary to a plasma and the condition of quasi-neutrality, which is true in the body of the plasma, is not valid near the probe. A "sheath" is formed in which ion and electron densities differ and significant electric field may exist in the sheath. Probe theory is particularly simple if the plasma is not located in an external magnetic field and the sheath is thin such that the ratio $a_p \equiv r_p/\lambda_D \gg 1$, where r_p is the probe radius and λ_D is the Debye length. In this case the classical Langmuir probe theory[93] can be used. The electron current drawn by the probe from the plasma is given by

$$I_- = AJ_{er}\, e^{-e(V_p-V)/kT_e} , \qquad (3.4)$$

where V is the probe potential, V_p is the plasma potential, T_e is the electron temperature, A is the effective area of collection of the probe and J_{er} is the random electron-current density and is given by

$$J_{er} = \frac{n_o e}{4}\sqrt{\frac{8kT_e}{m\pi}} \qquad (3.5)$$

for a Maxwellian electron-energy distribution. If the natural logarithm of the electron current is plotted as a function of the probe voltage, the electron temperature is determined by the slope (e/kT_e) of the line

thus obtained. Knowing the electron temperature, the electron density can be determined by the electron saturation current for $V > V_p$ which is limited by the random electron current.

Most laboratory plasmas of interest are produced in a magnetic field. In such a case if the Larmor radii of the particles is much less than the probe radius, the probe will drain the plasma from the lines of force intercepting the probe and the plasma density will be greatly perturbed. To avoid perturbing the plasma, the probe radius must be such that $r_p \ll r_{\ell e}, r_{\ell i}$ where $r_{\ell e}$ and $r_{\ell i}$ are the electron and ion Larmor radii. Due to the limitation on the physical strength of the probe, the probe radius cannot be made small enough to satisfy $r_p \ll r_{\ell e}$ for strong magnetic fields. However, the probe radius may be such that $r_{\ell e} < r_p < r_{\ell i}$. In this situation the electron saturation currents are less than those obtained in the absence of the magnetic field. However, since $r_{\ell i} > r_p$, the ion saturation current for sufficiently negative voltage may not differ from that obtained in the zero magnetic field case. Thus, it is a frequent practice to use the ion saturation current to determine the plasma density.[90]

For large negative probe potentials the ion-current collection depends essentially on the electron temperature and not on the ion temperature. This was shown by Bohm et al.[94] Allen et al.[95] and Garscadden and Palmer.[96] The ion current to the probe is given by

$$I_+ = Aen_o \left(\frac{2kT_e}{M} \right)^{1/2} . \qquad (3.6)$$

It expresses the fact that ions are accelerated into the sheath with an energy of about $(1/2)kT_e$ which is picked up as the ions flow through the

presheath. The electron temperature can still be determined by plotting the natural logarithm of I_- as a function of the probe potential. If $a_p \ll 1$ the sheath is very thick and all the particles entering the sheath will not hit the probe. The current will be governed by the particle orbital motions and the probe current may be independent of the potential distribution around the probe.[97]

For the density range (5×10^8 to $10^{10}/cm^3$) and the magnetic fields (300 to 800 G) of interest for the present work, it is generally not possible to satisfy $a_p \gg 1$ and $r_p \ll r_{\ell i}$ simultaneously. In the present investigation the ratio a_p is of the order of unity. In such a case the probe current will depend on the potential distribution around the probe. Several accurate theories[98,99] for current collection by a probe immersed in a plasma have been presented. These theories do not split the region around the probe into a sheath region and a plasma region. The collisionless Boltzmann equation and Poisson's equation are numerically solved for the current, the charge density and the potential distribution. A recognizable sheath-like region automatically emerges from these solutions.

Since the above theories utilize numerical solutions, the results are usually given for only a limited range of parameters. Moreover, the reduction of probe data to plasma density often requires an iterative process. Therefore, these theories are cumbersome to use. A simple and more convenient theory has been given by Scharfman[100] who showed that it gave results with a maximum difference of 60 percent compared to the more accurate theory of Laframboise.[99]

In the present investigation Scharfman's method for deducing the plasma density from the Langmuir probe data was used. In this method the

Child-Langmuir relation for a space-charge-limited coaxial diode is used to determine the sheath radius. The current collected through the sheath is then analyzed in terms of ions randomly drifting across the sheath edge at thermal velocities.

First, the electron temperature is determined by the plot of $\ell n\, I_-$ and the probe potential. The ratio of sheath radius to probe radius (a/r_p) is plotted in Fig. 3.5 as a function of the parameter[100]

$$\frac{a}{r_p} = f\left[\frac{L}{r_p}\cdot\frac{V^{3/2}}{I}\left(1+\frac{2.66}{\eta^{1/2}}\right)\right], \qquad (3.7)$$

where L is the probe length, r_p is the probe radius, V is the probe to plasma potential, I is the probe current, η is equal to eV/kT_e and T_e is the electron temperature. Thus a/r_p can be calculated for a given L/r_p, T_e, V and I at a single point on the probe current-voltage characteristic. When a/r_p is found, the ratio (I_i) of current collected to the random current density times the physical area of the probe (AJ_{ir}) may be found[100] from the curves in Fig. 3.6. This quantity can be used to determine the charge density. The random ion-current density is given by

$$J_{ir} = \frac{1}{4} n_o e \left(\frac{8kT_e}{\pi M}\right)^{1/2} \qquad (3.8)$$

and

$$I_i = \frac{I}{AJ_{ir}} . \qquad (3.9)$$

Again, J_{ir} is a function of electron temperature since the ions are accelerated into the sheath with an energy of about $(1/2)kT_e$. From Eqs. 3.8 and 3.9 the following is obtained:

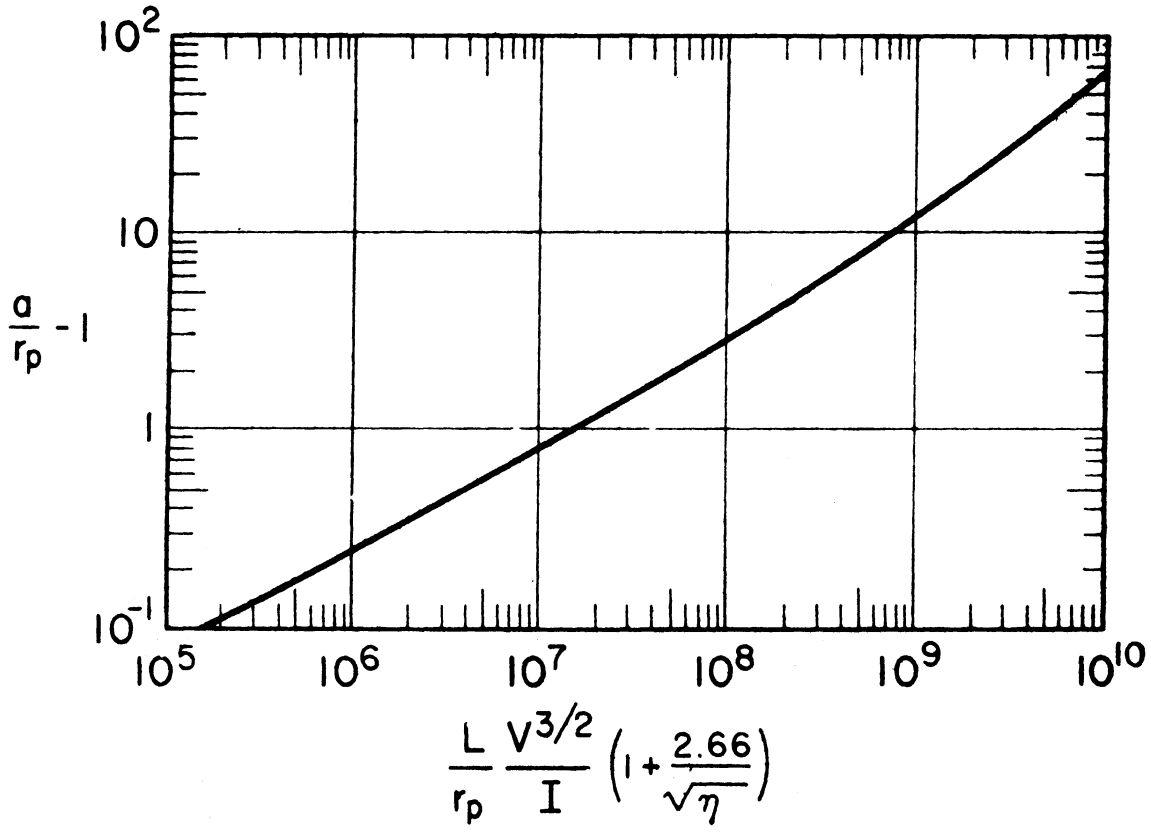

FIG. 3.5 a/r_p AS A FUNCTION OF THE MEASURED PARAMETERS.
(SCHARFMAN[100])

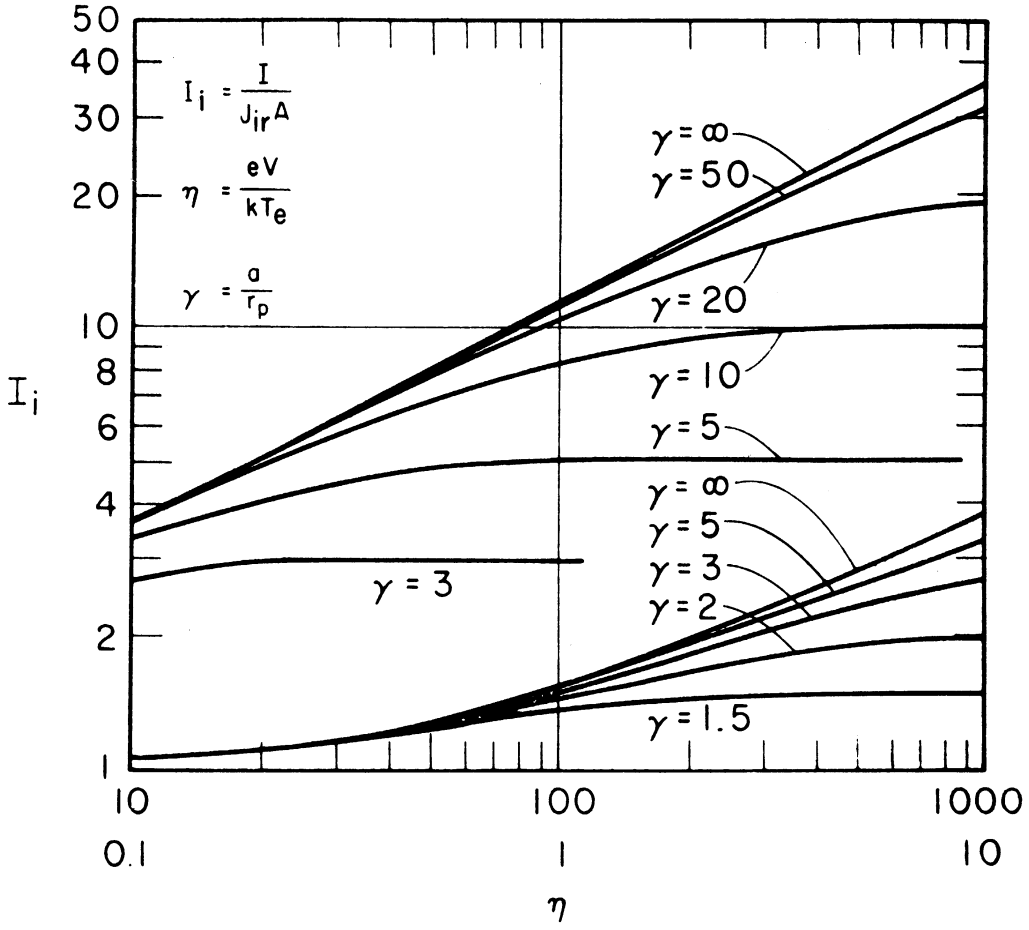

FIG. 3.6 NORMALIZED PROBE CURRENT AS A FUNCTION OF η WITH a/r_p AS A PARAMETER. (SCHARFMAN[100])

$$n_o = \frac{4I}{I_i eA}\left(\frac{\pi M}{8kT_e}\right)^{1/2} \qquad (3.10)$$

Typical probe data is given in Section 3.2.3 and this method is illustrated. The plasma density is calculated and compared with that obtained by using the microwave cavity.

3.1.7c Langmuir Probe for RF Field Detection. Two Langmuir probes with coaxial leads are used for RF field detection. The probe used initially was a wire bent at a 90-degree angle so that its axis was parallel to the plasma axis. Such a probe was sensitive to both the axial and radial component of the electric field. Later, this probe was changed so that it was simply a straight wire perpendicular to the plasma-column axis and then it detected only the radial RF electric field. This change resulted in a better comparison between the theoretically calculated radial electric field and that detected by the probe.

One of the probes is radially movable with the help of a bellows and the other is axially movable with the help of a double Wilson seal. The probes are usually biased at the floating potential. One of the circuit diagrams used for RF field detection by the Langmuir probe is shown in Fig. 3.7a. The 1000-Hz modulated RF signal picked up by the probe is amplitude detected and the resulting signal is amplified by a 1000-Hz narrow-band amplifier and subsequently peak detected for dc recording. The 1000-Hz signal amplitude is proportional to the local RF amplitude and is recorded. In certain cases the RF probe signal is fed to a matched preamplifier with 40 dB of voltage gain and detected with the help of an RF millivoltmeter.

The axially movable probe is used for interferometric measurements of the axial wavelength. The schematic circuit diagram for interferometric

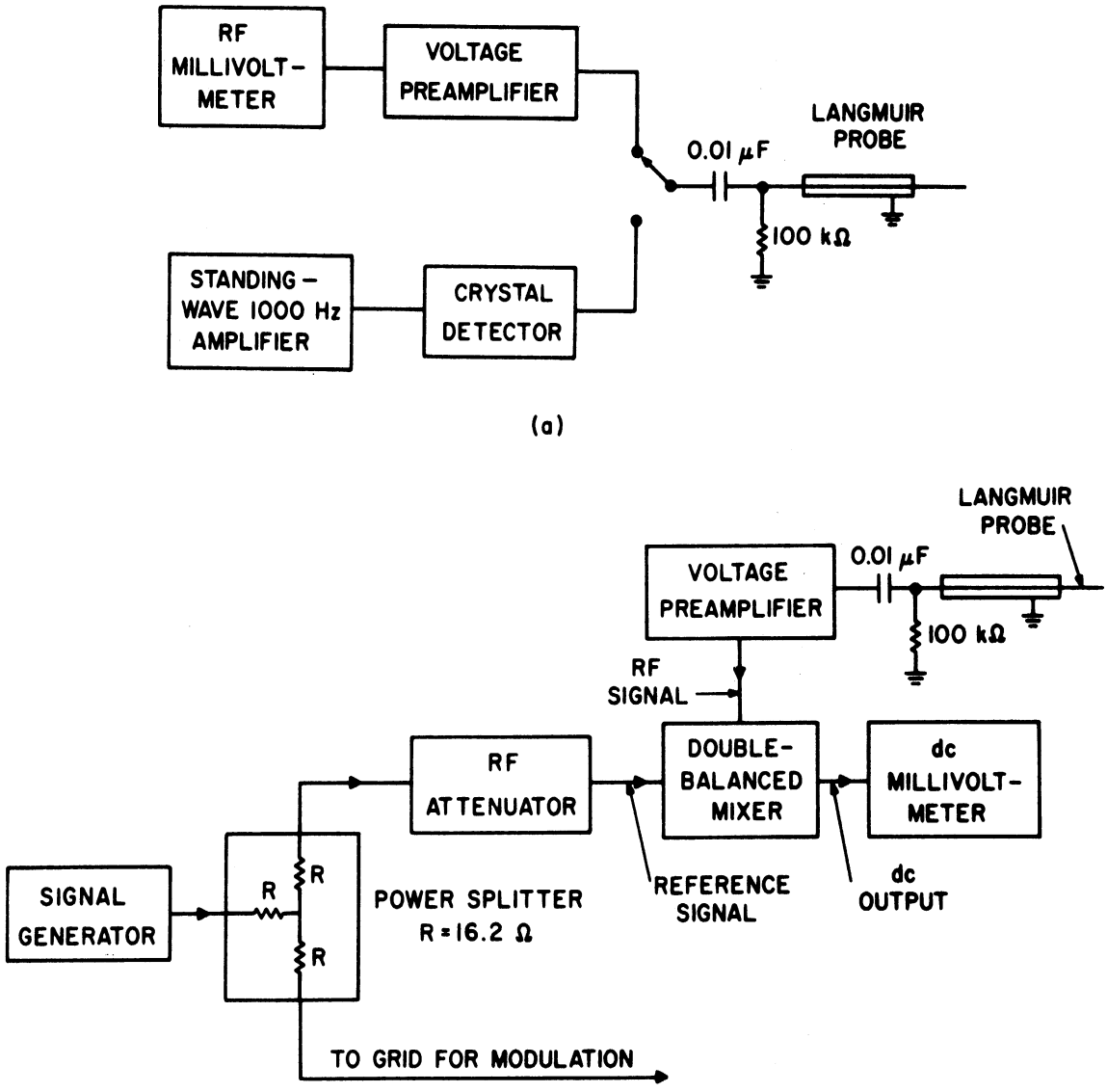

FIG. 3.7 SCHEMATIC DIAGRAMS FOR (a) RF FIELD DETECTION AND (b) INTERFEROMETRIC MEASUREMENT.

measurements is shown in Fig. 3.7b. A double-balanced RF mixer whose dc output is a function of the phase difference between the reference and the detected RF probe signal is used to measure the axial wavelength. The probe position is azimuthally adjustable and the probe is located outside the plasma. It is moved parallel to the axis of the plasma column and the output of the double-balanced mixer is detected by a dc millivoltmeter. If a standing wave is present, the dc output changes sign at a node. A similar arrangement can be used with the radially movable probe.

3.1.7d Gridded Probe Velocity Analyzer. A schematic diagram of the gridded probe is shown in Fig. 3.8. It is a retarding field electrostatic analyzer which is used to determine the distribution of velocities in a flux of charged particles. The gridded probe is positioned at a distance away from the axis of the plasma column such that it does not disturb the plasma, and outside a magnetic mirror peak. The probe points in the axial direction and is movable axially.

A flux of charged particles approaches the analyzer from the left-hand side as shown in Fig. 3.8. After passing through a grounded aperture plate which establishes a zero reference for potential, the particles reach Grid 1 which may be biased to discriminate between and repel all charges of either positive or negative sign. The discriminated particles then approach Grid 2 which is biased to repel all the particles whose energy is less than the corresponding potential on this grid. The particles of higher energy than this potential pass through the negatively biased Grid 3 whose function is to prevent secondary electrons from leaving the collector. The collector can be grounded or given an appropriate potential to collect the charged particles. Collector current vs. retarding voltage on Grid 2 gives the velocity distribution curve.

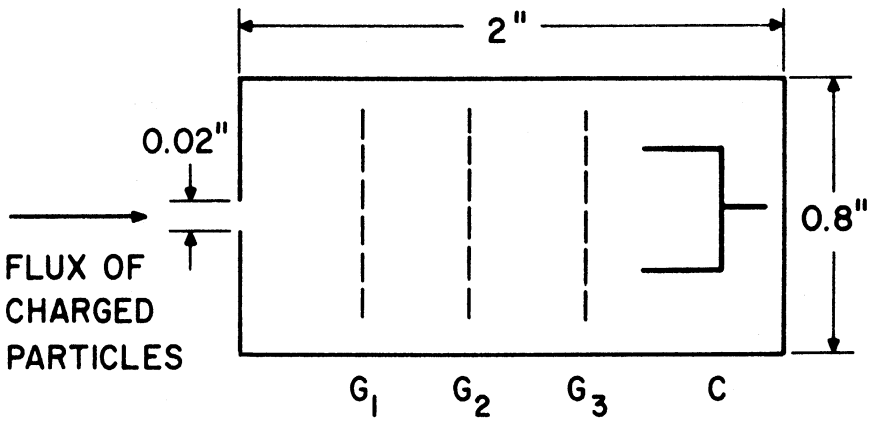

FIG. 3.8 SCHEMATIC DIAGRAM OF THE GRIDDED PROBE.

An analytic method for evaluating the resultant retarding potential curves has been given by Roth and Clark.[101,102] A computer program was used by them to obtain an iterated best fit of the experimental curve to an analytical expression which gives the kinetic temperature, floating potential, etc. In the present investigation the size of the gridded probe was comparable to the size of the plasma and the probe was located off-axis (outside the plasma) so that it did not disturb the plasma. Because of the off-axis location, the probe intercepted mostly energetic ions. Consequently, it did not give reliable ion temperature measurements but it was useful for detecting the presence of energetic ions at various frequencies or retarding voltages. The experimental measurements using the gridded probe are given in Section 3.3.

3.2 Initial Testing of the Apparatus

Some preliminary tests were performed on the apparatus before carrying out the actual experiment. Section 3.2.1 describes a calibration curve which is required to maintain a constant current modulation of the electron beam in the frequency range of interest. Using this calibration curve, a frequency response of the RF field detector probe is taken and is described in Section 3.2.2. Two methods were used to measure the plasma density and their results are compared in Section 3.2.3.

3.2.1 Calibration Curve. In order to determine the frequency response of a system using a current-modulated electron beam, it is necessary to maintain a constant current modulation over the desired frequency band (2 to 25 MHz). The beam-modulation current decreases as the frequency is increased partly due to the transit-time effects and partly due to the cathode lead inductance in the electron gun.

The variation of the current modulation due to the transit-time effects is due to the presence of the space-charge waves which exist on the electron beam and their effects can be easily calculated as shown in Appendix C. The beam current modulation is a function of cos $\beta_q L$ for an assumed maximum current modulation at z = 0. L is the length of the system and $\beta_q = \gamma_o \omega_{pb}/v_o$, where γ_o is the space-charge reduction factor for a thin beam.[103] The first zero of the beam-current modulation occurs when $\beta_q L = \pi/2$. Numerically, the first zero occurs at a frequency, as given in Appendix C, of

$$f = 853 \frac{V_b^{5/4}}{LI_b^{1/2}} ,$$

where V_b is the beam voltage in volts, I_b is the beam current in amperes, L is the length of the system in meters and f is in Hz. For an assumed V_b = 500, I_b = 2 mA and L = 1 m, f acquires a value of 45 MHz. In an experimental check the current modulation as observed at the collector was found to be minimum near 45 MHz.

In the initial phase of the experiment, it was found that the long lengths of the leads feeding the RF modulation signal to the electron-gun grid caused the beam modulation to decrease significantly even at low frequencies (1 to 2 MHz). To reduce the effect of the cathode and grid lead inductances, special efforts were made in mounting the circuits and gun. The electron gun was mounted such that cathode and grid connections were accessible from outside the vacuum envelope and therefore the length of leads could be made very short.

It is necessary to adjust the grid drive voltage according to the curve shown in Fig. 3.9 so that a constant current modulation can be maintained. The modulation current is monitored by observing the RF beam current directly at the beam collector with the help of an oscilloscope. The calibration curve thus obtained is shown in Fig. 3.9 and is used when observing the RF frequency response of the system and the energetic ion current as a function of frequency.

3.2.2 Frequency Response of the Langmuir Probe in the Absence of a Plasma. The RF field excited by the electron beam is observed as a function of frequency by a Langmuir probe and the circuits of Fig. 3.7. It is advantageous to know the frequency response of the probe itself in the absence of a plasma. Figure 3.10 shows the output voltage of the probe circuit as a function of frequency when a constant-current modulated electron beam passes near the tip of the probe. It is seen that the voltage induced in the probe increases as a function of frequency.

To understand this behavior, consider a system in which a modulated electron beam traverses a drift tube and is collected by a collector at the downstream end. A metallic probe is positioned in the tube such that it does not intercept the electron beam. In such a system, a charge is induced on the probe surface and is proportional to the instantaneous potential at the position of the probe.[104] The induced current which flows in the external circuit is simply the time-rate-of-change of this charge. For a sinusoidal steady state, the induced current I is proportional to

$$I = \frac{dq}{dt} \propto \omega Q_m \sin \omega t \quad .$$

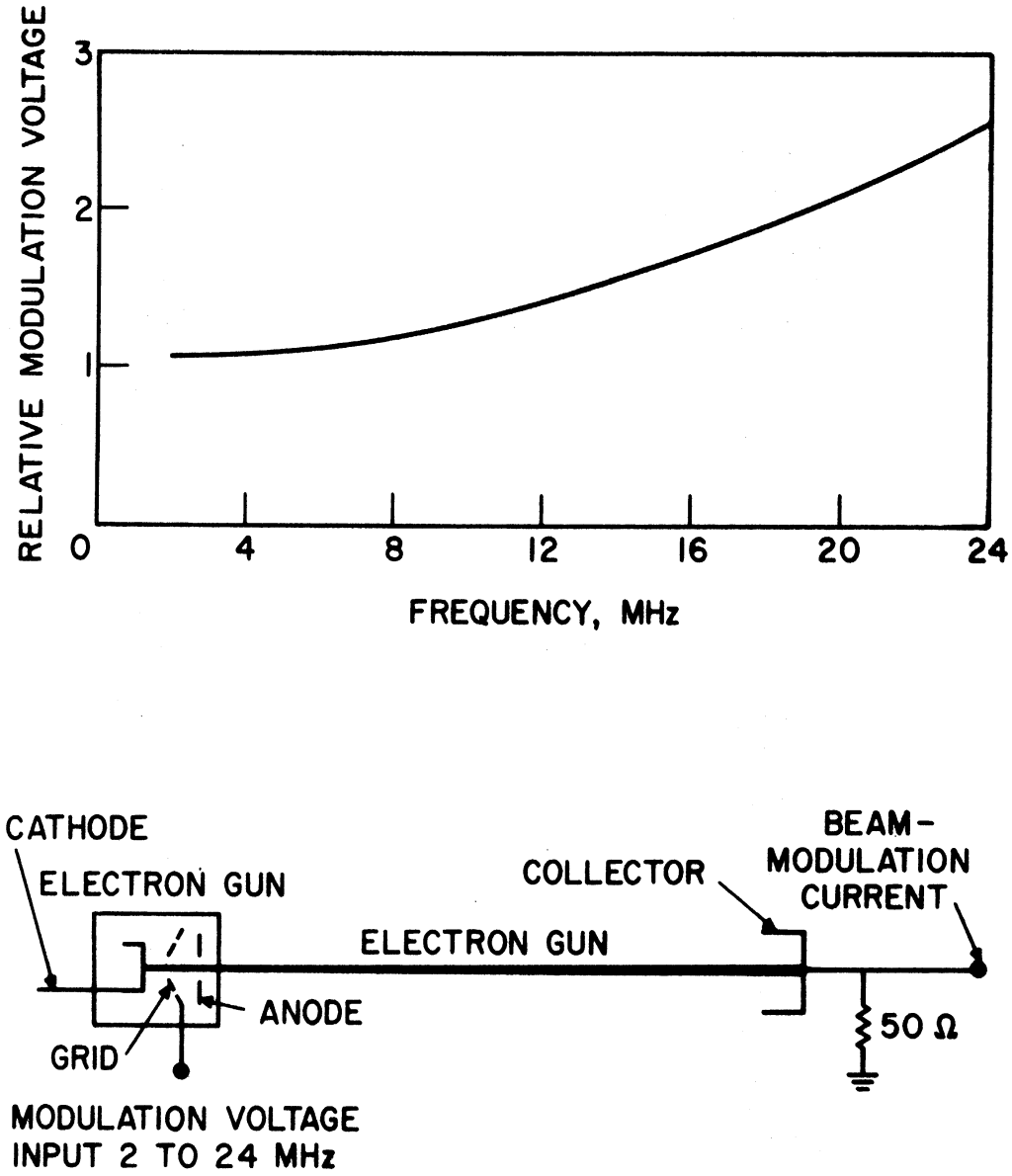

FIG. 3.9 CALIBRATION CURVE. RELATIVE MODULATION VOLTAGE AT THE GRID FOR CONSTANT BEAM-MODULATION CURRENT AT THE COLLECTOR AS A FUNCTION OF FREQUENCY.

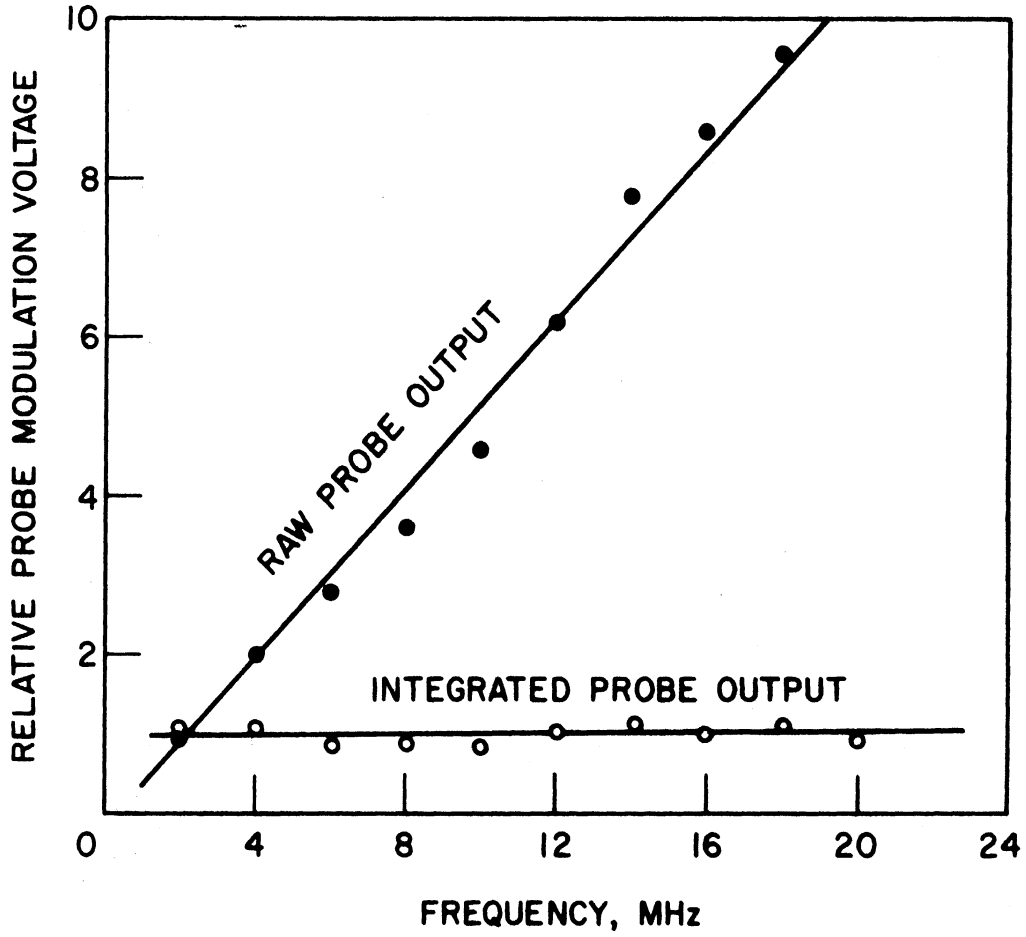

FIG. 3.10 PROBE RESPONSE IN HIGH VACUUM. RELATIVE PROBE MODULATION VOLTAGE AS A FUNCTION OF FREQUENCY FOR CONSTANT BEAM-MODULATION CURRENT.

Thus the voltage across an external resistor through which this induced current flows increases linearly with frequency. This was observed experimentally as shown in Fig. 3.10. Therefore, to obtain a uniform frequency response, i.e., output voltage with respect to RF field, a buffer integrator stage is required to cancel the increase of induced voltage with frequency. The output of an integrator falls off linearly as a function of frequency. Thus, an integrator plug-in unit for the oscilloscope was used as the buffer stage to obtain a uniform response as shown in Fig. 3.10.

3.2.3 Comparison of Plasma Density as Measured by a Langmuir Probe and a Microwave Cavity. The plasma density as measured by a Langmuir probe is compared with that obtained by a microwave cavity. The comparison was made only for the high range of densities and agreement between the two was satisfactory. The experimental values of the plasma density reported later in this investigation are deduced only from the Langmuir probe data because the density was too low to measure by the cavity.

For comparison of the plasma density measurement by the two methods, a plasma was produced by the PIG source. It was operated in the "glow" mode which is characterized by a large-diameter (1 to 2 inches) uniform plasma and a small (50 to 100 G) dc magnetic field. As mentioned in Section 3.1.7b, the Langmuir probe curve is obtained by measuring the current drawn by the probe as a function of the probe voltage. A typical x-y recorder plot of the Langmuir probe curve is shown in Fig. 3.11. From Fig. 3.11 the ion current component extrapolated according to the method of Sonin,[105] as shown by the dashed line, is subtracted from the total current to obtain the electron current component. To determine the electron

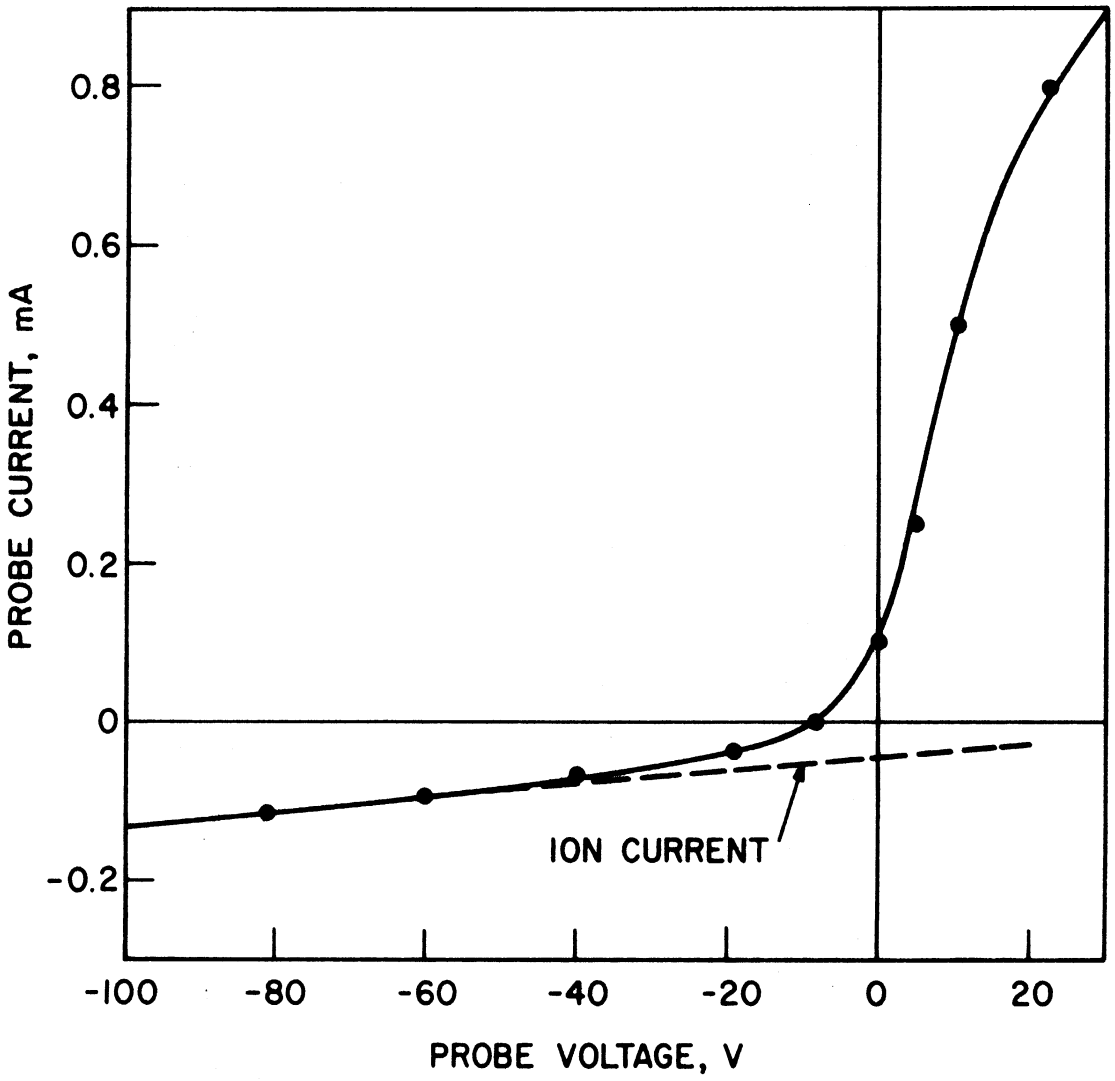

FIG. 3.11 LANGMUIR PROBE CURVE. PROBE CURRENT AS A FUNCTION OF PROBE VOLTAGE.

temperature, electron current and probe voltage are plotted on a semilogarithmic graph as shown in Fig. 3.12. A straight line is obtained if the electron energy distribution is Maxwellian. The slope of this line determines the electron temperature as discussed in Section 3.1.7b. The density of the ions is then calculated by using Scharfman's method as discussed in Section 3.1.7b.

The values of the necessary parameters for calculating the plasma density by the preceding method are tabulated in Table 3.3.

Table 3.3

Data for the Calculation of Plasma Density by a Langmuir Probe

$V = 90$ V

$I = 0.12$ mA

$kT/e = 3$ eV

$\eta = 30$

$D = 0.005$ inch

$L = 1.25$ cm

$L/r_p = 198.5$

$A = 5 \times 10^{-6}$ m^2

In Table 3.3, $\eta = eV/kT_e$, D is the probe wire diameter, L is the active length of the probe, r_p is the probe radius and A is the active area of the probe for current collection. Using the values of the above parameters from Table 3.3 gives

$$\frac{L}{r_p} \frac{V^{3/2}}{I} \left(1 + \frac{2.66}{\sqrt{\eta}}\right) = 2 \times 10^9 \quad .$$

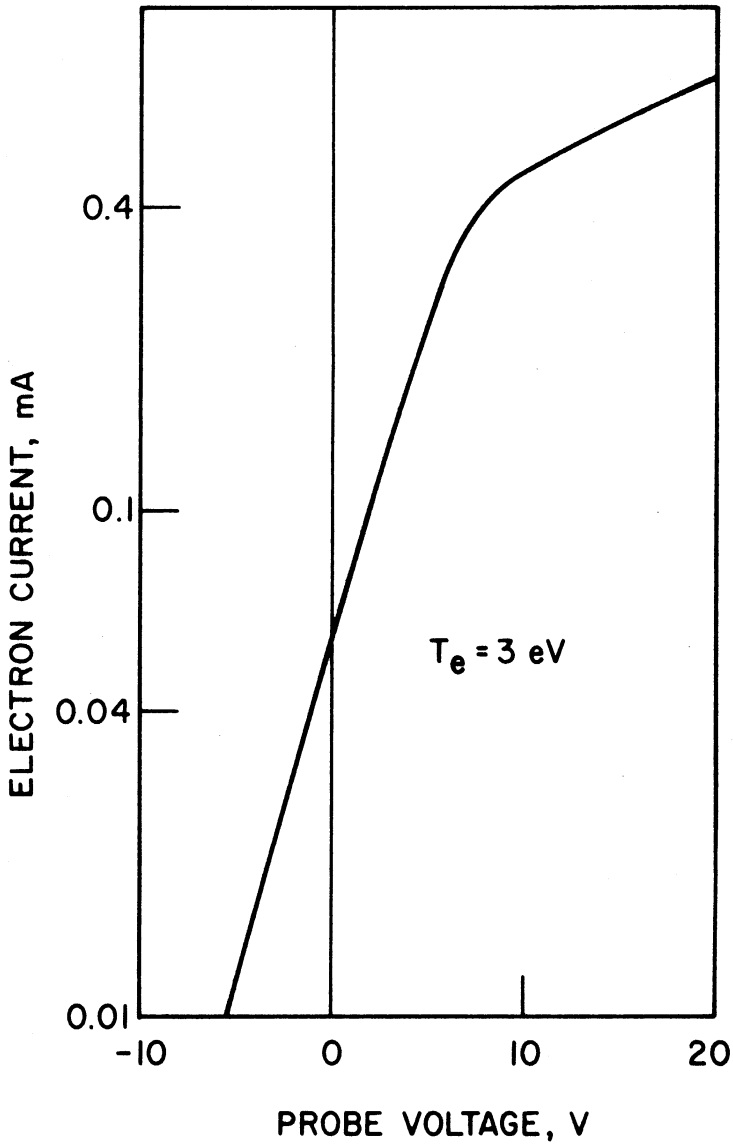

FIG. 3.12 PROBE ELECTRON CURRENT AS A FUNCTION OF PROBE VOLTAGE.

From Fig. 3.6, $I_i = 6.2$ is obtained. Since by this method I_i is always underestimated, it is multiplied by a factor of 1.3 to reduce the error in the density calculation.[100] Therefore, $I_i = 8.06$. If the values of the parameters from Table 3.3 are substituted into Eq. 3.10, it becomes

$$n_o = \frac{I}{I_i T_e^{1/2}} \; 3.24 \times 10^{20} \text{ cm}^{-3} \quad ,$$

where I is in amperes and T_e is in electron volts. Thus in the present case the density is found to be

$$n_o = 2.8 \times 10^9 \text{ cm}^{-3} \quad .$$

For deduction of the plasma density with the help of a microwave cavity, the setup shown in Fig. 3.3 is used. The shift in the cavity resonant frequency due to the presence of the plasma is measured. The various parameters introduced in Section 3.1.6 for the cavity measurement are given in Table 3.4.

Table 3.4

Parameters for Cavity Measurement

$\Delta f = 5.9$ MHz

$d = 1.51$ inches

$R/d = 0.289$

$k_o R = \frac{\omega}{c} R = 0.883$

$J_o(k_o R) = 0.883$

$J_1(k_o R) = 0.326$

$J_1^2(2.4) = 0.2$

Substitution of the values of the preceding parameters into Eq. 3.3 yields

$$S = 2.4 \times 0.1375 \ .$$

Thus Eq. 3.2 gives

$$n_o = 2.7 \times 10^8 \Delta f \ \ cm^{-3} \ ,$$

where Δf is the frequency shift in MHz. The effect of the end holes can be estimated by using the curves given in Reference 91. For the present cavity parameters, the effect of the end holes is to reduce the slope S by a factor of 0.92. Therefore

$$n_o = 2.9 \times 10^8 \Delta f \ \ cm^{-3} \ .$$

The plasma density is obtained by substituting the value of Δf in the last equation and is found to be

$$n_o = 1.7 \times 10^9 \ cm^{-3} \ .$$

Thus the density obtained by the Langmuir probe data is approximately 60 percent higher as compared to that obtained by the microwave cavity measurements.

3.3 Gridded Probe Measurements

The gridded probe described in Section 3.1.7d and shown in Fig. 3.8 is used to detect the presence of energetic ions. The first grid is used to reflect electrons and it is biased at a potential of -100 V. The second

grid is used to analyze ion energy and its bias is varied from zero to 25 V. The third grid is biased at -50 V to retard the secondary electrons from the collector. With a 0.020-inch diameter pinhole in the gridded probe, typical observed collector currents range from 0 to 100 nA.

3.3.1 Gridded Probe Retarding Potential Curves. It was found that the presence of RF modulation and the frequency of that modulation have an appreciable effect on the gridded probe retarding potential curve. Figure 3.13 shows the retarding potential curves for the unmodulated case and for modulation frequencies of 10, 14 and 18 MHz. The energy spread increases considerably when the frequency of modulation is 18 MHz. The spread in ion energies is over 20 V for the particular case shown here. Similar results are found under all operating conditions but the frequency at which the maximum effect occurs varies with operating conditions. The increase in the ion-energy spread indicated by the gridded probe is also accompanied by an increase in the visual diameter of the plasma. The two effects are consistent since the increase in ion energy increases the ion Larmor radii and hence the visual diameter of the plasma column. Thus it is concluded that the energetic ions are produced when the beam is modulated at certain frequencies.

3.3.2 Frequency Response of the Gridded Probe. The gridded probe was located off-axis. Therefore, it can only "see" ions which have large Larmor radii or have had enough collisions to get out to the probe. The frequency of the grid modulation signal is varied and the response of the gridded probe ion current is observed. The amplitude of the modulation voltage is adjusted at each frequency according to the calibration curve discussed in Section 3.2.1 to keep the beam-modulation current constant.

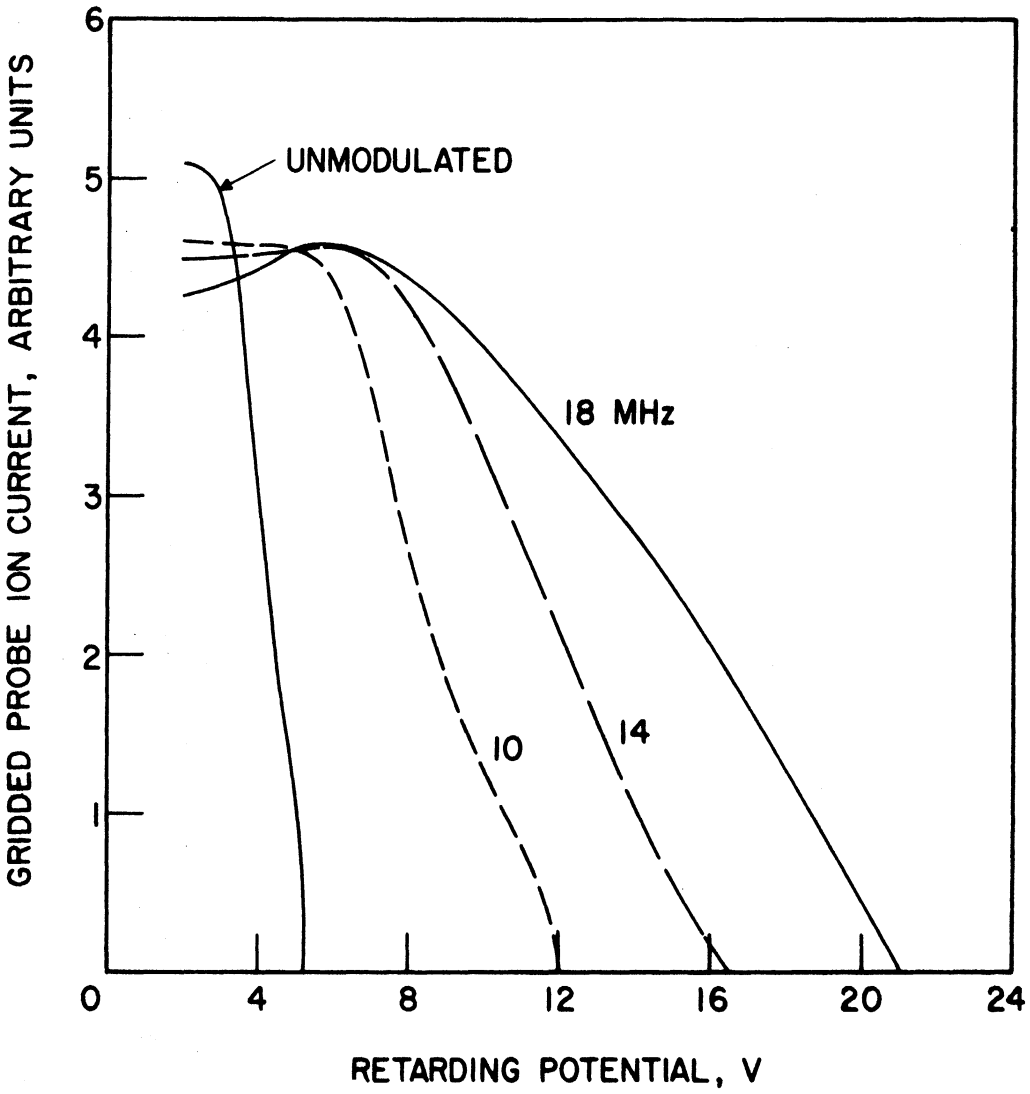

FIG. 3.13 GRIDDED PROBE RETARDING POTENTIAL CURVES WITH DIFFERENT BEAM-CURRENT MODULATION FREQUENCIES.

The gridded probe response as a function of frequency is shown by the curves of Fig. 3.14 for various pressures. A set of these curves is taken at several gridded probe retarding potentials (for ions) in the range of 0 to 10 V. The curves shown here are for a retarding potential of 5 V. As the pressure is increased the frequency of the peak in these curves moves toward higher frequencies.

The variation of the peak frequency, or "resonant" frequency with pressure is interpreted as a variation with plasma density. The plasma density was measured with the Langmuir probe and the ion-plasma frequency was calculated. The results are shown in Fig. 3.15 which is a plot of the resonant frequency and the calculated ion-plasma frequency as a function of pressure. The resonant frequency is always above the calculated ion-plasma frequency. The error in the Langmuir probe density measurement is expected to be always on the high side for the method used to interpret the Langmuir probe curves.[100]

Figure 3.16 shows a similar set of gridded probe response curves for another set of beam parameters and Fig. 3.17 shows the corresponding comparison with the ion-plasma frequency calculated from density measurement.

From the frequency response of the gridded probe measurements it is concluded that the resonant frequency lies just above the ion-plasma frequency. In the present case ($\omega_{ce}^2 \gg \omega_{pe}^2 \gg \omega_{ce}\omega_{ci}$) the lower-hybrid frequency is approximately equal to the ion-plasma frequency.

3.4 RF Langmuir Probe Measurements

The Langmuir probes were used to detect the RF field just outside the plasma as a function of frequency at a fixed position, or as a function

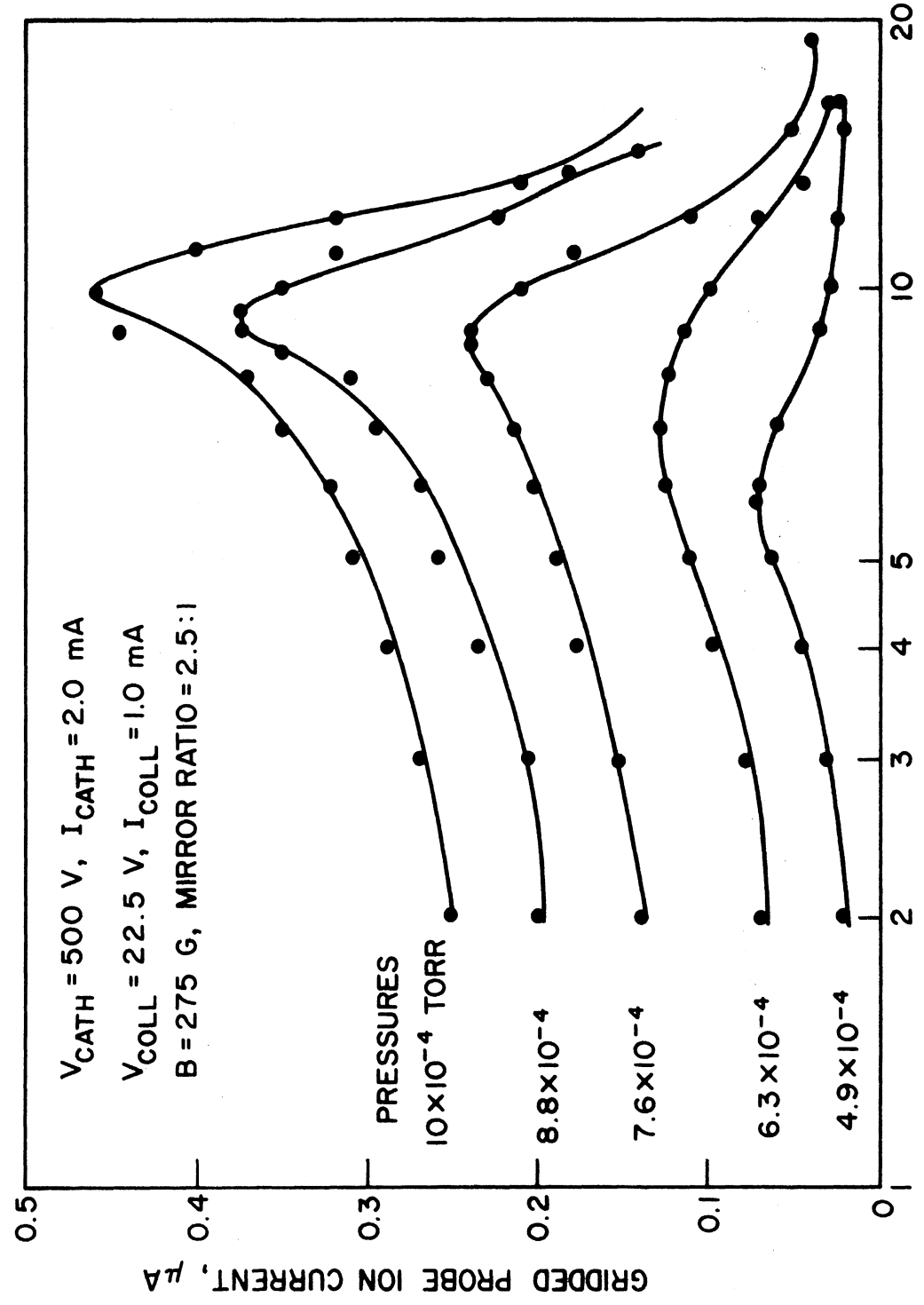

FIG. 3.14 GRIDDED PROBE COLLECTOR CURRENT AS A FUNCTION OF BEAM-MODULATION FREQUENCY FOR VARIOUS PRESSURES.

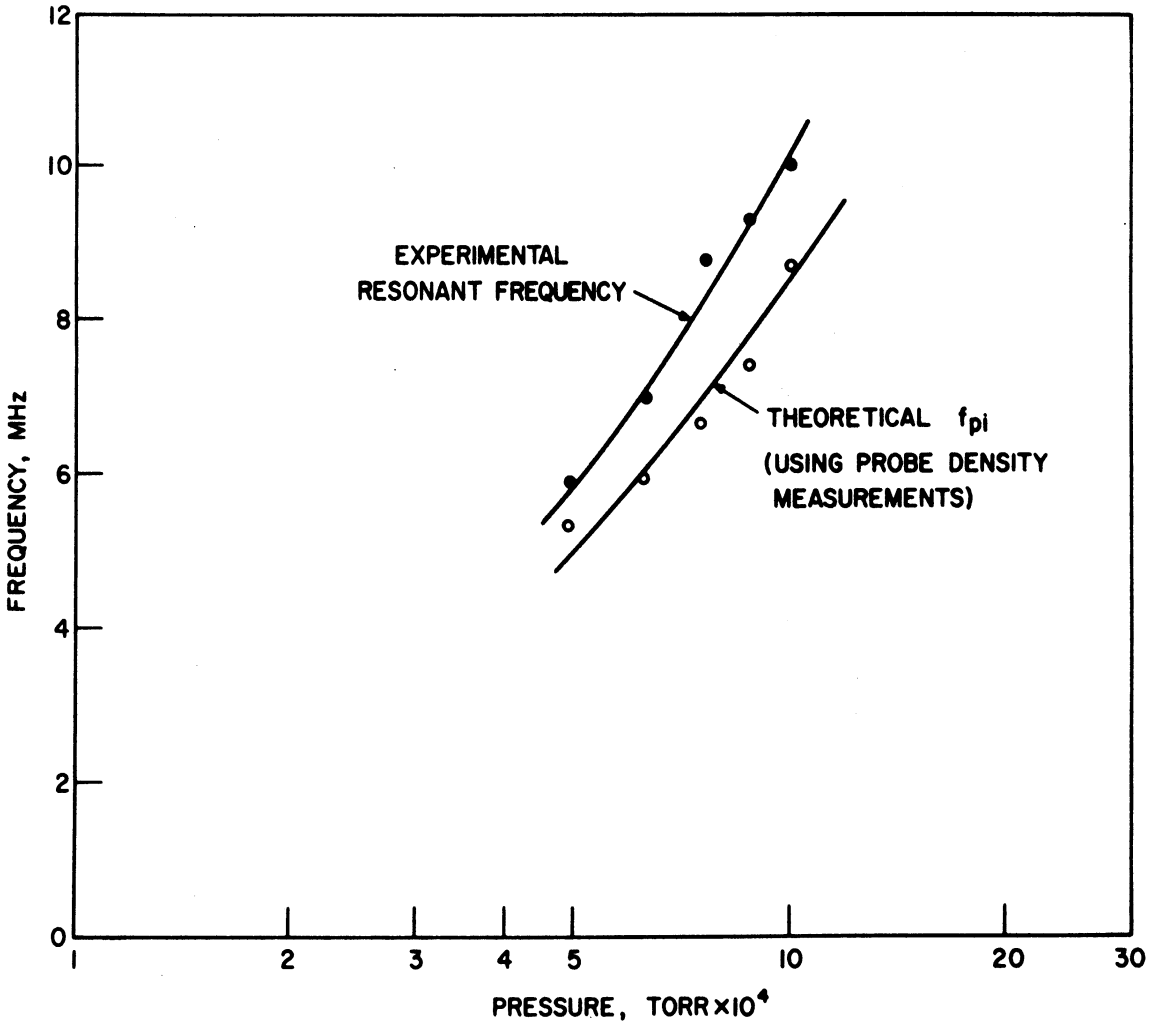

FIG. 3.15 THE RESONANT FREQUENCIES FROM THE CURVES OF FIG. 3.14 ARE COMPARED WITH THE ION-PLASMA FREQUENCY CALCULATED FROM DENSITY MEASUREMENTS FOR VARIOUS PRESSURES.

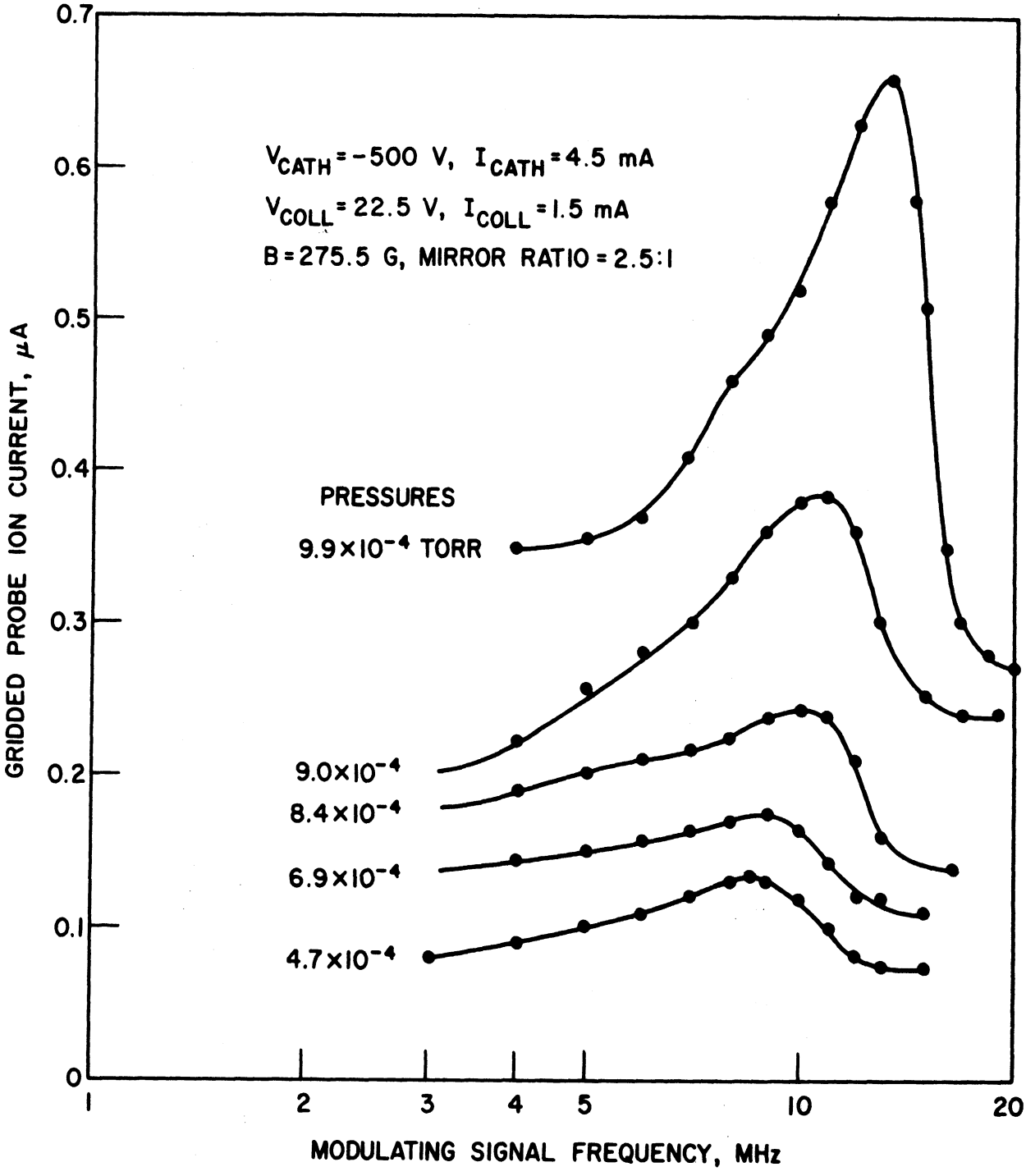

FIG. 3.16 GRIDDED PROBE COLLECTOR CURRENT AS A FUNCTION OF BEAM-MODULATION FREQUENCY FOR VARIOUS PRESSURES. THESE CURVES ARE SIMILAR TO THOSE OF FIG. 3.14 BUT WERE TAKEN FOR A DIFFERENT SET OF BEAM AND PLASMA PARAMETERS.

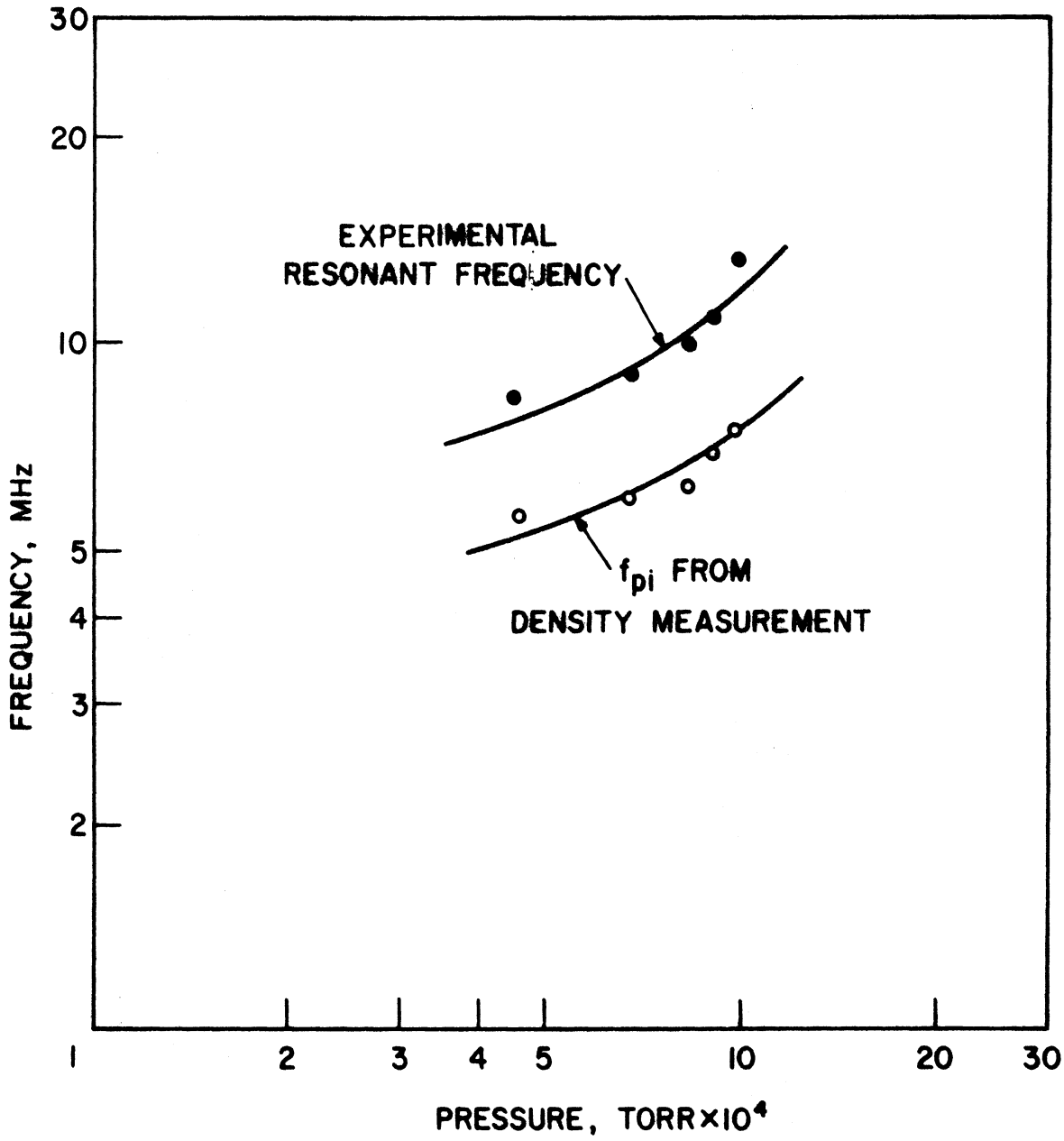

FIG. 3.17 THE RESONANT FREQUENCIES FROM THE CURVES OF FIG. 3.16 ARE COMPARED WITH THE ION-PLASMA FREQUENCY CALCULATED FROM DENSITY MEASUREMENTS FOR VARIOUS PRESSURES.

of axial or radial position at a fixed frequency. The setups used for RF field detection are those discussed in Section 3.1.7c. Again, the beam-modulation current is kept constant by adjusting the grid modulation signal at each frequency according to the calibration curve. The following measurements were carried out in a beam-generated plasma. The plasma density and magnetic field were such that the operation was in the low-density regime ($\omega_{ce}^2 \gg \omega_{pe}^2 \gg \omega_{ce}\omega_{ci}$).

3.4.1 Frequency Response of the Radially Movable Probe. The radially movable probe was located at a fixed axial position and was used to detect the radial RF electric field as a function of frequency. The probe tip was located approximately one plasma diameter away from the plasma axis. The effect of the variation of plasma density, beam voltage, ion mass and magnetic field was studied.

A typical probe response is shown in Fig. 3.18 in which the amplitude of the radial RF electric field is plotted as a function of beam-current modulation frequency. Two or three peaks or resonances are typically observed in the probe response at frequencies which are, in generated not harmonically related. The third peak was observed but was not as prominent as the first and second peaks. A set of these curves was taken as the plasma density was varied by changing the hydrogen gas pressure. Other parameters such as beam voltage, beam current and magnetic field were held constant. As the density is increased the resonant frequencies shift upward. The plasma density measured by a Langmuir probe indicates that the first resonant frequency is just above the ion-plasma frequency.

Figure 3.19 shows a set of frequency response curves for different beam voltages. The beam current was kept constant by adjusting the grid

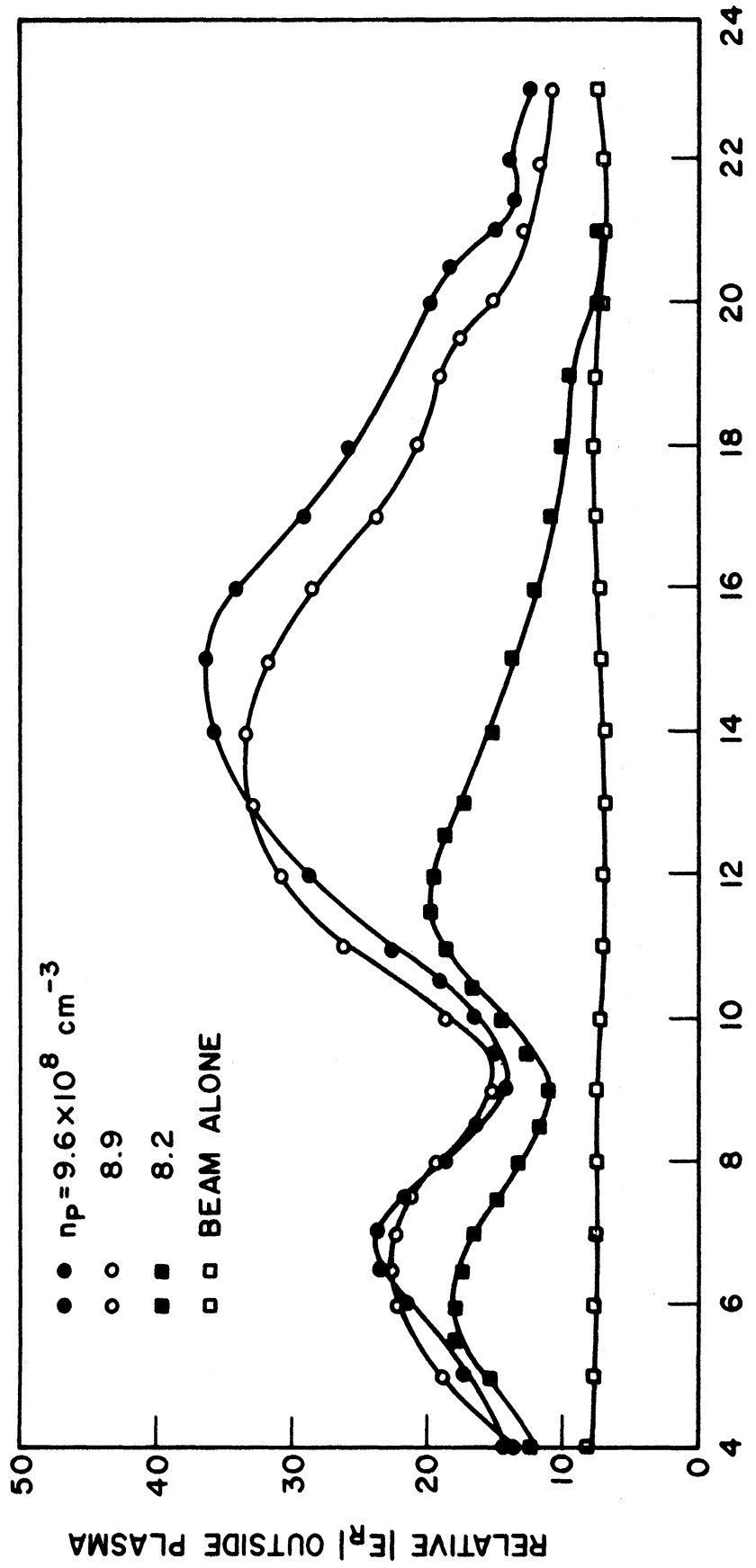

FIG. 3.18 EXPERIMENTALLY OBSERVED RADIAL ELECTRIC-FIELD AMPLITUDE AS A FUNCTION OF FREQUENCY FOR DIFFERENT DENSITIES. (V_b = 600 V, I_b = 2 mA, B_o = 335 G, HYDROGEN GAS)

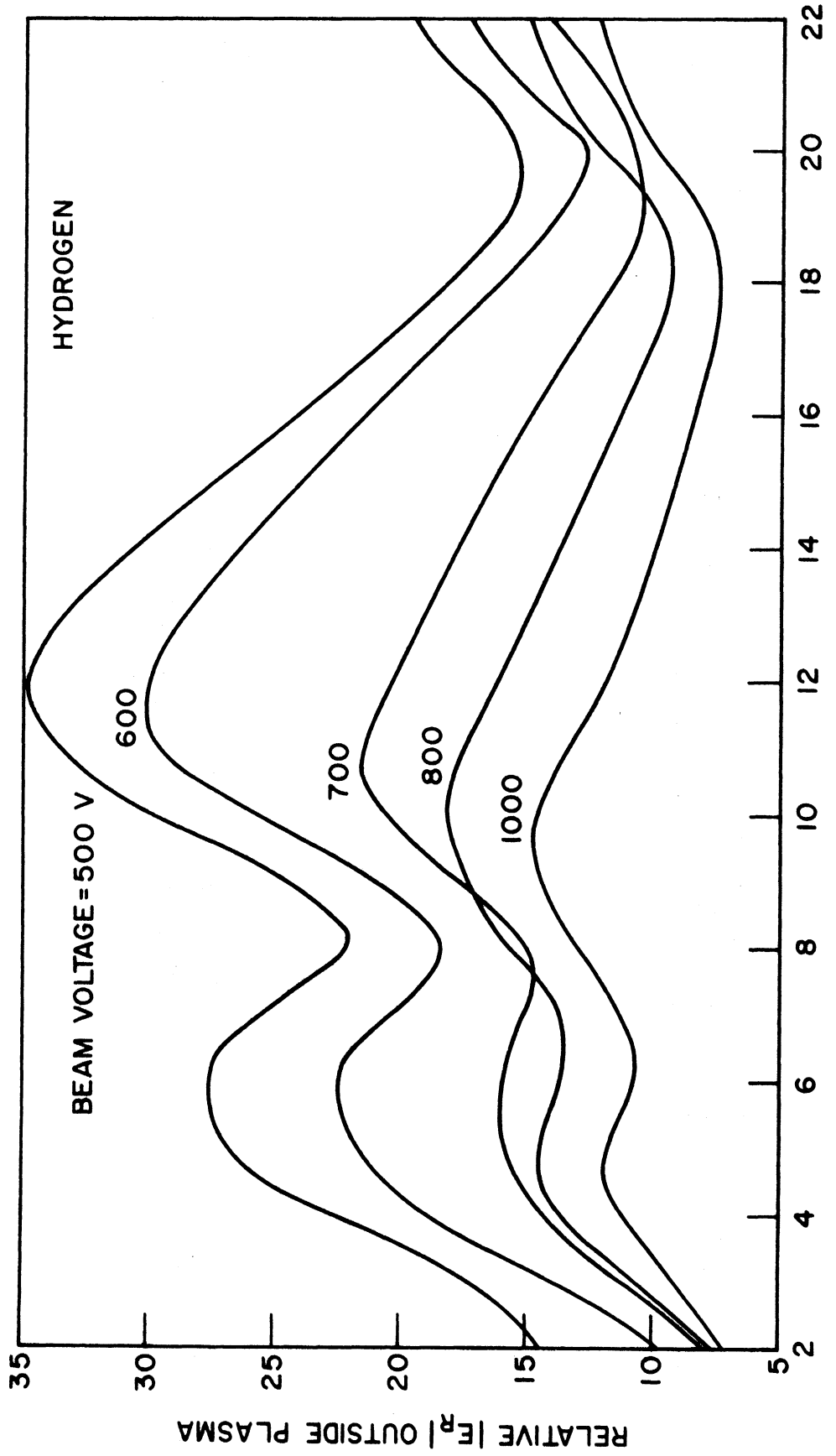

FIG. 3.19 EXPERIMENTALLY OBSERVED RADIAL ELECTRIC-FIELD AMPLITUDE AS A FUNCTION OF FREQUENCY FOR DIFFERENT BEAM VOLTAGES. ($n_p = 8.6 \times 10^8/cm^3$, $B_o = 335$ G, I = 2 mA)

bias in each case. The plasma density was also kept constant by minor changes in the gas pressure. It is found that both resonant frequencies decrease as the beam voltage is increased. The change in the first resonant frequency is smaller than the change in the second resonant frequency for the same change in the beam voltage.

Figure 3.20 shows typical frequency response curves obtained for neon gas. Similar response curves were obtained for argon and deuterium gases and are shown in Figs. 3.21 and 3.22. Again, it is found that the resonant frequencies increase with an increase in plasma density. By comparing the resonant frequencies obtained in hydrogen and neon plasmas for the same plasma density, it is found that the resonant frequencies for neon and argon plasmas are slightly smaller than the corresponding resonant frequencies for the hydrogen plasma. However, the changes in the resonant frequencies are much smaller than the changes in the ion-plasma frequencies in the two cases. Thus it is concluded that the resonant frequencies are relatively independent of the ion mass in the present investigation. For neon and argon plasmas two sets of frequency response curves for different beam voltages are shown in Figs. 3.23 and 3.24. These curves are similar to those obtained for the hydrogen plasma shown in Fig. 3.19. For the low-density regime ($\omega_{ce}^2 \gg \omega_{pe}^2 \gg \omega_{ce}\omega_{ci}$) of investigation, it was found that the resonant frequencies do not change significantly with the dc magnetic field. A set of frequency response curves for a hydrogen plasma is shown in Fig. 3.25 in which the dc magnetic field was different for each curve.

The variation of the RF electric field as a function of radial position is shown in Fig. 3.26. In these data the RF signal picked up

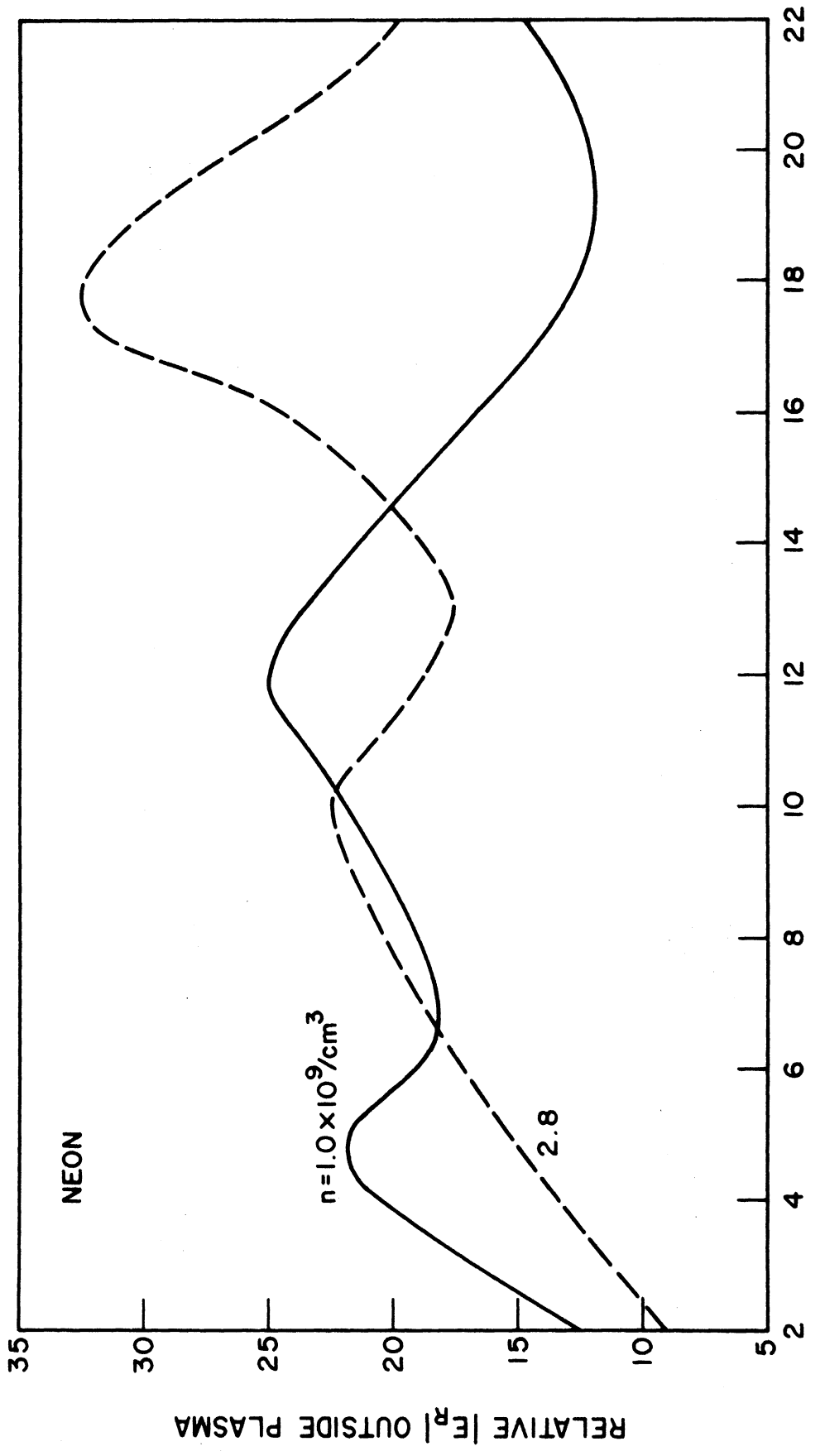

FIG. 3.20 RADIAL ELECTRIC-FIELD AMPLITUDE AS A FUNCTION OF FREQUENCY FOR DIFFERENT DENSITIES.

(V = 600 V, I_b = 2.7 mA, B_o = 310 G)

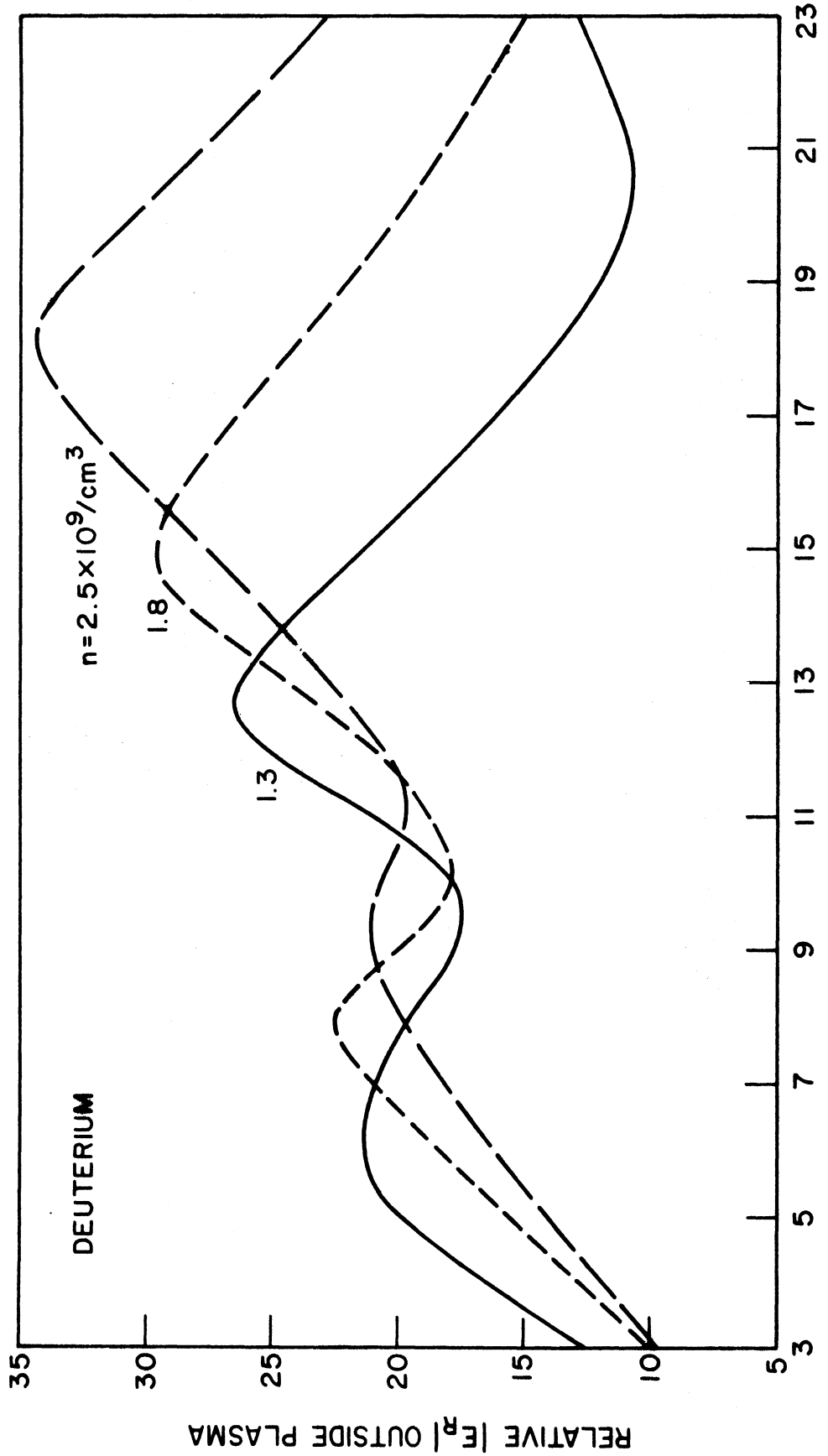

FIG. 3.21 RADIAL ELECTRIC-FIELD AMPLITUDE AS A FUNCTION OF FREQUENCY FOR DIFFERENT DENSITIES.

(V = 600 V, I_b = 3 mA, B_o = 310 G)

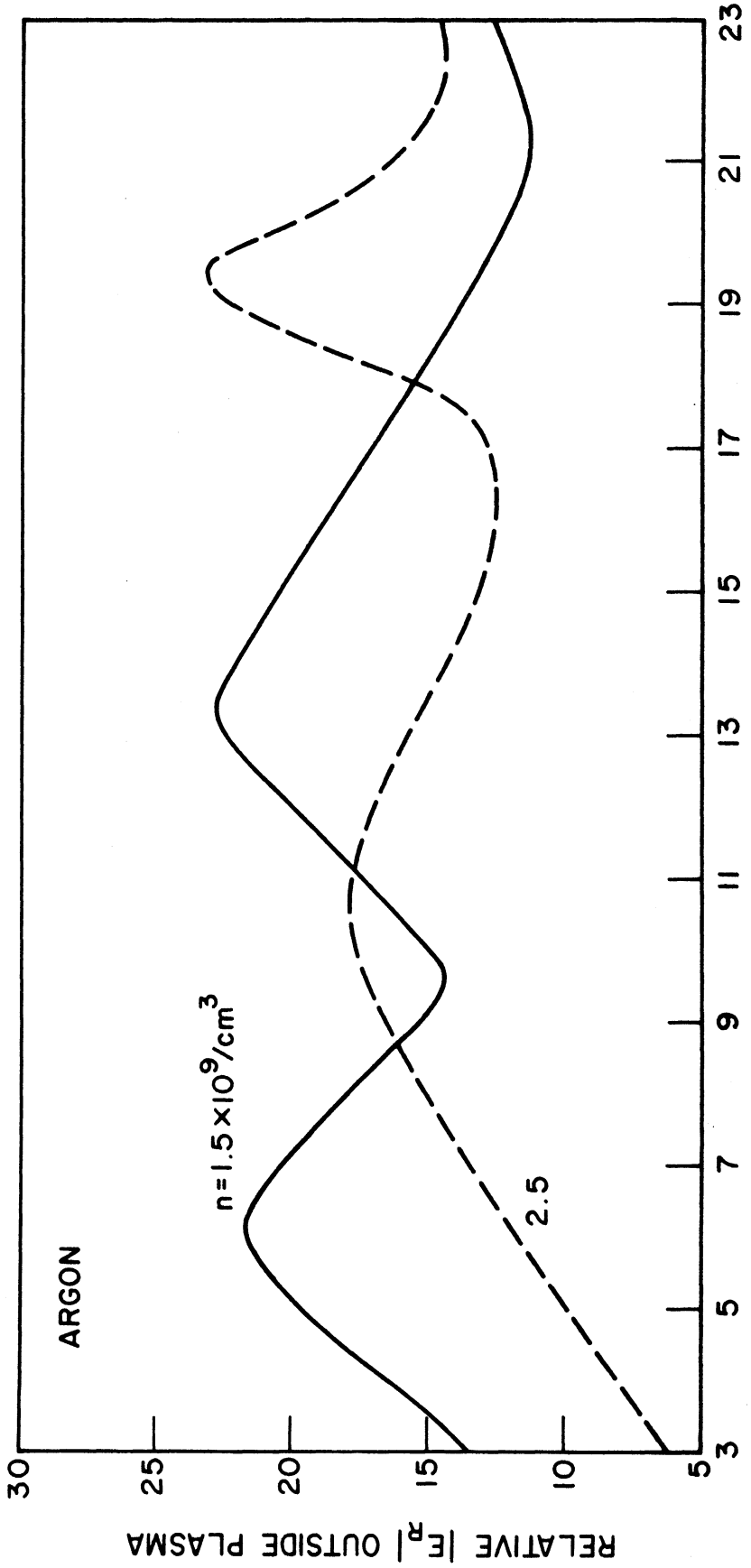

FIG. 3.22 RADIAL ELECTRIC-FIELD AMPLITUDE AS A FUNCTION OF FREQUENCY FOR DIFFERENT DENSITIES.

(V = 600 V, I_b = 2.3 mA, B_o = 400 G)

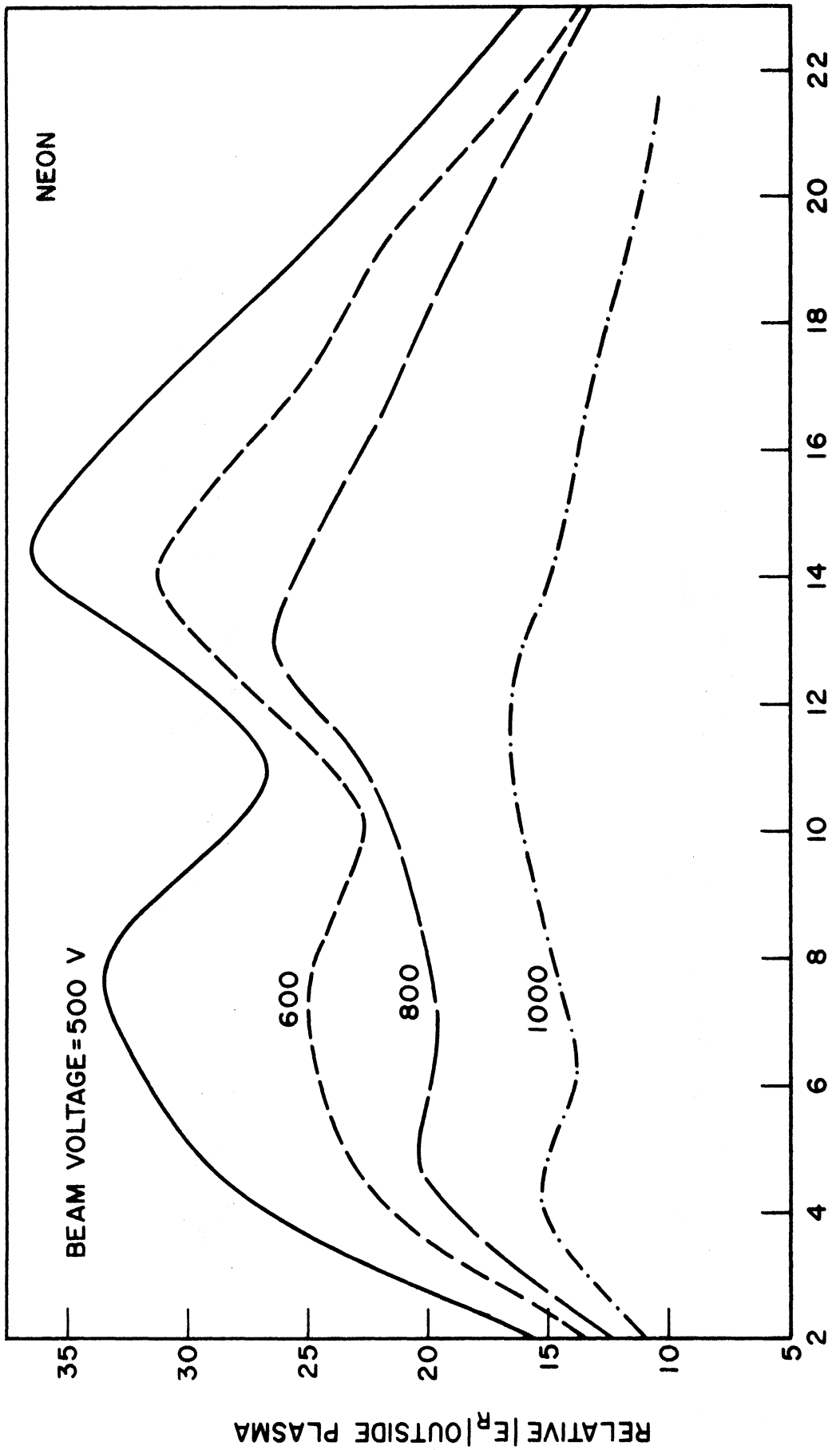

FIG. 3.23 RADIAL ELECTRIC-FIELD AMPLITUDE AS A FUNCTION OF FREQUENCY FOR DIFFERENT BEAM VOLTAGES.

($n = 1.5 \times 10^9/cm^3$, $I = 2.7$ mA, $B_o = 310$ G)

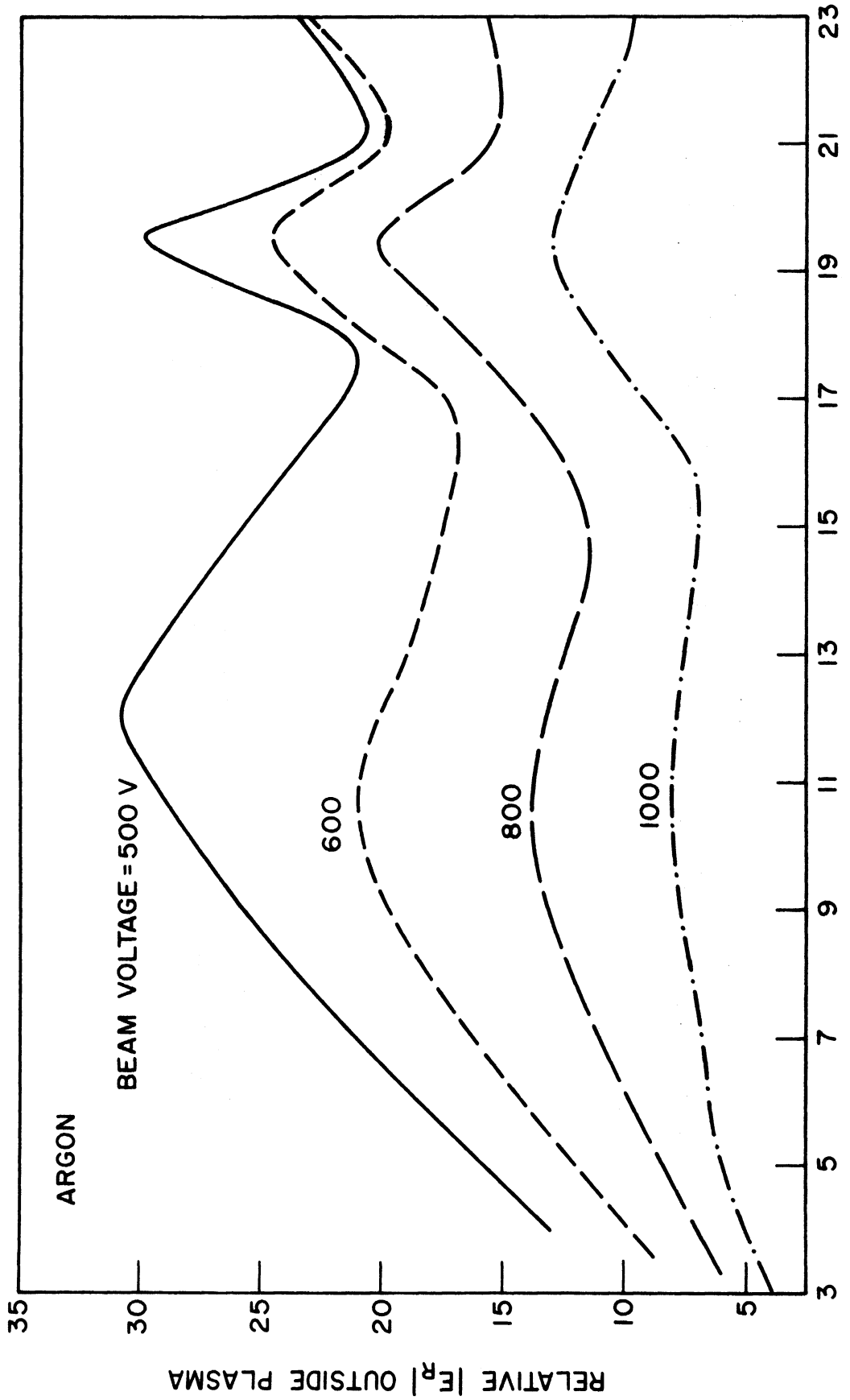

FIG. 3.24 RADIAL ELECTRIC-FIELD AMPLITUDE AS A FUNCTION OF FREQUENCY FOR DIFFERENT BEAM VOLTAGES.

($n = 2.5 \times 10^9/cm^3$, $I = 3$ mA, $B_o = 310$ G)

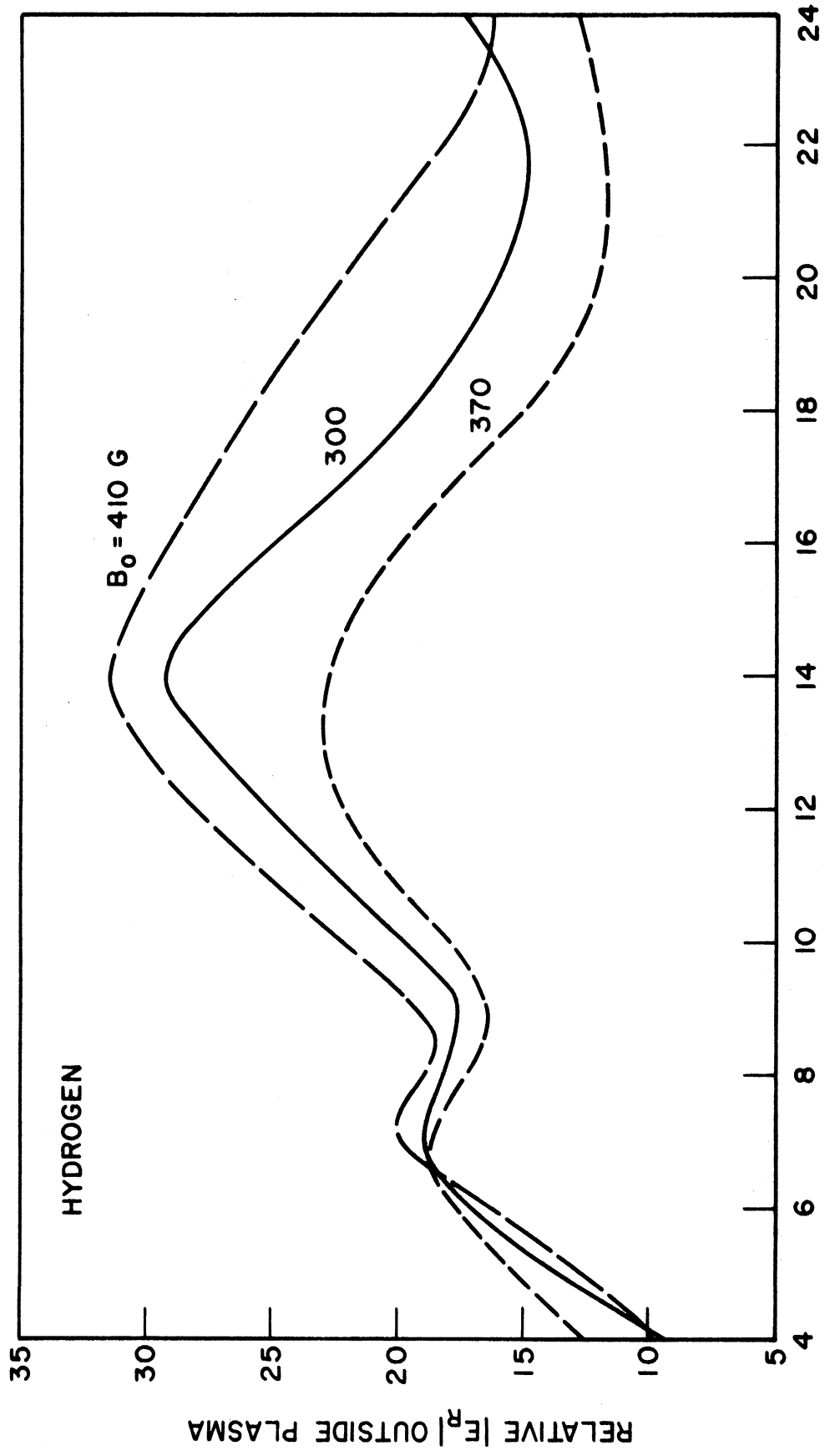

FIG. 3.25 EXPERIMENTALLY OBSERVED RELATIVE RADIAL ELECTRIC-FIELD AMPLITUDE AS A FUNCTION OF FREQUENCY FOR DIFFERENT MAGNETIC FIELDS. (V = 600 V, I_b = 2.5 mA, n_p = 8.5 x $10^8/cm^3$)

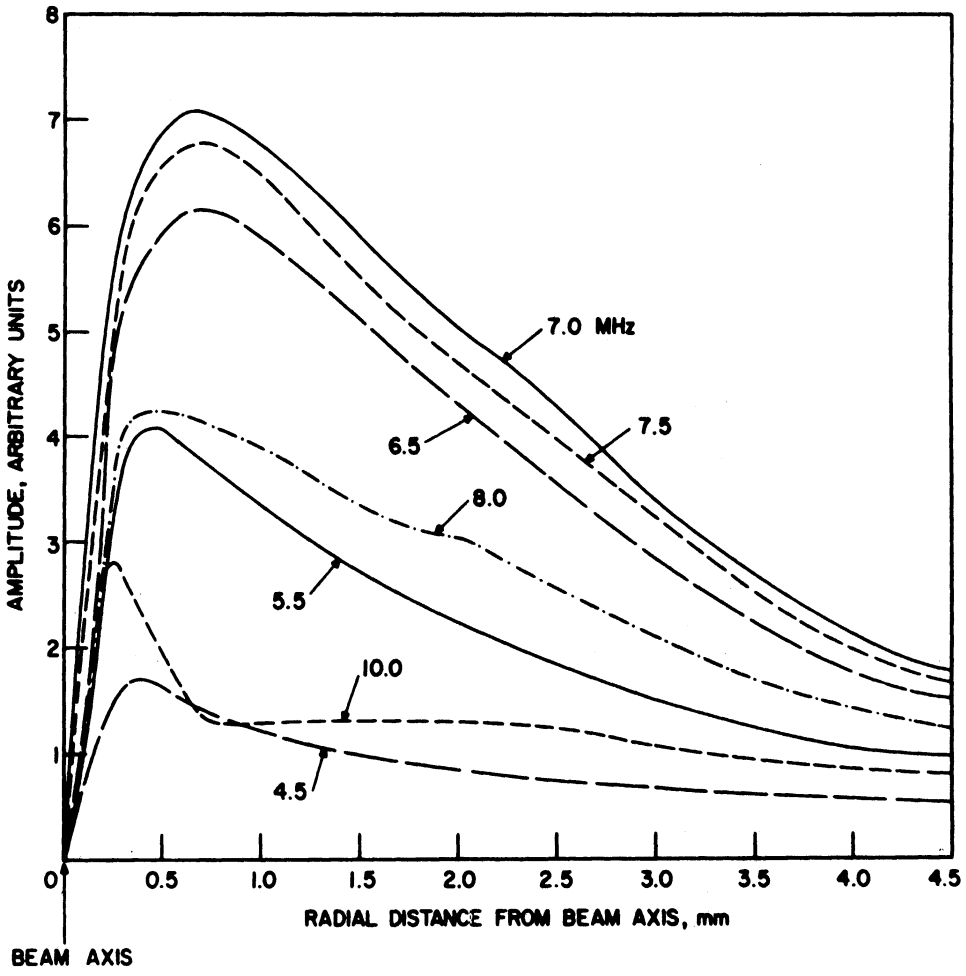

FIG. 3.26 RF SIGNAL PICKED UP BY A BIASED LANGMUIR PROBE AS A FUNCTION OF RADIUS. THE PARAMETER FOR EACH CURVE IS THE BEAM RF MODULATION FREQUENCY.

by the probe was amplitude detected, filtered and amplified by a 1000-Hz narrow-band amplifier. The 1000-Hz amplitude, which is proportional to the local RF amplitude, was recorded as a function of radius by an x-y recorder. The RF field outside the plasma falls off monotonically as a function of radius. The peak or resonance effect is also observed in these data. In the case shown in Fig. 3.26, the RF electric-field amplitude at a fixed radius is maximum at 7 MHz.

Thus it is concluded that two or three peaks are typically observed in the probe response. The peak frequencies lie above the ion-plasma frequencies and are, in general, not harmonically related. The peak frequencies decrease as the beam voltage is increased. The peak frequencies are relatively independent of ion mass and external dc magnetic field.

3.4.2 Interferometric Measurements. For the measurement of axial wavelength an axially movable Langmuir probe was used. The probe tip was along the radial direction and thus it detected the radial RF electric field. A double-balanced mixer was used as discussed in Section 3.1.7c. A typical measurement of the radial RF electric field as a function of axial position is shown in Fig. 3.27 at the first and second resonant frequencies. Since the probe could be moved a distance of only 10 inches from the collector, the data points near the gun end could not be taken. However, the data were sufficient to indicate that the first and second resonances are half-wave and full-wave resonances. The wavelengths thus found are much larger than the wavelength corresponding to the beam-cyclotron waves.

The radially and axially movable probes were positioned diametrically opposite just outside the plasma column. The RF signals from the two probes

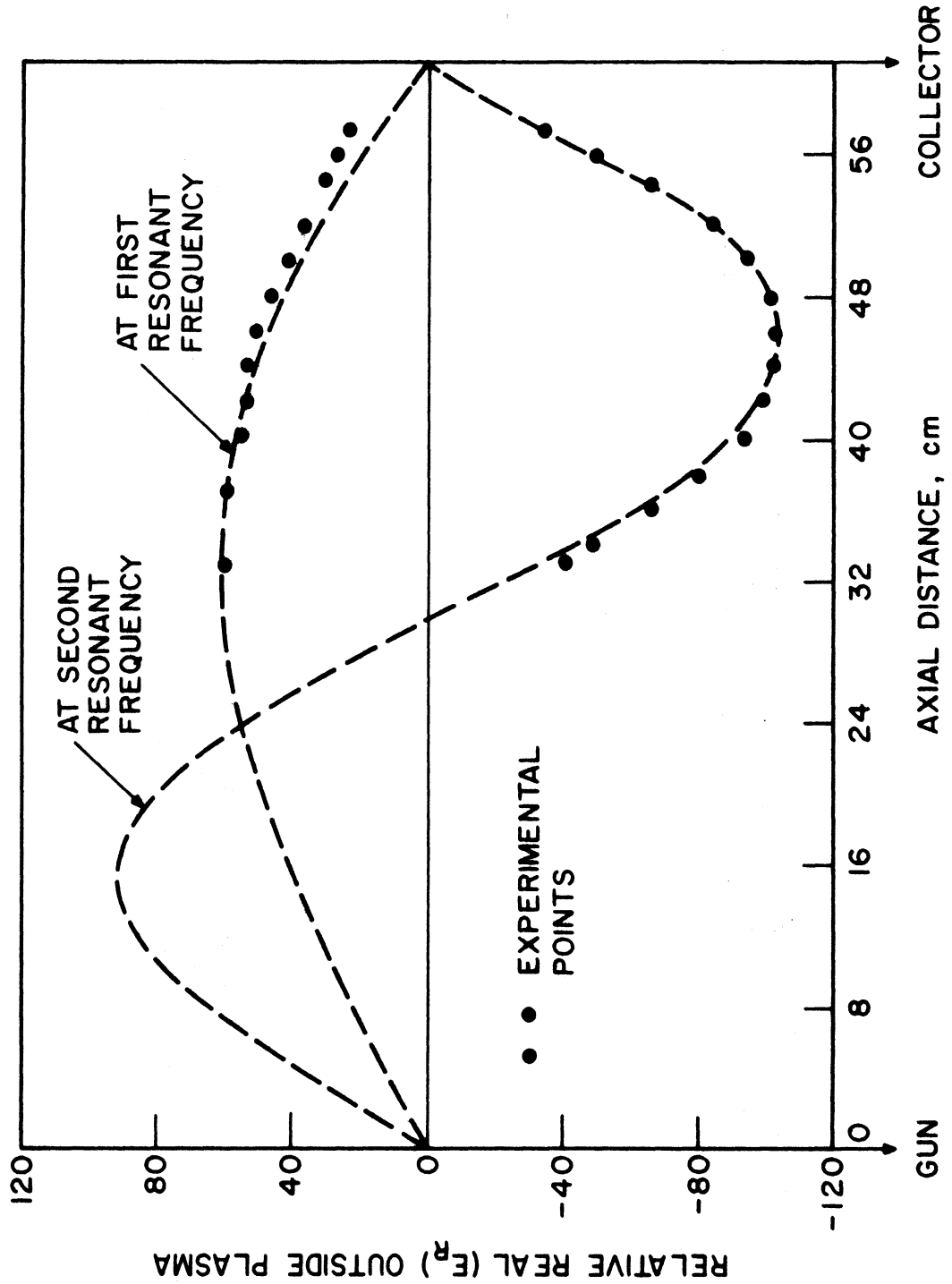

FIG. 3.27 THE OUTPUT OF A PHASE-SENSITIVE DETECTOR AS A FUNCTION OF AXIAL DISTANCE.

were amplified by two identical voltage amplifiers and fed to a double-beam oscilloscope. Comparison of the phases showed that the RF fields are in phase, suggesting that the mode is axisymmetric.

In summary, an experiment has been performed in a beam-generated plasma operating in the "quiescent" mode. The beam and plasma diameter are approximately equal and the metal waveguide diameter was much larger than the plasma diameter (about 15 times). The plasma was axially bounded at one end by the grid of the electron gun and at the other end by the collector. The plasma density and the magnetic field were such that the operation was in the low-density regime ($\omega_{ce}^2 \gg \omega_{pe}^2 \gg \omega_{ce}\omega_{ci}$).

In such a system when the electron beam is current modulated, two or three resonances are observed in the RF radial electric field frequency response curve. The resonant frequencies are not harmonically related and lie just above the ion-plasma frequency. At these resonant frequencies energetic ions are observed with the help of a gridded probe velocity analyzer.

The resonant frequencies are relatively independent of the external dc magnetic field and ion mass. The resonant frequencies decrease slightly with an increase in beam voltage and increase with increasing plasma density. The first and second resonances are half- and full-wavelength resonances of the axially bounded system, and the axial wavelength is much larger than the cyclotron wavelength. The excited mode is axisymmetric.

CHAPTER IV. THEORETICAL MODEL OF THE EXPERIMENT AND ITS ANALYSIS

In Chapter III the experiment carried out in the present investigation was described in which a modulated electron beam excites low-frequency resonances in a finite-sized plasma. At these resonances a relatively large radial RF electric field is excited in the plasma which produces the observed ion heating. In Section 4.1 a theoretical model based on the experimental arrangement is established. It is then analyzed in Section 4.2 to obtain the expressions for ac beam-velocity modulation, ac current-density modulation, ac quasi-static potential and ac electric field. The fields are then computed with the help of a digital computer (Model IBM 360/67) for the configuration experimentally investigated as well as for two other configurations.

4.1 Theoretical Model of the Experiment

A schematic drawing of the theoretical model is given in Fig. 4.1. It shows a homogeneous, monoenergetic, cylindrical electron beam of radius b passing through a homogeneous plasma of cold electrons and ions. The plasma is surrounded by a cylindrical metal vacuum envelope of radius d. The beam-plasma system is axially bounded by the grid of the electron gun and the electron-beam collector. The system is thus assumed to be axially bounded by perfectly conducting electrical short circuits. There is a steady magnetic field $\bar{B}_o$ along the axis of the electron beam (z-direction). Both electron and ion motion is included in the model because low-frequency modes are of interest.

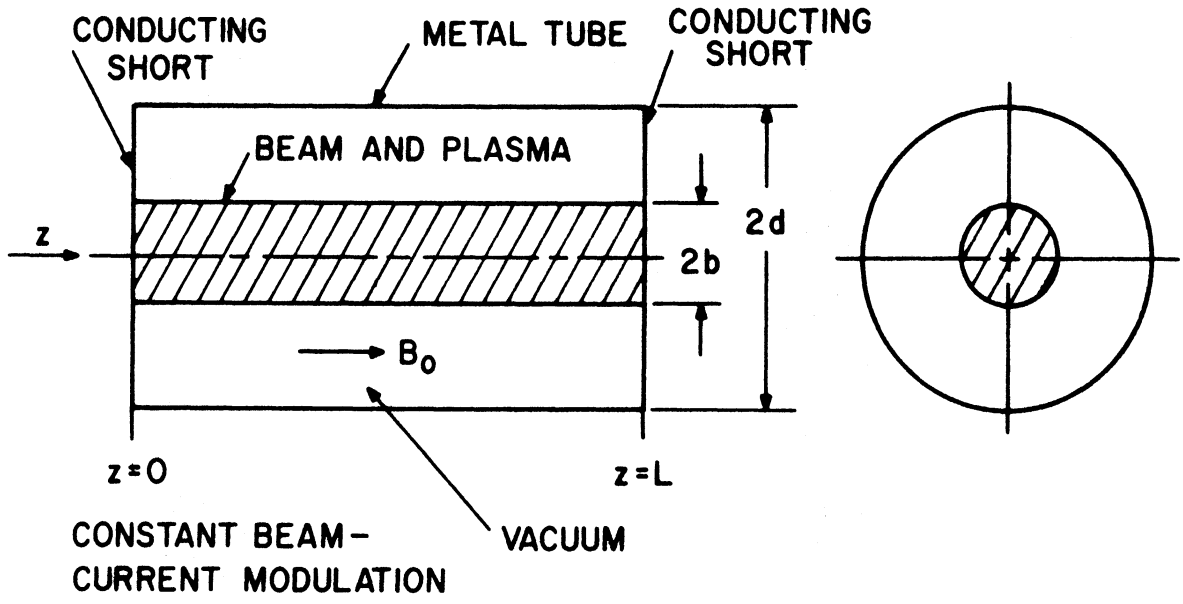

FIG. 4.1 SCHEMATIC DRAWING OF THE THEORETICAL MODEL OF THE EXPERIMENTAL BEAM-PLASMA SYSTEM.

The electron beam and plasma diameters are assumed to be equal since the beam-generated plasma was operated in the quiescent mode.[82] The metal vacuum tube radius is assumed to be infinite ($d \rightarrow \infty$) since the ratio of the metal tube diameter to the plasma diameter was approximately 17 in the experiment. A constant current modulation of the beam is imposed at the gun end as was done experimentally. The experiment was conducted with low percentage modulation to obtain sinusoidal drive; therefore the small-signal approximation is assumed to be valid. First-order quantities are assumed to vary as $\exp[j(\omega t - k_z z)]$. For the experimental parameters, electron-ion, ion-electron and ion-neutral collision frequencies are much less than the electron-neutral collision frequency, therefore only the electron-neutral collisions are included in the theoretical model. The axial phase velocities of the waves which are involved are all much higher than thermal velocities, $\omega >> k_z v_T$; therefore temperature effects such as Landau damping are neglected. Cyclotron damping effects are also neglected.

4.2 Analysis of the Theoretical Model

The aim of the present analysis of the beam-plasma system described in the preceding section is to obtain expressions for the electric field in terms of the beam-modulation current. Thus the experimentally observed RF electric field in the beam-plasma system can be compared to that obtained theoretically.

As mentioned in Section 2.3, obtaining the expressions for the potential and fields for a beam-plasma system requires the study of the dispersion characteristics of the waves which exist in such a system. The solutions of the dispersion equations given in Section 2.3.3 show

that six waves (solutions for k_z for real ω) exist in the beam-plasma system for each radial mode. Each of these waves contribute to the total electric field which is observed experimentally. Therefore to compare the theoretically calculated and experimentally observed fields, the contribution of each wave must be taken into account. The relative amplitude of each wave (or normal mode) that is excited is determined by applying the boundary conditions at the gun and collector end. The total field is then obtained by the superposition of all the normal modes in relative amounts proportional to their complex amplitudes.

The dispersion equation for the axial propagation constant k_z includes the effect of finite beam and plasma radii, electron-beam space charge, uniform axial magnetic field and plasma electron-neutral collisions. The experimental observations show that the axisymmetric ($m = 0$) mode is excited, therefore only the $m = 0$ mode has been included in the theoretical calculations. Two of the above mentioned six roots are associated with the electron-beam cyclotron waves and have an axial wavelength given approximately by v_o/f_{ce}. Since experimentally the electric field was found to have a much larger wavelength, these two roots are neglected. The dispersion equation for the three configurations of the beam-plasma system has been solved in Section 2.3.3. At each frequency, four k_z roots are obtained. Two of these roots correspond to the plasma waves and the other two to the beam space-charge waves. Although there are an infinite number of radial modes for a given azimuthal mode, only the lowest-order radial mode has been included in the solution given in Section 2.3.3. Higher-order radial modes could be included in principle, but at a great cost in complexity. The use of higher-order radial modes would require additional information about the field structure over a cross section of the beam.

The use of complex k_z solutions of the dispersion equation for real frequency ω implies that no absolute instabilities exist in the beam-plasma system under consideration. It is well known that absolute instabilities can exist in infinitely long beam-plasma systems. The parameters used in the present investigation do not permit an absolute instability in an infinitely long system in the ω_{pi} range. (Other frequency ranges were not checked.) This was verified by applying the Bers-Briggs stability criterion to the dispersion equation. If it is assumed that absolute instabilities do not exist at other frequencies (no experimental evidence was found in the present experiment to indicate that one might exist), then solving the dispersion equation for complex k_z for real ω is justified. The results give a weak convective instability as expected from the stability criterion.

As discussed in Section 3.2.1, the experimental data were taken by holding the beam-current modulation constant. For comparison of the experimental and theoretical results, field expressions in terms of the beam-current modulation are required. For this purpose, the value of the arbitrary constant A in the potential and field equations (Eq. 2.94) is determined in terms of the beam-current density modulation. The electron-beam and plasma equations are solved in a self-consistent manner.

If it is assumed that the total velocity $\bar{v}_b$, the charge density ρ_b and the convection current density $\bar{J}_b$ of the electron beam consists of an average value plus a small harmonic time-dependent perturbation, then

$$\bar{v}_b = \bar{v}_o + \bar{v}_{1b} e^{j(\omega t - k_z z)} , \qquad (4.1)$$

$$\rho_b = \rho_{ob} + \rho_{1b} e^{j(\omega t - k_z z)} \tag{4.2}$$

and

$$\bar{J}_b = \bar{J}_{ob} + \bar{J}_{1b} e^{j(\omega t - k_z z)} \quad . \tag{4.3}$$

Since $\bar{J}_b = \rho_b \bar{v}_b$,

$$\bar{J}_b = \rho_{ob}\bar{v}_o + (\rho_{1b}\bar{v}_o + \rho_{ob}\bar{v}_{1b}) e^{j(\omega t - k_z z)} \tag{4.4}$$

in which the product $\rho_{1b}\bar{v}_{1b}$ has been neglected since it is the product of perturbation quantities and is of second order. The ac current-density modulation can be written as

$$\bar{J}_{1b} = (\rho_{1b}\bar{v}_o + \rho_{ob}\bar{v}_{1b}) \quad . \tag{4.5}$$

From the continuity equation (Eq. 2.5), the force equation (Eq. 2.8) and Maxwell's equations, the small-signal axial ac beam velocity and beam-current density are given by (the derivation is given in Appendix D)

$$v_{1bz} = -\frac{e}{m}\frac{E_z}{j\omega_D} \tag{4.6}$$

and

$$J_{1bz} = -j\omega\epsilon_o \frac{\omega_{pb}^2}{\omega_D^2}(1 + \Delta)E_z \quad , \tag{4.7}$$

where

$$\omega_D = \omega - k_z v_o$$

and

$$\Delta = \frac{\omega_D^2}{\omega_D^2 - \omega_{ce}^2} \cdot \frac{T_1^2 v_o}{k_z \omega} .$$

For a wide range of parameters Δ may be very small compared to unity. Substitution of the expression for E_z from Eq. 2.109 into Eq. 4.7 yields

$$J_{1bz} = - j\omega\epsilon_o \frac{\omega_{pb}^2}{\omega_D^2} (1 + \Delta) \cdot jk_z A \frac{J_o(T_1 r)}{J_o(T_1 b)} e^{j(\omega t - k_z z)} \qquad (4.8)$$

in which m = 0 has been assumed. At r = 0 and z = 0 and omitting the time dependence,

$$J_{1bz}\Big|_{\substack{r=o,\\ z=o}} = A\omega\epsilon_o k_z \frac{\omega_{pb}^2}{\omega_D^2} \frac{(1 + \Delta)}{J_o(T_1 b)} \equiv J_{1boi}$$

or

$$A = \frac{J_{1boi}\omega_D^2 J_o(T_1 b)}{\omega\epsilon_o k_z \omega_{pb}^2 (1 + \Delta)} , \qquad (4.9)$$

where J_{1boi} is the ac beam-current modulation at the gun on the axis for the ith normal mode. Substituting the value of A in Eq. 4.8 yields

$$J_{1bz} = J_{1boi} J_o(T_1 r) e^{-jk_z z} \qquad (4.10)$$

and the other quantities are obtained as follows:

$$v_{1bz} = - J_{1boi} \frac{e}{m} \frac{\omega_D}{\omega\epsilon_o\omega_{pb}^2} J_o(T_1 r)\, e^{-k_z z} , \tag{4.11}$$

$$\Phi^I = J_{1boi} \frac{\omega_D^2}{\omega\epsilon_o k_z \omega_{pb}^2 (1 + \Delta)} J_o(T_1 r)\, e^{-k_z z} , \tag{4.12}$$

$$E_r^I = J_{1boi} \frac{T_1 \omega_D^2}{\omega\epsilon_o k_z \omega_{pb}^2 (1 + \Delta)} J_1(T_1 r)\, e^{-jk_z z} \tag{4.13}$$

and

$$E_z^I = J_{1boi} \frac{j\omega_D^2}{\omega\epsilon_o \omega_{pb}^2 (1 + \Delta)} J_o(T_1 r)\, e^{-jk_z z} . \tag{4.14}$$

Since at each frequency there are four waves, the total field is obtained by a normal mode summation:

$$J_{1bz} = J_{1bo} \sum_{i=1}^{4} X_i J_o(T_{1i} r)\, e^{-jk_{zi} z} , \tag{4.15}$$

$$v_{1bz} = - \frac{e}{m} \frac{J_{1bo}}{\omega\epsilon_o\omega_{pb}^2} \sum_{i=1}^{4} X_i(\omega - k_{zi} v_o) J_o(T_{1i} r)\, e^{-jk_{zi} z} , \tag{4.16}$$

$$\Phi^I = \frac{J_{1bo}}{\omega\epsilon_o\omega_{pb}^2} \sum_{i=1}^{4} \frac{X_i(\omega - k_{zi} v_o)^2}{k_{zi}(1 + \Delta_i)} J_o(T_{1i} r)\, e^{-jk_{zi} z} , \tag{4.17}$$

$$E_r^I = \frac{J_{1bo}}{\omega\epsilon_o\omega_{pb}^2} \sum_{i=1}^{4} \frac{X_i(\omega - k_{zi} v_o)^2}{(1 + \Delta_i)} \frac{T_{1i}}{k_{zi}} J_1(T_{1i} r)\, e^{-jk_{zi} z} \tag{4.18}$$

and

$$E_z^I = \frac{jJ_{1bo}}{\omega\epsilon_o\omega_{pb}^2} \sum_{i=1}^{4} X_i(\omega - k_{zi}v_o)^2 J_o(T_{1i}r)\, e^{-jk_{zi}z} \quad . \tag{4.19}$$

In the preceding expressions J_{1bo} is an experimentally identifiable quantity and is the beam-current modulation at the grid of the gun.

The boundary conditions at the two ends of the system are now imposed to obtain the coefficients X_i which determine the relative amplitude of each excited wave. The axial boundary conditions at the axis of the beam ($r = 0$) are:

1. at $z = 0$, $J_{1bz} = J_{1bo}\, e^{j\omega t}$;

2. at $z = 0$, $v_{1bz} = 0$;

3. at $z = 0$, $\Phi^I = 0$;

4. at $z = L$, $\Phi^I = 0$. (4.20)

Substituting the boundary conditions given by Eq. 4.20 into Eqs. 4.15 through 4.17 gives

$$X_1 + X_2 + X_3 + X_4 = 1 \ ,$$

$$F_1 X_1 + F_2 X_4 + F_3 X_3 + F_4 X_4 = 0 \ ,$$

$$S_1 X_1 + S_2 X_2 + S_3 X_3 + S_4 X_4 = 0 \ ,$$

$$S_1 e^{-jk_{z1}L} X_1 + S_2 e^{-jk_{z2}L} X_2 + S_3 e^{-jk_{z3}L} X_3 + S_4 e^{-jk_{z4}L} X_4 = 0 \ , \tag{4.21}$$

where

$$F_i = \omega - k_{zi}\, v_o$$

and

$$S_i = \frac{(\omega - k_{zi}v_o)^2}{k_{zi}(1 + \Delta_i)} \quad .$$

This set of simultaneous equations is solved on the computer to obtain X_i. Their values are substituted back into Eqs. 4.15 through 4.19 to determine the physical quantities given by these equations.

The electrostatic potential and the electric field in the region outside the beam can similarly be expressed as a normal-mode summation. Using Eqs. 2.115 and 2.116 for the open beam-plasma waveguide gives

$$\Phi^{II} = \sum_{i=1}^{4} \Phi_i^I \frac{J_o(T_{1i}b)}{K_o(T_{2i}b)} \frac{K_o(T_{2i}r)}{J_o(T_{1i}r)} \quad , \tag{4.22}$$

$$E_z^{II} = \frac{J_{1bo}}{\omega\epsilon_o\omega_{pb}^2} \sum_{i=1}^{4} X_i \frac{\omega_{Di}^2}{(1 + \Delta_i)} \frac{J_o(T_{1i}b)}{K_o(T_{2i}b)} K_o(T_{2i}r)\, e^{-jk_{zi}z} \tag{4.23}$$

and

$$E_r^{II} = \frac{J_{1bo}}{\omega\epsilon_o\omega_{pb}^2} \sum_{i=1}^{4} X_i \frac{\omega_{Di}^2}{(1 + \Delta_i)} \frac{T_{2i}}{k_{zi}} \frac{J_o(T_{1i}b)}{K_o(T_{2i}b)} K_1(T_{2i}r)\, e^{-jk_z z} \quad . \tag{4.24}$$

For the unfilled-beam, filled-plasma waveguide ($b < a = d$), the expression for the electrostatic potential and electric field become

$$\Phi^{II} = \sum_{i=1}^{4} \Phi_i^I \cdot \frac{J_o(T_{1i}b)}{J_o(T_{1i}r)} \left[\frac{I_o(T_{2i}r)K_o(T_{2i}a) - I_o(T_{2i}a)K_o(T_{2i}r)}{I_o(T_{2i}b)K_o(T_{2i}a) - I_o(T_{2i}a)K_o(T_{2i}b)} \right] ,$$

(4.25)

$$E_z^{II} = \frac{J_{1bo}}{\omega\epsilon_o\omega_{pb}^2} \sum_{i=1}^{4} X_i \frac{\omega_{Di}^2}{(1+\Delta_i)} J_o(T_{1i}b)$$

$$\cdot e^{-jk_z z}\left[\frac{I_o(T_{2i}r)K_o(T_{2i}a) - I_o(T_{2i}a)K_o(T_{2i}r)}{I_o(T_{2i}b)K_o(T_{2i}a) - I_o(T_{2i}a)K_o(T_{2i}b)}\right] \quad (4.26)$$

and

$$E_r^{II} = \frac{J_{1bo}}{\omega\epsilon_o\omega_{pb}^2} \sum_{i=1}^{4} X_i \frac{\omega_{Di}^2}{(1+\Delta_i)} \cdot \frac{T_{2i}}{k_{zi}} \cdot J_o(T_{1i}b)\, e^{-jk_{zi}z}$$

$$\cdot\left[\frac{I_1(T_{2i}r)K_o(T_{2i}a) + I_o(T_{2i}a)K_1(T_{2i}r)}{I_o(T_{2i}b)K_o(T_{2i}a) - I_o(T_{2i}a)K_o(T_{2i}b)}\right] . \quad (4.27)$$

The numerical solutions of these equations are obtained with the computer and are described in the following section.

4.3 Computer Solution of the Normal-Mode Field Equations

It is clear by examining Eqs. 4.15 through 4.19 and Eqs. 4.22 through 4.27 that the dispersion equation for a given beam-plasma configuration must be first solved to obtain k_{zi} $(i = 1,\ldots 4)$ at a given ω. The k_{zi} are then used to obtain the coefficients X_i and finally the total electric field and other quantities.

4.3.1 Outline of the Procedure for Computer Solution of the Normal-Mode Field Equations. A brief flow chart for computer solution of the normal-mode field equations is given in Fig. 4.2. The dispersion equation for a given beam-plasma waveguide configuration is first solved as described in Section 2.3.3. It is evident that there are four roots of k_z at a given real frequency ω. Each of the four roots is computed as a part of a continuous branch corresponding to that root. There are, therefore, essentially four branches in the dispersion diagram to be

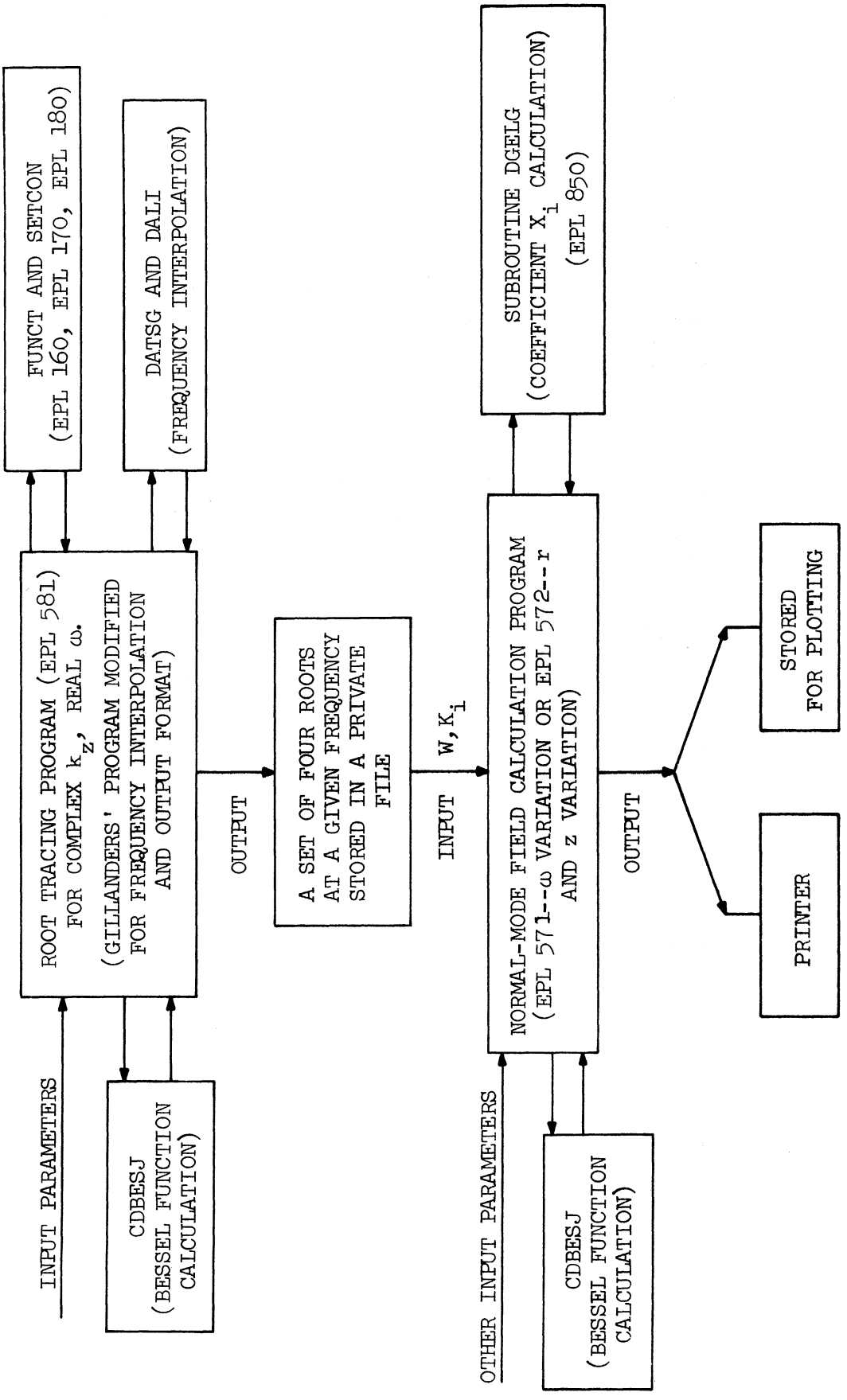

FIG. 4.2 FLOW CHART FOR NORMAL-MODE FIELD CALCULATIONS.

computed. The computation of each branch is independent of the other three branches. Four roots are required at a given frequency for calculation of the normal-mode field quantities. Since the root tracing program does not give roots at specified frequencies, a method of interpolation is used to obtain the value of each of the four roots at a given frequency. The interpolation is made between the points computed by the root tracing program for each given frequency until the desired frequency range is covered. Usually the given frequencies are chosen to be equally spaced. The subroutines DATSG and DALI obtained from the IBM System/360 Scientific Subroutine Package (SSP) are used for interpolation. A set of four roots for discrete values of frequencies is thus obtained and is stored in a private file.

For a given frequency, the four roots are read in by the program which is used to calculate the normal-mode field quantities. The subroutine DGELG obtained from the SSP is used to determine the coefficients X_i. This subroutine solves a system of general simultaneous linear equations by Gauss elimination.

The appropriate field equations for the chosen beam-plasma waveguide configuration are now selected with the help of three switches SW, SW2 and SW3 provided in the normal-mode field calculation program. The desired quantities, such as ac velocity modulation, ac current-density modulation, potential, radial and axial electric fields as a function of frequency at an arbitrary position, are computed by this program and the output is either printed or stored in a file for plotting by a digital plotter. A separate program is used to compute the axial and radial variation of the above quantities at a given frequency. A listing of the preceding computer programs is given in Appendix E.

4.3.2 Computer Results for an Open Beam-Plasma Waveguide. In this section theoretical results which were obtained with the preceding programs are given. A typical set of results for an open beam-plasma waveguide configuration are first presented because this was the configuration which most nearly models the experiment. The parameters chosen for this set are typical of the experimental parameters and are given in Table 4.1.

Table 4.1

Theoretical Parameters for Computer Analysis

(See Section 2.3.3a for Definition of Parameters)

$$CV = 0.873 \times 10^{-2}$$

$$R = 67.5$$

$$NU = 0.1$$

$$SYSL = 1.775$$

$$Z = 1.182$$

$$\omega_{ce}/\omega_{pe} = 3$$

$$RB1 = 0.5$$

$$RB2 = 2$$

$$V_b = 600 \text{ V}$$

$$I_b = 2.5 \text{ mA}$$

$$n_p = 1 \times 10^9/\text{cm}^3$$

In Table 4.1 SYSL represents the normalized length of the system [$SYSL = L/(v_o/f_{pi})$] and Z represents the normalized axial distance of the observation point (i.e., the probe position in the experiment) from the gun. RB1 and RB2 are the normalized radial position of the observation

point. The normalization factor in this case is the beam radius b. The other parameters have been previously defined in Section 2.3.3a.

Figure 4.3 shows the ac current-density modulation and the ac velocity modulation as a function of frequency at the axial position Z and the radial position RB1 given in Table 4.1. Three "peaks" or "resonances" are found in the frequency range of the investigation. The normalized radial and axial electric-field amplitudes in Region I (inside the plasma) plotted as functions of frequency are shown in Fig. 4.4. Again, three peaks in the frequency response curves are identified. Similar curves are obtained for radial and axial electric-field amplitudes in Region II (outside the plasma) and are shown in Fig. 4.5. The third peak in the radial electric-field response is not as prominent as the first and second peaks. Similarly, the first peak in the axial electric field response is not pronounced but the third peak has a large amplitude. The reason for this behavior may be explained by information from the curves given in Fig. 4.6. In Fig. 4.6 the real part of the radial and axial electric field is plotted as a function of the axial distance at the first three resonant frequencies. The real part of the complex field is proportional to the response of an interferometric detector of the type shown in Fig. 3.27. It is clear from Fig. 4.6 that the first, second and third resonances are half-wave, full-wave and three half-wave resonances, respectively. The axial electric field is maximum and the radial electric field is zero at the two conducting ends. It is noted that at the third resonant frequency the radial electric field has a node and the axial electric field has an antinode near the axial position of the observation point (coincident with the

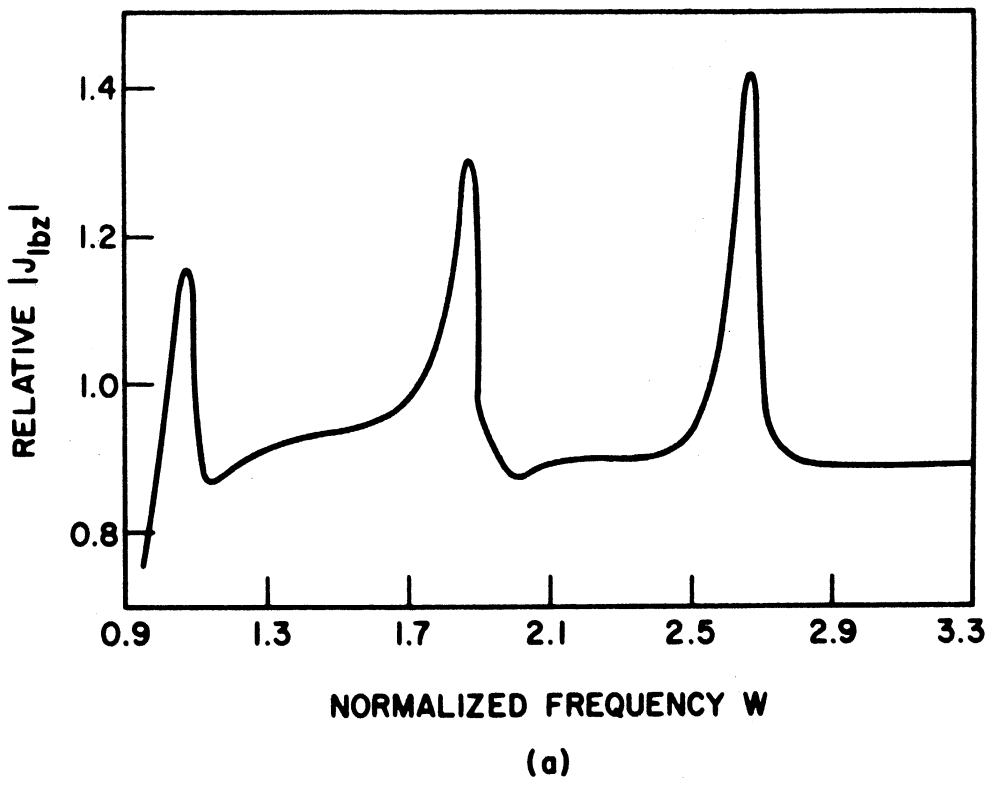

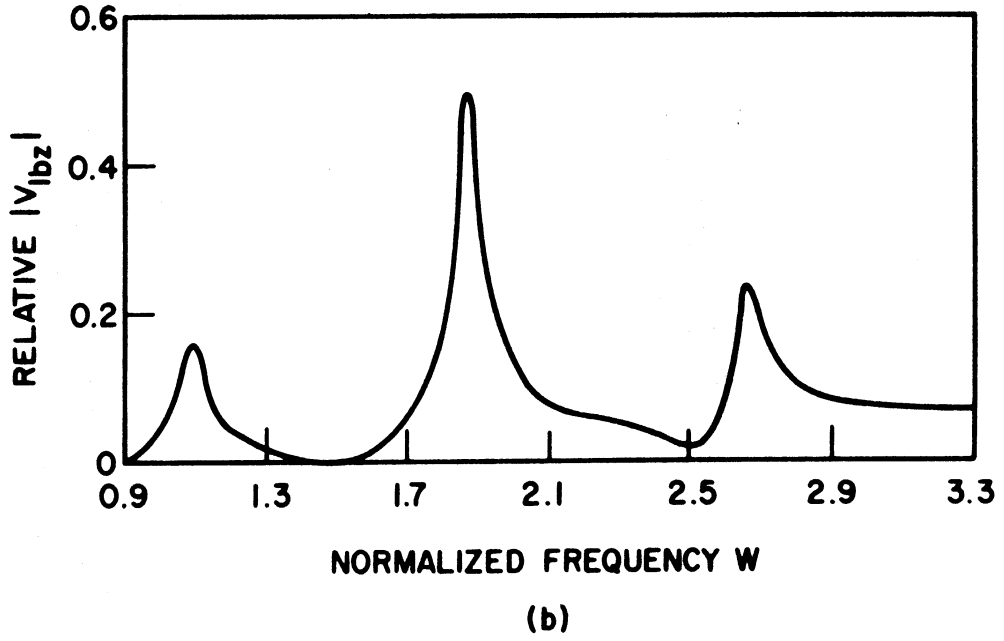

FIG. 4.3 VARIATION OF ac CURRENT-DENSITY MODULATION AND VELOCITY MODULATION IN AN OPEN BEAM-PLASMA WAVEGUIDE. (a) TOTAL ac CURRENT-DENSITY MODULATION AS A FUNCTION OF FREQUENCY. (b) TOTAL ac VELOCITY MODULATION AS A FUNCTION OF FREQUENCY. (THE PARAMETERS ARE GIVEN IN TABLE 4.1)

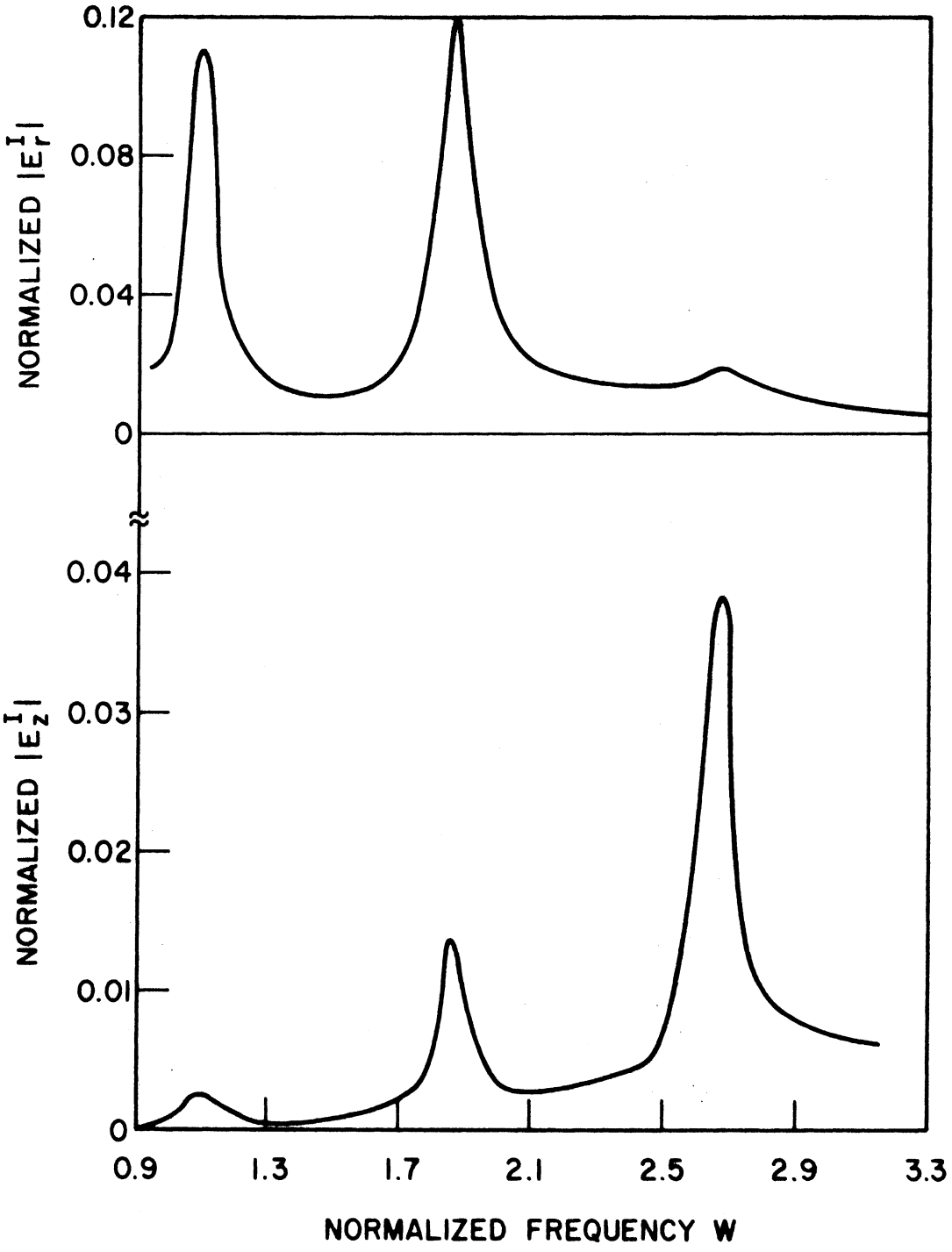

FIG. 4.4 NORMALIZED AMPLITUDE OF THE RADIAL AND AXIAL ELECTRIC FIELD INSIDE THE PLASMA AS A FUNCTION OF FREQUENCY IN AN OPEN BEAM-PLASMA WAVEGUIDE. (THE PARAMETERS ARE GIVEN IN TABLE 4.1)

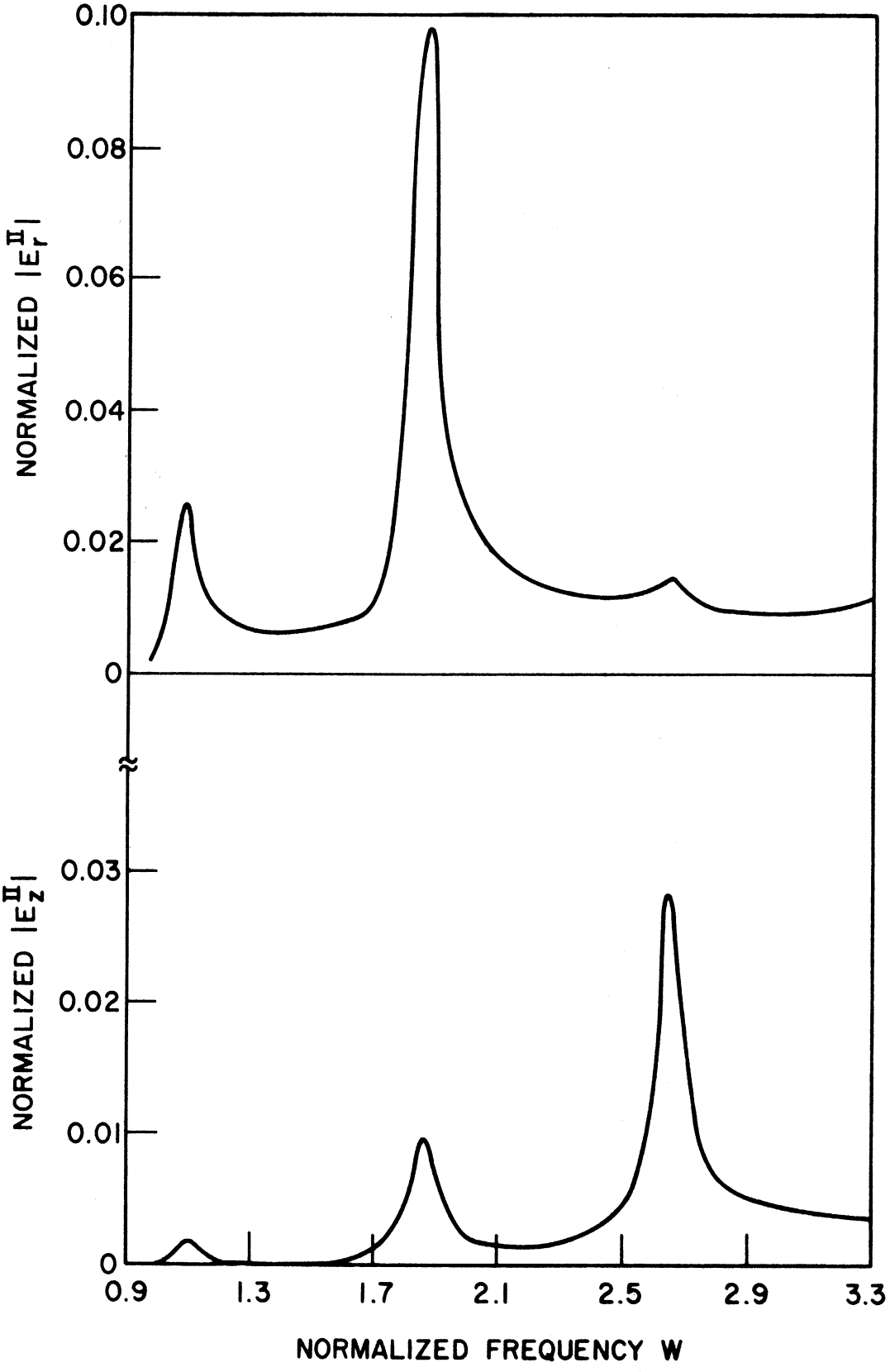

FIG. 4.5 NORMALIZED AMPLITUDE OF THE RADIAL AND AXIAL ELECTRIC FIELD OUTSIDE THE PLASMA AS A FUNCTION OF FREQUENCY IN AN OPEN BEAM-PLASMA WAVEGUIDE. (THE PARAMETERS ARE GIVEN IN TABLE 4.1)

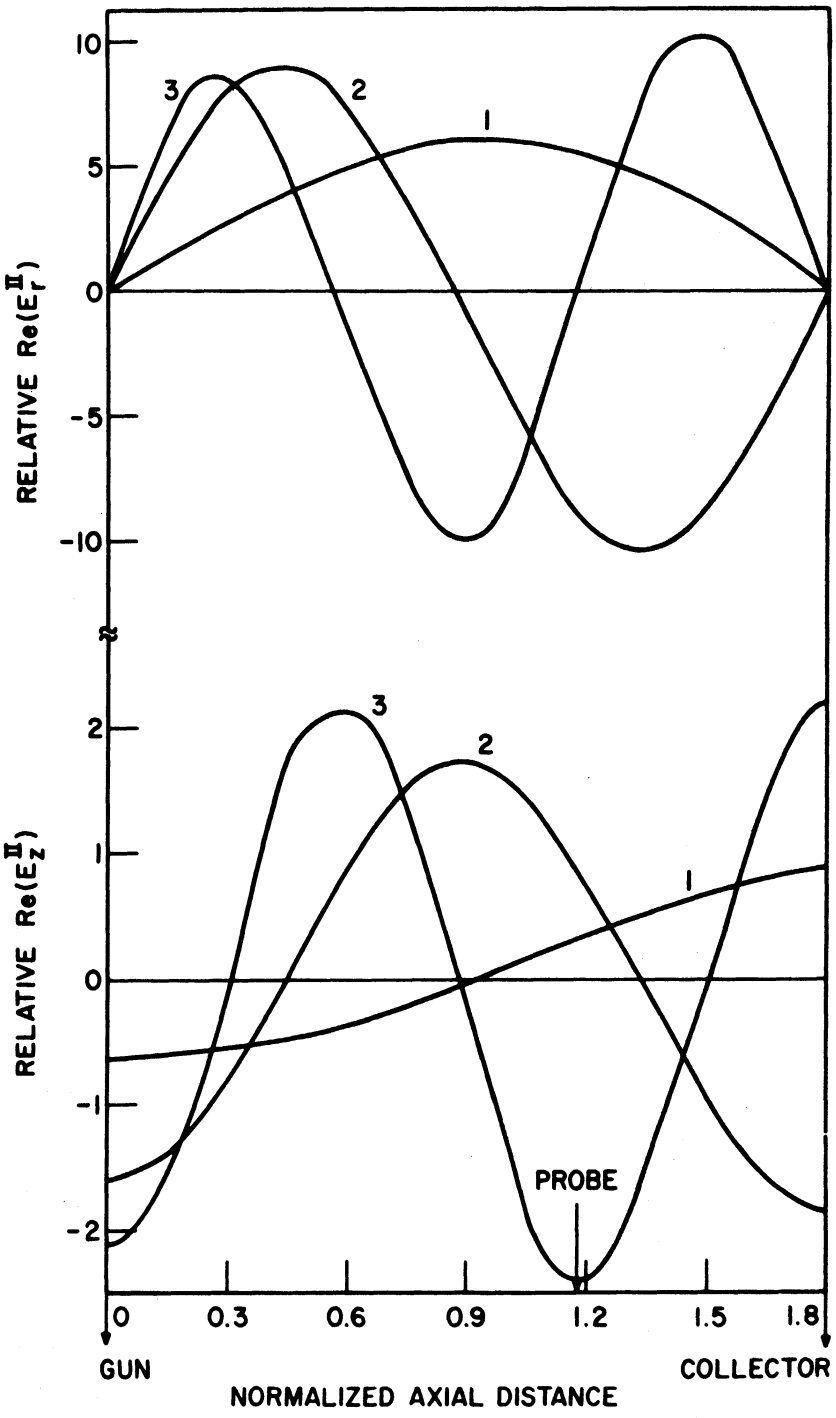

1. AT FIRST RESONANT FREQUENCY. 2. AT SECOND RESONANT FREQUENCY.

3. AT THIRD RESONANT FREQUENCY.

FIG. 4.6 REAL PART OF THE RADIAL AND AXIAL ELECTRIC FIELDS AS A FUNCTION OF AXIAL DISTANCE IN AN OPEN BEAM-PLASMA WAVEGUIDE. (THE PARAMETERS ARE GIVEN IN TABLE 4.1)

probe position in the experiment). The radial electric-field amplitude, therefore, is small at the third resonant frequency but the axial electric field has a relatively large amplitude at this frequency.

Figure 4.7 shows the ac charge density ρ_{1b} as a function of the axial distance at the first resonant frequency. It is noted that it remains essentially constant along the entire length of the system. The radial and axial electric-field amplitudes are plotted as functions of radius in Fig. 4.8. The axial field is continuous at the plasma surface but the radial field is discontinuous because of the equivalent surface charge. This is consistent with the boundary conditions which were imposed at the beam-plasma edge. In Fig. 4.8 the falloff of fields outside the plasma is that which corresponds to the modified Bessel function K_0 in the case of the axial electric field and K_1 in the case of the radial electric field. The fields fall off relatively slowly because k_z is small.

Examination of the frequency response curves of radial and axial electric fields given in Fig. 4.4 reveals that the resonant frequencies lie just above the ion-plasma frequency and that the resonant frequencies are not harmonically related.

Since these resonant frequencies are half-wave, full-wave and three half-wave resonances, it is concluded that these frequencies can be predicted quite accurately for any set of parameters from a dispersion diagram of the type shown in Fig. 4.9 by finding the frequencies where

$$k_z L = n\pi \quad , \qquad n = 1,2,\ldots$$

or

$$L = \frac{n\lambda_z}{2}$$

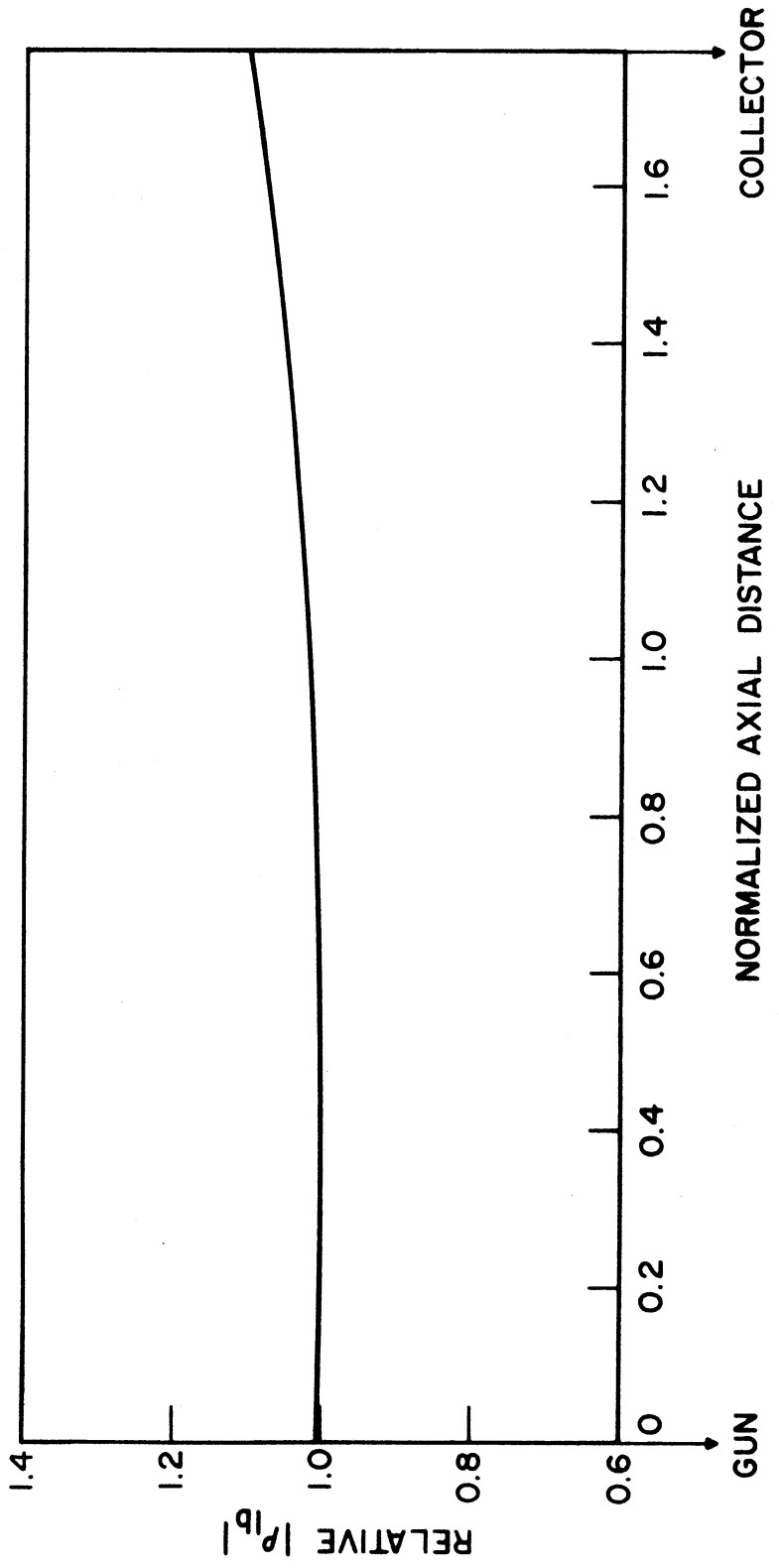

FIG. 4.7 TOTAL ac CHARGE DENSITY AS A FUNCTION OF AXIAL DISTANCE AT THE FIRST RESONANT FREQUENCY IN AN OPEN BEAM-PLASMA WAVEGUIDE. (THE PARAMETERS ARE GIVEN IN TABLE 4.1)

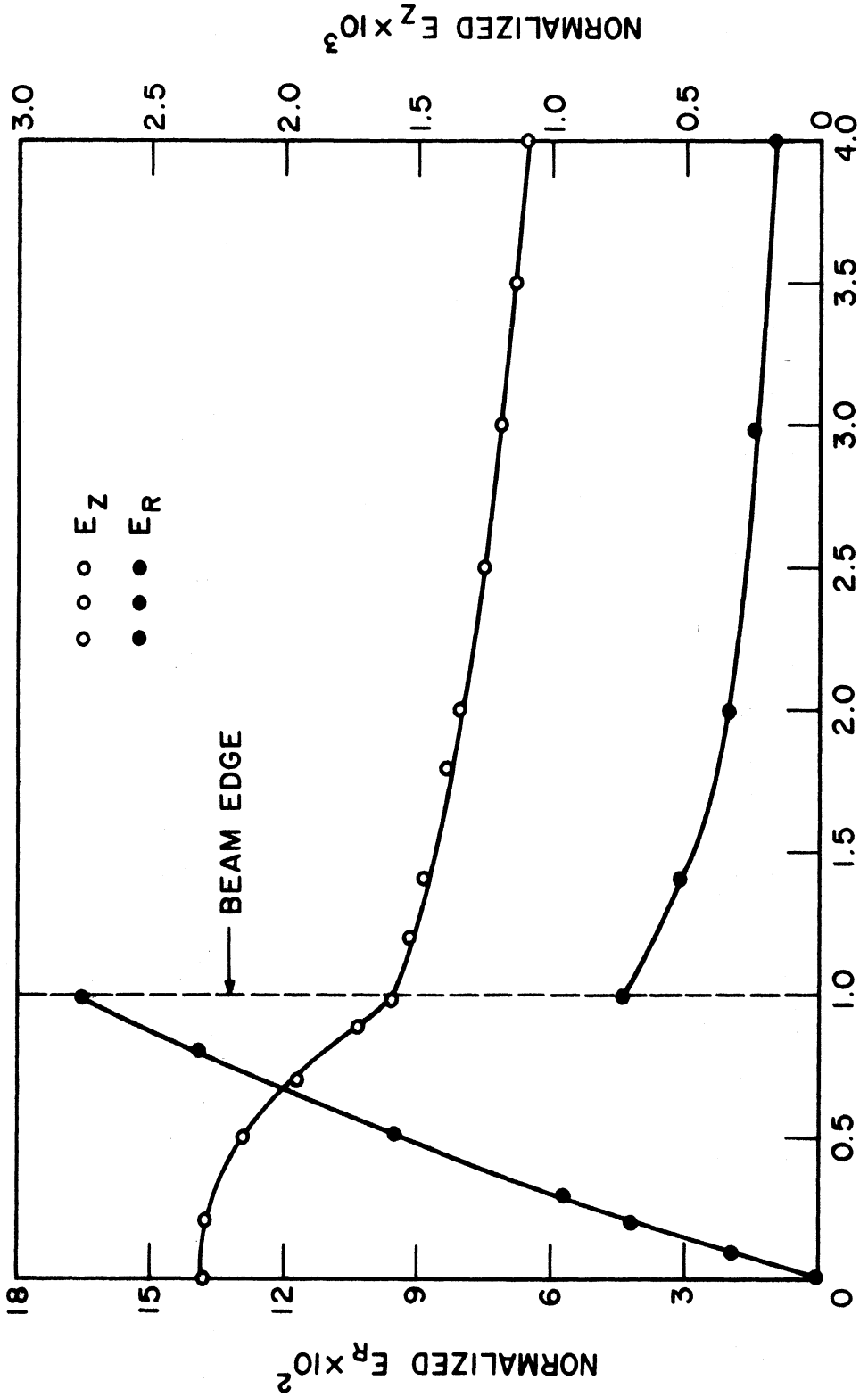

FIG. 4.8 RADIAL AND AXIAL ELECTRIC-FIELD COMPONENTS AS A FUNCTION OF RADIAL DISTANCE IN AN OPEN BEAM-PLASMA WAVEGUIDE. (THE PARAMETERS ARE GIVEN IN TABLE 4.1)

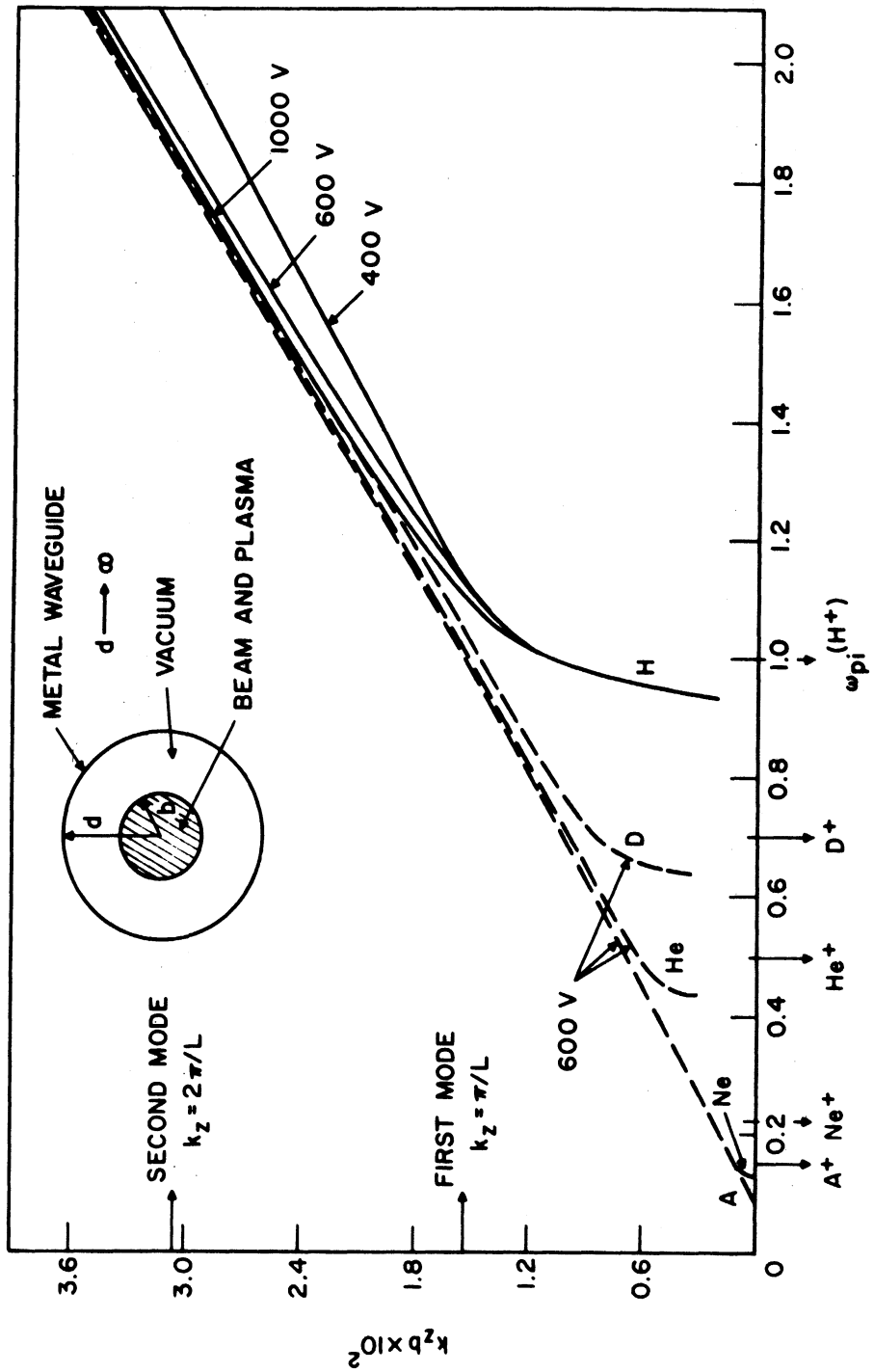

FIG. 4.9 DISPERSION DIAGRAM SHOWING THE POSITIVE PLASMA WAVE ROOT FOR THE OPEN BEAM-PLASMA

where the positive plasma wave root is used for k_z and L is the distance from the electron gun to the beam collector. Since these resonant frequencies are dependent on the length L of the beam-plasma system, they are called the "geometric" resonances.

The geometric resonant frequencies can be predicted conveniently by the preceding method and are found to lie very close to those obtained by the detailed normal-mode analysis. The effects of the variation of the plasma density, magnetic field, beam voltage and ion mass on the resonant frequencies can be easily predicted. In Fig. 4.9 the propagation constant k_z is normalized with respect to the plasma radius and the frequency is normalized with respect to the ion-plasma frequency of H^+. This normalization is used to emphasize the effect of ion mass and beam voltage on the dispersion curve. Figure 4.9 shows only the positive plasma wave root as a function of frequency for five different ion masses (corresponding to H^+, D^+, He^+, Ne^+ and Ar^+) and in the case of H^+ for three beam voltages.

The effect of ion mass can be predicted by finding the resonant frequencies from the intersections of the lines $k_z = \pi/L$ and $k_z = 2\pi/L$, etc., with the 600-V dispersion curves for argon and hydrogen. It is found that the resonant frequencies decrease with increasing ion mass but the amount of decrease is much less than the decrease in ω_{pi}. The decrease in resonant frequencies for Ne, He and D can similarly be predicted. By using the resonant frequencies for hydrogen as references, it can be clearly seen that the decrease in the first resonant frequency of Ar, Ne, He and D is more than the decrease in the second resonant frequency.

The effect of variation of beam voltage on the resonant frequencies can be similarly predicted from Fig. 4.9 using the curves for H^+. It is found that the resonant frequencies decrease as the beam voltage is increased. The decrease in the first resonant frequency is smaller than the decrease in the second resonant frequency. The effect of the variation of plasma density can be easily predicted since the frequency is normalized by ω_{pi} (H^+). For a given beam voltage, ion mass and plasma dimensions, the resonant frequencies increase as the square root of the plasma density.

The effect of the variation of the external dc magnetic field (or ω_{ce}/ω_{pe}) on the dispersion curve, such as that given in Fig. 4.9, is negligible in the low-density regime ($\omega_{ce}^2 \gg \omega_{pe}^2 \gg \omega_{ce}\omega_{ci}$). Thus it is found that the geometric resonant frequencies are rather independent of the dc magnetic field in the low-density range if the other parameters such as the plasma density, beam voltage, etc., are held constant.

In summary, the results of the normal-mode field calculations show that in the frequency range of interest there are three peaks or resonances in the electric field frequency response curves for an open beam-plasma waveguide configuration. These peaks are not harmonically related and are essentially independent of magnetic field in the low-density regime. The first and second resonances are shown to be half-wave and full-wave resonances, respectively. The resonant frequencies can be accurately predicted from a dispersion diagram by finding the frequencies at which $k_z L = n\pi$ where k_z is the plasma wave root. The resonant frequencies decrease slightly with increasing ion mass at constant plasma density but the decrease is much less than the decrease in ω_{pi}. The resonant frequencies also decrease with increasing beam voltage.

4.3.3 Computer Results for the Unfilled-Beam, Filled-Plasma Waveguide. Behavior similar to that given in the preceding section for the open beam-plasma waveguide is obtained for an unfilled-beam, filled-plasma waveguide. The latter configuration is achieved experimentally when an electron beam streams through a relatively large-diameter plasma which is generated by a separate plasma source (such as the PIG discharge) and which can be modeled as completely filling the waveguide. Although such a model does not fit the experiment performed in the present investigation, calculations on this model were carried out for parameters which might be obtained in a typical PIG or ECR discharge. The following results are for a proposed experiment for such a configuration. The plot of the radial electric-field amplitude as a function of frequency is shown in Fig. 4.10. Three peaks are observed in the frequency range of investigation. At these peak frequencies the real part of the radial electric field is plotted as a function of the axial distance as shown in Fig. 4.11. Again, the three resonances are half-wave, full-wave and three half-wave resonances. In the present case, however, the probe position was chosen such that it does not coincide with a node in Fig. 4.11. Therefore the third peak is as strong as the other two peaks. Again, it is easy to determine the effects of the variation of ion mass, beam voltage, etc., on the resonant frequencies as was done in the open beam-plasma waveguide. The parameters for this "computer experiment" are given in the figures.

4.3.4 Normal-Mode Field Calculations near the Lower-Hybrid Resonance. In Section 2.2 an analysis was given which showed that a source (such as an electron beam) at the axis of a cylindrical plasma column in a waveguide excites large radial electric fields at the

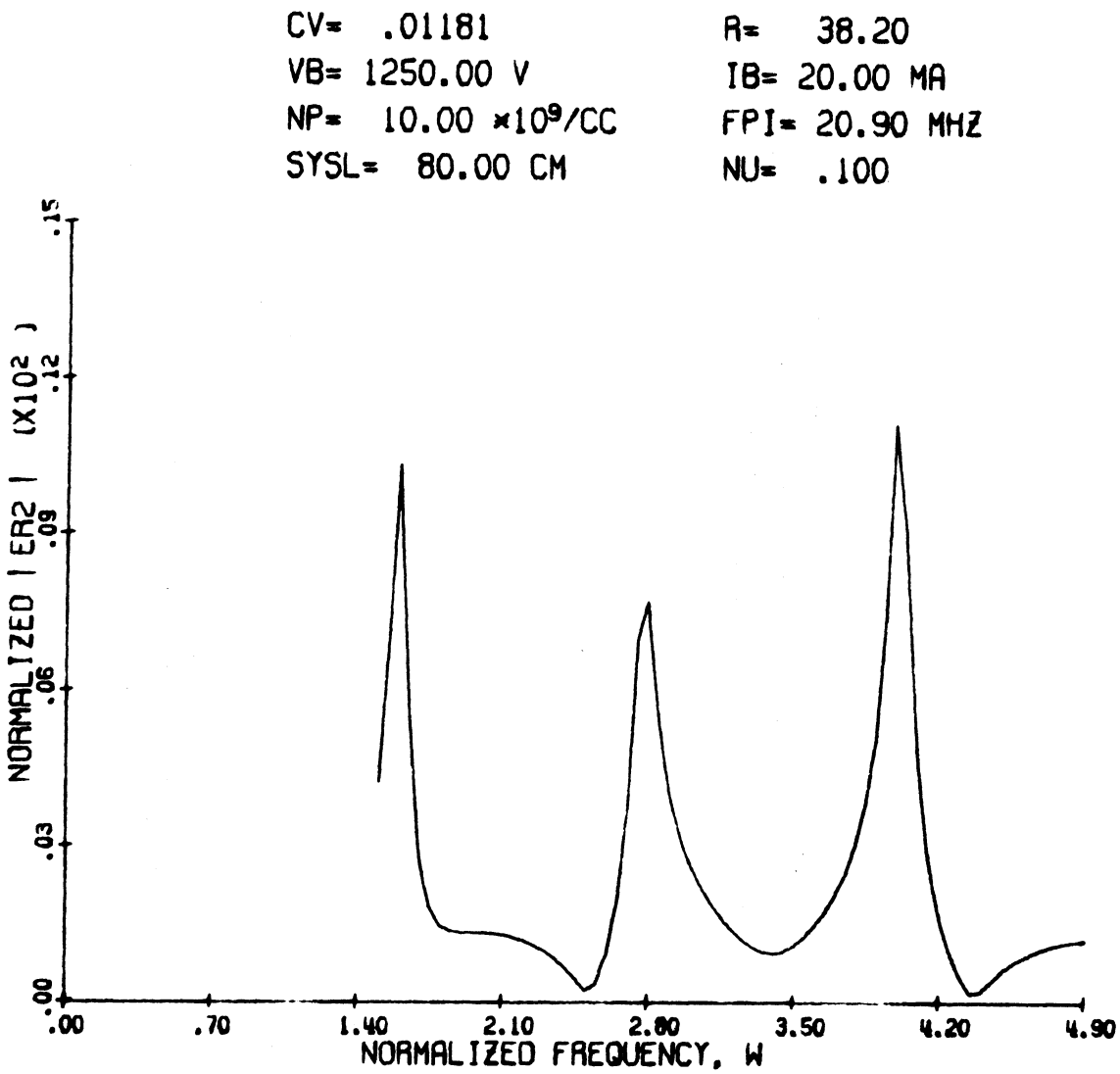

FIG. 4.10 RADIAL ELECTRIC-FIELD AMPLITUDE OUTSIDE THE BEAM AS A FUNCTION OF FREQUENCY FOR AN UNFILLED-BEAM, FILLED-PLASMA WAVEGUIDE. [ω_{ce}/ω_{pe} = 2.5, CV2 = $a/(v_o/f_{pi})$ = 0.125, H^+]

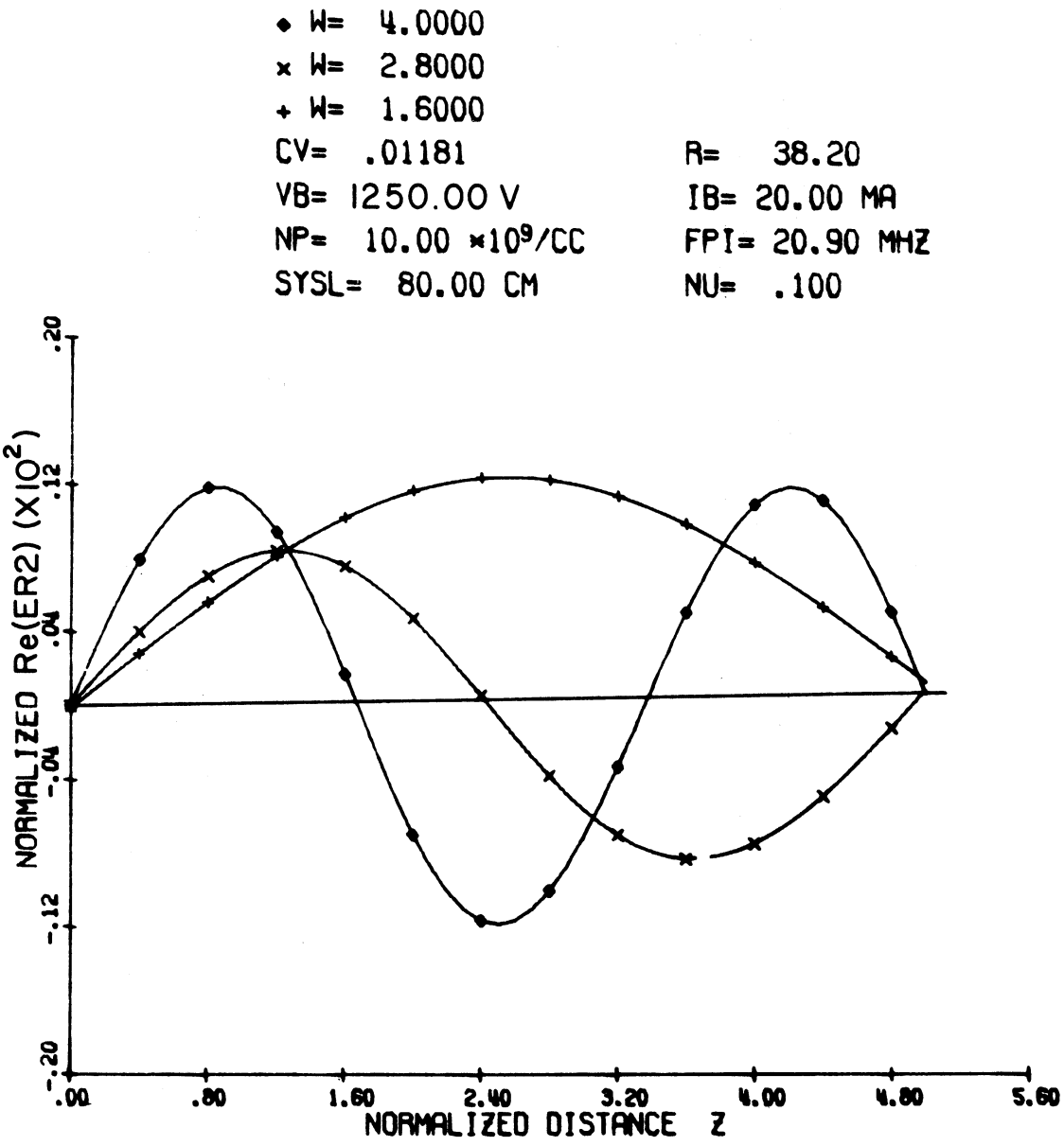

FIG. 4.11 REAL PART OF THE RADIAL ELECTRIC FIELD AS A FUNCTION OF DISTANCE AT THE FIRST THREE RESONANT FREQUENCIES FOR AN UNFILLED-BEAM, FILLED-PLASMA WAVEGUIDE. (ω_{ce}/ω_{pe} = 2.5, CV2 = 0.125, H^+)

lower-hybrid resonant frequency for perpendicular propagation. The present normal-mode field calculations were extended down to a frequency range such that it includes the lower-hybrid resonant frequency.

Figure 4.12 shows the radial electric-field amplitude as a function of frequency for an open beam-plasma waveguide. The frequency range of investigation is around the lower-hybrid resonant frequency. The parameters are the same as those given in Table 4.1. It is found that there is a peak in the radial electric field at the lower-hybrid frequency. It is called the "body" resonance. However, it is somewhat smaller in magnitude in comparison to the first geometric resonance.

The frequency region around the lower-hybrid frequency was also investigated for the proposed experiment studied in Section 4.3.3. Recall that in this model the waveguide is completely filled by plasma and partially filled by beam. The parameters are slightly different in comparison to those given in Section 4.3.3 but are given in Fig. 4.13. A peak in the radial electric-field amplitude is found at the lower-hybrid frequency as shown in Fig. 4.13. The plot of the real part of the radial electric field as a function of axial distance as shown in Fig. 4.14 indicates that this resonance is not a half-wave resonance and is thus fundamentally different from the geometric resonances. The radial electric-field amplitude as a function of radius is plotted in Fig. 4.15 at several frequencies near the lower-hybrid frequency. It can be seen in this figure that the radial electric-field amplitude at the lower-hybrid frequency has its maximum value at a position in the plasma which is several beam diameters away from the beam edge. Thus an appreciable field penetrates into the plasma away from the beam at the lower-hybrid frequency.

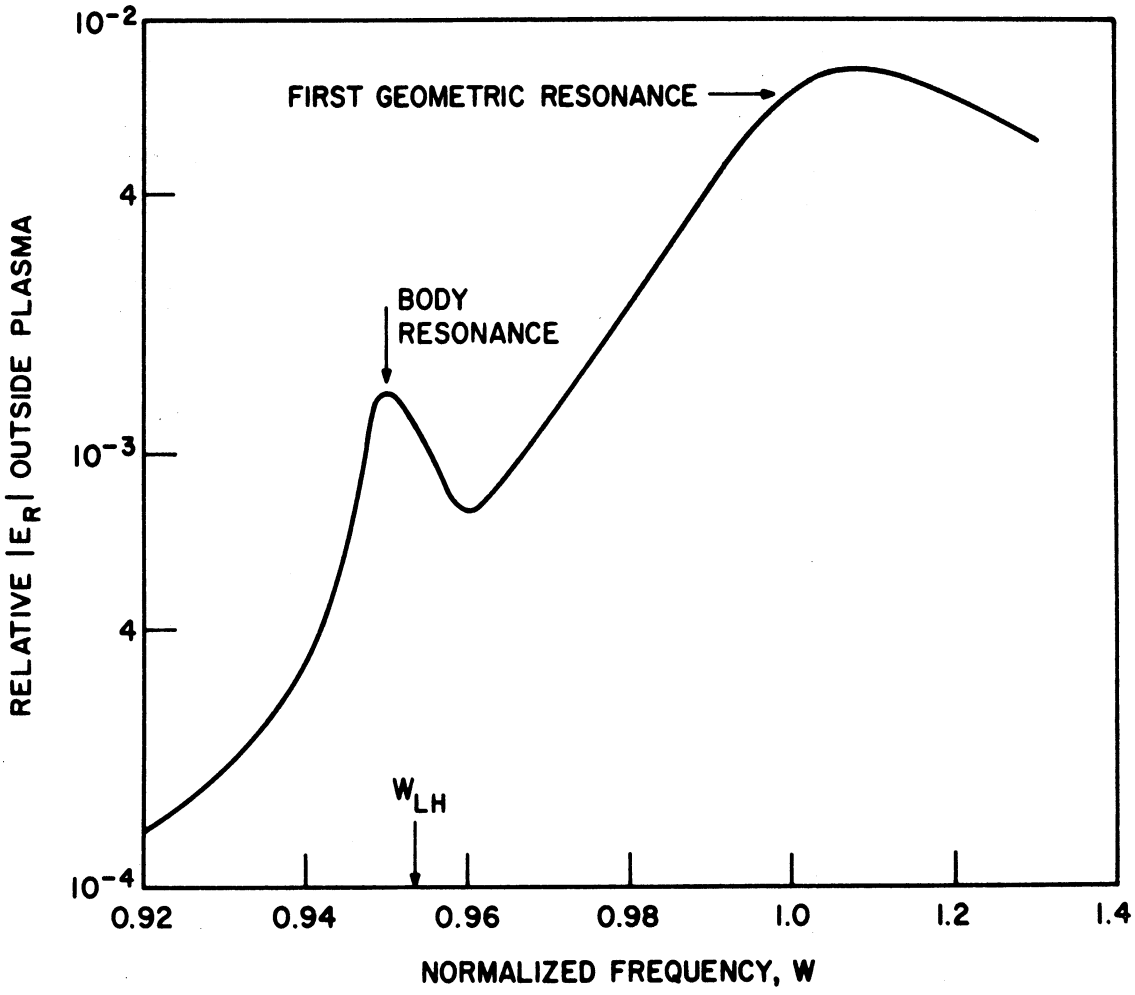

FIG. 4.12 RADIAL ELECTRIC-FIELD AMPLITUDE AS A FUNCTION OF FREQUENCY SHOWING BODY AND GEOMETRIC RESONANCES IN THE CASE OF THE OPEN BEAM-PLASMA WAVEGUIDE. (THE PARAMETERS ARE GIVEN IN TABLE 4.1)

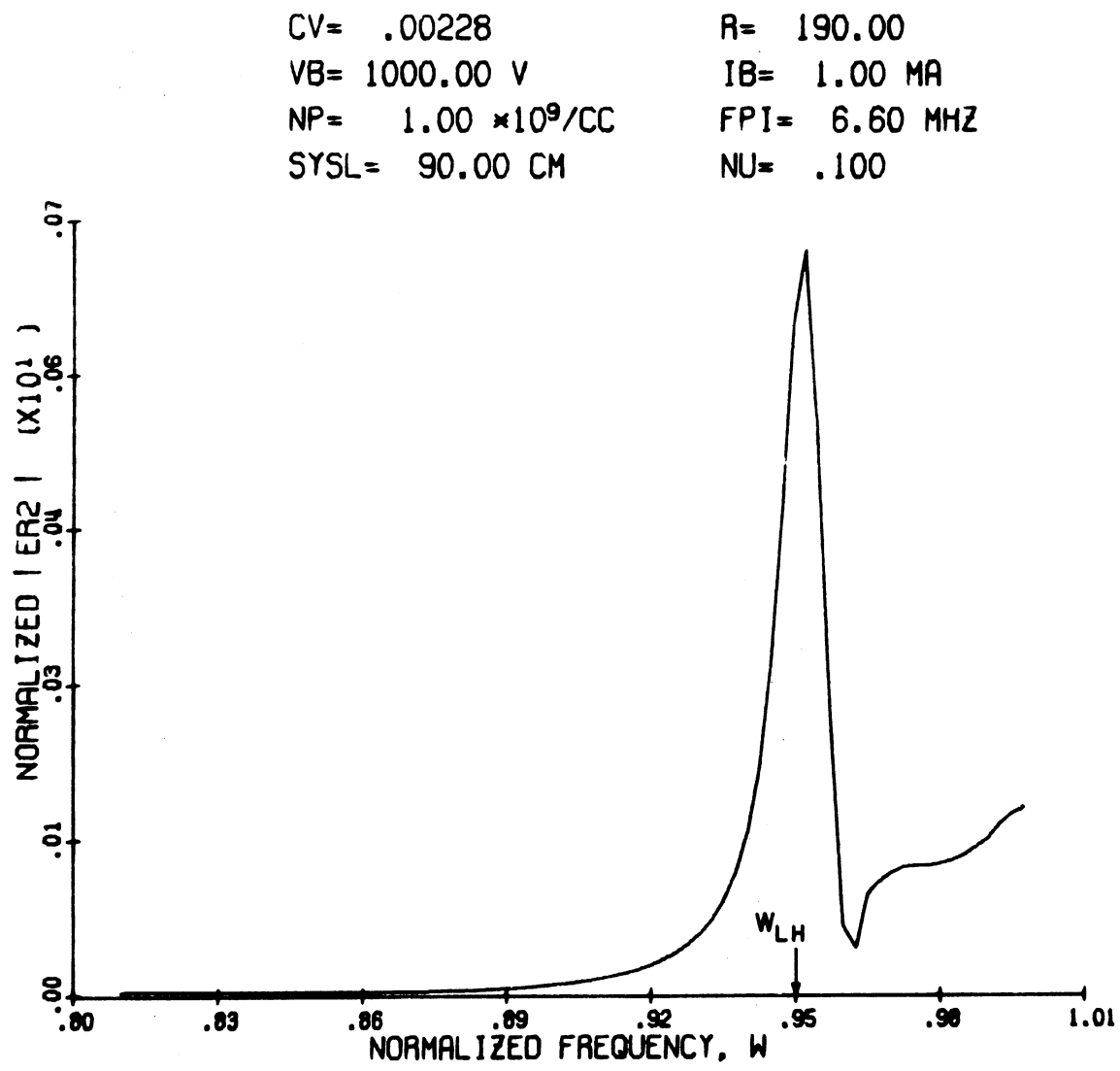

FIG. 4.13 RADIAL ELECTRIC-FIELD AMPLITUDE OUTSIDE THE PLASMA AS A FUNCTION OF FREQUENCY AROUND THE LOWER-HYBRID FREQUENCY IN THE CASE OF AN UNFILLED-BEAM, FILLED-PLASMA WAVEGUIDE. (ω_{ce}/ω_{pe} = 3, CV2 = 0.0111, H^+)

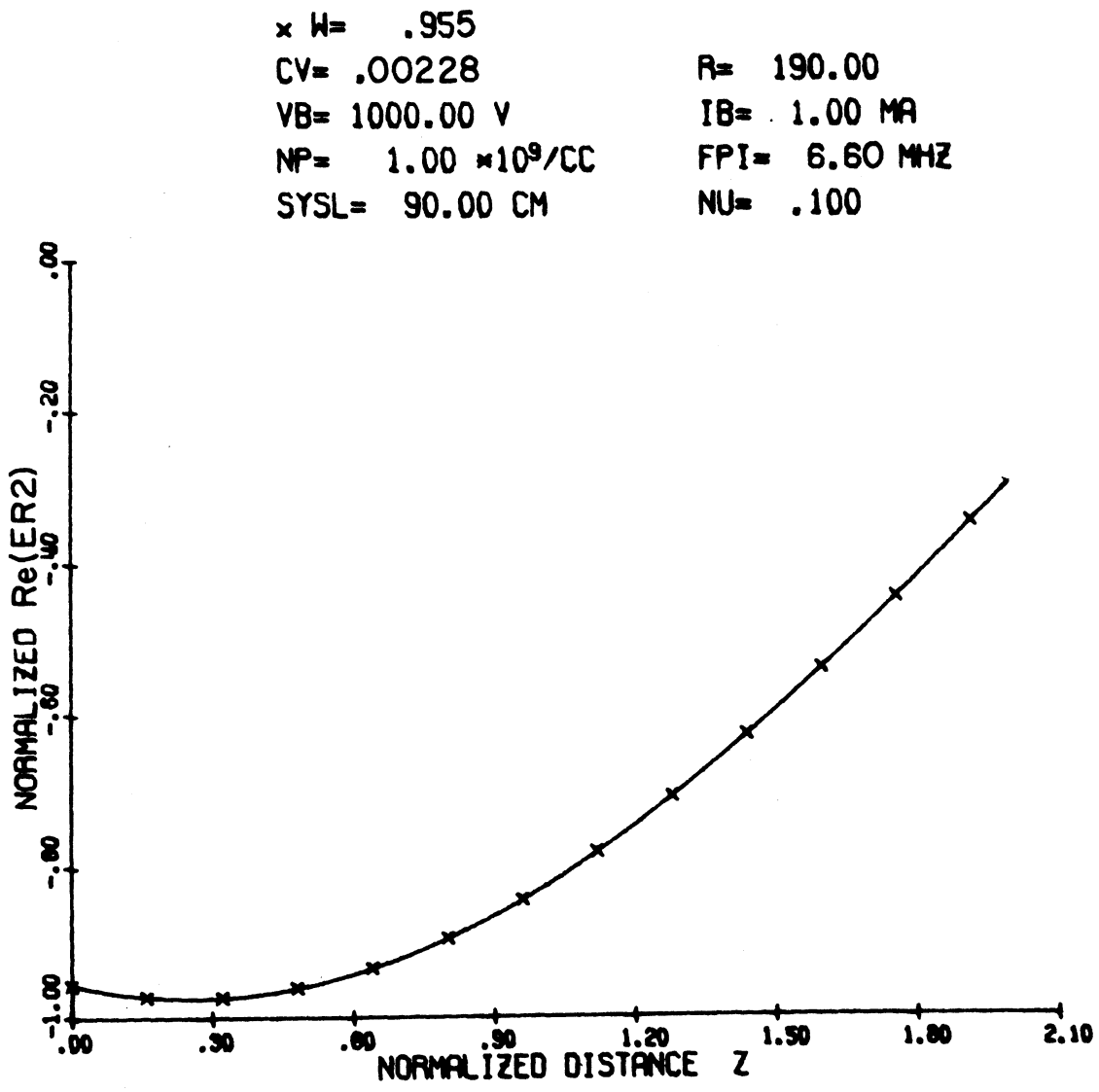

FIG. 4.14 REAL PART OF THE RADIAL ELECTRIC FIELD OUTSIDE THE PLASMA AS A FUNCTION OF AXIAL DISTANCE AT THE PEAK FREQUENCY IN THE CASE OF AN UNFILLED-BEAM, FILLED-PLASMA WAVEGUIDE. (ω_{ce}/ω_{pe} = 3, CV2 = 0.0111, H^+)

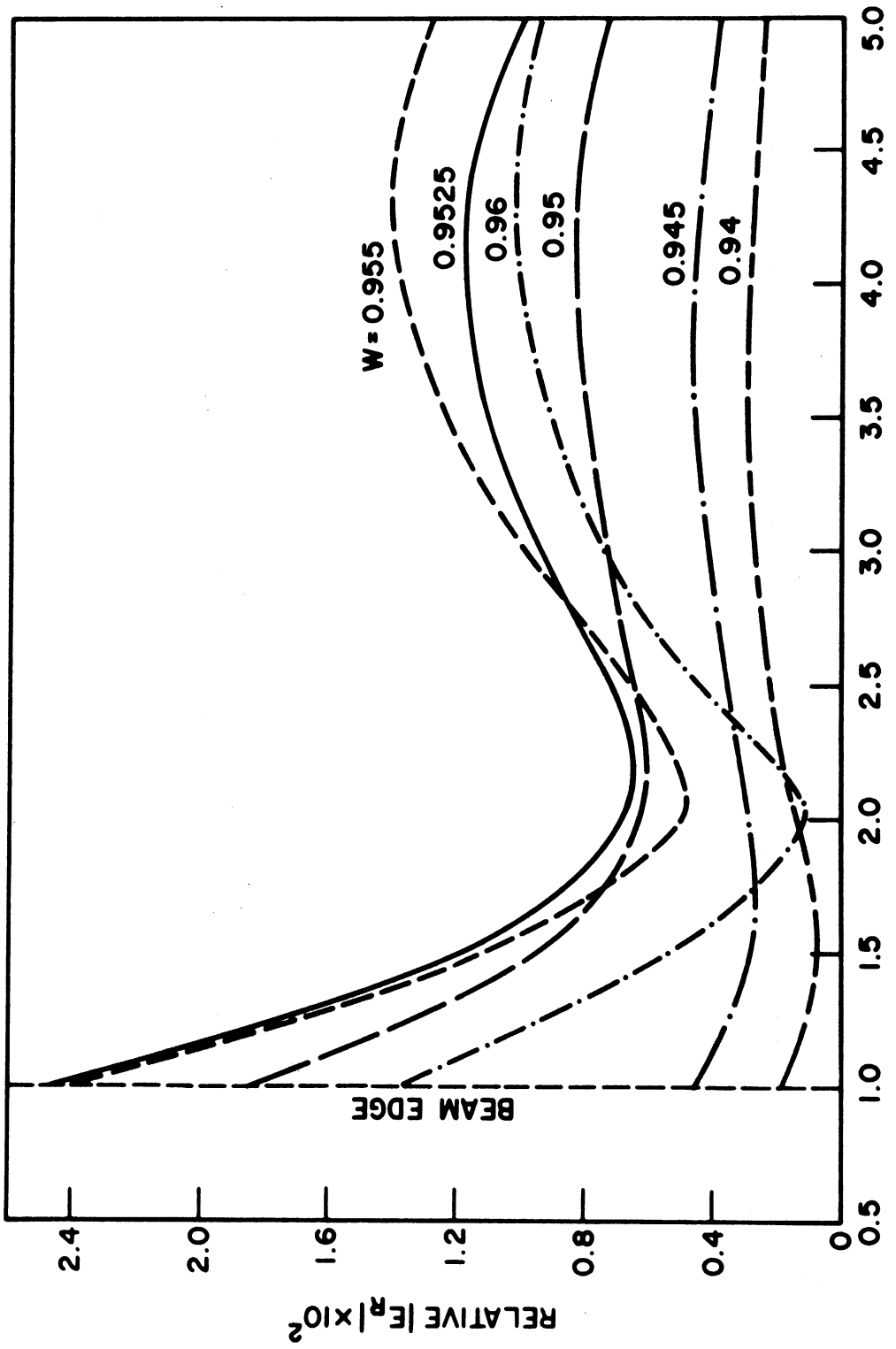

FIG. 4.15 RADIAL ELECTRIC FIELD AS A FUNCTION OF RADIAL DISTANCE AROUND THE LOWER-HYBRID FREQUENCY IN THE CASE OF AN UNFILLED-BEAM, FILLED-PLASMA WAVEGUIDE. (ω_{ce}/ω_{pe} = 3, CV2 = 0.0111, H^+)

The same calculation was performed for the beam-plasma filled waveguide (a = b = d); Fig. 4.16 shows the behavior of the radial electric field as a function of frequency around the lower-hybrid frequency. Again, there is a peak in the radial field at the lower-hybrid frequency. The second peak at higher frequency is due to the first geometric resonance.

All the curves given in the preceding figures were for a low-density regime ($\omega_{ce}^2 \gg \omega_{pe}^2 \gg \omega_{ce}\omega_{ci}$). A curve for the high-density regime ($\omega_{pe}^2 \gg \omega_{ce}^2$) is shown in Fig. 4.17 in which the radial electric-field amplitude is plotted as a function of frequency near the lower-hybrid frequency. The configuration studied is the beam-plasma filled waveguide. In the high-density regime the lower-hybrid resonance is near the geometric mean frequency. There is a peak in the radial field at the lower-hybrid frequency.

It is found that there is a peak in the radial electric field frequency response curves at the lower-hybrid frequency for all three configurations. The axial variation of the field shows that this body resonance is not a half-wave or a full-wave resonance and is therefore fundamentally different from geometric resonances.

The use of the quasi-static assumption is open to question in the immediate frequency range near the lower-hybrid frequency. The quasi-static assumption is used in the analysis presented here. At or very close to the lower-hybrid frequency, k_z tends toward zero and the phase velocity may not be negligible in comparison to the velocity of light. The quasi-static assumption may not be valid at the lower-hybrid frequency and therefore an electromagnetic analysis should be carried out near this resonant frequency.

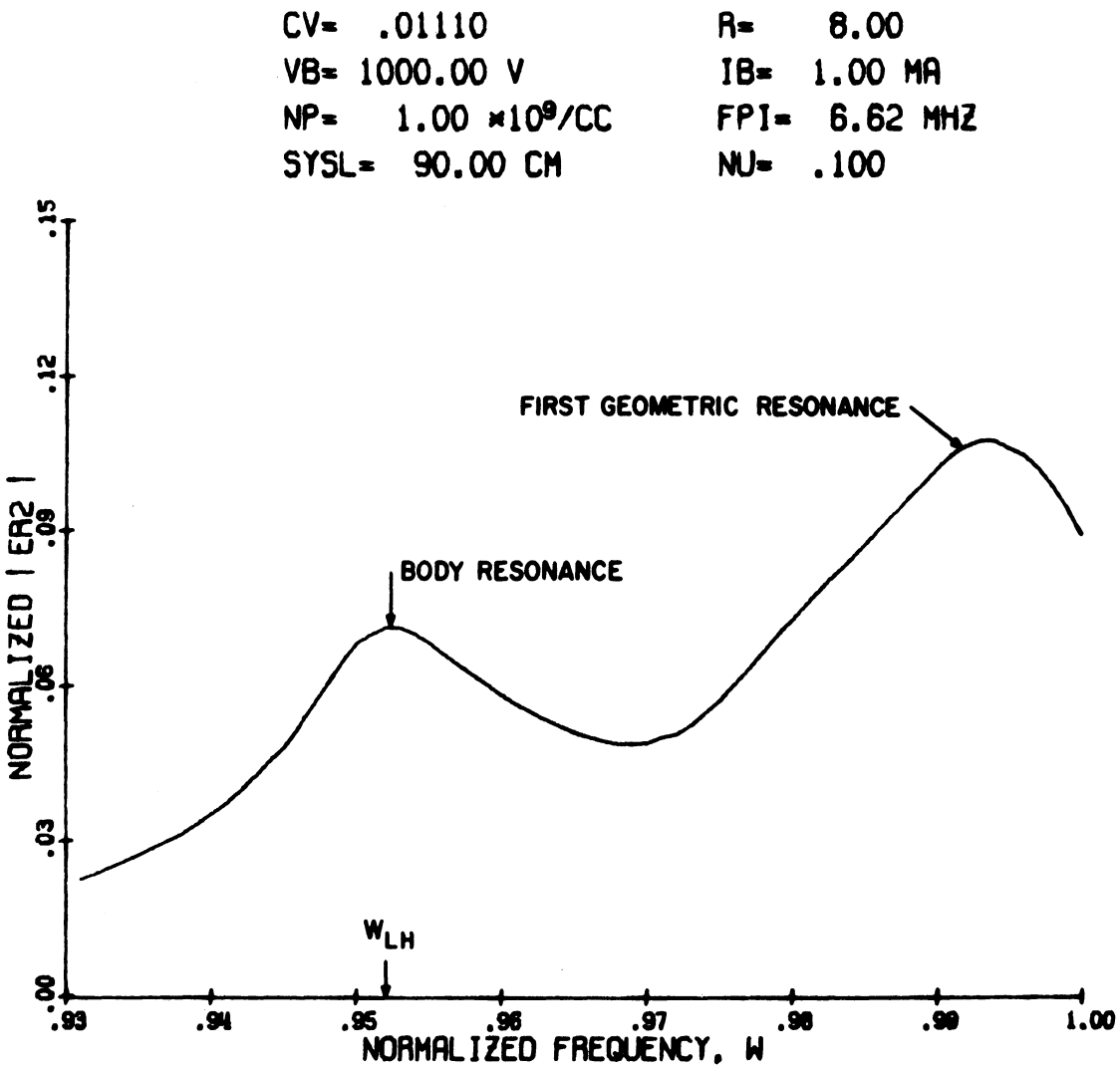

FIG. 4.16 RADIAL ELECTRIC-FIELD AMPLITUDE AS A FUNCTION OF FREQUENCY SHOWING BODY AND GEOMETRIC RESONANCES IN THE CASE OF A BEAM-PLASMA FILLED WAVEGUIDE. (ω_{ce}/ω_{pe} = 3, H^+)

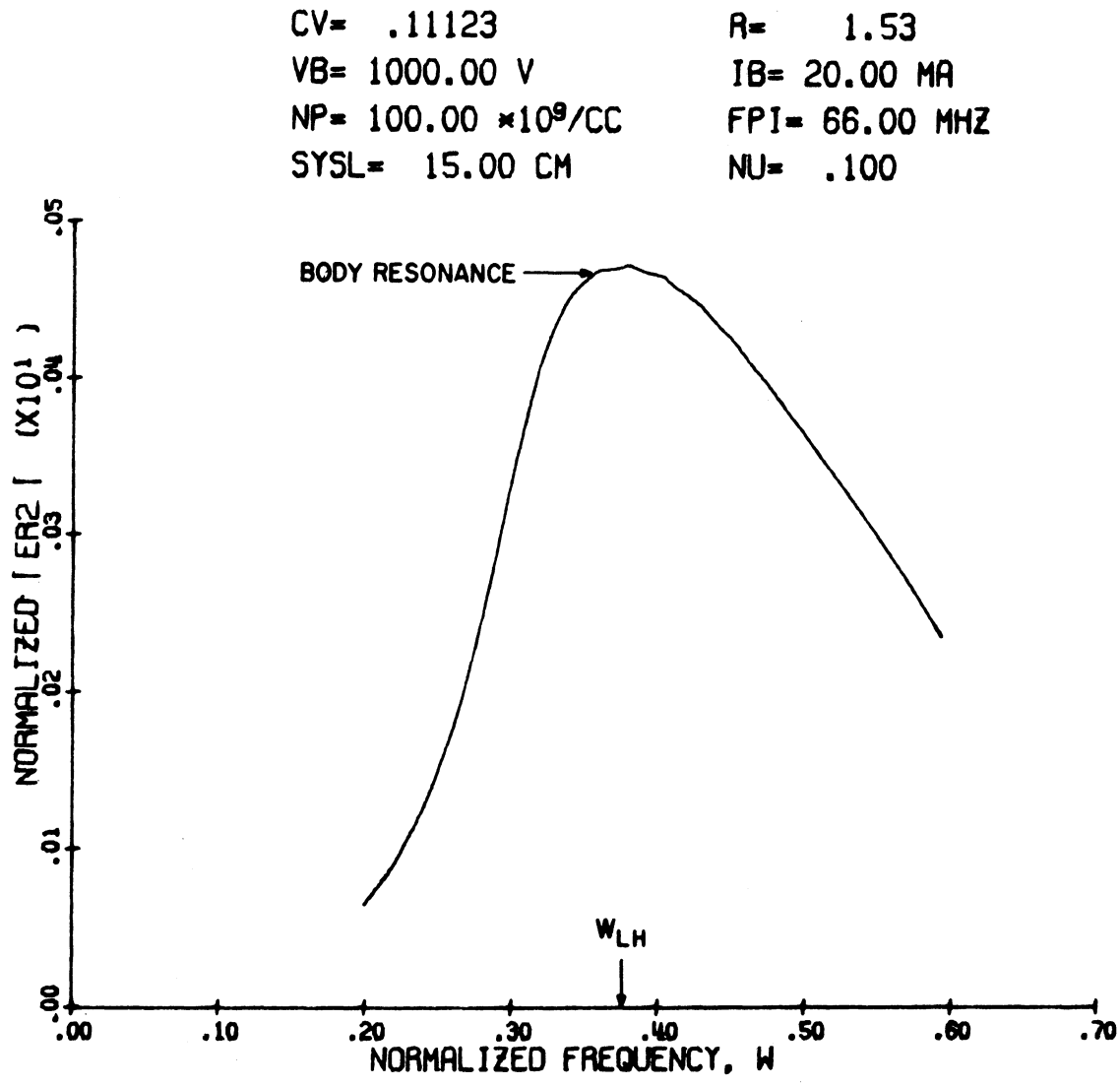

FIG. 4.17 RADIAL ELECTRIC-FIELD AMPLITUDE AS A FUNCTION OF FREQUENCY AROUND THE LOWER-HYBRID FREQUENCY IN THE HIGH-DENSITY CASE FOR A BEAM-PLASMA FILLED WAVEGUIDE. (ω_{ce}/ω_{pe} = 1/3, H^+)

The theoretical results obtained in Section 4.3 are compared in Chapter V to those obtained experimentally for the open beam-plasma waveguide configuration.

4.4 Negative Conductance Analysis and Energy Transfer

The field analysis does not give much insight into the energy transfer mechanism by which ions in the plasma are heated by the electron beam. Another viewpoint based on the beam loading admittance of the cavity and developed by Bartsch[75] is discussed in this section.

The finite-length beam-plasma system analyzed in the preceding section can be described alternatively as a system in which a modulated electron beam streams through a low-frequency plasma cavity which is axially bounded by the electron gun and the collector. The problem can be described as that of the interaction of a modulated electron beam with the standing slow-wave field of the plasma cavity. The general relation between the small-signal beam current and an externally applied standing-wave electric field has been determined by Wesselberg[76] for arbitrary transit angles. The small-signal beam admittance* is determined from the complex power-flow expression. They found that for certain ranges of parameters the beam conductance is negative. The existence of the negative beam conductance indicates that there is a real power flow from the electron beam to the standing-wave field. Such results have been used and extended by Bartsch,[75] who plotted his results in the form of energy-loss contours in a standing-wave field. He found that there are frequencies of maximum energy loss for $k_z L = \pi, 2\pi \ldots$, etc.

---

* The beam admittance y_e is defined by[75] $P = (1/2) y_e |E|^2$, where P is the complex power flow.

On the basis of Bartsch's analysis, it can be said that a modulated electron beam traversing through a plasma cavity excites the plasma-cavity modes by losing energy to the initially small cavity fields. At the cavity resonances a large radial electric field is created in the plasma which excites ion oscillations. The generation of this large RF field at low frequencies results in ion heating through collisions.

CHAPTER V. COMPARISON OF EXPERIMENTAL AND THEORETICAL RESULTS OF LOW-FREQUENCY BEAM-PLASMA INTERACTIONS IN A FINITE-SIZED PLASMA

5.1 Comparison of Experimental and Theoretical Results

In this section the experimental results described in Section 3.4 for a finite-length open beam-plasma waveguide are compared with the predictions based on the normal-mode analysis for such a system given in Section 4.3. Experimental and theoretical RF electric field frequency response curves, the location of the resonant or peak frequencies and the variation of RF radial electric field as a function of radial and axial distance are compared. Also, the effect of the variation of plasma density, ion mass, beam voltage and magnetic field on the resonant frequencies are compared. The theoretical and experimental results are found to be in good agreement.

5.1.1 Comparison of the RF Radial Electric Field as a Function of Frequency and Position. A set of experimentally obtained RF radial electric field frequency response curves have been given in Section 3.4.1 for hydrogen, deuterium, neon and argon plasmas. Examination of these curves reveals that they are essentially of the same general form except that the resonant frequencies are different due to different beam and plasma parameters. In this section the frequency response curve which was obtained experimentally for a hydrogen plasma is compared with that calculated theoretically. Experimentally obtained radial and axial variations of the radial RF electric field are also compared in this section with those calculated theoretically.

The relative amplitude of the radial RF electric field outside the plasma (Region II) is plotted as a function of unnormalized frequency in Fig. 5.1. The frequency response of the probe which was experimentally determined with the help of the modulated electron beam in high vacuum is also shown in Fig. 5.1. It is found to be relatively flat over the frequency range of investigation. A beam-generated plasma is produced when hydrogen gas is introduced into the system. A typical probe response curve outside the plasma is shown by the line drawn through the solid circles in Fig. 5.1. The beam and plasma parameters are given in the title of the figure. Two or three peaks or resonances are typically observed in the probe response at frequencies which are, in general, not harmonically related. In the present case, the resonances are at 7.0, 12.5 and 19.5 MHz.

A radial RF electric field frequency response curve calculated theoretically from the normal-mode field analysis is also drawn in Fig. 5.1 as shown by the continuous lines. The chosen axial observation position coincides with that used for the Langmuir probe in the experiment. The parameters chosen for theoretical calculation are the same as those of the experiment. Resonances in the theoretical curve are found at the frequencies 7.0, 12.5 and 17.5 MHz in Fig. 5.1. The theoretical variation of radial field strength with frequency in Fig. 5.1 shows sharper resonances than the experimental curves. Electron-neutral collisions are dominant in the experiment and realistic values of collision frequency give $\nu_{eN}/\omega_{pi} \cong 0.25$. Curves for $\nu_{eN}/\omega_{pi} = 0.1$, 0.25 and 0.5 are shown in Fig. 5.1 at the second resonance only. The experimental curve in Fig. 5.1 has a broader resonance probably because of the nonhomogeneous plasma density profile. In the theoretical

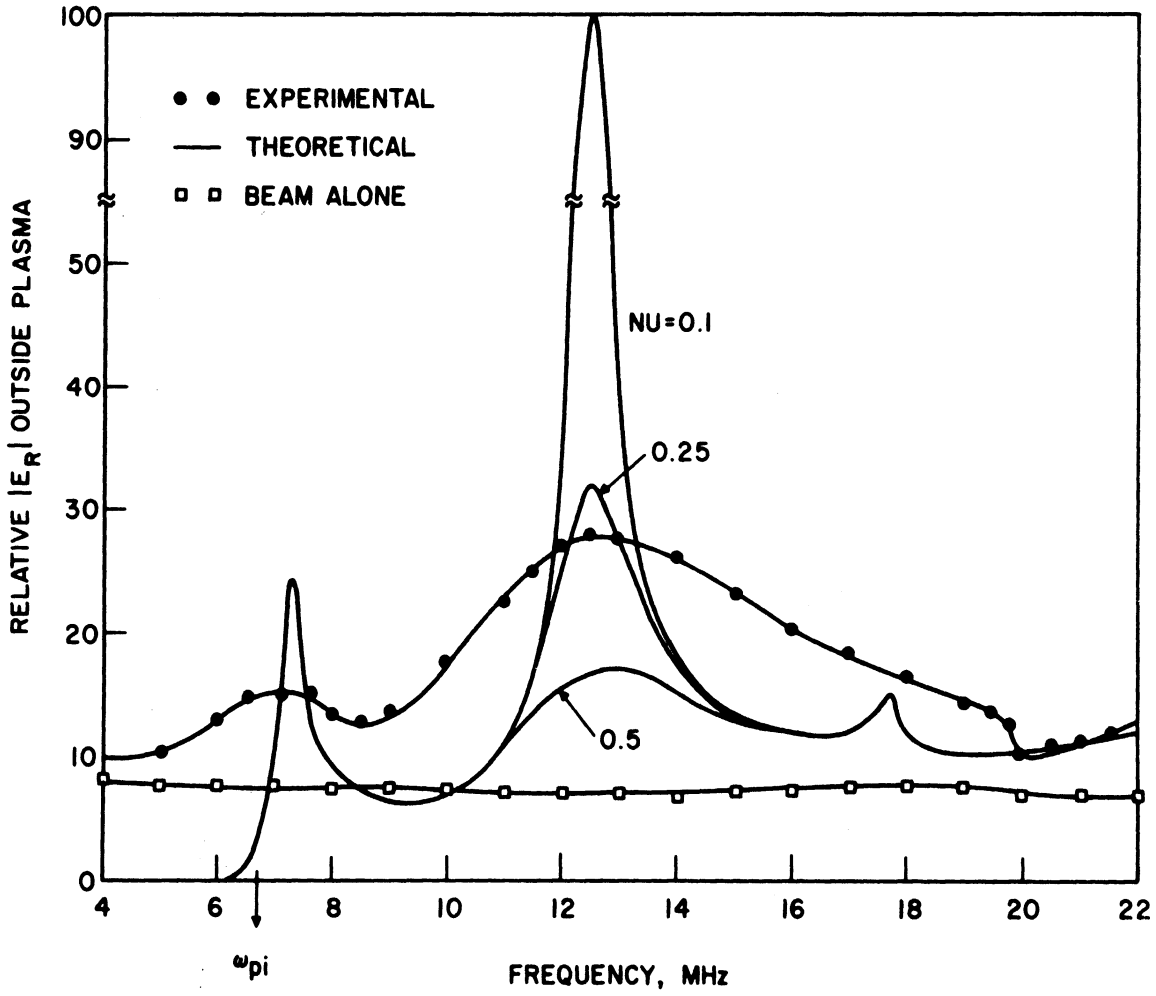

FIG. 5.1 RADIAL ELECTRIC-FIELD AMPLITUDE AT r = 2b AND z = 0.66 L AS A FUNCTION OF FREQUENCY. [V = 600 V, I_b = 2.5 mA, B_o = 310 G, n_p = 1 x $10^9/cm^3$, L = 61 cm, b = 3 mm, NU = ν/ω_{pi} (H^+), HYDROGEN GAS]

calculation, a sharp boundary at the plasma edge was assumed which also may result in sharper resonances. The unnormalized field strengths at the first two resonances for the case of $\nu_{eN}/\omega_{pi} = 0.25$ in Fig. 5.1 are 35 V/cm and 48 V/cm, respectively. Measurements in other experiments have indicated that the electric-field strength is of the same order of magnitude.[106]

A simple calculation is made to deduce the radial RF electric-field strength outside the plasma from the RF Langmuir probe measurements. It is based on the fact that an oscillatory charge is induced on the probe surface in the presence of the RF field. Since the probe is grounded through a 50-Ω resistor, an ac current flows through the resistor and develops an ac voltage across it. This voltage is then detected by a VTVM after passing through an amplifier and an integrator. The calculation of the field strength from such measurements is given in Appendix F. It is found that an electric-field strength of the order of 10 to 20 V/cm is detected by the probe, and this value compares favorably with that predicted from the normal-mode field calculations.

The first two resonances have the axial distribution shown in Fig. 5.2 and are therefore relatively large at the axial position chosen in Fig. 5.1. The third resonance has an antinode in the radial electric-field pattern near the observation position and therefore appears only as a small peak near 17.5 MHz. This point has been discussed in Section 4.3.2 in regard to Fig. 4.4. If the observation point is moved away from the antinode position, a large peak occurs in Fig. 5.1 at 17.5 MHz. This was illustrated theoretically for the case of an unfilled-beam, filled-plasma waveguide configuration and was discussed in connection with Figs. 4.10 and 4.11.

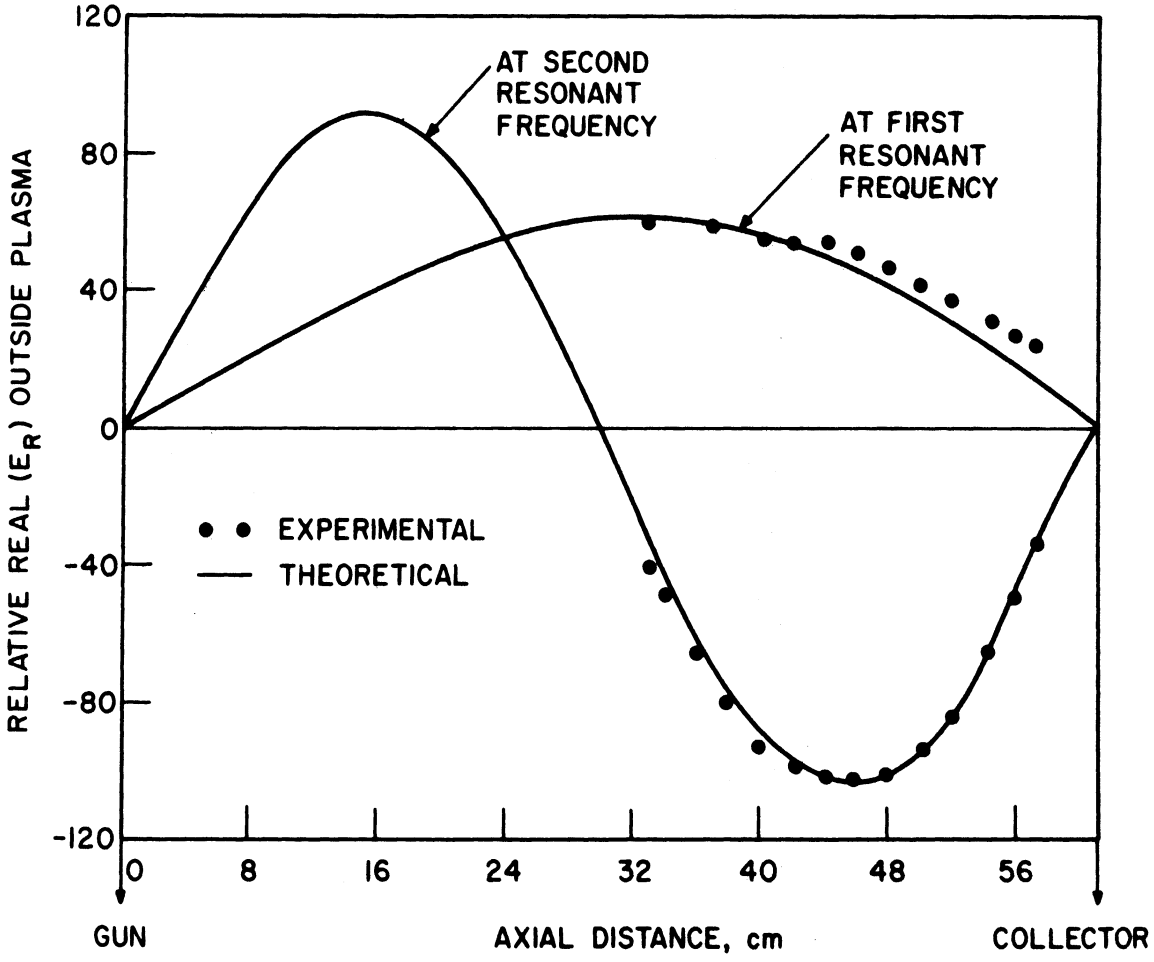

FIG. 5.2 REAL PART OF THE RADIAL ELECTRIC FIELD AT r = 2b AS A FUNCTION OF AXIAL DISTANCE. (V = 600 V, I_b = 2.5 mA, B_o = 310 G, n_p = 1 x $10^9/cm^3$, L = 61 cm, b = 3 mm, NU = 0.1, HYDROGEN GAS)

The quantity $Re(E_R)$ plotted in Fig. 5.2 would be the output of a phase-sensitive detector and is in good agreement with the field strength measured by such means (Section 3.1.7c). The resonances occur when the length of the system is an integral number of half-wavelengths.

The theoretical variation of the radial field strength as a function of radius is shown in Fig. 4.8 and the experimental curve is shown in Fig. 3.26. The theoretically calculated and experimentally obtained radial variation of the field strength outside the plasma is of the same general shape, i.e., a decay of the fields corresponding to that of the modified Bessel function K_1 and K_0.

5.1.2 Comparison of the Resonant Frequencies as a Function of Plasma Density and Ion Mass. Two or three peaks or resonances were generally found in the RF field response curves in the frequency range of investigation and the resonant frequencies were found to lie just above the ion-plasma frequency. The effect of variation of plasma density and ion mass on the resonant frequencies is presented in this section and comparison is made between theoretical prediction and experimental observation.

Figure 3.18 shows the RF field frequency response curves for a hydrogen plasma in which the parameter for the three curves is plasma density. By examination of this figure it is found that the resonant frequencies increase with increasing plasma density. Similar curves are given for neon, deuterium and argon in Figs. 3.20, 3.21 and 3.22, respectively. The first and second peak frequencies obtained from these curves are plotted as a function of plasma density on a log-log graph for hydrogen, deuterium, neon and argon plasmas in Fig. 5.3. As discussed

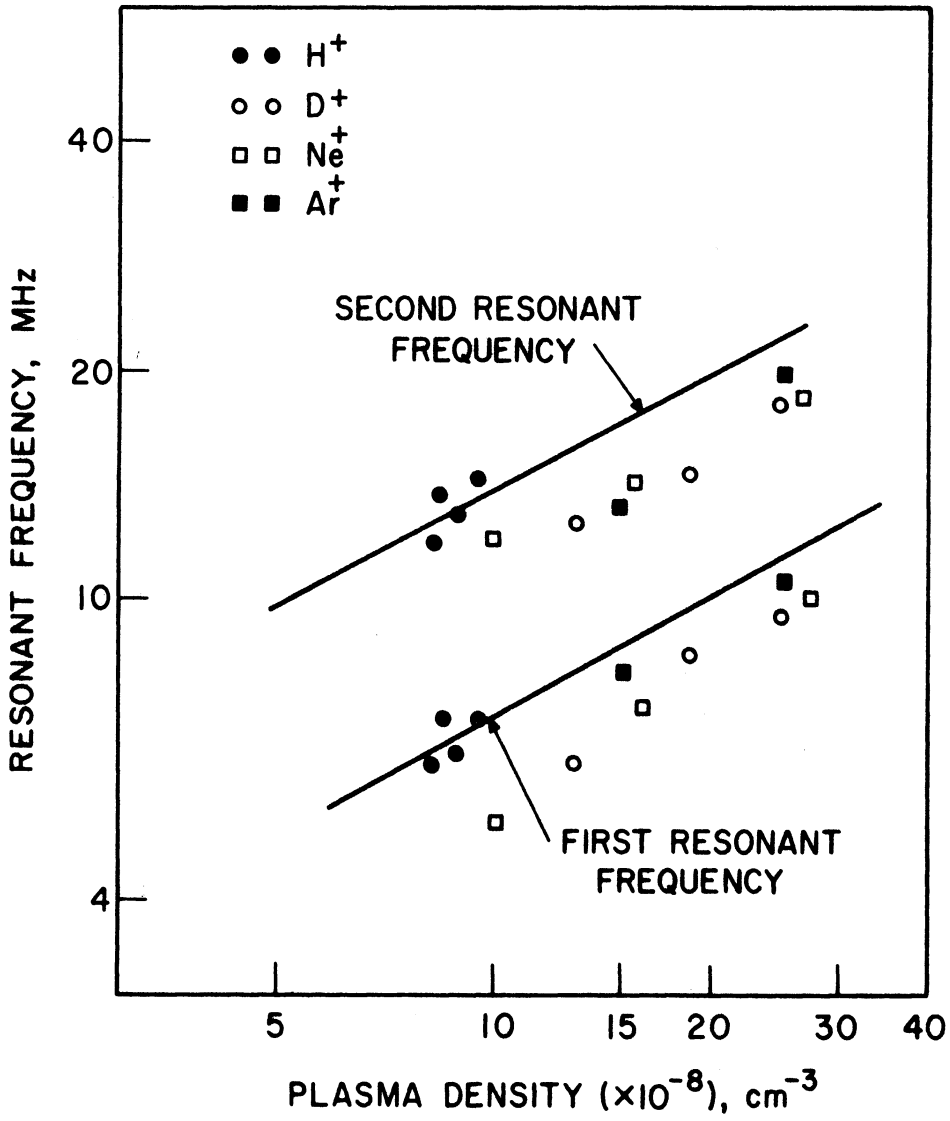

FIG. 5.3 VARIATION OF RESONANT FREQUENCIES AS A FUNCTION OF PLASMA DENSITY FOR HYDROGEN, DEUTERIUM, NEON AND ARGON.

in Section 4.3.2, theoretical calculations predict that the resonant frequencies should increase as the square root of the plasma density. A straight line with a slope of one-half is drawn in Fig. 5.3 through the points corresponding to the hydrogen plasma. Similar lines can be drawn through the points of other gases. There is some scatter in the data but they confirm the theoretical prediction that the resonant frequencies increase as the square root of the plasma density.

The effect of the variation of ion mass on the resonant frequencies was theoretically predicted in Section 4.3.2. It was found that the resonant frequencies decrease with increasing ion mass but the decrease is much less than the decrease in the ion-plasma frequency. Such behavior is evident from the resonant frequency data plotted in Fig. 5.3. The theoretical analysis in the case of argon and neon predicts that the first resonant frequency should decrease by a factor of 1.13 and the second by a factor of 1.04 compared to the resonant frequencies for a hydrogen plasma with the same density. The experimental data show a decrease of the same order, however, these factors are in the range of experimental error which occurs in the determination of plasma density.

5.1.3 Comparison of the Resonant Frequencies as a Function of Beam Voltage and Magnetic Field. The experimentally observed RF electric field frequency response curves in which the parameter for different curves is the beam voltage were presented in Section 3.4.1. Curves for hydrogen, neon and argon plasmas are given in Figs. 3.19, 3.23 and 3.24, respectively. Examination of these curves reveals that they are essentially of the same form for these three gases. The first and second resonant frequencies in the case of hydrogen plasma are plotted as a function of beam voltage in Fig. 5.4. The two curves show that the resonant frequencies

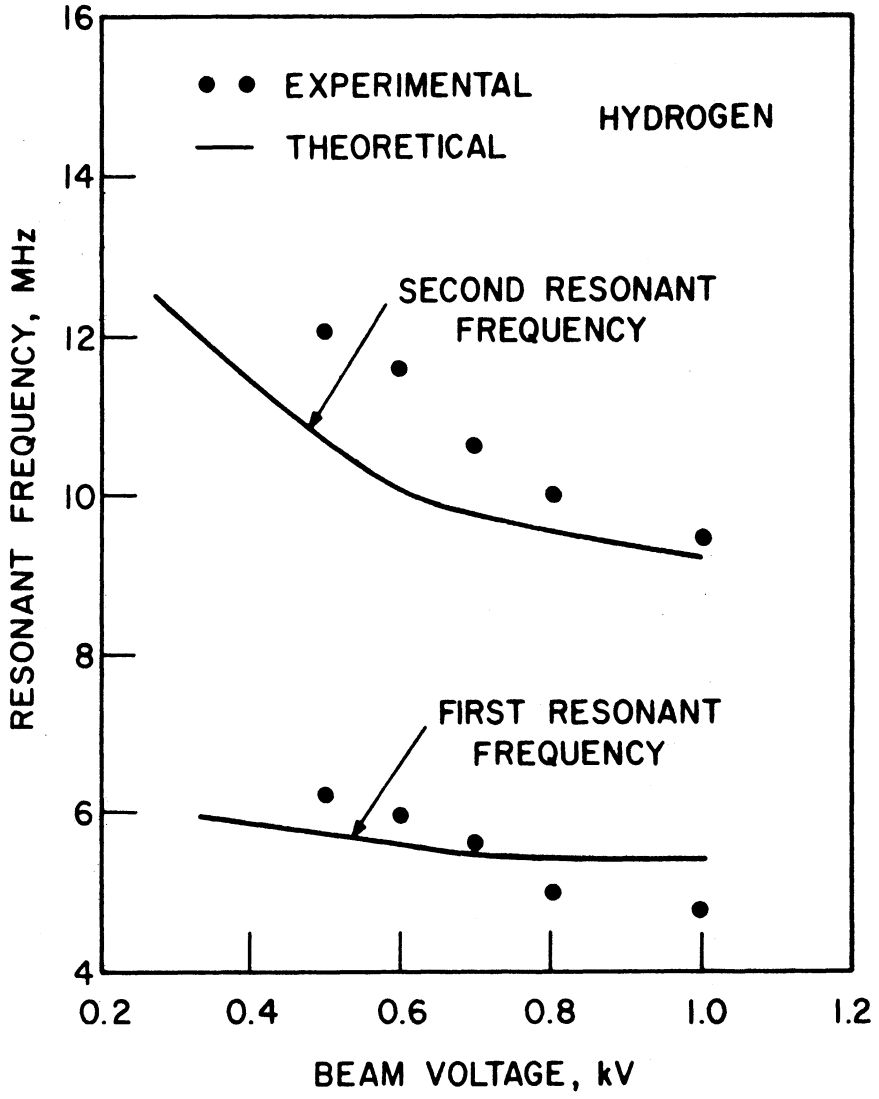

FIG. 5.4 VARIATION OF RESONANT FREQUENCIES AS A FUNCTION OF BEAM VOLTAGE FOR A HYDROGEN PLASMA.

decrease as the beam voltage is increased. The decrease in the second resonant frequency is more than that of the first for the same change of beam voltage. This behavior is predicted by the theoretical analysis as discussed in Section 4.3.2 and was obtained from Fig. 4.9. The continuous lines drawn in Fig. 5.4 represent the theoretical curves for the variation of the resonant frequencies as functions of beam voltage. The agreement between theory and experiment is good considering the influence of experimental errors in the measurement of plasma density.

The effect of the variation of the external dc magnetic field on the resonant frequencies was experimentally studied and the results are shown in Fig. 3.25. It is found that the resonant frequencies do not change appreciably with the change in the magnetic field for the range of parameters under study. The same behavior was predicted theoretically in Section 4.3.2 for the low-density regime in which the experiments were carried out.

5.2 Conclusions

The normal-mode field analysis of the beam-plasma, finite-length system is in good agreement with the major results of the experiments with the beam-generated plasma. This is particularly true in the case of the resonant-frequency values and their dependence on the various experimental parameters.

CHAPTER VI. SUMMARY, CONCLUSIONS AND SUGGESTIONS FOR FURTHER STUDY

6.1 Summary

Experimental measurements and theoretical calculations have been presented for a system in which a modulated electron beam excites resonances in a bounded plasma. As a result of the excitation of these resonances plasma ions are heated. The experimental and theoretical results show that a relatively large, radial RF electric field is excited in the plasma at the resonances and it is hypothesized that this field produces the observed ion heating.

The experimental investigation was carried out in a beam-generated plasma. The beam voltage was 400 to 1000 V and average beam current was about 2.5 mA. The modulation frequency was in the ion-plasma frequency regime. Either hydrogen, deuterium, neon or argon gas was used at pressures in the range of 10^{-4} to 10^{-3} Torr. The excitation of plasma-cavity modes was observed directly by measuring the RF electric field as a function of beam-modulation frequency, and indirectly by measuring the current carried by energetic ions to a gridded probe as a function of frequency. Two or three resonances lying slightly above the ion-plasma frequency are typically observed in the probe responses. Interferometric measurements at the lowest two resonant frequencies show that they are half- and full-wavelength axisymmetric resonances. The retarding potential energy-analyzer curves show that the largest ion-energy spread occurs when the beam is modulated at a resonant frequency.

The beam-plasma system is analyzed as a finite-length, boundary-value problem with a specified driving current. The dispersion equation includes the effect of finite beam and plasma radii, electron-beam space charge, uniform axial magnetic field and plasma electron-neutral collisions. The plasma is assumed to be cold. The quasi-static assumption is assumed to be valid and only the lowest-order, radial, axisymmetric modes are considered. The quasi-static potential, beam-modulation current and beam-modulation velocity are expressed as superpositions of four normal modes of the beam-plasma waveguide. Appropriate boundary conditions are applied at both ends of the system.

The results of the normal-mode analysis are in good agreement with the experiment and can be used to predict the values of the resonant frequencies and their variation with plasma density, beam voltage, ion mass and magnetic field. A comparison of the theory and experiment resulted in good agreement when the above-mentioned parameters were varied. The effect of electron-neutral collisions was to introduce small imaginary parts to all the four roots in the entire frequency range and to significantly reduce the RF electric-field strength at the resonances.

6.2 Conclusions

The predictions based on the normal-mode analysis of the axially bounded beam-plasma system are in good agreement with the experimental observations particularly with regard to the resonant frequencies, the relative RF electric-field amplitudes and their spatial variations. Therefore, the theory presented in this investigation may be useful for predicting the behavior of other actual and proposed experiments utilizing similar beam-plasma configurations. This has been done in the case of an

experiment performed by Haas and Eisner[51] and the results of the analysis are in good agreement with his experiment.[52] It is found that the interaction encountered in the present beam-plasma system is that of the beam space-charge waves and not that of the cyclotron waves. The beam-plasma system is not absolutely unstable for the parameters of the present experiment.

The gridded probe measurements show that energetic ions are produced when the modulated electron beam is passed through an axially bounded system. Evidence of the production of energetic ions is also obtained by the observation of increased plasma diameter when the beam modulation is at a resonant frequency. Ion temperature cannot be deduced from the gridded probe measurements because of its off-axis location.

The theoretical analysis and experiment suggest that the ions are heated due to the creation of a radial RF electric field (of the order of a few tens of V/cm) in the plasma. This radial electric field transfers energy to the ions through collisions. The importance of this result is that the electron beam can transfer energy directly to the plasma ions at frequencies other than those at which there is a strong beam-plasma instability. A beam-plasma instability of the convective or absolute type which is usually desired for plasma heating is not directly involved in the mechanism.

In the present experiment the RF fields in the plasma are easily produced by a modulated electron beam which is internal to the plasma. This appears to have an advantage over those methods which utilize coils external to the plasma and thus must meet conditions of accessibility through the outer low-density region of the plasma. It has the disadvantage of introducing a beam into the plasma but the beam need not be strong enough to excite strong beam-plasma instabilities.

It has been shown in Chapter II that the geometric resonance effect observed experimentally can be considered to be the lower-hybrid resonance for a plane wave propagating obliquely with respect to B_o. For oblique propagation the time-average oscillatory kinetic energy of the ions is much less than that of the electrons. The oblique propagation introduces a small axial electric field and as a result the wave is strongly affected by axial ac electron motion. The ions tend to participate rather weakly when E_z is present. This manifests itself in the dispersion characteristics by the fact that the plasma-wave branch of the dispersion diagram becomes independent of ion mass very rapidly above ω_{pi}. The plane-wave angle of propagation need only be less than $\cos^{-1}\sqrt{m/M}$ for this to happen.

The normal-mode field analysis shows a peak of electric-field strength at the lower-hybrid frequency where k_z tends toward zero. This was the body resonance as discussed in Section 4.3.4. In the experimental investigation this resonance is not observed, perhaps because it is either heavily damped due to cyclotron collisionless damping or it is a false prediction of the quasi-static analysis. Another possibility is that the longitudinally current-modulated electron beam does not couple to this resonance.

6.3 Suggestions for Further Study

The theoretical variation of the radial field strength with frequency showed sharper resonances than the experimental curves. A possible reason for this behavior is the nonhomogeneous plasma-density profile. The plasma nonuniformity should therefore be included in the theoretical analysis. As a first step the plasma density variation with position

could be taken into account by letting the equivalent dielectric tensor of the plasma column be a function of the axial and radial position.

Since the ratio of ion-to-electron time-average kinetic energy decreases quickly for oblique propagation, there remains an incentive for finding a method to excite the lower-hybrid resonance (body resonance) for 90-degree propagation. Further theoretical work is required for the study of the excitation of this resonance. The theory should include temperature effects and collisionless damping. A nonquasi-static analysis should be carried out to prove or disprove whether or not the body resonance is a false prediction of the quasi-static analysis.

The results of the present investigation have clearly shown that a current-modulated electron beam excites strong geometric resonances and therefore couples to them significantly. However, it is unknown whether the coupling occurs because the beam presents a charge source or because axial current couples to the wave when $k_z \neq 0$. It is reasonable that the beam acts as a current; however, it may also act like a "charge density." The beam velocity is nearly constant and thus an ac space charge accompanies the ac current. If it acts as a charge density, the present beam source may excite the body resonance. On the other hand, if the modulated beam acts as a current source it may not be an optimum source for excitation of this resonance. It has been shown that an azimuthal current couples strongly with the lower-hybrid resonance for 90-degree propagation. Such a current can be produced by passing currents in an RF coil wrapped around the plasma column. Other methods of beam excitation can be imagined such as a dipole charge source consisting of a positive and negative charge $\pm\rho_L$(C/m) a distance d apart. This source could be produced by radially displacing the electron

beam. Also, this and other methods of excitation should be studied theoretically when $k_z \neq 0$ to determine the coupling between the wave and the axial and azimuthal currents.

A mechanism of ion heating in the present experiment was proposed based on the fact that the bounded beam-plasma system can be described as a system in which an electron beam passes through a standing slow-wave field. For certain ranges of parameters the electron beam loses energy to the field and finally to the ions via collisions. Further numerical calculations are required to determine the actual rate of loss of beam energy to the fields and to the plasma.

The present investigation has shown that the ions can be heated by a modulated electron beam streaming through a bounded plasma. This heating scheme must be evaluated completely by using a nonlinear analysis in order to obtain accurate estimates of the degree of ion heating achievable. The ion-heating rate and its variation as a function of temperature must also be evaluated. This would be of great importance in determining the merits of this method of ion heating in thermonuclear plasmas.

In the experiment the size of the gridded probe velocity analyzer was comparable to the size of the plasma. Therefore when the probe was brought close to the plasma it tended to disturb it. To obtain an accurate measurement of ion temperature and ion-energy distribution, the gridded probe should be modified so that it is smaller in size and gives reliable ion temperature measurements. It would be necessary to arrange the probe so that it received ions from the main body of the plasma rather than only those ions which had sufficient energy to reach a radius several centimeters from the plasma.

The present experiment was carried out in the beam-generated plasma only and the operation was in the low-density regime. From the point of view of thermonuclear plasmas, it is of interest to study this method of ion heating in large-diameter (separately generated) plasmas and in the high-density regime. In this regime the lower-hybrid resonance is at the geometric mean frequency $(\omega_{ce}\omega_{ci})^{1/2}$. Auer et al.[30] have shown that the effects of nonzero k_z are less important when the density is increased. Therefore, finite geometry effects which are inevitable in a laboratory plasma may be less detrimental in the high-density regime.

APPENDIX A. DERIVATION OF TRANSVERSE AND LONGITUDINAL CURRENTS AT THE LOWER-HYBRID RESONANCE FOR AN ARBITRARY ANGLE OF PROPAGATION

The expressions for longitudinal and transverse currents J_k and J_t for 90-degree propagation have been given by Allis et al.[4] Here expressions for J_k and J_t are derived for an arbitrary angle of propagation.

Consider a spherical coordinate system (k,θ,φ) in the notation of Allis et al. and a Cartesian coordinate system (x,y,z). The conductivity tensor $\bar{\bar{\sigma}}$ is readily available in the Cartesian system as given by Eq. 2.11. To obtain the expressions for J_k and J_t in terms of $\sigma_\perp$, σ_x, $\sigma_\parallel$, etc., a coordinate transformation is required. The conductivity tensor in terms of spherical coordinates is given by

$$\bar{\bar{\sigma}}_{k,\theta,\varphi} = \bar{\bar{T}}^{-1} \cdot \bar{\bar{\sigma}}_{x,y,z} \cdot \bar{\bar{T}} \quad , \tag{A.1}$$

where $\bar{\bar{T}}$ represents a transformation matrix ($\bar{E}_{x,y,z} = \bar{\bar{T}} \cdot E_{k,\theta,\varphi}$) and is given by

$$\bar{\bar{T}} = \begin{bmatrix} \sin\theta & \cos\theta & 0 \\ 0 & 0 & 1 \\ \cos\theta & -\sin\theta & 0 \end{bmatrix}$$

and

$$\bar{\bar{T}}^{-1} = \begin{bmatrix} \sin\theta & 0 & \cos\theta \\ \cos\theta & 0 & -\sin\theta \\ 0 & 1 & 0 \end{bmatrix}$$

Carrying out the matrix multiplication in Eq. A.1 yields

$$\bar{\bar{\sigma}}_{k,\theta,\varphi} = \begin{bmatrix} \sigma_\perp \sin^2\theta + \sigma_\parallel \cos^2\theta & \sigma_\perp \sin\theta\cos\theta - \sigma_\parallel \sin\theta\cos\theta & -\sigma_x \sin\theta \\ \sigma_\perp \sin\theta\cos\theta - \sigma_\parallel \sin\theta\cos\theta & \sigma_\perp \cos^2\theta + \sigma_\parallel \sin^2\theta & -\sigma_x \cos\theta \\ \sigma_x \sin\theta & \sigma_x \cos\theta & \sigma_\perp \end{bmatrix} \tag{A.2}$$

The current density in spherical coordinates is given by

$$\bar{J}_{k,\theta,\varphi} = \bar{\bar{\sigma}}_{k,\theta,\varphi} \; \bar{E}_{k,\theta,\varphi} \tag{A.3}$$

From Eqs. A.2 and A.3 J_k is obtained as follows

$$J_k = (\sigma_\perp \sin^2\theta + \sigma_\parallel \cos^2\theta) E_k + (\sigma_\perp - \sigma_\parallel) \sin\theta\cos\theta E_\theta - \sigma_x \sin\theta E_\varphi \; . \tag{A.4}$$

The inverse transformation matrix $\bar{\bar{T}}^{-1}$ is used to obtain E_k, E_θ and E_φ in terms of E_x, E_y and E_z. Therefore, Eq. A.4 can be written as follows:

$$J_k = (\sigma_\perp \sin^2\theta + \sigma_\parallel \cos^2\theta)(\sin\theta E_x + \cos\theta E_z) + (\sigma_\perp - \sigma_\parallel) \sin\theta\cos\theta (\cos\theta E_x - \sin\theta E_z) - \sigma_x \sin\theta E_y \tag{A.5}$$

At resonance the propagation vector is in the electric field direction ($\bar{k} \parallel \bar{E}$) and if the angle of propagation θ is assumed to lie in the x-z plane the following is obtained:

$$E_y = 0 \tag{A.6}$$

If Eq. A.6 is used, J_k is given by

$$J_k = \frac{E_x}{\sin\theta}\left(\sigma_\perp \sin^2\theta + \sigma_\parallel \cos^2\theta\right) \tag{A.7}$$

Similarly, J_φ is obtained from Eqs. A.2 and A.3 and is given by

$$J_\varphi = \sigma_x \sin\theta\, E_k + \sigma_x \cos\theta\, E_\theta + \sigma_\perp E_\varphi$$

Substituting for E_k, E_θ and E_φ in terms of E_x, E_y and E_z and cancelling out the terms gives

$$J_\varphi = \sigma_x E_x \tag{A.8}$$

From the transformation matrix it is seen that $J_\varphi = J_y$. The transverse current J_t is defined to lie is a direction perpendicular to the plane containing the propagation vector. Therefore $J_\varphi \equiv J_t$.

The ratio of transverse to longitudinal current at resonance for an arbitrary angle of propagation is thus obtained from Eqs. A.7 and A.8 and is given by

$$\frac{J_t}{J_k} = \frac{\sigma_x \sin\theta}{\sigma_\perp \sin^2\theta + \sigma_\parallel \cos^2\theta} \tag{A.9}$$

Substituting for σ_x, $\sigma_\perp$ and $\sigma_\parallel$ from Eq. 2.12 in Eq. A.9 and for an operation in the frequency range such that $\omega_{ci}^2 \ll \omega^2 \ll \omega_{ce}^2$ gives, after some manipulations,

$$\frac{J_t}{J_k} = -\frac{j}{\sin\theta}\left[\frac{\omega\,\omega_{ce}}{\omega^2 - \omega_{ce}\omega_{ci}\left(1 + \frac{M}{m}\cot^2\theta\right)}\right] \tag{A.10}$$

APPENDIX B. LISTINGS OF THE COMPUTER PROGRAMS OF THE SUBROUTINE FUNCT FOR THE THREE DISPERSION EQUATIONS

As mentioned in Section 2.3, Gillanders'[83] computer program was used to trace the roots of the dispersion equations. The program requires subroutines FUNCT and SETCON for each dispersion equation. The listings of the subroutine FUNCT are given here. Subroutine SETCON is empty since no constants were separately calculated.

B.1 Listing of the Subroutine FUNCT for a Filled Beam-Plasma Waveguide

The dispersion equation for this configuration is given in Section 2.3.2a. In FUNCT the first three statements declare the modes and precision of the variables used. The COMMON statement is used so that the subroutine FUNCT can obtain data from and return data to the main program through the common storage area COMM. PAR is a vector of fifty numbers which may be used to enter any constants or parameters which are required in the evaluation of the dispersion equation. The EQUIVALENCE declaration allows one to refer to the same storage location by two or more names. In the present case, CV, G, R, S, CWE, CWI and NU refer to the same storage locations as PAR(1) through PAR(7), respectively. The remaining statements in FUNCT are for the computation of the dispersion function. In the following listings of the computer programs, commands commencing with $ refer to the Michigan Terminal System and must be modified for use on other systems.

```
$RUN *FORTRAN  SPUNCH=EPL160      PAR=MAP
      SUBROUTINE SETCON
C     SUBROUTINE SETCON IS EMPTY IN THIS CASE SINCE NO CONSTANTS
C     ARE CALCULATED SEPARATELY
      END
      SUBROUTINE FUNCT
      IMPLICIT COMPLEX*16(W,K,D,F),COMPLEX*8(V)
      COMPLEX*16 RWK,RWKCE
      REAL*4 NU
      COMMON/COMM/W,K,D,DDK,DDW,F,PAR(50),ITYPE,H
      EQUIVALENCE (PAR(1),CV),(PAR(2),G),(PAR(3),R),(PAR(5),CWE),
     1(PAR(6),CWI),(PAR(7),NU)
      VJ=CMPLX(0.0,1.0)
      CV2=CV*CV
      CV1=5.783/CV2
      KK=K*K
      WW=W*W
      WCI=WW-CWI
      WCI2=WCI*WCI
      WCE=WW-CWE
      WCE2=WCE*WCE
      WK=W-K
      WK2=WK*WK
      WKCE=WK2-CWE
      RWK=R/WK2
      RWKCE=R/WKCE
      WNUJ=W-VJ*NU
      WNUJ2=WNUJ*WNUJ
      WNUCE=WNUJ2-CWE
      WNUCE2=WNUCE*WNUCE
      KII2=1.-1./WW-G/(W*WNUJ)
      KII1=KII2-RWK
      KPER2=1.-1./WCI-G/(W*WNUCE)*WNUJ
      KPER1=KPER2-RWKCE
      KII1PK=-2.*RWK/WK
      KPE1PK=-2./WKCE*WK*RWKCE
      KII2P=2./(W*WW) + 2.*G/(W*WNUJ2) - VJ*NU*G/(WW*WNUJ2)
      KII1P=KII2P-KII1PK
      KPER2P=2.*W/WCI2 + 2.*G*WNUJ2/(W*WNUCE2) - VJ*NU*G/(WW*WNUCE)
      KPER1P=KPER2P-KPE1PK
      D=CV1*KPER1 + KK*KII1
      DDW=CV1*KPER1P + KK*KII1P
      DDK=CV1*KPE1PK + 2.*K*KII1 + KK*KII1PK
      IF (ITYPE.EQ.2) DDW=(0.,1.)*DDW
      F=-DDW/DDK
      RETURN
      END
$ENDFILE

*****NORMAL TERMINATION: THE NUMBER OF RECORDS PROCESSED IS 00000048
```

B.2 Listing of the Subroutine FUNCT for an Unfilled-Beam, Filled-Plasma Waveguide

The dispersion equation for this configuration is given by Eq. 2.145. The same remarks as those given in Section B.1 apply in the present case also. In addition, PAR(8) and CV2 refer to the same storage location where the variable CV2 is the normalized waveguide radius.

```
$RUN *FORTRAN   SPUNCH=EPL170    PAR=MAP
      SUBROUTINE SETCON
C     SUBROUTINE SETCON IS EMPTY IN THIS CASE SINCE NO CONSTANTS
C     ARE CALCULATED SEPARATELY
      END
C     CWE AND CWI ARE THE SQUARES OF ELECTRON CYCLOTRON FREQUENCY
C     AND ION CYCLOTRON FREQUENCY, RESPECTIVELY
      SUBROUTINE FUNCT
      IMPLICIT COMPLEX*16 (W,K,D,F,J,Y),COMPLEX*8(V)
      COMPLEX*16 CVJ,P1,PT1,PA1,PA12,PAT1,PATT1,PT1P,PT1PK,TA1,TA1P,
     1TA1PK,TA2,TA2J,RWK,RWKCE,P2,PT2,PA2,PA22,PAT2,PATT2,TA2,PT2P,TA2P,
     2TA2PK,RNR,RDR,RDR2,RNDR,RNDR2,RNDRP,RNDRPK,RPT2M,PBTT2,TB2,
     3TB2P,TB2PK,TB2J
      COMPLEX*8 A1,A2
      REAL*8 AT2,NU*4
      COMMON/COMM/W,K,D,DDK,DDW,F,PAR(50),ITYPE,H
      EQUIVALENCE (PAR(1),CV),(PAR(2),G),(PAR(3),R),(PAR(5),CWE),
     1(PAR(6),CWI),(PAR(7),NU),(PAR(8),CV2)
      VJ=CMPLX(0.0,1.0)
      CVJ=VJ*CV
      KK=K*K
      WW=W*W
      WCI=WW-CWI
      WCI2=WCI*WCI
      WCE=WW-CWE
      WCE2=WCE*WCE
      WK=W-K
      WK2=WK*WK
      WKCE=WK2-CWE
      RWK=R/WK2
      RWKCE=R/WKCE
      WNUJ=W-VJ*NU
      WNUJ2=WNUJ*WNUJ
      WNUCE=WNUJ2-CWE
      WNUCE2=WNUCE*WNUCE
      KII2=1.-1./WW-G/(W*WNUJ)
      KII1=KII2-RWK
      KPER2=1.-1./WCI-G/(W*WNUCE)*WNUJ
      KPER1=KPER2-RWKCE
      KPER22=KPER2*KPER2
      KPER12=KPER1*KPER1
      KII1PK=-2.*RWK/WK
      KPE1PK=-2./WKCE*WK*RWKCE
      KII2P=2./(W*WW) + 2.*G/(W*WNUJ2) - VJ*NU*G/(WW*WNUJ2)
      KII1P=KII2P-KII1PK
      KPER2P=2.*W/WCI2 + 2.*G*WNUJ2/(W*WNUCE2) - VJ*NU*G/(WW*WNUCE)
```

```
      KPER1P=KPER2P-KPE1PK
      P1=KPER1*KII1
      PT1=CDSQRT(P1)
      PA1=KII1/KPER1
      PA12=PA1/KPER1
      PAT1=CDSQRT(PA1)
      PATT1=CVJ*PAT1
      TA1=K*PATT1
      PT1P=.5/PT1*(KII1P*KPER1 + KPER1P*KII1)
      PT1PK=.5/PT1*(KII1PK*KPER1 + KPE1PK*KII1)
      TA1P=.5*CVJ*K/PAT1*(KII1P/KPER1-PA12*KPER1P)
      TA1PK=PATT1+ .5*CVJ*K/PAT1*(KII1PK/KPER1-PA12*KPE1PK)
      P2=KPER2*KII2
      PT2=CDSQRT(P2)
      PA2=KII2/KPER2
      PA22=PA2/KPER2
      PAT2=CDSQRT(PA2)
      PATT2=CV*PAT2
      PBTT2=CV2*PAT2
      TA2=K*PATT2
      TB2=K*PBTT2
      PT2P=0.5/PT2*(KII2P*KPER2+KPER2P*KII2)
C     PT2PK=0.0
      TA2P=0.5*CV*K/PAT2*(KII2P/KPER2-PA22*KPER2P)
      TB2P=CV2/CV*TA2P
      TA2PK=PATT2
      TB2PK=PBTT2
  150 A1=TA1
      TA2J=VJ*TA2
      TB2J=VJ*TB2
      IF(ABS(AIMAG(A1)).GT.170) GO TO 180
      GO TO 200
  180 CALL BJ1JOR(TA1,J1JOR)
      GO TO 220
  200 CALL CDBESJ(TA1,JOTA1,J1TA1,YOTA1,Y1TA1)
      J1JOR=J1TA1/JOTA1
  220 CALL CDBESJ(TB2J,JOTB2J,J1TB2J,YOTB2J,Y1TB2J)
  300 CALL CDBESJ(TA2J,JOTA2J,J1TA2J,YOTA2J,Y1TA2J)
      Y11TA2=-VJ*J1TA2J
      Y1OTA2=JOTA2J
      Y11TB2=-VJ*J1TB2J
      Y1OTB2=JOTB2J
C     PI/2=1.570796
      KOTA2=1.570796*(VJ*JOTA2J-YOTA2J)
      K1TA2=-1.570796*(J1TA2J+VJ*Y1TA2J)
      KOTB2=1.570796*(VJ*JOTB2J - YOTB2J)
      K1TB2=-1.570796*(J1TB2J+VJ*Y1TB2J)
  320 JACK=1.-J1JOR/TA1 + J1JOR*J1JOR
      RNR=Y11TA2*KOTB2 + Y1OTB2*K1TA2
      RDR=Y1OTA2*KOTB2 - Y1OTB2*KOTA2
      RDR2=RDR*RDR
      RNDR=RNR/RDR
      RNDR2=RNDR*RNDR
      Y1KAB=Y11TB2*K1TA2 - Y11TA2*K1TB2
      Y1K1O=RNR*(Y1OTA2*K1TB2 + Y11TB2*KOTA2)
      Y1KABR=Y1KAB/RDR
      Y1K1OR=Y1K1O/RDR2
      KACK=1. - RNDR/TA2 - RNDR2
      J1JOR2=J1JOR*J1JOR
      JPT1M=2.*PT1*J1JOR
      RPT2M=2.*PT2*RNDR
      RNDRP=TA2P*KACK + TB2P*(Y1KABR + Y1K1CR)
      RNDRPK=TA2PK*KACK + TB2PK*(Y1KABR + Y1K1OR)
```

```
      D=P1*J1JOR2 + P2*RNDR2
      DDW=JPT1M*(PT1P*J1JOR + PT1*TA1P*JACK) + RPT2M*(PT2P*RNDR +
     1PT2*RNDRP)
      DDK=JPT1M*(PT1PK*J1JOR+PT1*TA1PK*JACK)+RPT2M*PT2*RNDRPK
      IF (ITYPE.EQ.2) DDW=(0.,1.)*DDW
      F=-DDW/DDK
      RETURN
      END
C     BJ1JOR(Z,J1JOR) IS USED TO CALCULATE RATIO J1(Z)/J0(Z)
C     DIRECTLY FOR VERY LARGE IMAGINARY ARGUMENT
      SUBROUTINE  BJ1JOR(Z,J1JOR)
      IMPLICIT COMPLEX*16(A,B,Z,J),REAL*8(P,X)
      COMPLEX*8 VJ
      PI=3.14159265
      VJ=CMPLX(0.0,1.0)
      X=Z
      PARG=X-PI/4.
      A0=-0.125/Z
      B0=1.+.5625/Z*A0
      A1=-3.0*A0
      B1=1.+0.3125/Z*A1
      PCOS=DCOS(PARG)
      PSIN=DSIN(PARG)
      A11=B1*PSIN + A1*PCOS
      A12=B1*PCOS - A1*PSIN
      A21=B0*PCOS - A0*PSIN
      A22=B0*PSIN + A0*PCOS
      J1JOR=(A11+VJ*A12)/(A21-VJ*A22)
      RETURN
      END
$ENDFILE
```

*****NORMAL TERMINATION: THE NUMBER OF RECORDS PROCESSED IS 00000140

B.3 Listing of the Subroutine FUNCT for an Open Beam-Plasma Waveguide

The dispersion equation for this configuration is given by Eq. 2.145. The remarks given in Section B.1 also apply in this case as well.

```
$RUN *FORTRAN      SPUNCH=EPL180      PAR=MAP
      SUBROUTINE SETCON
C     SUBROUTINE SETCON IS EMPTY IN THIS CASE SINCE NO CONSTANTS
C     ARE CALCULATED SEPARATELY
      END
C     CWE AND CWI ARE THE SQUARES OF ELECTRON CYCLOTRON FREQUENCY
C     AND ION CYCLOTRON FREQUENCY, RESPECTIVELY
      SUBROUTINE FUNCT
      IMPLICIT COMPLEX*16 (W,K,D,F,J,Y),COMPLEX*8(V)
      COMPLEX*16 CVJ,P1,PT1,PA1,PA12,PAT1,PATT1,PT1P,PT1PK,TA1,TA1P,
     1TA1PK,TA2,TA2J,RWK,RWKCE,PT12
      COMPLEX*8 A1,A2
      REAL*8 AT2,PATT2,NU*4
      COMMON/COMM/W,K,D,DDK,DDW,F,PAR(50),ITYPE,H
      EQUIVALENCE (PAR(1),CV),(PAR(2),G),(PAR(3),R),(PAR(5),CWE),
     1(PAR(6),CWI),(PAR(7),NU)
      VJ=CMPLX(0.0,1.0)
      CVJ=VJ*CV
      KK=K*K
      WW=W*W
      WCI=WW-CWI
      WCI2=WCI*WCI
      WCE=WW-CWE
      WCE2=WCE*WCE
      WK=W-K
      WK2=WK*WK
      WKCE=WK2-CWE
      RWK=R/WK2
      RWKCE=R/WKCE
      WNUJ=W-VJ*NU
      WNUJ2=WNUJ*WNUJ
      WNUCE=WNUJ2-CWE
      WNUCE2=WNUCE*WNUCE
      KII2=1.-1./WW-G/(W*WNUJ)
      KII1=KII2-RWK
      KPER2=1.-1./WCI-G/(W*WNUCE)*WNUJ
      KPER1=KPER2-RWKCE
      KPER22=KPER2*KPER2
      KPER12=KPER1*KPER1
      KII1PK=-2.*RWK/WK
      KPE1PK=-2./WKCE*WK*RWKCE
      KII2P=2./(W*WW) + 2.*G/(W*WNUJ2) - VJ*NU*G/(WW*WNUJ2)
      KII1P=KII2P-KII1PK
      KPER2P=2.*W/WCI2 + 2.*G*WNUJ2/(W*WNUCE2) - VJ*NU*G/(WW*WNUCE)
      KPER1P=KPER2P-KPE1PK
      P1=KPER1*KII1
      PT1=CDSQRT(P1)
      PA1=KII1/KPER1
      PA12=PA1/KPER1
      PAT1=CDSQRT(PA1)
      PATT1=CVJ*PAT1
      TA1=K*PATT1
      PT1P=.5/PT1*(KII1P*KPER1 + KPER1P*KII1)
      PT1PK=.5/PT1*(KII1PK*KPER1 + KPE1PK*KII1)
```

```
C       PT2PK=0
        TA1P=.5*CVJ*K/PAT1*(KIT1P/KPER1-PA12*KPER1P)
        TA1PK=PATT1+ .5*CVJ*K/PAT1*(KIT1PK/KPER1-PA12*KPE1PK)
        PATT2=CV
        TA2=K*PATT2
C       TA2PK=PATT2
        AT2=TA2
        IF (AT2.LT.0.) GO TO 100
        GO TO 150
  100   TA2=-TA2
        PATT2=-PATT2
  150   A1=TA1
        TA2J=VJ*TA2
        A2=TA2J
        IF(ABS(AIMAG(A1)).GT.170) GO TO 180
        GO TO 200
  180   CALL BJ1JOR(TA1,J1JOR)
        GO TO 220
  200   CALL CDBESJ(TA1,J0TA1,J1TA1,Y0TA1,Y1TA1)
        J1JOR=J1TA1/J0TA1
  220   IF(ABS(AIMAG(A2)).GT.120.)  GO TO 280
        GO TO 300
  280   K1K0R=-VJ*VJ
        GO TO 320
  300   CALL CDBESJ(TA2J,J0TA2J,J1TA2J,Y0TA2J,Y1TA2J)
C       PI/2=1.570796
        K0TA2=1.570796*(VJ*J0TA2J-Y0TA2J)
        K1TA2=-1.570796*(J1TA2J+VJ*Y1TA2J)
        K1K0R=K1TA2/K0TA2
  320   JACK=1.-J1JOR/TA1 + J1JOR*J1JOR
        KACK=-1.-K1K0R/TA2 + K1K0R*K1K0R
        PT12=PT1*PT1
        J1JOR2=J1JOR*J1JOR
        K1K0R2=K1K0R*K1K0R
        D=PT12*J1JOR2 + K1K0R2
        DDW=2.*PT1*J1JOR*(PT1P*J1JOR+PT1*TA1P*JACK)
        DDK=2.*PT1*J1JOR*(PT1PK*J1JOR+PT1*TA1PK*JACK)+2.*K1K0R*PATT2*KACK
        IF (ITYPE.EQ.2) DDW=(0.,1.)*DDW
        F=-DDW/DDK
        RETURN
        END
C       BJ1JOR(Z,J1JOR) IS USED TO CALCULATE RATIO J1(Z)/J0(Z)
C       DIRECTLY FOR VERY LARGE IMAGINARY ARGUMENT
        SUBROUTINE  BJ1JOR(Z,J1JOR)
        IMPLICIT COMPLEX*16(A,P,Z,J),REAL*8(P,X)
        COMPLEX*8 VJ
        PI=3.14159265
        VJ=CMPLX(0.0,1.0)
        X=Z
        PARG=X-PI/4.
        A0=-0.125/Z
        B0=1.+.5625/Z*A0
        A1=-3.0*A0
        B1=1.+0.3125/Z*A1
        PCOS=DCOS(PARG)
        PSIN=DSIN(PARG)
        A11=B1*PSIN + A1*PCOS
        A12=B1*PCOS - A1*PSIN
        A21=B0*PCOS - A0*PSIN
        A22=B0*PSIN + A0*PCOS
        J1JOR=(A11+VJ*A12)/(A21-VJ*A22)
        RETURN
        END
$ENDFILE

*****NORMAL TERMINATION: THE NUMBER OF RECORDS PROCESSED IS 00000118
```

B.4 Listing of the Subroutine CDBESJ which Calculates the Bessel Function of Complex Arguments

The dispersion equations for the unfilled-beam, filled-plasma waveguide and the open beam-plasma waveguide require the evaluation of the Bessel functions J_1 and J_0 and the modified Bessel function K_1 and K_0 of complex arguments.

A program given in subroutine CDBESJ was written to compute J_1, J_0, Y_1 and Y_0 for arbitrary complex arguments. For a complex argument Z such that $|Z| > 20$, asymptotic forms for J_0, J_1, Y_0 and Y_1 which are given below were used:

$$J_n(Z) \cong \left(\frac{2}{\pi Z}\right)^{1/2} \left[\cos\left(Z - \frac{n\pi}{2} - \frac{\pi}{4}\right) \cdot P_n(Z) - Q_n(Z) \cdot \sin\left(Z - \frac{n\pi}{2} - \frac{\pi}{4}\right) \right] \tag{B.1}$$

and

$$Y_n(Z) \cong \left(\frac{2}{\pi Z}\right)^{1/2} \left[\sin\left(Z - \frac{n\pi}{2} - \frac{\pi}{4}\right) P_n(Z) + Q_n(Z) \cdot \cos\left(Z - \frac{n\pi}{2} - \frac{\pi}{4}\right) \right] \tag{B.2}$$

where

$$P_n(Z) = 1 + \sum_{k=1}^{\infty} (-1)^k \frac{(4n^2 - 1)(4n^2 - 3^2) \cdots [4n^2 - (4k - 1)^2]}{2k!\, 2^{6k}\, Z^{2k}}$$

and

$$Q_n(Z) = \sum_{k=1}^{\infty} (-1)^{k+1} \frac{(4n^2 - 1)^2 (4n^2 - 3^2) \cdots [4n^2 - (4k - 3)^2]}{(2k - 1)!\, 2^{6k-3}\, Z^{2k-1}}$$

In the preceding equations, n = 0 and n = 1 are used for J_o, Y_o and J_1, Y_1, respectively. For an argument such that $|Z| < 16$, the following expressions for J and Y are used:

$$J_n(Z) = \frac{Z^n}{2^n n!}\left(1 - \frac{Z^2}{2^2(n+1)\,1!} + \frac{Z^4}{2^4(n+1)(n+2)\,2!} - \cdots\right) \qquad (B.3)$$

and

$$Y_n(Z) = \frac{2}{\pi}\left[J_n(Z)\left(\gamma + \log\frac{Z}{2}\right) - \frac{1}{2}\sum_{n=o}^{n-1}\frac{n-k-1!}{k!}\left(\frac{Z}{2}\right)^{2k-n} + \frac{1}{\pi}\sum_{k=o}^{\infty}(-1)^{k+1}\frac{(Z/2)^{n+2k}}{k!\;k+n!}\left(\varphi(k) + \varphi(n+k)\right)\right], \qquad (B.4)$$

where γ is Euler's constant ($\gamma = 0.57721$),

$$\varphi(n) = 1 + \frac{1}{2} + \cdots \frac{1}{n}$$

and

$$\varphi(0) = 0$$

Again in Eqs. B.3 and B.4, n = 0 and n = 1 are used. Since the J_o and J_1 functions are required each time the Y_o and Y_1 functions are used, the Y_n functions are obtained by calculating the series terms for J_n and multiplying each by the appropriate constant to obtain the Y_n series term.

For an argument Z such that $16 < |Z| < 20$, a linear combination of the values calculated from the two expressions is used. The listing of the program follows.

```
$RUN *FORTRAN    SPUNCH=EPL280         PAR=MAP
      SUBROUTINE CDBESJ(Z,J0,J1,Y0,Y1)
      IMPLICIT COMPLEX*16(X,Y,Z,A,B,D,J),REAL*8(P,T)
      DATA PI,TMAX,TMIN,TD/3.14159265358979238,16.,20.,4./
      DATA TGAM/.57721566490153286O6/
      T=CDABS(Z)
      IF (T .LT. TMIN) GO TO 10
      A=Z-PI/4.0000000
      B=CDSQRT((2.000000000/PI)/Z)
      Y=-.125/Z
      X=1.0000+Y*.5625/Z
      J0=B*(CDCOS(A)*X-CDSIN(A)*Y)
      Y0=B*(CDSIN(A)*X+CDCOS(A)*Y)
      A=Z-.750000000*PI
      Y=-3.00000000*Y
      X=1.0000+Y*.3125/Z
      J1=B*(CDCOS(A)*X-CDSIN(A)*Y)
      Y1=B*(CDSIN(A)*X+CDCOS(A)*Y)
      IF (T .GT. TMAX) RETURN
      J01=J0
      J11=J1
      Y01=Y0
      Y11=Y1
      T1=(T-TMIN)/TD
      T2=1.00000000-T1
10    TEST=.0000001/DEXP(T*T/4.)
      A=1.000000000
      B=Z/2.00000000
      D=Z*Z/4.
      Y=B*B
      X=Y*Y
      PK=1.500000000
      PK1=10.000000000/3.000000000
      J0=1.000000000-Y
      J1=(1.000000000-Y/2.000000000)*B
      Y0=(.375000000*Y-1.000000000)*Y
      Y1=2.50000000*(Y/9.000000000-.500000000)*Y +1.
      DO 20 I=2,100,2
      N=I*(I-1)
      M=I+1
      PK2=PK+1.000000000/M
      PK3=PK1+1.000000000/M+1.000000000/(M+1)
      PK=PK2+1.000000000/(M+1)
      PK1=PK3+1.000000000/(M+1)+1.000000000/(M+2)
      A=A*X/(N*N)
      B=B*X/(N*I*M)
      D=D*X/(I*I*M*M)
      J0=J0+A*(1.000000000-Y/(M*M))
      J1=J1+B*(1.000000000-Y/(M*(M+1)))
      Y0=Y0-D*(PK2-PK*Y/((M+1)*(M+1)))
      Y1=Y1-D*(PK3/(M+1)-PK1*Y/((M+2)*(M+1)*(M+1)))
      IF (CDABS(B) .LT. TEST) GO TO 30
20    CONTINUE
30    Y0=((CDLOG(Z/2.)+TGAM)*J0-Y0)*2.000000000/PI
      Y1=-2.00/(Z*PI) + 2.0/PI*(CDLOG(Z/2.)+TGAM)*J1-Z/(2.*PI)*Y1
      IF (T .LT. TMIN) RETURN
      J0=J0*T2+J01*T1
      J1=J1*T2+J11*T1
      Y0=Y0*T2+Y01*T1
      Y1=Y1*T2+Y11*T1
      RETURN
      END
$ENDFILE

*****NORMAL TERMINATION: THE NUMBER OF RECORDS PROCESSED IS 00000063
```

APPENDIX C. STUDY OF TRANSIT-TIME EFFECTS ON THE BEAM-CURRENT MODULATION

The effects of the transit time of an electron beam streaming through a drift tube of length L on the beam-current modulation is studied. The effects are due to the presence of the space-charge waves which exist on the electron beam.

The relations for the space-charge waves in a thin beam ($\beta_e b \ll 1$) are given by Haus.[103] The kinetic voltage V and the ac current distribution through the beam are given below in the notation of Haus:

$$V = \left(V_+ e^{j\beta_q z} + V_- e^{-j\beta_q z} \right) e^{-j\beta_e z} \tag{C.1}$$

and

$$i = Y_o \left(V_+ e^{j\beta_q z} - V_- e^{j\beta_q z} \right) e^{-j\beta_e z} \tag{C.2}$$

where

$$Y_o = \frac{I_o}{2V_o} \frac{\beta_e}{\beta_q} ,$$

I_o is the dc beam current, V_o is the beam voltage, $\beta_e = \omega/v_o$, $\beta_q = \gamma_o \omega_{pb} / v_o$ and γ_o is the space-charge reduction factor for a thin beam.

The conditions at the entrance plane z = 0 of the drift tube are

$$\text{at } z = 0 , \quad V = 0 \quad \text{(no velocity modulation)}$$

$$i = I_m \quad \text{(a current modulation)}$$

Substitution of these conditions at z = 0 in Eqs. C.1 and C.2 gives

$$V_+ + V_- = 0 \tag{C.3}$$

and

$$Y_o(V_+ - V_-) = I_m \tag{C.4}$$

Equations C.3 and C.4 yield

$$V_+ = -V_- = \frac{I_m}{2Y_o} \tag{C.5}$$

Substitution of V_+ and V_- from Eq. C.5 into Eq. C.2 yields

$$i = I_m \cos \beta_q z \, e^{-j\beta_e z} \tag{C.6}$$

The magnitude of the ac beam current at the collector ($z = L$) is then given by

$$|i(L)| = I_m \, |\cos \beta_q L| \tag{C.7}$$

The first zero of the ac current at the collector occurs when

$$\beta_q L = \frac{\gamma_o \omega_{pb} L}{v_o} = \frac{\pi}{2} \tag{C.8}$$

The reduction factor can be obtained from the plot given by Haus. For the present experiment where $d/b \cong \infty$, $\beta_e b \ll 1$. Thus $\gamma_o \cong \beta_e b$. Substitution of the value of γ_o into Eq. C.8 yields

$$f = \frac{v_o^2}{4\omega_{pb} bL} \tag{C.9}$$

The beam-electron plasma frequency, the dc beam current and the dc beam voltage are given by

$$\omega_{pb}^2 = \frac{n_b e^2}{m\epsilon_o} \tag{C.10}$$

$$I_o = n_b e v_o \pi b^2 \tag{C.11}$$

and

$$V_o = \frac{1}{2} \frac{m v_o^2}{e} \tag{C.12}$$

Equations C.9 through C.11 yield

$$f = \frac{2^{3/4} \cdot (e/m)^{1/4} (\epsilon_o \pi)^{1/2} V_o^{5/4}}{L I_o^{1/2}} \tag{C.13}$$

Numerically,

$$f = 853 \frac{V_o^{5/4}}{L I_o^{1/2}}, \tag{C.14}$$

where f is in Hz, V_o is in volts, L is in meters and I_o is in amperes. The ac beam current assumes a minimum at a frequency given by Eq. C.14.

APPENDIX D. DERIVATION OF THE EXPRESSIONS FOR ac BEAM-VELOCITY MODULATION AND ac BEAM CURRENT-DENSITY MODULATION

Consider an electron beam drifting along the z-direction with a velocity v_o and confined by a magnetic field $\bar{B}_o = \hat{z}B_o$. A small-signal approximation is assumed to be valid, i.e., all ac quantities are assumed to be small perturbations of their corresponding dc values. Moreover, all ac quantities are assumed to have the wave-like dependence $\exp[j(\omega t - k_z z)]$.

Beam current density $\bar{J}_b$ is given by

$$\bar{J}_b = \rho_b \bar{v}_b = \rho_{ob}\bar{v}_o + (\rho_{1b}\bar{v}_o + \rho_{ob}\bar{v}_{1b})\, e^{j(\omega t - k_z z)}, \qquad (D.1)$$

where ρ_b and $\bar{v}_b$ have been defined in Eqs. 4.1 and 4.2. The ac current-density modulation is therefore given by

$$\bar{J}_{1b} = (\rho_{1b}\bar{v}_o + \rho_{ob}\bar{v}_{1b}) \qquad (D.2)$$

For the assumed time and space dependence the ac current and ac charge density are related by the equation of continuity (Eq. 2.5) and on substitution from Eq. D.2 it yields

$$j(\omega - k_z v_o)\rho_{1b} = -\rho_{ob}\nabla \cdot \bar{v}_{1b} \qquad (D.3)$$

Neglecting the beam-electron collisions with other particles, the equation of motion (Eq. 2.8) for beam electrons can be written as

$$j(\omega - k_z v_o)m\bar{v}_{1b} = -e\bar{E} - e\bar{v}_{1b} \times \bar{B}_o \qquad (D.4)$$

The quasi-static assumption is invoked ($\nabla \times \bar{E} = 0$). The curl and the divergence of Eq. D.4 together with the vector identity,

$$\nabla \cdot (\bar{A} \times \bar{B}) = \bar{B} \cdot \nabla \times \bar{A} - \bar{A} \cdot \nabla \times \bar{B} \quad ,$$

and some manipulation yields

$$\nabla \cdot \bar{v}_{1b} = j \frac{e}{m} \frac{\omega_D \nabla \cdot \bar{E}}{\omega_D^2 - \omega_{ce}^2} + \frac{jk_z \omega_{ce}^2 v_{1bz}}{\omega_D^2 - \omega_{ce}^2} \quad , \tag{D.5}$$

where

$$\omega_D = \omega - k_z v_o$$

Substitution of Eq. D.5 into Eq. D.3 yields

$$\rho_{1b} = \frac{\epsilon_o \omega_{pb}^2}{\omega_D^2 - \omega_{ce}^2} \left[\nabla \cdot \bar{E} + jk_z \frac{\omega_{ce}^2}{\omega_D^2} E_z \right] \quad , \tag{D.6}$$

where

$$\omega_{pb}^2 = - \frac{\rho_{ob} e}{m \epsilon_o}$$

The z-components of Eqs. D.2 and D.4 yield

$$J_{1bz} = \rho_{1b} v_o + \rho_{ob} v_{1bz} \tag{D.7}$$

and

$$v_{1bz} = - \frac{e}{m} \cdot \frac{E_z}{j\omega_D} \tag{D.8}$$

Substitution of Eqs. D.8 and D.6 into Eq. D.7 gives

$$J_{1bz} = \epsilon_o \omega_{pb}^2 \left[\frac{v_o \nabla \cdot \bar{E}}{\omega_D^2 - \omega_{ce}^2} + \frac{jk_z v_o}{(\omega_D^2 - \omega_{ce}^2)} \frac{\omega_{ce}^2}{\omega_D^2} E_z - j \frac{E_z}{\omega_D} \right] \qquad (D.9)$$

Equation D.9 on simplification can be written as

$$J_{1bz} = \frac{\epsilon_o \omega_{pb}^2}{\omega_D^2 - \omega_{ce}^2} \left[v_o \nabla \cdot \bar{E} + j \left(\frac{\omega \omega_{ce}^2}{\omega_D^2} - \omega_D \right) E_z \right] \qquad (D.10)$$

For the assumed spatial dependence, the operator ∇ can be separated into transverse and axial components as follows:

$$\nabla = \nabla_\perp - jk_z \qquad (D.11)$$

and

$$\nabla \cdot \bar{E} = \nabla_\perp \cdot \bar{E}_\perp - jk_z E_z \quad . \qquad (D.12)$$

Using the quasi-static assumption, the electric field can be expressed as the negative gradient of potential, therefore,

$$\bar{E}_\perp = - \nabla_\perp \Phi \qquad (D.13)$$

and

$$E_z = jk_z \Phi \quad . \qquad (D.14)$$

$\nabla \cdot \bar{E}$ can thus be written as

$$\nabla \cdot \bar{E} = - \nabla_\perp^2 \Phi - jk_z E_z$$

or

$$\nabla \cdot \bar{E} = (T^2 + k_z^2)\Phi = (T^2 + k_z^2) \frac{E_z}{jk_z} \quad , \qquad (D.15)$$

where T is the transverse propagation constant. Substitution of Eq. D.15 into Eq. D.10 yields

$$J_{1bz} = - j\omega\epsilon_o E_z \left[\frac{\omega_{pb}^2}{\omega_D^2} + \frac{\omega_{pb}^2}{\omega_D^2 - \omega_{ce}^2} \frac{T^2 v_o}{k_z \omega} \right] \qquad (D.16)$$

Equations D.8 and D.16 are the required expressions for axial beam-velocity modulation and current-density modulation.

APPENDIX E. DESCRIPTION OF THE COMPUTER PROGRAM WHICH IS USED FOR NORMAL-MODE FIELD CALCULATIONS

A brief description of the Fortran IV computer program which is used for normal-mode field calculations is given here. A listing of the program is presented at the end of this appendix. Commands commencing with $ refer to the Michigan Terminal System and must be modified for use on other systems. Section E.1 describes the program for field calculation as a function of frequency and Section E.2, as a function of radial and axial distance.

E.1 Computer Program for Normal-Mode Field Calculation as a Function of Frequency

The first few statements declare the mode and precision of the variables used in the program. The dimension statement assures the appropriate storage space. These are mainly required to print the output in the desired form as indicated by the format statements at the end of the program.

The NAMELIST type of input is used. Some of the variables are initialized by the data statement but others are read in at the beginning of the program. The variables W and K which have been previously calculated by solving the dispersion equation and which are stored in a private file are now read in. The program calculates the variables needed to transfer data from the main program to the subroutine DCOEFF which is now called. The subroutine DCOEFF calculates the coefficients X_i, i = 1...4, and returns data to the main program. With the help of switches SW and SW2

the program chooses a particular section of the program which is used for normal-mode field calculation for one of the three beam-plasma waveguide configurations. SW = 1 and SW2 = 1 bypass the program for the open beam-plasma waveguide and choose the unfilled-beam, filled-plasma waveguide and beam-plasma filled waveguide configurations, respectively. The Bessel functions encountered during the calculations are computed by the subroutine CDBESJ which is described in Section B.4. A few quantities of interest, such as axial and radial electric-field amplitude as functions of frequency, are stored in a private file for plotting by a digital plotting system (Calcomp 763). Other desired quantities are printed out in a prescribed format by a printer. The listing of the computer program follows.

```
$RUN *FORTRAN      SPUNCH=EPL571     PAR=MAP
      IMPLICIT COMPLEX*16(W,K,X,V,J,P,T,E,F,Y), REAL*8(B)
      COMPLEX*16  RWK,RWKCE,DELTA,DELTAA,RDR,RNR1,RNR,RNDR1,RNDR
      COMPLEX*8 A1,A2
      REAL*8 CV,CWE,CWI,G,R,AT2,AR2,Z,RB1,RB2,ABSJ1B,ABSV1B,ABSPOT,
     1ABSER1,ABSER2,ABSEZ1,ABSEZ2,SYSL,RB1INC,RB2INC,ZINCR,AJKZ ,
     1NU,RBB1,CV2
      DIMENSION WA(200),KA(200,4),XA(200,4),K(4),X(4),RWK(4),RWKCE(4),
     1KK(4),WK(4),WK2(4),WKCE(4),KI11(4),KPER1(4),PA1(4),PAT1(4),
     1PATT1(4),TA1(4),TA2(4),TR1(4),TR2(4),AT2(4),AR2(4),TA2J(4),
     1TR2J(4),J1JOR(4),JOTA1(4),J1TA1(4),YOTA1(4),Y1TA1(4),JOTR1(4),
     1J1TR1(4),YOTR1(4),Y1TR1(4),K1KOR(4),JOTA2J(4),J1TA2J(4),YOTA2J(4),
     1Y1TA2J(4),KOTA2(4),JOTR2J(4),J1TR2J(4),YOTR2J(4),Y1TR2J(4),
     1K1TR2(4),VJKZ(4),F(4),FF(4),FK(4),J1BZ(200,4),V1BZ(200,4),
     1POT(200,4),ER1(200,4),EZ1(200,4),ER2(200,4),EZ2(200,4),
     1J1BZT(200),V1BZT(200),POTT(200),ER1T(200),EZ1T(200),ER2T(200),
     1EZ2T(200),FFF(4),KOTR2(4),KORAR(4),ABSJ1B(200),YIOTR2(4),
     1ABSV1B(200),ABSPOT(200),ABSER1(200),ABSER2(200),ABSEZ1(200),
     1ABSEZ2(200),A1(4),A2(4), AJKZ(4),AEZ(200),AER(200),AWA(200),DELTA(
     14),FFFF(4), BBSJBZ(200,4),BBSVBZ(200,4),BBSPOT(200,4),BBSER1(200,
     14),BBSER2(200,4),BBSEZ1(200,4),BBSEZ2(200,4),TB2(4),TB2J(4),
     1JOTB2J(4),J1TB2J(4),YOTB2J(4),Y1TB2J(4),YIOTA2(4),YIOTB2(4),
     1KOTB2(4),YI1TR2(4),RDR(4),RNR1(4),RNR(4),RNDR1(4),RNDR(4),RBB1(4)
      NAMELIST/INPUT/N,Z,RB1,RB2,CV,CWE,CWI,G,R,SYSL,NU,CV2,SW,SW2
      DATA N,Z,RB1,RB2,G,SYSL,SW,SW2/5,C.2,C.5,2.0,1.843E3,0.25,0.0,0.0/
      VJ=DCMPLX(0.DO,1.DO)
1     READ(5,INPUT)
      WRITE(6,INPUT)
      VJZ=Z*VJ
      DO 500 L=1,N
      READ(7,50)   W,K
50    FORMAT(10E13.5)
      WA(L)=W
      CO 40  I=1,4
```

```
  2   KA(L,I)=K(I)
      KK(I)=K(I)*K(I)
      WW=W*W
      WCI=WW-CWI
      WCI2=WCI*WCI
      WCE=WW-CWE
      WCE2=WCE*WCE
      WNUJ=W-VJ*NU
      WNUJ2=WNUJ*WNUJ
      WNUCE=WNUJ2-CWE
      WK(I)=W-K(I)
      WK2(I)=WK(I)*WK(I)
      WKCE(I)=WK2(I)-CWE
      RWK(I)=R/WK2(I)
      RWKCE(I)=R/WKCE(I)
      KII2=1.-1./WW-G/(W*WNUJ)
      KII1(I)=KII2-RWK(I)
      KPER2=1.-1./WCI-G/(W*WNUCE)*WNUJ
      KPER1(I)=KPER2-RWKCE(I)
      PA1(I)=KII1(I)/KPER1(I)
 40   DELTA(I)=1.+WK2(I)*K(I)/(W*CWE)*PA1(I)
      CALL DCOEFF(W,K,SYSL,DELTA,X(1),X(2),X(3),X(4))
      DO 400 I=1,4
  3   XA(L,I)=X(I)
      PAT1(I)=CDSQRT(PA1(I))
      IF (SW2.EQ.1.) GO TO 375
      PATT1(I)=CV*PAT1(I)*VJ
      TA1(I)=K(I)*PATT1(I)
      IF(SW.EQ.1.) GO TO 45
      TA2(I)=K(I)*CV
      GO TO 55
 45   P2=KPER2*KII2
      PT2=CDSQRT(P2)
      PA2=KII2/KPER2
      PAT2=CDSQRT(PA2)
      PATT2=CV*PAT2
      PBTT2=CV2*PAT2
      TA2(I)=K(I)*PATT2
      TB2(I)=K(I)*PBTT2
 55   TR1(I)=RB1*TA1(I)
      TR2(I)=RB2*TA2(I)
      IF(SW.EQ.1.) GO TO 25C
      AT2(I)=TA2(I)
      AR2(I)=TR2(I)
      IF(AT2(I).LT.0.) GO TO 100
      GO TO 150
 100  TA2(I)=-TA2(I)
 150  IF(AR2(I).LT.0.) GO TO 200
      GO TO 250
 200  TR2(I)=-TR2(I)
 250  TA2J(I)=TA2(I)*VJ
      TR2J(I)=TR2(I)*VJ
      IF (SW.EQ.1.) GO TO 26C
      A2(I)=TR2J(I)
      GO TO 270
 260  TB2J(I)=TB2(I)*VJ
 270  A1(I)=TA1(I)
      IF(ABS(AIMAG(A1(I))).GT.170.) GO TO 280
      GO TO 300
 280  JOTA1(I)=DCMPLX(1.0D5C,1.0D50)
      JOTR1(I)=DCMPLX(1.0D5C,1.0D50)
      J1TR1(I)=DCMPLX(1.0D5C,1.0D5C)
      GO TO 320
```

```
300   CALL CDBESJ(TA1(I),JOTA1(I),J1TA1(I),YOTA1(I),Y1TA1(I))
      CALL CDBESJ(TR1(I),JOTR1(I),J1TR1(I),YOTR1(I),Y1TR1(I))
      J1JOR(I)=J1TR1(I)/JCTA1(I)
320   IF(SW.EQ.1.) GO TO 36C
      IF(ABS(AIMAG(A2(I))).GT.170.) GO TO 340
      GO TO 360
340   K1KOR(I)=-VJ*VJ
      KORAR(I)=-VJ*VJ
      GO TO 380
360   CALL CDBESJ(TA2J(I),JCTA2J(I),J1TA2J(I),YOTA2J(I),Y1TA2J(I))
      CALL CDBESJ(TR2J(I),JOTR2J(I),J1TR2J(I),YOTR2J(I),Y1TR2J(I))
      KOTA2(I)=1.57C796*(VJ*JOTA2J(I)-YOTA2J(I))
      K1TR2(I)=-1.570796*(J1TR2J(I)+VJ*Y1TR2J(I))
      KOTR2(I)=1.57C796*(VJ*JOTR2J(I)-YOTR2J(I))
      K1KOR(I)=K1TR2(I)/KCTA2(I)
      KORAR(I)=KOTR2(I)/KOTA2(I)
      IF (SW.EQ.0.) GO TO 38C
      CALL  CDBESJ(TB2J(I),JCTB2J(I),J1TB2J(I),YOTB2J(I),Y1TB2J(I))
      YIOTA2(I)=JOTA2J(I)
      YIOTB2(I)=JCTB2J(I)
      YIOTR2(I)=JOTR2J(I)
      YI1TR2(I)=-VJ*J1TR2J(I)
      KOTB2(I)=1.570796*(VJ*JOTB2J(I)-YOTB2J(I))
      RDR(I)=YIOTA2(I)*KOTB2(I)-YIOTB2(I)*KOTA2(I)
      RNR1(I)=YI1TR2(I)*KOTB2(I) +YIOTB2(I)*K1TR2(I)
      RNR(I)=YIOTR2(I)*KCTB2(I) - YIOTB2(I)*KOTR2(I)
      RNDR1(I)=RNR1(I)/RDR(I)
      RNDR(I)=RNR(I)/RCR(I)
      GO TO 380
375   RBB1(I)=2.4048*RB1
      TR1(I)=DCMPLX(RBB1(I),C.DO)
      CALL CDBESJ(TR1(I),JOTR1(I),J1TR1(I),YOTR1(I),Y1TR1(I))
380   VJKZ(I)=VJZ*K(I)
      F(I)=W-K(I)
      FF(I)=F(I)*F(I)
      AJKZ(I)=-VJKZ(I)
      FK(I)=CDEXP(-VJKZ(I))
      FFF(I)=1./R*FF(I)*FK(I)
      FFFF(I)=XA(L,I)/DELTA(I)*FFF(I)
      J1BZ(L,I)=XA(L,I)*JCTR1(I)*FK(I)
      V1BZ(L,I)=-1./(W*DELTA(I))*F(I)*J1BZ(L,I)
      POT(L,I)=1./(W*K(I)*DELTA(I))*FF(I)*J1BZ(L,I)
      ER1(L,I)=FFFF(I)*PAT1(I)*J1TR1(I)/W
      EZ1(L,I)=FFFF(I)*JOTR1(I)/W
      IF(SW.EQ.1.) GC TO 381
      IF (SW2.EQ.1.) GO TO 382
      ER2(L,I)=-VJ*TA2(I)/(K(I)*CV)*FFFF(I)*K1KOR(I)*JOTA1(I)/(W)
      EZ2(L,I)=FFFF(I)*KORAR(I)*JOTA1(I)/W
      GO TO 379
381   ER2(L,I)=VJ/W*PAT2    *FFFF(I)*JOTA1(I)*RNDR1(I)
      EZ2(L,I)=1./W*FFFF(I)*JOTA1(I)*RNDR(I)
379   CONTINUE
      BBSER2(L,I)=CDABS(ER2(L,I))
      BBSEZ2(L,I)=CDABS(EZ2(L,I))
382   BBSJBZ(L,I)=CDABS(J1BZ(L,I))
      BBSVBZ(L,I)=CDABS(V1BZ(L,I))
      BBSPOT(L,I)=CDABS(POT(L,I))
      BBSER1(L,I)=CDABS(ER1(L,I))
400   BBSEZ1(L,I)=CDABS(EZ1(L,I))
383   J1BZT(L)=J1BZ(L,1)+J1BZ(L,2)+J1BZ(L,3)+J1BZ(L,4)
      V1BZT(L)=V1BZ(L,1)+V1BZ(L,2)+V1BZ(L,3)+V1BZ(L,4)
      POTT(L)=POT(L,1)+POT(L,2)+POT(L,3)+POT(L,4)
      ER1T(L)=ER1(L,1)+ER1(L,2)+ER1(L,3)+ER1(L,4)
```

```
      EZ1T(L)=EZ1(L,1)+EZ1(L,2)+EZ1(L,3)+EZ1(L,4)
      IF (SW2.EQ.1.) GO TO 384
      ER2T(L)=ER2(L,1)+ER2(L,2)+ER2(L,3)+ER2(L,4)
      EZ2T(L)=EZ2(L,1)+EZ2(L,2)+EZ2(L,3)+EZ2(L,4)
      ABSER2(L)=CDABS(ER2T(L))
      ABSEZ2(L)=CDABS(EZ2T(L))
      AER(L)=ABSER2(L)
      AEZ(L)=ABSEZ2(L)
384   ABSJ1B(L)=CDABS(J1BZT(L))
      ABSV1B(L)=CDABS(V1BZT(L))
      ABSPOT(L)=CDABS(POTT(L))
      ABSER1(L)=CDABS(ER1T(L))
      ABSEZ1(L)=CDABS(EZ1T(L))
      IF (SW2.EQ.0.) GO TO  391
      AEZ(L)=ABSEZ1(L)
      AER(L)=ABSER1(L)
391   CONTINUE
      AWA(L)=WA(L)
500   CONTINUE
505   WRITE(6,600) (WA(L),(KA(L,I),I=1,4),L=1,N)
      WRITE(6,595) (WA(L),(XA(L,I),I=1,4),L=1,N)
      WRITE(6,610) (WA(L),(J1BZ(L,I),I=1,4),L=1,N)
      WRITE(6,730) (WA(L),(BBSJBZ(L,I),I=1,4),L=1,N)
      WRITE (6,615)(WA(L),J1BZT(L),ABSJ1B(L),L=1,N)
      WRITE(6,620) (WA(L),(V1BZ(L,I),I=1,4),L=1,N)
      WRITE(6,740) (WA(L),(BBSVBZ(L,I),I=1,4),L=1,N)
      WRITE (6,625)(WA(L),V1BZT(L),ABSV1B(L),L=1,N)
      WRITE(6,630)  (WA(L), (POT(L,I),I=1,4),L=1,N)
      WRITE(6,750) (WA(L),(BBSPOT(L,I),I=1,4),L=1,N)
      WRITE (6,635)(WA(L), POTT(L),ABSPOT(L),L=1,N)
      WRITE(6,640)  (WA(L), (ER1(L,I),I=1,4),L=1,N)
      WRITE(6,760) (WA(L),(BBSER1(L,I),I=1,4),L=1,N)
      WRITE (6,645)(WA(L), ER1T(L),ABSER1(L),L=1,N)
      WRITE(6,650)  (WA(L), (EZ1(L,I),I=1,4),L=1,N)
      WRITE(6,780) (WA(L),(BBSEZ1(L,I),I=1,4),L=1,N)
      WRITE (6,655)   (WA(L),EZ1T(L),ABSEZ1(L),L=1,N)
      IF (SW2.EQ.1.) GO TO 385
      WRITE(6,660)  (WA(L), (ER2(L,I),I=1,4),L=1,N)
      WRITE(6,770) (WA(L),(BBSER2(L,I),I=1,4),L=1,N)
      WRITE (6,665)   (WA(L),ER2T(L),ABSER2(L),L=1,N)
      WRITE(6,670)  (WA(L), (EZ2(L,I),I=1,4),L=1,N)
      WRITE(6,790) (WA(L),(BBSEZ2(L,I),I=1,4),L=1,N)
      WRITE (6,675)   (WA(L),EZ2T(L),ABSEZ2(L),L=1,N)
385   WRITE(2,INPUT)
      WRITE(2,900)  (AWA(L),AEZ(L),AER(L),L=1,N)
595   FORMAT('1',T28,'X(I)  VALUES FOR DIFFERENT K VS FREQUENCY'
     1/1X/1X/(2F8.3,8E14.4))
600   FORMAT ('1',T35,'K VALUES OF THE FOUR WAVES VS. FREQUENCY'/1X/
     1T8,'W',T29,'K(1)',T57,'K(2)',T85,'K(3)',T114,'K(4)'/1X/
     1(2F8.3,8E14.4))
610   FORMAT ('1',T28,'AC CURRENT DENSITY MODULATION OF FOUR WAVES VS
     1FREQUENCY'/1X/T8,'W',T27,'J1BZ(1)',T55,'J1BZ(2)',T83,'J1BZ(3)'
     1,T111,'J1BZ(4)'/1X/(2F8.3,8E14.4))
615   FORMAT ('1',T35,'TOTAL AC CURRENT-DENSITY MODULATION VS FREQUENCY'
     1/1X/T30,'W',T65,'J1BZT',T92,'ABSJ1BZT'/1X/1X/(20X,2F10.3,3E20.4))
620   FORMAT('1',T28,'AC VELOCITY MODULATION OF FOUR WAVES VS FREQUENCY'
     1/1X/T8,'W',T27,'V1BZ(1)',T55,'V1BZ(2)',T83,'V1BZ(3)',T111,'V1BZ(4)
     1'/1X/(2F8.3,8E14.4))
625   FORMAT('1',T35,'TOTAL AC VELOCITY MODULATION VS FREQUENCY'/1X/
     1T30,'W',T65,'V1BZT',T92,'ABSV1BZT'/1X/1X/(20X,2F10.3,3E20.4))
630   FORMAT('1',T28,'POTENTIAL INSIDE BEAM OF FOUR WAVES VS FREQUENCY'
     1/1X/T8,'W',T27,'POT(1)',T55,'POT(2)',T83,'POT(3)' ,T111,'POT(4)'
     1/1X/(2F8.3,8E14.4))
```

```
  635  FORMAT ('1', T35,'TOTAL POTENTIAL FUNCTION INSIDE BEAM VS FREQUENC
      1Y'/1X/T30,'W',T65,'POTT',T92,'ABSPOTT'/1X/1X/(20X,2F10.3,3E20.4))
  640  FORMAT ('1',T25,'RADIAL ELECTRIC FIELD INSIDE BEAM OF FOUR WAVES
      1VS FREQUENCY'/1X/T8,'W',T27,'ER1(1)',T55,'ER1(2)',T83,'ER1(3)',
      1T111,'ER1(4)'/1X/(2F8.3,8E14.4))
  645  FORMAT ('1',T30,'TOTAL RADIAL ELECTRIC FIELD INSIDE BEAM VS FREQUE
      1NCY'/1X/T30,'W',T65,'ER1T',T92,'ABSER1T'/1X/1X/(20X,2F10.3,3E20.4
      1))
  650  FORMAT ('1',T25,'AXIAL ELECTRIC FIELD INSIDE BEAMOF FOUR WAVES
      1VS FREQUENCY'/1X
      1/T8,'W',T27,'EZ1(1)',T55,'EZ1(2)',T83,'EZ1(3)',T111,'EZ1(4)'/1X/
      1(2F8.3,8E14.4))
  655  FORMAT ('1',T30,'TOTAL AXIAL ELECTRIC FIELD INSIDE BEAM VS FREQUEN
      1CY'/1X/T30,'W',T65,'EZ1T',T92,'ABSEZ1T'/1X/1X/(20X,2F10.3,3E20.4
      1))
  660  FORMAT ('1',T25,'RADIAL ELECTRIC FIELD OUTSIDE BEAM OF FOUR WAVES
      1VS FREQUENCY'/1X/T8,'W',T27,'ER2(1)',T55,'ER2(2)',T83,'ER2(3)',
      1T111,'ER2(4)'/1X/(2F8.3,8E14.4))
  665  FORMAT ('1',T30,'TOTAL RADIAL ELECTRIC FIELD OUTSIDE BEAM VS FREQU
      1ENCY'/1X/T30,'W',T65,'ER2T',T92,'ABSER2T'/1X/1X/(20X,2F10.3,3E20.
      14))
  670  FORMAT ('1',T25,'AXIAL ELECTRIC FIELD OUTSIDE BEAM OF FOUR WAVES
      1VS FREQUENCY'/1X/T8,'W',T27,'EZ2(1)',T55,'EZ2(2)',T83,'EZ2(3)',
      1T111,'EZ2(4)'/1X/(2F8.3,8E14.4))
  675  FORMAT ('1',T30,'TOTAL AXIAL ELECTRIC FIELD OUTSIDE BEAM VS FREQUE
      1NCY'/1X/T30,'W',T65,'EZ2T',T92,'ABSEZ2T'/1X/1X/(20X,2F10.3,3E20.4
      1))
  730  FORMAT('1',T28,'ABSJ1BZ  VALUES FOR DIFFERENT K VS FREQUENCY '
      1/1X/1X/(2F8.3,4D25.6))
  740  FORMAT('1',T28,'ABSV1BZ  VALUES FOR DIFFERENT K VS FREQUENCY '
      1/1X/1X/(2F8.3,4D25.6))
  750  FORMAT('1',T28,'ABSPOT   VALUES FOR DIFFERENT K VS FREQUENCY '
      1/1X/1X/(2F8.3,4D25.6))
  760  FORMAT('1',T28,'ABSER1   VALUES FOR DIFFERENT K VS FREQUENCY '
      1/1X/1X/(2F8.3,4D25.6))
  770  FORMAT('1',T28,'ABSER2   VALUES FOR DIFFERENT K VS FREQUENCY '
      1/1X/1X/(2F8.3,4D25.6))
  780  FORMAT('1',T28,'ABSEZ1   VALUES FOR DIFFERENT K VS FREQUENCY '
      1/1X/1X/(2F8.3,4D25.6))
  790  FORMAT('1',T28,'ABSEZ2   VALUES FOR DIFFERENT K VS FREQUENCY '
      1/1X/1X/(2F8.3,4D25.6))
  900  FORMAT(3E20.4)
       END
$ENDFILE
```

*****NORMAL TERMINATION: THE NUMBER OF RECORDS PROCESSED IS 00000267

E.2 Computer Program for Normal-Mode Field Calculation as a Function of Axial and Radial Distance

This computer program is essentially the same as the one given in Section E.1 except that in this case the normal-mode quantities are calculated as a function of radius or axial distance at a fixed frequency. Approximately the first two thirds of the program calculates the quantities which are required for normal-mode field calculation at a given frequency. Again switches SW and SW2 have the same meaning as that given in Section E.1. The last one third of the program computes the variation of normal-mode quantities as functions of radius or axial distance. Switch SW3 = 0 allows the program to bypass a section of the program which calculates the radial variation. Again the quantities of interest, such as the real part of the axial and radial electric field and axial distance, are stored in a private file for plotting. Other quantities are printed out in the desired format by a printer. The listing of the computer program follows.

```
$RUN *FORTRAN     SPUNCH=EPL572      PAR=MAP
      IMPLICIT COMPLEX*16(W,K,X,V,J,P,T,E,F,Y), REAL*8(B)
      COMPLEX*16  RWK,RWKCE,DELTA,DELTAA,RDR,RNR1,RNR,RNDR1,RNDR
      COMPLEX*16 RO1BZ,RO1BZT
      COMPLEX*8 A1,A2,AR1
      REAL*8 CV,CWE,CWI,G,R,AT2,AR2,Z,RB1,RB2,ABSJ1B,ABSV1B,ABSPOT,
     1ABSER1,ABSER2,ABSEZ1,ABSEZ2,SYSL,R1INCR,R2INCR,ZINCR,AJKZ,NU,
     2RBB1,CV2,RB1I,RB2I ,ABSRO1
      DIMENSION ZA(200),DELTA(4),XA(200,4), K(4),X(4),RWK(4),RWKCE(4),
     1KK(4),WK(4),WK2(4),WKCE(4),KII1(4),KPER1(4),PA1(4),PAT1(4),
     1PATT1(4),TA1(4),TA2(4),TR1(4),TR2(4),AT2(4),AR2(4),TA2J(4),
     1TR2J(4),J1JOR(4),JOTA1(4),J1TA1(4),YOTA1(4),Y1TA1(4),JOTR1(4),
     1J1TR1(4),YOTR1(4),Y1TR1(4),K1KOR(4),JOTA2J(4),J1TA2J(4),YOTA2J(4),
     1Y1TA2J(4),KOTA2(4),JOTR2J(4),J1TR2J(4),YOTR2J(4),Y1TR2J(4),
     1K1TR2(4),VJKZ(4),F(4),FF(4),FK(4),J1BZ(200,4),V1BZ(200,4),
     1POT(200,4),ER1(200,4),EZ1(200,4),ER2(200,4),EZ2(200,4),
     1J1BZT(200),V1BZT(200),POTT(200),ER1T(200),EZ1T(200),ER2T(200),
     1EZ2T(200),FFF(4),KOTR2(4),KORAR(4),YIOTR2(4)  ,ABSJ1B(200),
     1ABSV1B(200),ABSPOT(200),ABSER1(200),ABSER2(200),ABSEZ1(200),
     1ABSEZ2(200),A1(4),A2(4), AJKZ(4),AEZ(200),AER(200),AWA(200)
     1,FFFF(4),TB2(4),TB2J(4),JOTB2J(4),J1TB2J(4),YOTB2J(4),Y1TB2J(4),
     1YIOTA2(4),YIOTB2(4),KOTB2(4),YI1TR2(4),RDR(4),RNR1(4),RNR(4),
     1RNDR1(4),RNDR(4),RBB1(4),RA(200),AR1(4),AR1R(4),AR1I(4),RO1BZ(200,
     14),RO1BZT(200),ABSRO1(200),BBSRO1(200,4)
      NAMELIST/INPUT1/Z,ZINCR,ZI,RB1,RB2,R1INCR,R2INCR,RB1I,RB2I/INPUT/
     1W,K,N,N1,CV,CV2,CWE,CWI,G,R,SYSL,NU,SW,SW2,SW3
      DATA N,N1,Z,ZI,ZINCR,RB1,RB1I,RB2,RB2I,R1INCR,R2INCR,SW,SW2,SW3/
     110,5,0.0,0.0,0.0,0.0,0.0,0.0,0.0,0.0,0.0,0.0,0.0,0.0/,CWE,CWI,G,
     2NU /1.66E4,0.00489,1.843E3,0.1/
      VJ=DCMPLX(0.D0,1.D0)
      VZERO=DCMPLX(0.D0,0.D0)
      READ(5,INPUT1)
      WRITE(6,INPUT1)
1     READ(5,INPUT,END=999)
      WRITE(6,INPUT)
      WW=W*W
      WCI=WW-CWI
      WCI2=WCI*WCI
      WCE=WW-CWE
      WCE2=WCE*WCE
      WNUJ=W-VJ*NU
      WNUJ2=WNUJ*WNUJ
      WNUCE=WNUJ2-CWE
      DO 40  I=1,4
      KK(I)=K(I)*K(I)
      WK(I)=W-K(I)
      WK2(I)=WK(I)*WK(I)
      WKCE(I)=WK2(I)-CWE
      RWK(I)=R/WK2(I)
      RWKCE(I)=R/WKCE(I)
      KII2=1.-1./WW-G/(W*WNUJ)
      KII1(I)=KII2-RWK(I)
      KPER2=1.-1./WCI-G/(W*WNUCE)*WNUJ
      KPER1(I)=KPER2-RWKCE(I)
      PA1(I)=KII1(I)/KPER1(I)
40    DELTA(I)=1.+WK2(I)*K(I)/(W*CWE)*PA1(I)
      CALL DCOEFF(W,K,SYSL,DELTA,X(1),X(2),X(3),X(4))
      IF(SW3.EQ.0.) GO TO 41
      RB1=0.0
      RB2=RB2I
```

```
41    Z=Z*0.+ZI
      DO 500 L=1,N
      IF (SW3.EQ.1.0) GO TO 43
      IF (L.GT.1) GO TO  377
43    DO 380 I=1,4
      PAT1(I)=DSQRT(PA1(I))
      IF (SW2.EQ.1.) GO TO 375
      PATT1(I)=CV*PAT1(I)*VJ
      TA1(I)=K(I)*PATT1(I)
      IF(SW.EQ.1.) GO TO 45
      TA2(I)=K(I)*CV
      GO TO 55
45    P2=KPER2*KII2
      PT2=DSQRT(P2)
      PA2=KII2/KPER2
      PAT2=DSQRT(PA2)
      PATT2=CV*PAT2
      PBTT2=CV2*PAT2
      TA2(I)=K(I)*PATT2
      TB2(I)=K(I)*PBTT2
55    TR1(I)=RB1*TA1(I)
      TR2(I)=RB2*TA2(I)
      IF(SW.EQ.1.) GO TO 250
      AT2(I)=TA2(I)
      AR2(I)=TR2(I)
      IF(AT2(I).LT.0.) GO TO 100
      GO TO 150
100   TA2(I)=-TA2(I)
150   IF(AR2(I).LT.0.) GO TO 200
      GO TO 250
200   TR2(I)=-TR2(I)
250   TA2J(I)=TA2(I)*VJ
      TR2J(I)=TR2(I)*VJ
      IF (SW.EQ.1.) GO TO 260
      A2(I)=TR2J(I)
      GO TO 270
260   TB2J(I)=TB2(I)*VJ
270   A1(I)=TA1(I)
      IF(ABS(AIMAG(A1(I))).GT.170.) GO TO 280
      GO TO 300
280   JOTA1(I)=DCMPLX(1.0D50,1.0D50)
      JOTR1(I)=DCMPLX(1.0D50,1.0D50)
      J1TR1(I)=DCMPLX(1.0D50,1.0D50)
      GO TO 320
300   CALL CDBESJ(TA1(I),JOTA1(I),J1TA1(I),YOTA1(I),Y1TA1(I))
      AR1(I)=TR1(I)
      AR1R(I)=REAL(AR1(I))
      AR1I(I)=AIMAG(AR1(I))
      IF(AR1R(I).EQ.0.0.AND.AR1I(I).EQ.0.0) GO TO 301
      CALL CDBESJ(TR1(I),JOTR1(I),J1TR1(I),YOTR1(I),Y1TR1(I))
      GO TO 302
301   JOTR1(I)=DCMPLX(1.D0,0.D0)
      J1TR1(I)=VZERO
302   J1JOR(I)=J1TR1(I)/JOTA1(I)
320   IF(SW.EQ.1.) GO TO 360
      IF(ABS(AIMAG(A2(I))).GT.170.) GO TO 340
      GO TO 360
340   K1KOR(I)=-VJ*VJ
      KORAR(I)=-VJ*VJ
      GO TO 380
```

```
360   CALL CDBESJ(TA2J(I),JOTA2J(I),J1TA2J(I),YOTA2J(I),Y1TA2J(I))
      CALL CDBESJ(TR2J(I),JOTR2J(I),J1TR2J(I),YOTR2J(I),Y1TR2J(I))
      KOTA2(I)=1.570796*(VJ*JOTA2J(I)-YOTA2J(I))
      K1TR2(I)=-1.570796*(J1TR2J(I)+VJ*Y1TR2J(I))
      KOTR2(I)=1.570796*(VJ*JOTR2J(I)-YOTR2J(I))
      K1KOR(I)=K1TR2(I)/KOTA2(I)
      KORAR(I)=KOTR2(I)/KOTA2(I)
      IF (SW.EQ.0.) GO TO 380
      CALL  CDBESJ(TB2J(I),JOTB2J(I),J1TB2J(I),YOTB2J(I),Y1TB2J(I))
      YIOTA2(I)=JOTA2J(I)
      YIOTB2(I)=JOTB2J(I)
      YIOTR2(I)=JOTR2J(I)
      YI1TR2(I)=-VJ*J1TR2J(I)
      KOTB2(I)=1.570796*(VJ*JOTB2J(I)-YOTB2J(I))
      RDR(I)=YIOTA2(I)*KOTB2(I)-YIOTB2(I)*KOTA2(I)
      RNR1(I)=YI1TR2(I)*KOTB2(I) +YIOTB2(I)*K1TR2(I)
      RNR(I)=YIOTR2(I)*KOTB2(I) - YIOTB2(I)*KOTR2(I)
      RNDR1(I)=RNR1(I)/RDR(I)
      RNDR(I)=RNR(I)/RDR(I)
      GO TO 380
375   RBB1(I)=2.4048*RB1
      TR1(I)=DCMPLX(RBB1(I),0.D0)
      AR1(I)=TR1(I)
      AR1R(I)=REAL(AR1(I))
      AR1I(I)=AIMAG(AR1(I))
      IF(AR1R(I).EQ.0.C.AND.AR1I(I).EQ.C.0) GO TO 376
370   CALL CDBESJ(TR1(I),JOTR1(I),J1TR1(I),YOTR1(I),Y1TR1(I))
      GO TO 380
376   JOTR1(I)=DCMPLX(1.D0,C.D0)
      J1TR1(I)=VZERO
380   CONTINUE
377   ZA(L)=Z
      VJZ=Z*VJ
      DO 400 I=1,4
      XA(L,I)=X(I)
      VJKZ(I)=VJZ*K(I)
      F(I)=W-K(I)
      FF(I)=F(I)*F(I)
      AJKZ(I)=-VJKZ(I)
      FK(I)=CDEXP(-VJKZ(I))
      FFF(I)=1./R*FF(I)*FK(I)
      FFFF(I)=XA(L,I)/DELTA(I)*FFF(I)
      J1BZ(L,I)=XA(L,I)*JOTR1(I)*FK(I)
      V1BZ(L,I)=-1./(W*DELTA(I))*F(I)*J1BZ(L,I)
      POT(L,I)=1./(W*K(I)*DELTA(I))*FF(I)*J1BZ(L,I)
      ER1(L,I)=FFFF(I)*PAT1(I)*J1TR1(I)/W
      EZ1(L,I)=FFFF(I)*JOTR1(I)/W
      RO1BZ(L,I)=K(I)*(RWK(I)-RWKCE(I)*PA1(I)) *EZ1(L,I)
      BBSRO1(L,I)=CDABS(RO1BZ(L,I))
      IF(SW.EQ.1.) GO TO 381
      IF (SW2.EQ.1.) GO TO 4C0
      ER2(L,I)=-VJ*TA2(I)/(K(I)*CV)*FFFF(I)*K1KOR(I)*JOTA1(I)/(W)
      EZ2(L,I)=FFFF(I)*KORAR(I)*JOTA1(I)/W
      GO TO 400
381   ER2(L,I)=VJ/W*PAT2    *FFFF(I)*JOTA1(I)*RNDR1(I)
      EZ2(L,I)=1./W*FFFF(I)*JOTA1(I)*RNDR(I)
400   CONTINUE
      J1BZT(L)=J1BZ(L,1)+J1BZ(L,2)+J1BZ(L,3)+J1BZ(L,4)
      V1BZT(L)=V1BZ(L,1)+V1BZ(L,2)+V1BZ(L,3)+V1BZ(L,4)
      POTT(L)=POT(L,1)+POT(L,2)+POT(L,3)+POT(L,4)
```

```
      ER1T(L)=ER1(L,1)+ER1(L,2)+ER1(L,3)+ER1(L,4)
      EZ1T(L)=EZ1(L,1)+EZ1(L,2)+EZ1(L,3)+EZ1(L,4)
      RO1BZT(L)=RO1BZ(L,1)+RO1BZ(L,2)+RO1BZ(L,3)+RO1BZ(L,4)
      IF (SW2.EQ.1.) GO TO 384
      ER2T(L)=ER2(L,1)+ER2(L,2)+ER2(L,3)+ER2(L,4)
      EZ2T(L)=EZ2(L,1)+EZ2(L,2)+EZ2(L,3)+EZ2(L,4)
      ABSER2(L)=CDABS(ER2T(L))
      ABSEZ2(L)=CDABS(EZ2T(L))
      AER(L)=ER2T(L)
      AEZ(L)=EZ2T(L)
  384 ABSJ1B(L)=CDABS(J1BZT(L))
      ABSV1B(L)=CDABS(V1BZT(L))
      ABSPOT(L)=CDABS(POTT(L))
      ABSER1(L)=CDABS(ER1T(L))
      ABSEZ1(L)=CDABS(EZ1T(L))
      ABSRO1(L)=CDABS(RO1BZT(L))
      IF (SW2.EQ.0.) GO TO  391
      AEZ(L)=EZ1T(L)
      AER(L)=ER1T(L)
  391 CONTINUE
      Z=Z+ZINCR
      IF (SW3.EQ.0.0) GO TO 500
      IF(L.GE.N1+2) GO TO 386
      RA(L)=RB1
      GO TO 387
  386 RA(L)=RB2
  387 IF (L.GT.N1) GO TO 392
      RB1=RB1+R1INCR
      GO TO 500
  392 IF(L.GE.N1+2) GO TO 393
      RB2=1.0
      GO TO 394
  393 RB2=RB2+R2INCR
  394 RB1=RB1I
  500 CONTINUE
  505 WRITE(6,595) W, (X(I),I=1,4)
      IF(SW3.EQ.1.) GO TO 510
      WRITE(6,602) (ZA(L),(RO1BZ(L,I),I=1,4),L=1,N)
      WRITE(6,603) (ZA(L),(BBSRO1(L,I),I=1,4),L=1,N)
      WRITE(6,604) (ZA(L),RO1BZT(L),ABSRO1(L),L=1,N)
      WRITE (6,615)(ZA(L),J1BZT(L),ABSJ1B(L),L=1,N)
      WRITE (6,625)(ZA(L),V1BZT(L),ABSV1B(L),L=1,N)
      WRITE (6,635)(ZA(L), POTT(L),ABSPOT(L),L=1,N)
      WRITE (6,645)(ZA(L), ER1T(L),ABSER1(L),L=1,N)
      WRITE (6,655)   (ZA(L),EZ1T(L),ABSEZ1(L),L=1,N)
      IF (SW2.EQ.1.) GO TO 385
      WRITE (6,665)   (ZA(L),ER2T(L),ABSER2(L),L=1,N)
      WRITE (6,675)   (ZA(L),EZ2T(L),ABSEZ2(L),L=1,N)
      GO TO 385
  510 WRITE (6,815)(RA(L),J1BZT(L),ABSJ1B(L),L=1,N)
      WRITE (6,825)(RA(L),V1BZT(L),ABSV1B(L),L=1,N)
      WRITE (6,835)(RA(L), POTT(L),ABSPOT(L),L=1,N)
      WRITE (6,845)(RA(L), ER1T(L),ABSER1(L),L=1,N)
      WRITE (6,855)   (RA(L),EZ1T(L),ABSEZ1(L),L=1,N)
      IF (SW2.EQ.1.) GO TO 385
      WRITE (6,865)   (RA(L),ER2T(L),ABSER2(L),L=1,N)
      WRITE (6,875)   (RA(L),EZ2T(L),ABSEZ2(L),L=1,N)
  385 WRITE(2,INPUT)
      IF(SW3.EQ.1.0) GO TO 389
      WRITE(2,900)  ( ZA(L),AEZ(L),AER(L),L=1,N)
```

```
      GO TO 991
  389 WRITE(2,900)  ( RA(L),AEZ(L),AER(L),L=1,N)
  595 FORMAT('1',T28,'X(I)  VALUES FOR DIFFERENT K '
     1/1X/1X/(2F8.3,8E14.4))
  602 FORMAT('1',T28,' AC CHARGE DENSITY MODULATION OF FOUR WAVES
     1 VS Z'/1X/1X/T8,'Z',T27,'RO1BZ(1)',T55,'RO1BZ(2)',T83,'RO1BZ(3)',
     2T111,'RO1BZ(4)'/1X/1X/(F16.3,8E14.4))
  603 FORMAT('1',T28,'ABSRO1BZ VALUES OF FOUR WAVES  VS Z' /1X/1X/
     1(F16.3,4D25.6))
  604 FORMAT('1',T35,'TOTAL CHARGE DENSITY MODULATION VS Z'/1X/1X/
     1T30,'Z',T65,'RO1BZT',T92,'ABSRO1BZT'/1X/1X/(25X,F10.3,5X,
     23E20.4))
  615 FORMAT ('1',T45,'TOTAL AC CURRENT-DENSITY MODULATION VS Z '
     1/1X/T38,'Z',T65,'J1BZT',T92,'ABSJ1BZT'/1X/1X/(20X,1F20.3,3E20.4))
  625 FORMAT('1',T45,'TOTAL AC VELOCITY MODULATION VS   Z      '/1X/
     1T38,'Z',T65,'V1BZT',T92,'ABSV1BZT'/1X/1X/(20X,1F20.3,3E20.4))
  635 FORMAT ('1', T45,'TOTAL POTENTIAL FUNCTION INSIDE BEAM VERSES
     1Z'/1X/T38,'Z',T65,'POTT',T92,'ABSPOTT'/1X/1X/(20X,1F20.3,3E20.4))
  645 FORMAT ('1',T45,'TOTAL RADIAL ELECTRIC FIELD INSIDE BEAM VS
     1Z  '/1X/T38,'Z',T65,'ER1T',T92,'ABSER1T'/1X/1X/(20X,1F20.3,3E20.4
     11))
  655 FORMAT ('1',T45,'TOTAL AXIAL ELECTRIC FIELD INSIDE BEAM VS
     1Z '/1X/T38,'Z',T65,'EZ1T',T92,'ABSEZ1T'/1X/1X/(20X,1F20.3,3E20.4
     11))
  665 FORMAT ('1',T45,'TOTAL RADIAL ELECTRIC FIELD OUTSIDE BEAM VS
     1Z   '/1X/T38,'Z',T65,'ER2T',T92,'ABSER2T'/1X/1X/(20X,1F20.3,3E20.
     14))
  675 FORMAT ('1',T45,'TOTAL AXIAL ELECTRIC FIELD OUTSIDE BEAM VS
     1Z  '/1X/T38,'Z',T65,'EZ2T',T92,'ABSEZ2T'/1X/1X/(20X,1F20.3,3E20.4
     11))
  815 FORMAT ('1',T45,'TOTAL AC CURRENT-DENSITY MODULATION VS R '
     1/1X/T38,'R',T65,'J1BZT',T92,'ABSJ1BZT'/1X/1X/(20X,1F20.3,3E20.4))
  825 FORMAT('1',T45,'TOTAL AC VELOCITY MODULATION VS   R      '/1X/
     1T38,'R',T65,'V1BZT',T92,'ABSV1BZT'/1X/1X/(20X,1F20.3,3E20.4))
  835 FORMAT ('1', T45,'TOTAL POTENTIAL FUNCTION INSIDE BEAM VERSES
     1R'/1X/T38,'R',T65,'POTT',T92,'ABSPOTT'/1X/1X/(20X,1F20.3,3E20.4))
  845 FORMAT ('1',T45,'TOTAL RADIAL ELECTRIC FIELD INSIDE BEAM VS
     1R  '/1X/T38,'R',T65,'ER1T',T92,'ABSER1T'/1X/1X/(20X,1F20.3,3E20.4
     11))
  855 FORMAT ('1',T45,'TOTAL AXIAL ELECTRIC FIELD INSIDE BEAM VS
     1R '/1X/T38,'R',T65,'EZ1T',T92,'ABSEZ1T'/1X/1X/(20X,1F20.3,3E20.4
     11))
  865 FORMAT ('1',T45,'TOTAL RADIAL ELECTRIC FIELD OUTSIDE BEAM VS
     1R   '/1X/T38,'R',T65,'ER2T',T92,'ABSER2T'/1X/1X/(20X,1F20.3,3E20.
     14))
  875 FORMAT ('1',T45,'TOTAL AXIAL ELECTRIC FIELD OUTSIDE BEAM VS
     1R  '/1X/T38,'R',T65,'EZ2T',T92,'ABSEZ2T'/1X/1X/(20X,1F20.3,3E20.4
     11))
  900 FORMAT(3E20.4)
  991 CONTINUE
      GO TO 1
  999 CONTINUE
      END
$ENDFILE
```

*****NORMAL TERMINATION: THE NUMBER OF RECORDS PROCESSED IS 00000294

```
$RUN *FORTRAN   SPUNCH=EPL850   PAR=MAP
      SUBROUTINE DCOEFF(W,K,L,DELTA,X1,X2,X3,X4)
      IMPLICIT COMPLEX*16(W,K,F,S,G,X,V)
      COMPLEX*16 DELTA
      REAL*8 A,R,L
      DIMENSION  A(8,8), R(8,1),K(4),F(4),S(4),G(4),VJKL(4),VJF(4),
     1VJS(4),VJG(4),DELTA(4)
      VJ=DCMPLX(0.D0,1.D0)
      VJL=VJ*L
      EPS=.0000001
      N=1
      M=8
      DO 10  I=1,4
      F(I)=W-K(I)
      F(I)=F(I)/DELTA(I)
      S(I)=1./K(I)*(W-K(I))**2
      S(I)=S(I)/DELTA(I)
      VJKL(I)=VJL*K(I)
 10   G(I)=S(I)*CDEXP(-VJKL(I))
      DO  20  J=1,4
      VJF(J)=VJ*F(J)
      VJS(J)=VJ*S(J)
 20   VJG(J)=VJ*G(J)
      DO 30 I=1,4
      J=2*I-1
      A(2,J)=0.0
      A(1,J)=1.0
      A(3,J)=F(I)
      A(4,J)=-VJF(I)
      A(5,J)=S(I)
      A(6,J)=-VJS(I)
      A(7,J)=G(I)
 30   A(8,J)=-VJG(I)
      DO 40  I=1,4
      J=2*I
      A(1,J)=0.0
      A(2,J)=1.0
      A(3,J)=VJF(I)
      A(4,J)=F(I)
      A(5,J)=VJS(I)
      A(6,J)=S(I)
      A(7,J)=VJG(I)
 40   A(8,J)=G(I)
      R(1,1)=1.0
      DO 50  I=2,8
 50   R(I,1)=0.0
      CALL DGELG(R,A,M,N,EPS,IER)
      X1=DCMPLX(R(1,1),R(2,1))
      X2=DCMPLX(R(3,1),R(4,1))
      X3=DCMPLX(R(5,1),R(6,1))
      X4=DCMPLX(R(7,1),R(8,1))
      RETURN
      END
$ENDFILE

*****NORMAL TERMINATION: THE NUMBER OF RECORDS PROCESSED IS 00000054
```

APPENDIX F. CALCULATION OF RF FIELD STRENGTH FROM RF LANGMUIR PROBE MEASUREMENTS

A simple calculation is presented here to deduce the radial RF electric-field strength from the RF Langmuir probe measurements. A schematic circuit diagram is shown in Fig. F.1. The probe is connected to a dc ground through a 100-kΩ resistor and the capacitively coupled ac voltage is fed to a wideband RF amplifier. The output of this amplifier is measured by a VTVM via an integrator (the need for the integrator is discussed in Section 3.2.2).

The oscillatory charge induced on the probe surface in the presence of an RF electric field E is given by

$$Q = \epsilon_o E A_{eff} = \epsilon_o E F A \quad , \tag{F.1}$$

where A is the actual area of the probe surface and F is a factor by which the probe area is multiplied to obtain the effective probe area A_{eff}. The factor F appears because of distortion of the field by the presence of the probe. The current which flows through the external circuit is obtained by dQ/dt and for the steady state is given by

$$|i| = |j\omega Q| \quad . \tag{F.2}$$

The voltage which appears across the input of the amplifier terminals is thus

$$v_i = R_o i \quad , \tag{F.3}$$

where $R_o = 50\ \Omega$ and is the input resistance of the amplifier. The voltage

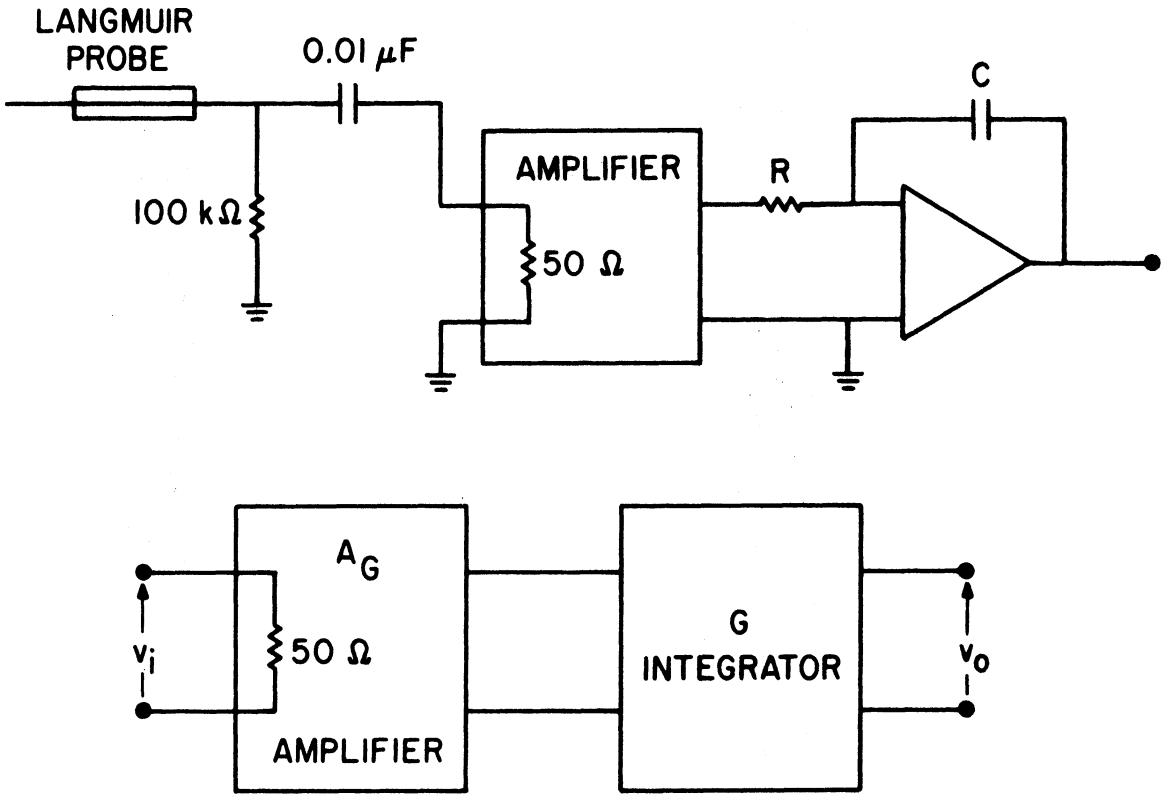

FIG. F.1 SCHEMATIC CIRCUIT DIAGRAM OF THE RF LANGMUIR PROBE DETECTION CIRCUITS.

at the output of the integrator is simply

$$|v_o| = |A_G| \, |G| \, |v_i| \quad , \tag{F.4}$$

where A_G is the voltage gain of the amplifier and G is the gain of the integrator.

From Eqs. F.1 through F.4 the electric-field strength is given by

$$E = \frac{v_o}{R_o} \frac{RC}{A_G \epsilon_o AF} \quad , \tag{F.5}$$

where the gain of the integration has been assumed to be

$$|G| = \frac{1}{\omega RC} \quad .$$

R and C are the values of the resistor and capacitor of the integrator.

In a typical measurement at the second peak v_o = 35 mV. The other parameters are A_G = 100, R_o = 50 Ω and the product RC = 1 x 10^{-8} for the particular gain characteristic of the integrator used. The diameter of the probe wire is 0.01 inch and the length is 1.25 cm, therefore the probe area is A = 1 x 10^{-5} m^2. Substitution of these values in Eq. F.5 yields

$$E \cong \frac{8}{F} \ (V/cm) \quad . \tag{F.6}$$

For $0 < F < 1$, the field strength is of the order of a few tens of volts per centimeter.

LIST OF REFERENCES

1. Tonks, L. and Langmuir, I., "Oscillations in Ionized Gases," Phys. Rev., vol. 33, No. 2, pp. 195-210, February 1929.

2. Gould, R. W., Furth, H. P., Post, R. F. and Ribe, F. L., "Progress in Controlled Thermonuclear Research," Division of Research, U. S. Atomic Energy Commission, December 1970.

3. Lawson, J. D., "Some Criteria for a Power Producing Thermonuclear Reactor," Proc. Phys. Soc. (London), vol. B-70, pp. 6-10, January 1957.

4. Allis, W. A., Buchsbaum, S. J. and Bers, A., Waves in Anisotropic Plasmas, The M.I.T. Press, Cambridge, Mass., 1963.

5. Stix, T. H., The Theory of Plasma Waves, McGraw-Hill Book Co., Inc., New York, 1962.

6. Bohm, D. and Gross, E. P., "Theory of Plasma Oscillations. A. Origin of Medium-Like Behavior," Phys. Rev., vol. 75, No. 12, pp. 1851-1864, June 15, 1949.

7. Bohm, D. and Gross, E. P., "Theory of Plasma Oscillations. B. Excitation and Damping of Oscillations," Phys. Rev. vol. 75, No. 12, pp. 1864-1876, June 15, 1949.

8. Ramo, S., "Space Charge and Field Waves in an Electron Beam," Phys. Rev., vol. 56, No. 3, pp. 276-283, August 1939.

9. Trivelpiece, A. W., Slow Wave Propagation in Plasma Waveguides, San Francisco Press, Inc., San Francisco, Calif., 1967.

10. Trivelpiece, A. W. and Gould, R. W., "Space-Charge Waves in a Cylindrical Plasma Column," J. Appl. Phys., vol. 30, No. 11, pp. 1784-1793, November 1959.

11. Chorney, P., "Propagation in Plasma Waveguides," Quarterly Progress Report No. 57, Research Laboratory of Electronics, Massachusetts Institute of Technology, Cambridge, Mass., April 15, 1960.

12. Suhl, H. and Walker, L. R., "Topics in Guided-Wave Propagation Through Gyrotropic Media," Bell System Tech. J., vol. 33, No. 3, pp. 579-659, May 1954.

13. van Trier, A.A.Th.M., "Guided Electromagnetic Waves in Anisotropic Media," Appl. Sci. Res., Section B, vol. 3, No. 4-5, pp. 305-371, 1954.

14. Ferrari, F. A. and Reddish, A., "Propagation in a Plasma-Filled Waveguide," Proc. Int. Congress on Microwave Tubes, Munich, pp. 548-553, June 1960.

15. Bevc, V., "Power Flow in Plasma-Filled Waveguides," J. Appl. Phys., vol. 37, No. 8, pp. 3128-3137, July 1966.

16. Vlaardingerbroek, M. T. and Weimer, K.R.U., "On Wave Propagation in Beam Plasma Systems in a Finite Magnetic Field," Philips Res. Reports, vol. 18, No. 2, pp. 95-108, April 1963.

17. Berrett, P. O. and Johnson, C. C., "Waves in a Circular Column with General Impedance Boundary Conditions," IEEE Trans. on Nuclear Science, vol. NS-11, No. 1, pp. 34-40, January 1964.

18. Groendijk, H., Vlaardingerbroek, M. T. and Weimer, K.R.U., "Waves in Cylindrical Beam Plasma Systems Immersed in a Longitudinal Magnetic Field," Philips Res. Reports, vol. 20, No. 5, pp. 485-504, October 1965.

19. Bevc, V. and Everhart, T. E., "Fast-Wave Propagation in Plasma-Filled Waveguides," J. Electronics and Control, vol. 13, No. 3, pp. 185-212, September 1962.

20. Likuski, R., "Free and Driven Modes in Anisotropic Plasma Guides and Resonators," Ph.D. Thesis, University of Illinois, 1964.

21. Beck, A.H.W., Space-Charge Waves, Pergamon Press, New York, 1958.

22. Crawford, F. W., "Microwave Plasma Devices--Promise and Progress," Proc. IEEE, vol. 59, No. 1, pp. 4-19, January 1971.

23. Smullin, L. D. and Getty, W. D., "Generation of a Hot, Dense Plasma by a Collective Beam-Plasma Interaction," Phys. Rev. Letters, vol. 9, No. 1, pp. 3-6, July 1, 1962.

24. Kharchenko, I. F., Fainberg, Ya. B., Nikolaev, R. M., Kornilov, E. A., Lutsenko, E. I. and Pedenko, N. S., "The Interaction of an Electron Beam with a Plasma in a Magnetic Field," Soviet Phys.--Tech. Phys., vol. 6, No. 7, pp. 551-553, January 1962.

25. Kharchenko, I. F., Fainberg, Ya. F., Kornilov, E. A. and Pedenko, N. S., "Excitation of Oscillations in Plasma by an Electron Beam," Soviet Phys.--Tech. Phys., vol. 9, No. 6, pp. 798-802, December 1964.

26. Oakes, M. E. and Schluter, H., "Damping at the Lower Hybrid Resonance in a Warm Partially Ionized Plasma," Ann. Phys., vol. 35, No. 3, pp. 396-409, December 1965.

27. Frank-Kamenetskii, D. A., "Magnetosonic Resonance in Plasma," Soviet Phys.--Tech. Phys. vol. 5, No. 8, pp. 847-852, February 1961.

28. Haas, G. M., Ard, W. B., Becker, M. C., Dandl, R. A., England, A. C., Livesey, R. L., Matlock, O. D. and McGuffin, M. W., "Ion Heating Using a Modulated Electron Beam," Report No. ORNL 4063, Thermonuclear Division, Oak Ridge National Laboratory, Oak Ridge, Tenn., pp. 40-52, January 1967.

29. Korper, V. K., "Schwingung eines Plasmazylinders in einen Auberen Magnetfeld," Z. Naturforsch., vol. 12a, pp. 815-821, 1957. Also in Z. Naturforsch., vol. 15a, pp. 220-226, 1960.

30. Auer, P. L., Hurwitz, H., Jr. and Miller, R. D., "Collective Oscillations in a Cold Plasma," Phys. Fluids, vol. 1, No. 6, pp. 501-514, November-December 1958.

31. Seshadri, S. R., "Excitation of Plasma Waves in an Unbounded Homogeneous Plasma by a Line Source," IEEE Trans. on Microwave Theory and Techniques, vol. MTT-11, No. 1, pp. 39-50, January 1963.

32. Kuehl, H. H., "Excitation of Waves in a Warm Plasma by a Current Source," Phys. Fluids, vol. 6, No. 10, pp. 1465-1469, October 1963.

33. Demidov, V. P., "The Excitation of a Waveguide with Plasma by Means of Specified Currents," Soviet Phys.--Tech. Phys., vol. 7, No. 5, pp. 400-403, November 1962.

34. Mikhailovskii, A. B. and Pashitski, E. A., "Convective Excitation of Ion Plasma Waves by an Inhomogeneous Electron Beam," Soviet Phys.--Tech. Phys., vol. 11, No. 5, pp. 571-580, November 1966.

35. Aleksin, V. F. and Stepanov, K. N., "External Current Excitation of Electromagnetic Waves in a Plasma," Soviet Phys.--Tech. Phys., vol. 9, No. 7, pp. 938-947, January 1965.

36. Kino, G. S. and Gerchberg, R., "Transverse Field Interactions of a Beam and Plasma," Phys. Rev. Letters, vol. 11, No. 5, pp. 185-187, September 1963.

37. Vermeer, A., Matitti, T., Hopman, H. J. and Kistemaker, J., "Excitation of Ion Oscillations by a Beam Plasma Interaction," Plasma Phys., vol. 9, No. 3, pp. 241-254, May/June 1967.

38. Schluter, H., "Observation on the Hybrid Ion Electron Resonance," Phys. Letters, vol. 13, No. 2, pp. 137-138, November 15, 1964.

39. Schluter, H. and Oakes, M. E., "Electrodeless Ring Discharges at the Hybrid Ion Electron Resonances," Proc. 7th Int. Conf. on Phenomenon in Ionized Gases, Belgrade, vol. 2, pp. 374-376, August 1965.

40. Mills, G. S., Oakes, M. E. and Schluter, H., "Hybrid Ion Electron Resonance Frequencies in Finite Plasmas," Phys. Letters, vol. 21, No. 1, pp. 45-47, April 15, 1966.

41. Schluter, H. and Ransom, C. J., "Radio Frequency Plasmas at the Hybrid Ion Electron Resonance," Ann. Phys., vol. 33, No. 3, pp. 360-380, July 1965.

42. Oakes, M. E., Schluter, H. and Wheatley, B. N., "Ion-Electron Hybrid Resonance with Partial Propagation Along the Magnetic Field," Ann. Phys., vol. 41, No. 2, pp. 339-346, February 1967.

43. Reshotko, E., "Resonances in a Cold Multiconstituent Plasma at Arbitrary Orientation to the Magnetic Field," NASA Tech. Note D-1875, Lewis Research Center, Cleveland, Ohio, 1963.

44. Frank-Kamenetskii, D. A., "Natural Oscillations of a Bounded Plasma," Soviet Phys.--JETP, vol. 12, No. 3, pp. 469-475, March 1961.

45. Yakimenko, V. L., "Oscillations in a Cold Plasma Containing Two Ion Species," Soviet Phys.--Tech. Phys., vol. 7, No. 2, pp. 117-124, August 1962.

46. Frank-Kamenetskii, D. A., "Magnetic Sound in Three-Component Plasma," Soviet Phys.--Tech. Phys., vol. 5, No. 8, pp. 842-846, February 1961.

47. Demidov, V. D., Frank-Kamenetskii, D. A. and Yakimenko, V. L., "Magnetic Sound in Hot Plasma," Soviet Phys.--Tech. Phys., vol. 7, No. 19, pp. 875-878, April 1963.

48. Shvets, O. M., Sotnikov, S. M., Tarasenko, V. F. and Ovchinnikov, S. S., "Excitation of Plasma Waves Near the Lower-Hybrid Resonance," Soviet Phys.--Tech. Phys., vol. 14, No. 4, pp. 459-463, October 1969.

49. Hiroe, S. and Ikegami, H., "Excitation of Lower-Hybrid Oscillations at Upper-Hybrid Resonance by Microwaves," Phys. Rev. Letters, vol. 19, No. 25, pp. 1414-1416, December 18, 1967.

50. Haas, G. M. and Eisner, M. A., "Ion Heating at the Electron-Ion Hybrid Resonance Frequency," Bull. Amer. Phys. Soc., Series 2, vol. 13, p. 1517, November 1968.

51. Haas, G. M. and Eisner, M., "Ion Heating by a Modulated Electron Beam," Phys. Fluids, vol. 14, No. 3, pp. 606-610, March 1971.

52. Bhatnagar, V. P. and Getty, W. D., "Comments on Ion Heating by a Modulated Electron Beam," Phys. Fluids (to be published).

53. Kovan, I. A. and Spektor, A. M., "Ion Heating in the Excitation of Magneto-Acoustic Oscillations in Plasma," Soviet Phys.--JETP, vol. 26, No. 4, pp. 747-751, April 1968.

54. Bartov, A. V., Zavoysky, E. K., Kovan, I. A., Patrushev, B. I., Rusanov, V. D. and Frank-Kamenetskii, D. A., "Experimental Study of Magneto-Acoustic Resonance," Nucl. Fusion Supplement, Part 3, pp. 1067-1071, 1962.

55. Akhmartov, A. P. et al., "Magneto-Acoustic Resonance in a Plasma," Soviet Phys.--JETP, vol. 12, No. 3, pp. 376-381, March 1961.

56. Pashitski, E. A., "Interaction of a Modulated Charged Particle Beam with a Plasma in a Magnetic Field," Soviet Phys.--Tech. Phys., vol. 14, No. 2, pp. 149-162, August 1969.

57. Pashitskii, E. A., "Interaction of an Electron Beam with a Plasma in a Magnetic Field," Soviet Phys.--Tech. Phys., vol. 8, No. 1, pp. 34-42, July 1963.

58. Vodyanitiski, A. A. and Kondratenko, A. V., "Energy Loss of a Modulated Axial Current in a Bounded Magnetoactive Plasma," Soviet Phys.--Tech. Phys., vol. 13, No. 1, pp. 34-40, July 1968.

59. Vermeer, A., Hopman, H. J., Matitti, T. and Kistemaker, J., "Survey of Instabilities in a Beam Plasma Experiment," Proc. 7th Int. Conf. on Phenomenon in Ionized Gases, Belgrade, vol. 2, pp. 386-393, August 1965.

60. Vermeer, A. and Kistemaker, J., "The Instability Near the Ion-Plasma Frequency in a Beam-Plasma System," Plasma Phys., vol. 12, No. 2, pp. 95-103, February 1970.

61. Crawford, F. W., "Beam-Plasma Interaction in a Warm Plasma," Int. J. Electronics, vol. 19, No. 3, pp. 217-232, September 1965.

62. Hahn, W. C., "Small-Signal Theory of Velocity-Modulated Electron Beams," General Electric Rev., vol. 42, No. 6, pp. 258-270, June 1939.

63. Shoucri, M. M., "Dispersive Properties for a Bounded Finite-Temperature Beam-Plasma System," Plasma Phys., vol. 11, No. 5, pp. 429-447, May 1969.

64. Seidl, M., "Temperature Effects on High-Frequency Beam-Plasma Interactions," Phys. Fluids, vol. 13, No. 4, pp. 966-979, April 1970.

65. Rogashkova, A. I. and Tseitlin, M. B., "Effect of Inhomogeneities in a Plasma Waveguide on the Propagation of Slow Waves and on Electron-Beam Interactions," Soviet Phys.--Tech. Phys., vol. 15, No. 9, pp. 1463-1470, March 1971.

66. Briggs, R. J., Electron-Stream Interaction with Plasmas, The M.I.T. Press, Cambridge, Mass., 1964.

67. Lieberman, M. A., "Ion Oscillations Excited by Electron Beam-Plasma Interaction," Ph.D. Thesis, Massachusetts Institute of Technology, 1966.

68. Puri, S., "Electron-Beam Interactions with Ions in a Warm Plasma," Masters Thesis, Massachusetts Institute of Technology, 1964.

69. Wallace, R. N., "An Investigation of Complex Waves in an Electron Beam-Plasma System," Masters Thesis, Massachusetts Institute of Technology, 1964.

70. Chou, S., "Electron-Beam Interaction with Ions in a Plasma," Masters Thesis, Massachusetts Institute of Technology, 1967.

71. Benham, W. E., "Theory of the Internal Action of Thermionic Systems at Moderately High Frequencies," Phil. Mag., Part I, vol. 5, pp. 641-662, 1928; Part II, vol. 11, pp. 457-517, 1931.

72. Llewellyn, F. B. and Bowen, A. E., "The Production of Ultra-High-Frequency Oscillation by Means of Diodes," Bell System Tech. J., vol. 18, No. 2, pp. 280-291, April 1939.

73. Marcum, J., "Interchange of Energy Between an Electron Beam and Oscillating Electric Field," J. Appl. Phys., vol. 17, No. 1, pp. 4-11, January 1946.

74. Jepsen, R. L., "Ion Oscillations in Electron Beam Tubes; Ion Motion and Energy Transfer," Proc. IRE, vol. 45, No. 8, pp. 1069-1080, August 1957.

75. Bartsch, R. R., "Investigation of Nonsynchronous Beam-Plasma Interaction," Ph.D. Thesis, Massachusetts Institute of Technology, 1968.

76. Wesselberg, T., "A General Theory of Klystrons with Arbitrary Extended Interaction Fields," Report No. 376, Microwave Laboratory, Stanford University, Stanford, Calif., March 1957.

77. Frey, J. and Birdsall, C. K., "Instabilities in a Neutralized Electron Stream in a Finite Length Drift Tube," J. Appl. Phys., vol. 37, No. 5, pp. 2051-2061, April 1966.

78. Gerwin, R. and Nelson, D. J., "Two-Stream Instability in a Finite Length," Report No. D1-82-0332, Boeing Scientific Research Laboratories, Seattle, Wash., March 1964.

79. Ketterer, F. D., "Electro-Mechanical Streaming Interaction," Ph.D. Thesis, Massachusetts Institute of Technology, 1965.

80. Buchsbaum, S. J., "Resonance in a Plasma with Two Ion Species," Phys. Fluids, vol. 3, No. 3, pp. 418-420, May/June 1960.

81. Åström, E., "On Waves in an Ionized Gas," Arkiv Fysik, vol. 2, No. 5, pp. 443-457, 1951.

82. Dunn, D. A., Nichparenko, W., Simpson, J. E. and Thomassen, K. I., "Oscillations and Noise Generation in a Beam-Generated Plasma," J. Appl. Phys., vol. 36, No. 10, pp. 3273-3275, October 1965.

83. Gillanders, J. D., Private communication.

84. Rosser, J. B., "A Runge-Kutta for all Seasons," SIAM Rev., vol. 9, No. 3, pp. 417-452, July 1967.

85. Birdsall, C. K., Brewer, G. R. and Haeff, A. V., "The Resistive Wall Amplifier," Proc. Inst. Radio Engineers, vol. 41, No. 7, pp. 865-875, July 1953.

86. Self, S. A., "Interaction of a Cylindrical Beam with a Plasma. I. Theory," J. Appl. Phys., vol. 40, No. 13, pp. 5217-5231, December 1969.

87. Thomassen, K. I., "Turbulent Diffusion in a Penning-Type Discharge," Phys. Fluids, vol. 9, No. 9, pp. 1836-1842, September 1966.

88. Spangenberg, K. R., Vacuum Tubes, McGraw-Hill Book Co., Inc., New York, Chap. 13, 1948.

89. Buchsbaum, S. J., Mower, L. and Brown, S. C., "Interaction Between Cold Plasmas and Guided Electromagnetic Waves," Phys. Fluids, vol. 3, No. 5, pp. 806-819, September-October 1960.

90. Chen, F. F., Etievant, C. and Mosher, D., "Measurement of Low-Plasma Densities in a Magnetic Field," Phys. Fluids, vol. 11, No. 14, pp. 811-821, April 1968.

91. Thomassen, K. I., "Microwave Plasma Density Measurements," J. Appl. Phys., vol. 36, No. 11, pp. 3642-3644, November 1965.

92. Drecier, H. and Rich, W. F., "Effect of Plasma Access Holes in Microwave Resonators Used for Determination of Electron Density," Proc. Int. Conf. on Phys. of Quiescent Plasmas, Part III, Paris Ecole Polytechnique, pp. 135-140, 1969.

93. Cobine, J. D., Gaseous Conductors, Theory and Engineering Applications, Dover Publications, Inc., New York, 1952.

94. Bohm, D., Bishop, E.H.S. and Massey, H.S.W., Characteristics of Electrical Discharges in Magnetic Fields, Guthrie, A. and Wakerling, R. K. (Eds.), McGraw-Hill Book Co., Inc., New York, 1949.

95. Allen, J. E., Boyd, R.L.F. and Reynolds, P., "The Collection of Positive Ions by a Probe Immersed in a Plasma," Proc. Phys. Soc. (London), vol. 70, Part 3, No. 447B, pp. 297-304, March 1, 1957.

96. Garscadden, A. and Palmer, R. A., "Comment on the Use of Langmuir Probes for Low-Density Plasma Diagnostics," Amer. J. Phys., vol. 35, No. 11, pp. 1093-1094, November 1967.

97. Chen, F. F., Plasma Diagnostic Techniques, Huddlestone, R. H. and Leonard, S. L. (Eds.), Academic Press, Inc., New York, Chap. 4, 1965.

98. Chen, F. F., "Numerical Computations for Ion Probe Characteristics in a Collisionless Plasma," J. Nuclear Energy, Part C, vol. 7, No. 1, pp. 47-67, January/February 1965.

99. Laframboise, J. G., "Theory of Spherical and Cylindrical Langmuir Probes in a Collisionless Plasma at Rest," Ph.D. Thesis, University of Toronto, 1966.

100. Scharfman, W. E., "Comparison of Modified-Langmuir-Probe Analysis with Computer Solutions of Electrostatic Probes," Phys. Fluids, vol. 11, No. 3, pp. 689-691, March 1968.

101. Roth, J. R. and Clark, M., "Analysis of Integrated Charged Particle Energy Spectra from Gridded Electrostatic Analyzers," NASA Tech. Note D-4718, Lewis Research Center, Cleveland, Ohio, August 1968.

102. Roth, J. R. and Clark, M., "Analysis of Integrated Charged Particle Energy Spectra from Gridded Electrostatic Analyzers," Plasma Phys., vol. 11, No. 2, pp. 131-143, February 1969.

103. Haus, H. A., "Electron-Beam Waves in Microwave Tubes," Proc. Symp. on Electronic Waveguides, New York, pp. 89-132, April 1958.

104. Spangenberg, K. R., Vacuum Tubes, McGraw-Hill Book Co., Inc., New York, Chap. 16, 1948.

105. Sonin, A. A., "Free-Molecule Langmuir Probe and Its Use in Flow Field Studies," Amer. Inst. Aeronautics and Astronautics J., vol. 4, No. 9, pp. 1588-1596, September 1966.

106. Beeth, D. R., Haas, G. M. and Eisner, M., "Beam Heated Ions in a Non-Beam Formed Plasma," Bull. Amer. Phys. Soc., Series 2, vol. 15, No. 11, p. 1408, November 1970.

LIST OF SYMBOLS

A	Effective area of collection of Langmuir probe.
a	Plasma radius.
a_p	Ratio of probe radius to Debye length.
$\hat{a}_x, \hat{a}_y, \hat{a}_z$	Unit vectors along the x-, y- and z-directions.
$\bar{B}_o$	External dc magnetic field intensity (Wb/m^2).
b	Electron-beam radius.
CV	Normalized plasma radius.
c	Velocity of light.
D	Diameter of the probe wire.
$\bar{D}$	Displacement vector.
d	Average distance between the charged particles.
d	Plasma waveguide radius.
d	Inner radius of the microwave cavity.
$\bar{E}$	Electric field of the wave.
$E_{\bar{k}}$	Electric field of the wave in the direction of the propagation of the wave.
E_r, E_φ, E_z	Radial, azimuthal and axial components of the wave electric field.
E_x, E_y, E_z	x-, y- and z-components of the wave electric field.
e	Absolute value of the charge of an electron, and base of natural logarithm.
f	Frequency of operation.
G	Ion-to-electron mass ratio.
$\bar{H}$	Magnetic field intensity of the wave.
He^3	Isotope of helium with mass of three times that of a hydrogen atom.

He^4	Isotope of helium with mass of four times that of a hydrogen atom.
I	Langmuir probe current.
I_o	Zero order modified Bessel function of the first kind.
I_1	First order modified Bessel function of the first kind.
I_b	Average beam current.
I_i	Ratio of ion current collected by the probe to random ion current.
I_m	mth order modified Bessel function of the first kind.
I'_m	Derivative of the mth order modified Bessel function of the first kind with respect to the argument.
I_+	Ion current drawn by a Langmuir probe.
I_-	Electron current drawn by a Langmuir probe.
J	Plasma current density.
J_o	Zero order Bessel function of the first kind.
J_{ob}	Average beam-current density.
J_1	First order Bessel function of the first kind.
J_{1b}	Beam current-density modulation.
J_{1bo}	Beam current-density modulation at the gun end.
J_{1bz}	Axial ac beam-modulation current density.
J_b	Beam convection-current density.
J_{er}	Random electron-current density.
$J_{\bar{k}}$	Current density in the direction of propagation.
J_m	mth order Bessel function of the first kind.
J'_m	Derivation of the mth order Bessel function of the first kind with respect to the argument.
J_s	Source current density.
$J_{sr}, J_{s\varphi}, J_{sz}$	r-, φ- and z-component of the source current density.

J_t	Plasma transverse convection-current density.
J_x	Plasma convection-current density in the x-direction.
K	Normalized propagation constant.
K_o	Zero order modified Bessel function of the second kind.
K_1	First order modified Bessel function of the second kind.
$\bar{\bar{K}}$	Dielectric tensor of a cold plasma.
K_ℓ	Diagonal element of the dielectric tensor of a cold plasma representing a left-hand wave.
K_m	mth order modified Bessel function of the second kind.
K_m	Derivative of the modified Bessel function of the second kind with respect to the argument.
K_r	Diagonal element of the dielectric tensor of a cold plasma representing a right-hand wave.
K_x	Off-diagonal element of the dielectric tensor of a cold plasma.
K_x^o	Off-diagonal element of the dielectric tensor of a cold beam and plasma.
$K_\parallel$	Dielectric constant of a cold plasma parallel to the magnetic field.
$K_\parallel^o$	Dielectric constant of a cold beam and plasma parallel to the magnetic field.
$K_\perp$	Dielectric constant of a cold plasma perpendicular to the magnetic field.
$K_\perp^o$	Dielectric constant of a cold beam and plasma perpendicular to the magnetic field.
k	Boltzmann constant, 1.38×10^{-23} J/°K.
k_o	Free-space propagation constant.
$\bar{k}$	Propagation vector.
k, θ, φ	Spherical coordinate system for the propagation vector k.
k_z	Axial propagation constant.

k_{zi}	Axial propagation constant for the ith mode.
L	Langmuir probe length, m.
L	Length of the system, m.
M	Mass of an ion, kg.
m	Mass of an electron, kg.
m	Azimuthal mode number.
m_k	Mass of the kth particle, kg.
N	Neutral-particle density, cm^{-3}.
N_D	Number of charged particles in a Debye sphere.
NU	Normalized collision frequency.
n	Particle density, electron density, radial mode number, and neutron.
n_o	Plasma density.
$\bar{n}$	Refractive index.
n_i	Ion density.
n_k	Density of the kth particle.
n_p	Peak plasma density.
n(r)	Radial plasma density profile.
p	Proton.
p_{mn}	nth root of the mth order Bessel function of the first kind.
Q_m	Peak value of the ac induced charge on the probe.
q	Electric charge of a particle.
q_k	Electric charge of the kth particle.
R	Radius of the plasma in the microwave cavity.
RB1	Normalized radial distance in Region I.
RB2	Normalized radial distance in Region II.
r	Radius vector.

r,θ,z	Cylindrical coordinate system.
$r_{\ell e}$	Electron Larmor radius.
$r_{\ell i}$	Ion Larmor radius.
r_p	Probe radius.
S	Perveance of the electron beam.
SYSL	Normalized length of the system.
T	Temperature in °K characterizing the motion of particles, and transverse propagation constant.
T_1	Transverse propagation constant in Region I.
T_{1i}	Transverse propagation constant for the ith mode in Region I.
T_2	Transverse propagation constant in Region II.
T_{2i}	Transverse propagation constant for the ith mode in Region II.
$\bar{\bar{T}}$	Matrix of coordinate transformation.
T_e	Electron temperature.
$\bar{\bar{U}}$	Unity tensor.
U_e	Time-averaged electron energy.
U_i	Time-averaged ion energy.
V	Langmuir probe potential.
V_b	Beam voltage.
V_p	Plasma potential.
v_o	Drift velocity of the plasma electrons, and drift velocity of the electron beam.
v_{1bz}	Axial ac beam-modulation velocity.
$\bar{v}_b$	Beam velocity.
$\bar{v}_k$	Macroscopic particle velocity for the kth particle.
v_p	Phase velocity of the wave.
v_T	Mean square longitudinal thermal velocity of the electrons.

W	Normalized frequency.
WCE	Normalized electron-cyclotron frequency.
WCI	Normalized ion-cyclotron frequency.
X_i	Coefficients in the normal-mode analysis.
x,y,z	Rectangular coordinate system.
Z	Normalized axial distance.
$Z_k e$	Magnitude of the charge.
β_e	Electronic propagation constant.
β_q	Change in electronic propagation constant due to finite geometry effects.
γ_o	Space-charge reduction factor.
$\Delta\omega$	Resonant frequency shift of the microwave cavity due to the plasma (rad/s).
ϵ	Dielectric constant of the medium.
ϵ_o	Permittivity of free space, 8.854×10^{-12} F/m.
ϵ_k	Sign of the electronic charge.
η	Ratio of probe voltage to electron temperature in eV.
θ	Angle of propagation vector with respect to external magnetic field.
θ_{res}	Resonant cone angle.
λ_D	Debye length.
μ	Reduced mass of an electron.
μ_o	Permeability of free space.
$\bar{\nu}$	Charge exchange collision frequency.
ν^*	Effective collision frequency (Eq. 1.20).
ν_{ei}	Electron-ion collision frequency.
ν_{eN}	Electron-neutral collision frequency.

ν_{kN} Collision frequency of the collisions between kth and neutral particles.

ρ Plasma charge density.

ρ_o Average plasma charge density.

ρ_{ob} Average electron-beam charge density.

ρ_{1b} Ac beam-modulation charge density.

ρ_b Electron-beam charge density.

ρ_L Line charge density.

ρ_m Mass density of the particles.

ρ_s Source charge density.

$\bar{\bar{\sigma}}$ Conductivity tensor for a cold plasma.

σ_x Off-diagonal element of the conductivity tensor of a cold plasma.

Lower

$\sigma_{\parallel}$ Conductivity of a cold plasma parallel to the magnetic field.

$\sigma_{\perp}$ Conductivity of a cold plasma perpendicular to the magnetic field.

er

Φ^I Electrostatic potential in Region I.

Φ^{II} Electrostatic potential in Region II.

ω Frequency of operation (rad/s).

ω' Doppler-shifted frequency modified by collisions (rad/s).

ω_{ce} Electron-cyclotron frequency (rad/s).

ω_{ci} Ion-cyclotron frequency (rad/s).

ω_{ck} Cyclotron frequency for the kth particle (rad/s).

ω_{co} Cutoff frequency of the plasma waveguide (rad/s).

ω_D Doppler-shifted frequency (rad/s).

ω_{Di} Doppler-shifted frequency for the ith mode (rad/s).

ω_{LH} Lower-hybrid resonant frequency (rad/s).

$\omega_{LH\theta}$	Lower-hybrid resonant frequency for oblique propagation (rad/s).
ω_p	Plasma frequency (rad/s).
ω_{pb}	Beam-electron plasma frequency (rad/s).
ω_{pe}	Electron-plasma frequency (rad/s).
ω_{pi}	Ion-plasma frequency (rad/s).
ω_{po}	Peak plasma frequency (rad/s).
ω_r	Resonant frequency of the microwave cavity (rad/s).
ω_{UH}	Upper-hybrid resonant frequency (rad/s).

ν_{eN}	Electron-neutral collision frequency.